Journal of Heat Transfer

Published Monthly by ASME

VOLUME 128 • NUMBER 12 • DECEMBER 2006

SPECIAL ISSUE ON BOILING, TWO-PHASE FLOW HEAT TRANSFER, AND INTERFACIAL PHENOMENA

PREFACE

REVIEW ARTICLE

RESEARCH PAPERS

TECHNICAL BRIEF

(**Contents continued on inside back cover**)

Editor, **YOGESH JALURIA (2010)**
Assistant to the Editor, **S. PATEL**

Associate Editors
Gautam Biswas, Indian Institute of Technology, Kanpur (2009)
Louis C. Burmeister, University of Kansas (2008)
Minking Chyu, University of Pittsburgh (2009)
Suresh V. Garimella, Purdue University (2007)
A. Haji-Sheikh, University of Texas at Arlington (2008)
Anthony M. Jacobi, University of Illinois (2008)
Yogendra Joshi, Georgia Institute of Technology (2008)
Satish G. Kandlikar, Rochester Institute of Technology (2007)
Jay M. Khodadadi, Auburn University (2007)
Jose L. Lage, Southern Methodist University (2008)
Sai C. Lau, Texas A&M University (2009)
Ben Q. Li, University of Michigan, Dearborn (2009)
Raj M. Manglik, University of Cincinnati (2009)
Chang H. Oh, Idaho National Laboratory (2007)
Ranga Pitchumani, University of Connecticut (2007)
Ramendra P. Roy, Arizona State University (2007)
Jamal Seyed-Yagoobi, Illinois Institute of Technology (2009)
Bengt Sunden, Lund Institute of Technology, Sweden (2008)
Walter W. Yuen, University of California at Santa Barbara (2008)

Past Editors
V. DHIR
J. R. HOWELL
R. VISKANTA
G. M. FAETH
K. T. YANG
E. M. SPARROW

HEAT TRANSFER DIVISION
Chair, **RODNEY DOUGLASS**
Vice Chair, **TIM TONG**
Past Chair, **MICHAEL JENSEN**

PUBLICATIONS COMMITTEE
Chair, **BAHRAM RAVANI**

OFFICERS OF THE ASME
President, **TERRY E. SHOUP**
Executive Director,
VIRGIL R. CARTER
Treasurer,
THOMAS D. PESTORIUS

PUBLISHING STAFF

Managing Director, Publishing
PHILIP DI VIETRO

Manager, Journals
COLIN McATEER

Production Assistant
MARISOL ANDINO

Transactions of the ASME, Journal of Heat Transfer (ISSN 0022-1481) is published monthly by The American Society of Mechanical Engineers, Three Park Avenue, New York, NY 10016. Periodicals postage paid at New York, NY and additional mailing offices. POSTMASTER: Send address changes to Transactions of the ASME, Journal of Heat Transfer, c/o THE AMERICAN SOCIETY OF MECHANICAL ENGINEERS, 22 Law Drive, Box 2300, Fairfield, NJ 07007-2300. **CHANGES OF ADDRESS** must be received at Society headquarters seven weeks before they are to be effective. Please send old label and new address.

STATEMENT from By-Laws. The Society shall not be responsible for statements or opinions advanced in papers or ... printed in its publications (B7.1, Para. 3).

COPYRIGHT © 2006 by The American Society of Mechanical Engineers. For authorization to photocopy material for internal or personal use under those circumstances not falling within the fair use provisions of the Copyright Act, contact the Copyright Clearance Center (CCC), 222 Rosewood Drive, Danvers, MA 01923, tel: 978-750-8400, www.copyright.com. Request for special permission or bulk copying should be addressed to Reprints/Permission Department.

Canadian Goods & Services Tax Registration #126148048

This journal is printed on acid-free paper, which exceeds the ANSI Z39.48-1992 specification for permanence of paper and library materials. ♾™
♲ 85% recycled content, including 10% post-consumer fibers.

Downloaded 04 Feb 2011 to 194.85.80.107. Redistribution subject to ASME license or copyright; see http://www.asme.org/terms/Terms_Use.cfm

Journal of Heat Transfer Volume 128, Number 12 DECEMBER 2006

DISCUSSION AND CLOSURE

The ASME Journal of Heat Transfer is abstracted and indexed in the following:

Applied Science and Technology Index, Chemical Abstracts, Chemical Engineering and Biotechnology Abstracts (Electronic equivalent of Process and Chemical Engineering), Civil Engineering Abstracts, Compendex (The electronic equivalent of Engineering Index), Corrosion Abstracts, Current Contents, E & P Health, Safety, and Environment, Ei EncompassLit, Engineered Materials Abstracts, Engineering Index, Enviroline (The electronic equivalent of Environment Abstracts), Environment Abstracts, Environmental Engineering Abstracts, Environmental Science and Pollution Management, Fluidex, Fuel and Energy Abstracts, Index to Scientific Reviews, INSPEC, International Building Services Abstracts, Mechanical & Transportation Engineering Abstracts, Mechanical Engineering Abstracts, METADEX (The electronic equivalent of Metals Abstracts and Alloys Index), Petroleum Abstracts, Process and Chemical Engineering, Referativnyi Zhurnal, Science Citation Index, SciSearch (The electronic equivalent of Science Citation Index), Theoretical Chemical Engineering

Journal of Heat Transfer

Preface

On the Advancements in Boiling, Two-Phase Flow Heat Transfer, and Interfacial Phenomena

Raj M. Manglik
Special Issue Editor
Fellow ASME
Thermal-Fluids and Thermal Processing Laboratory,
Department of Mechanical, Industrial and
Nuclear Engineering,
University of Cincinnati,
Cincinnati, OH 45221-0072
e-mail: raj.manglik@uc.edu

Introduction

Phase change by boiling or evaporation is a highly efficient heat transport mechanism, which accommodates large heat fluxes with relatively small driving temperature differences. This mode of heat transfer is in fact encountered in a wide spectrum of engineering systems that include, among others, energy conversion, refrigeration and air-conditioning, chemical thermal processing, heat treatment and manufacturing, microelectronic cooling, and numerous microscale devices (microelectromechanical systems (MEMS), MTMS, μ-TAS, sensors, microheat pipes, biochips or lab-on-chips, etc.) that are emerging in the current wave of new developments and changing applications. The consequent research interest, spanning more than two centuries of work with an ever-increasing literature database, is therefore not surprising [1–10]. The energy crunch with attendant needs for higher thermal efficiencies and demands for mitigation of environmental degradation in recent years have further led to efforts to enhance boiling heat transfer [11–15].

The explosive growth in research and its technical literature generation in the last six decades or so [8–10,14,16,17] has considered a variety of fundamental and applied aspects of this intrinsically complex heat transport process in order to advance our basic understanding as well as provide design tools. The continued interest in the field is further articulated in the set of papers appearing in this special issue of the *Journal of Heat Transfer*, and they address the many technical challenges that are still presented by the intricacies of heat transfer by means of boiling and forced-convective two-phase flow, and the concomitant interfacial phenomena. In its evolutionary essence, this field of scientific and engineering engagement is at once quite ancient in its simplicity and elegance of application, and yet complexly modern in its experimental investigations, theoretical modeling, and computational simulations [16,18–20].

Historical Antecedents

Given the present-day advancements in our understanding of boiling, two-phase flow heat transfer, and interfacial phenomena, and the many yet to be resolved issues with the fundamental physics and optimal applications, it is instructive to reflect briefly upon the historical antecedents of the field. An excellent and insightful review of the work up to 1981, with exhaustive annotations that characterize both fundamental and applications-driven developments in the multifacetted unfolding of phase-change heat transfer, has been provided by Bergles [16]. This is further supplemented by the 1987 review by Nishikawa [18], providing a good commentary to link the evolution of basic understanding of boiling with engineering practice as well as the development of enhancement techniques.

The quest to develop mechanical devices based on two-phase processes in ancient western traditions, and as recounted by Bergles [16], can be traced to Archimedes (~287–212 B.C.E.) [21] and the whirling aeolipile of Heron of Alexandria (~60 C.E.) [22]. It was more than 1650 years later that phase-change machines became the prime movers of the Industrial Revolution (~1750–1850), epitomized by the development of a single-acting steam engine by Watt and the subsequent steam-engine-powered locomotives [16,23]. An understanding of the phase-change process represented by film boiling also appeared in this period, when in 1756 the German medical doctor Leidenfrost recorded the evaporation behavior of distilled water droplets on a hot iron spoon and the application of this phenomena (distillation or separation by boiling) to determine the quality or proof of wine or brandy [24]. An advanced and elaborate knowledge of distillation and its practical applications, however, predate this in the ancient eastern traditions [19,25–27]. The classical Indian text *Rasarnavam Rastantram* (~500 B.C.E.), and subsequently Nagarjuna's *Rasratnakar* and *Rasaratna Samuchchaya* (~2nd century C.E.) describe the attendant boiling and condensation processes, and a rather intricately refined distillation technology and apparatus were used in ancient India for the distillation of water, wine, mercury, and zinc, among others [26,28]. Also, quite remarkably, a sophisticated understanding of liquid wetting, surface-tension-driven liquid motion, and capillary forces was available in ancient India [25,27]. In the present-day context, these phenomena form an essential part of the interfacial behavior associated with phase-change heat transfer, and are a basis for developing techniques for enhancing boiling and two-phase flow as well as newer microchannel heat exchangers and microfluidic devices [7,13,29,30].

The beginnings of modern day advancements can perhaps be ascribed to the pioneering work in the 1930s by Jakob and Fritz [31,32], and Nukiyama [33]. Jakob and Fritz [31,32] explored effects of boiling history (or nonreproducibility), heater surface roughness, bubble dynamics, and increase in nucleation sites with heat flux. Nukiyama [33] essentially established the complete boiling curve (as measured by heat transfer from an electrically heated platinum wire) and which has become the cornerstone of representing virtually all nucleate boiling results. In the subsequent decade, McAdams [34] reported the subcooled fully devel-

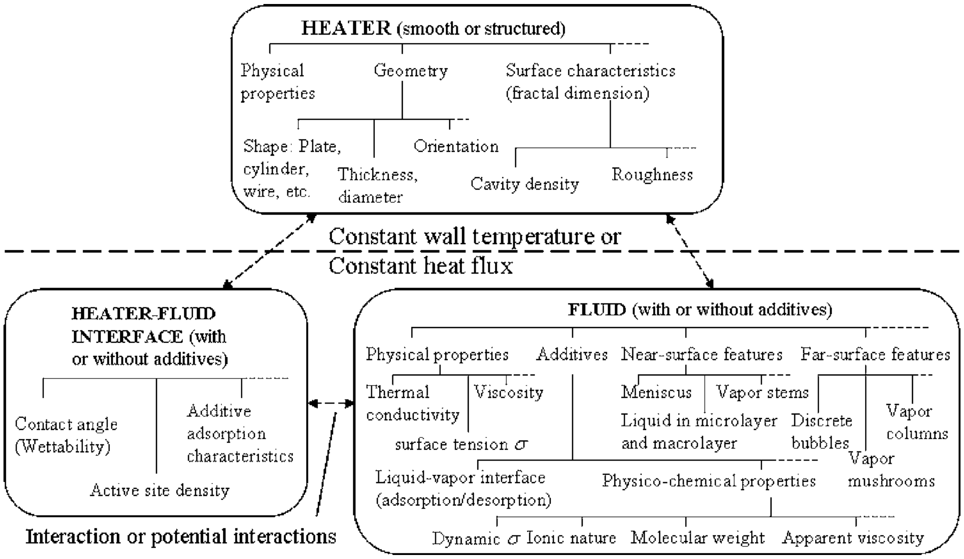

Fig. 1 Schematic statement of the conjugate problem in modeling nucleate boiling heat transfer and attendant interfacial processes (Ref. [43] adapted from Ref. [40])

oped nucleate boiling curve, and Lockhart and Martinelli [35] considered separated two-phase flow pressure drop to develop the classical multiplier function. With rapid developments in nuclear power and aerospace industries in the 1950s, there was an exponential growth in the research literature [16,18]. Notable advancements included the classical nucleate pool boiling correlation proposed by Rohsenow [36], which endures to this day [1–6]. Theoretical models for various mechanistic aspects of the phase-change process (bubble dynamics, microlayer evaporation, nucleation site density and stability, burnout, etc.) were attempted, and they continue to provide the framework for current research. The growing demands for energy and improved process heat transfer efficiencies in the 1960s brought efforts to augment or enhance heat transfer to the fore [12,13,37]. This exploded as a major field of study in the 1970s, driven in part by the space and energy programs and later by the Mid-Eastern countries' "oil embargo." The present-day energy crisis, which is compounded by pressures for mitigating environmental degradation due to excessive energy consumption and imperatives for sustainable development, warrants a generational growth in enhancement science and technology [13,14,38].

In this unfolding, there has been ever growing interest over the last two decades in addressing the problems of two-phase flow and boiling heat transfer, and the concomitant interfacial phenomena. Some of the issues that baffled early research still engage continued activity, as more refined experiments are conducted and theoretical models developed to advance our fundamental as well as applications-oriented understanding [7,12,39–42]. The primary determinants of the general nucleate boiling problem in pure or additive-laden liquids, which has been referred to as a conjugate problem [40,43] that can be essentially classified under three broad categories (heater, fluid, and heater-fluid interface), and the associated potential mechanisms are depicted in Fig. 1. This broad description includes two more prominently employed passive enhancement techniques, by either structuring the heater surface or adding reagents, electrolytes, and/or nanoparticles to the liquid [13,14,44–46]. A direct correlation of the heat transfer with suitable descriptive parameters for all possible phenomenological effects, however, remains elusive because of the intricate nature of the problem.

Current Research

While the complex phase-change heat transfer process in nucleate and/or flow boiling has many parametric determinants, a major part can be considered to be associated with the local heat transfer and hydrodynamics phenomena in the vicinity of ebullience and governed by the solid-liquid-vapor interfacial activity. Schematic illustrations of the primary flow-boiling and CHF regime map, and the interfacial mechanisms that affect liquid-vapor bubble dynamics are given in Fig. 2. In essence, liquid-solid interface wetting and the consequent "film" behavior, along with the transient liquid-vapor interface dynamics and the attendant bubbling characteristics significantly influence boiling performance. The set of papers in this special issue of *Journal of Heat Transfer* address some basic aspects of these processes, as well as issues of heat transfer enhancement and applications of surface-tension driven flow phenomenon.

An extended review of both empirical correlations and mechanistic heat transfer models for predicting the wall heat flux in subcooled flow nucleate boiling is given by Warrier and Dhir [47]. Recognizing the importance of interfacial and microscale effects to the basic boiling and phase-change processes, Fuchs et al. [48], Panchamgam et al. [49], Carey and Wemhoff [50], and Mukherjee and Kandlikar [51] have considered different aspects of thin-film evaporation. Computational simulation, theoretical modeling, and microscale experimentation results are presented to inform the mechanisms that fundamentally govern heat and mass transfer in nucleate pool boiling of pure liquids, binary mixture evaporation, and thin-film phase-change in micropassages. As would be expected in current research [13,14,52], enhancement of heat transfer is the focus of papers by Schneider et al. [53], Ghiu and Joshi [54], and Ahn et al. [55], which explore microchannel flows, performance characteristics of structured surfaces, and novel techniques. Li et al. [56,57] and Cai et al. [58], respectively, have investigated evaporation and CHF in thin capillary wicks, and thermal characteristics of a pulsating heat pipe. Finally, in the best traditions of technical debate and scientific dissemination that bodes well for the vibrancy of heat transfer research, a discussion and its response consider some aspects of the motion of bubbles emanating from a microwire heater.

In his eloquent recounting of the early modern history of boiling and two-phase flow heat transfer, Bergles [16] had predicted that "Looking into the future, there will be much more emphasis on computer solutions of two-phase phenomena." There was also a caveat ("We must remember, however, that the computer codes are only as good as the basic thermal-hydraulic input") with a reminder that experimentation, along with mechanistic modeling, would continue to occupy center stage in scientific and techno-

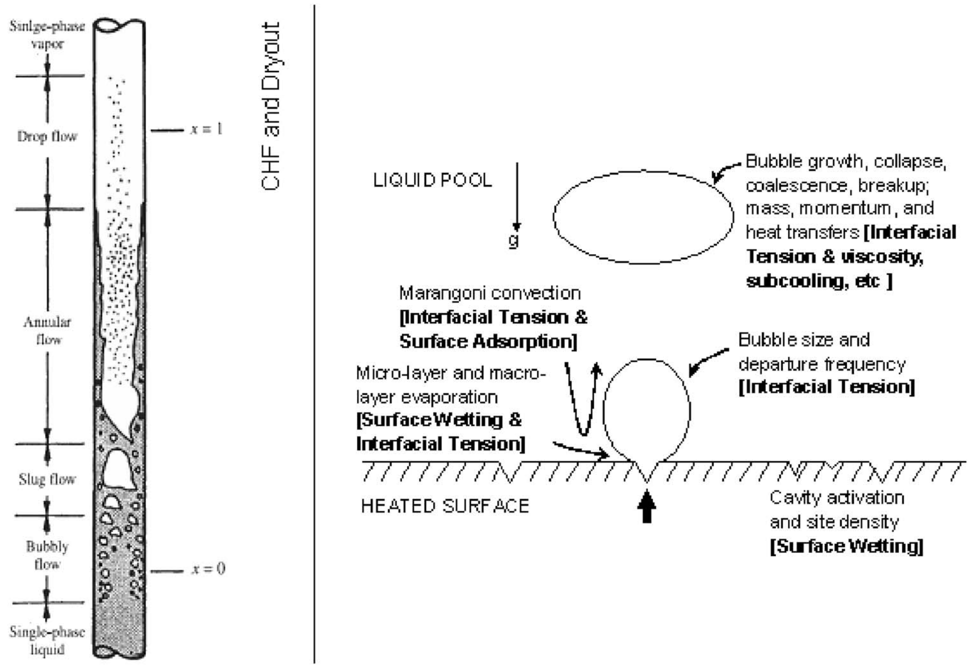

Fig. 2 Flow boiling regimes and CHF in a vertical tube, and the influence of interfacial properties on the nucleation and dynamics of a boiling bubble

logical discoveries. This foresight is indeed reflected in the ensuing articles, and they represent critical efforts in ameliorating imperfections in our understanding of many areas of boiling, two-phase flow heat transfer, and interfacial phenomena, as well as extending the exploitation of these processes to novel and emerging applications.

Future Prospects and Directions

One can safely surmise a vibrant and challenging future of this field of study, which can perhaps be predicted to be marked by many more fundamental studies (both experimental and theoretical or computational) that resolve the gaps in our phenomenological understanding, as well as expand the development of application-oriented performance evaluation and design tools. For the latter, as an example, the scrutiny of diminishing length and time scales (mili-, micro-, and nanoscale) has generated various novel devices (MEMS, MTMS, μ-TAS, microsensors, and lab-on-chips, among others) that in many cases exploit boiling and interfacial phenomena. This has attracted considerable attention to issues relating to microchannel flows [7,59,60], particularly for sustaining very high heat fluxes and thermal management of microelectronic devices, and some enterprising sensor and actuator development. Regardless of the scales of applications, nevertheless, the problems in ebullient phase change and interfacial heat and mass transfer abound [16,18,20,38,40] to provide opportunities for exploring hitherto uncharted dimensions as well as advancing our basic understanding.

An especially vital component of future research, given the growing problems of diminishing energy availability, environmental damage, and thermal management in new technologies, is enhancement of boiling heat transfer. A variety of techniques and schemes have been proposed, developed, and transferred into every-day use [13,15,38]. Prominent among these is to either structure the heated surface to provide pre-existing nucleation sites that tend to be active and stable, or to treat the surface so as to change wetting. A few novel passive and/or active schemes have been proposed in some recent studies [29,30,45,61,62] that exploit surface adsorption and electrokinetics of surface-active molecular additives in solvents in different ways, along with some

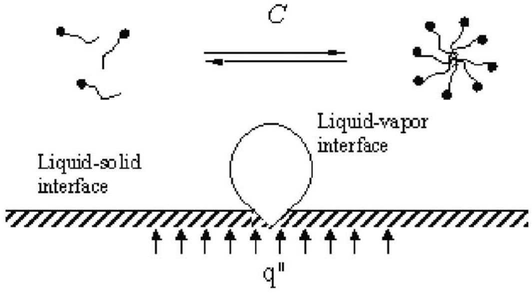

(*a*) Schematic of a nucleated bubble

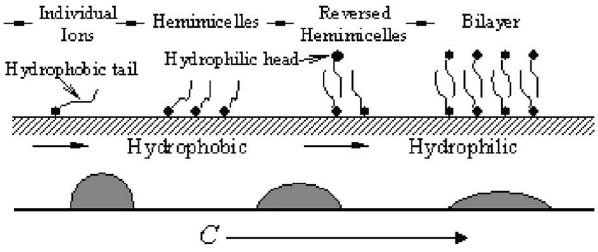

(*b*) Adsorption at the solid-liquid interface

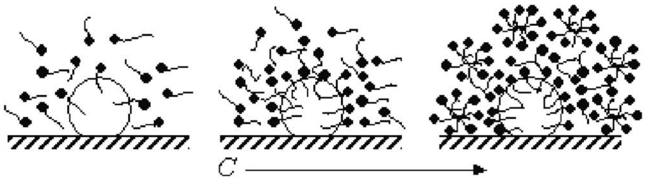

(*c*) Adsorption at the liquid-vapor interface

Fig. 3 Representation of the modification of interfacial phenomena in nucleate boiling in aqueous surfactant solutions (not to scale) Ref. [45]

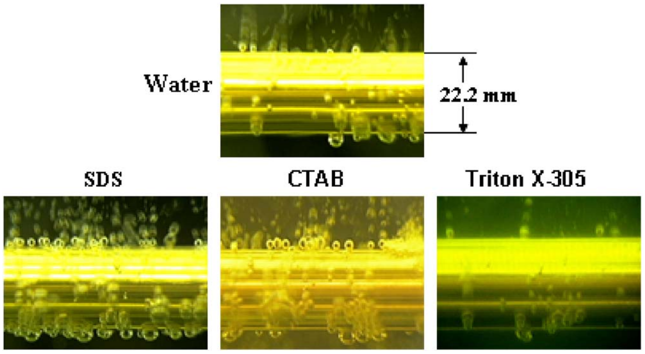

Fig. 4 Boiling behavior in distilled water, and aqueous surfactant (SDS, CTAB, and Triton X-305) solutions in their respective half-micellar concentrations (or $C=0.5\text{CMC}$) and at a heater wall heat flux of $q''_w=20\ \text{kW/m}^2$

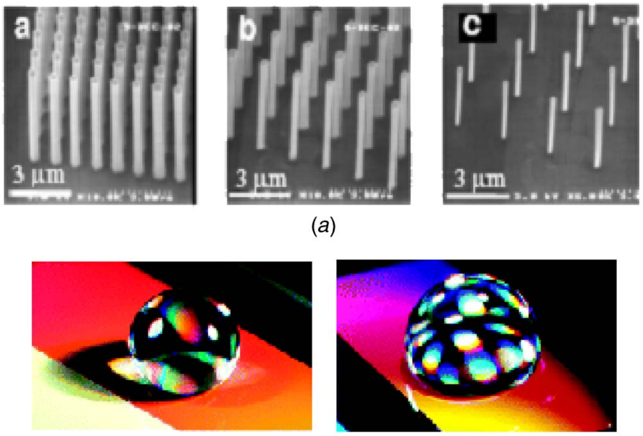

(*a*)

(*b*)

Fig. 6 Dynamic tuning of surface wetting on a nanostructured hydrophobic surface with application of electrical potential Ref. [30] (*a*) surface structure produced on a silicon substrate and (*b*) change in droplet contact angle when an electrical potential is applied

external stimulus in some cases, to produce self-assembled monolayers or micellar layers on the surface and thereby doctoring interfacial properties and wetting.

In a recent set of studies [43–46,63], it has been shown that by adding small quantities of surface-active soluble agents (polymers and surfactants, for example) the liquid-vapor interfacial tension (surface tension) and liquid-solid interfacial tension (wetting) can be altered and decoupled. The additives have a unique long-chain molecular structure composed of a hydrophilic head and a hydrophobic tail, with a natural tendency to adsorb at surfaces and interfaces when added in low concentrations in water. The interfacial changes are caused by their molecular mobility at interfaces, which manifests in a dynamic surface tension behavior (adsorption-desportion at the liquid-vapor interface) and varying surface wetting (physisorption and electrokinetics at the solid-liquid interface). A conceptualization of the molecular dynamics and altered surface tension and wetting is depicted in Fig. 3. These molecular-scale phenomena, modulated by the monomer and/or micellar structure of reagent, distinguishably alter the boiling bubble dynamics, as seen in the typical boiling signatures in three different reagent solutions given in Fig. 4 [45], thereby providing an attractive passive technique for changing (enhancing or degrading, and controlling) "on demand" the nucleate boiling behavior.

A similar theme of controlling surface wettability by using self-assembled monolayers of polymers, or other long-chain molecules that have a hydrophilic head and a hydrophobic tail, but coupling it with the application of an electric potential to tune the surface charge is documented by Lahann et al. [62]. By altering its charge, a surface can be "reversibly" switched from a hydrophobic to hydrophilic state, and vice versa, as schematically depicted in Fig. 5. Another method [30] considers the application of an electrical field to a nanostructured superhydrophobic surface to alter the contact angle of pure liquids. A typical set of surfaces used in this study [30], produced by etching arrays of cylindrical nanosized pins or posts on a silicon wafer, and the changed droplet contact angle when an electrical potential is applied between the droplet and substrate are shown, respectively, in Figs. 6(*a*) and 6(*b*). In yet another scheme, light-induced modification of liquid wetting on a photoresponsive surface (produced by a photoirradiated cover of photoisomerizable monolayer), shown by the droplet motion in Fig. 7, has been reported by Ichimura et al. [61]. All of these techniques, it may be noted, represent what would be termed as compound techniques and require external input of active energy (electric charge or light) along with some form of passive surface modification, and they are a part of growing trend in the enhancement literature [13,38].

In closing, it is perhaps appropriate to reiterate that the challenges of advancing the science and engineering of boiling and two-phase flow heat transfer, and the concomitant interfacial phenomena would expand considerably in the foreseeable future. These would undoubtedly be driven by both large-scale (given our globe's ever increasing energy needs for domestic, commercial,

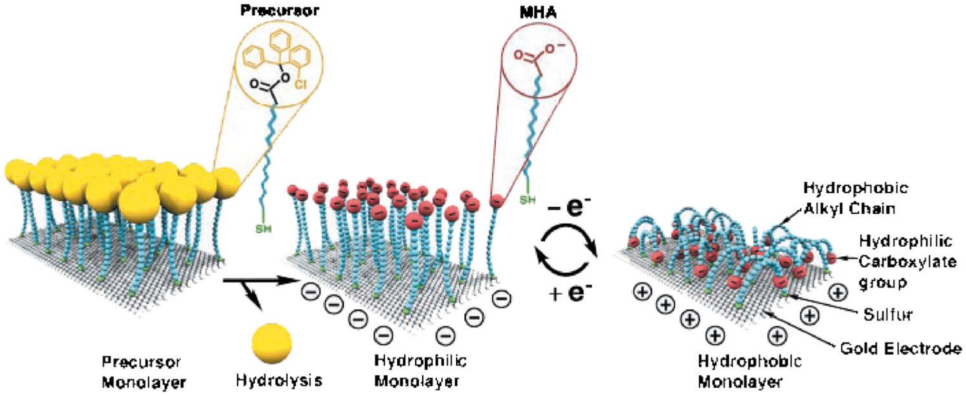

Fig. 5 Conceptual representation of a "reversibly switching surface" by applying an electrical charge to dynamically tune the orientation of self-assembled molecular monolayers and render the surface hydrophilic or hydrophobic Ref. [62]

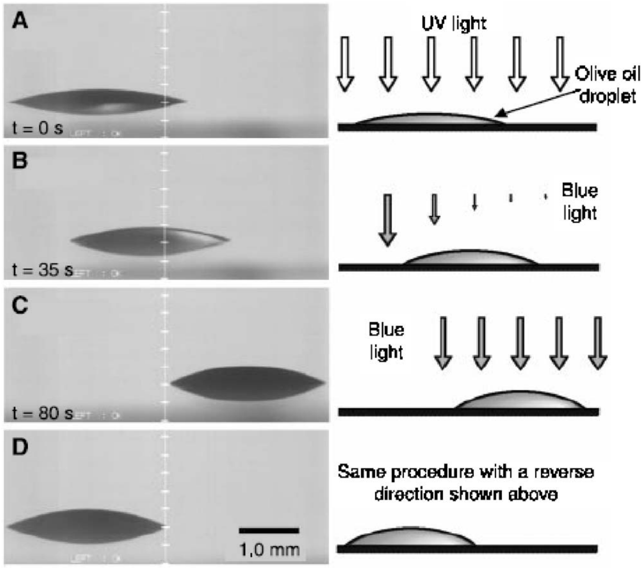

Fig. 7 Light-driven droplet motion on a surface that is photoirradiated with a coating of a photoisomerizable monolayer Ref. [61]

and industrial consumption) and small-scale (emerging applications in sensors, microactuators, and electromechanical-thermal machines, among others) applications and their design needs. This special issue of *the Journal of Heat Transfer* and its collection of technical contributions certainly reflect this direction.

References

[1] Bergles, A. E., 1988, "Fundamentals of Boiling and Evaporation," in *Two-Phase Flow Heat Exchangers: Thermal-Hydraulic Fundamentals and Design*, S. Kakac et al., eds., Kluwer, The Netherlands, pp. 159–200.
[2] Kakaç, S., Bergles, A. E., and Fernandes, E. O., 1988, *Two-Phase Flow Heat Exchangers: Thermal-Hydraulic Fundamentals and Design*, Kluwer, Dordrecht.
[3] Carey, V. P., 1992, *Liquid-Vapor Phase-Change Phenomena*, Hemisphere, Washington, DC.
[4] Dhir, V. K., 1998, "Boiling Heat Transfer," Annu. Rev. Fluid Mech., **30**, pp. 365–401.
[5] Kandlikar, S. G., Shoji, M., and Dhir, V. K., 1999, *Handbook of Phase Change: Boiling and Condensation*, Taylor & Francis, Philadelphia.
[6] Collier, J. G., and Thome, J. R., 2001, *Convective Boiling and Condensation*, 3rd ed., Oxford University Press, Oxford.
[7] Bergles, A. E., Lienhard, J. H., Kendall, G. E., and Griffith, P., 2003, "Boiling and Evaporation in Small Diameter Channels," Heat Transfer Eng., **24**(1), pp. 18–40.
[8] Martynenko, O. G., 2004, "Heat and Mass Transfer Bibliography—CIS Works," Int. J. Heat Mass Transfer, **47**, pp. 4005–4018.
[9] Goldstein, R. J., Ibele, W. E., Patankar, S. V., Simon, T. W., Kuehn, T. H., Strykowski, P. J., Tamma, K. K., Heberlein, J. H., Davidson, J. H., Bischof, J., Kulacki, F. A., Kortshagen, U., Garrick, S., and Srinivasan, V., 2006, "Heat Transfer—A Review of 2003 Literature," Int. J. Heat Mass Transfer, **49**(3–4), pp. 451–534.
[10] Suzuki, K., Nishio, S., Yoshida, H., Takeishi, K., Kunugi, T., Kawara, Z., Iwai, H., Saito, M., and Oda, Y., 2006, "Heat Transfer Bibliography—Japanese Works 2004," Int. J. Heat Mass Transfer, **49**, pp. 3771–3783.
[11] Thome, J. R., 1990, *Enhanced Boiling Heat Transfer*, Hemisphere, New York.
[12] Bergles, A. E., 1997, "Enhancement of Pool Boiling," Int. J. Refrig., **20**(8), pp. 545–551.
[13] Manglik, R. M., 2003, "Heat Transfer Enhancement," in *Heat Transfer Handbook*, A. Bejan, and A. D. Kraus, eds., Wiley, New York, Chap. 14.
[14] Manglik, R. M., and Bergles, A. E., 2004, "Enhanced Heat and Mass Transfer in the New Millennium: A Review of the 2001 Literature," J. Enhanced Heat Transfer, **11**(2), pp. 87–118.
[15] Webb, R. L., and Kim, N.-H., 2005, *Principles of Enhanced Heat Transfer*, 2nd ed., Taylor & Francis, Boca Raton, FL.
[16] Bergles, A. E., 1981, "Two-Phase Flow and Heat Transfer, 1756–1981," Heat Transfer Eng., **2**(3–4), pp. 101–114.
[17] Manglik, R. M., and Kraus, A. D., 1996, *Process, Enhanced, and Multiphase Heat Transfer*, Begell House, New York.
[18] Nishikawa, K., 1987, "Historical Developments in the Research of Boiling Heat Transfer," JSME Int. J., Ser. III, **30**(264), pp. 897–905.
[19] Saraswati, S. S. P., 1990, *Founders of Sciences in Ancient India*, Govindram Hasanand, New Delhi, India.
[20] Kopp, I. Z., 2005, "Problems of Thermophysics and Thermal Engineering for the New Technologies of the Twenty-First Century," Appl. Mech. Rev., **58**, pp. 206–223.
[21] Matschoss, C., 1908, *Die Entwicklung der Dampfmaschine*, Springer, Berlin.
[22] De Camp, L. S., 1963, *The Ancient Engineers*, Doubleday, Garden City, NY.
[23] Burstall, A. F., 1965, *A History of Mechanical Engineering*, MIT Press, Cambridge, MA.
[24] Leidenfrost, J. G., 1966, "On the Fixation of Water in Diverse Fire," Int. J. Heat Mass Transfer, **9**, pp. 1154–1166 (translation of 1756 publication: A Tract About Some Qualities of Common Water).
[25] Shamasundar, S., 2006, "Science in Classical Indian Texts," http://www.infinityfoundation.com/mandala/t_es/ht_es_science_frameset.htm.
[26] Agrawal, D. P., 2000, *Ancient Metal Technology & Archaeology of South Asia*, Aryan Books International, Delhi, India.
[27] Wikipedia, 2006, "Science and Technology in Ancient India," http://en.wikipedia.org/wiki/Science_and_technology_in_ancient_India.
[28] Craddock, P. T., Freestone, I. C., Gurjar, L. K., Middleton, A., and Willies, L., 1989, "The Production of Lead, Silver and Zinc in Early India," in *Old World Archaeometallurgy*, A. Hauptmann, E. Pernicka, and G. Wagner, eds., Selbstverlag des Deutschen Bergbau-Museums, Bochum, Germany, pp. 51–69.
[29] Chen, J. C., 2003, "Surface Contact and its Significance for Multiphase Heat Transfer: Diverse Examples," ASME J. Heat Transfer, **125**(4), pp. 549–566.
[30] Krupenkin, T. N., Taylor, J. A., Schneider, T. M., and Yang, S., 2004, "From Rolling Ball to Complete Wetting: The Dynamic Tuning of Liquids on Nanostructured Surfaces," Langmuir, **20**, pp. 3824–3827.
[31] Jakob, M., and Fritz, W., 1931, "Versuche über den Verdampfungsvorgang," Forsch. Geb. Ingenieurwes., **2**, pp. 435–447.
[32] Jakob, M., 1936, "Heat Transfer in Evaporation and Condensation—I," Mech. Eng. (Am. Soc. Mech. Eng.), **58**, p. 643–660.
[33] Nukiyama, S., 1934, "The Maximum and Minimum Values of the Heat Q Transmitted From Metal to Boiling Water Under Atmospheric Pressure," J. Jpn. Soc. Mech. Eng., **37**, pp. 367–374; [1966, Int. J. Heat Mass Transfer, **9**, pp. 1419–1433].
[34] McAdams, W. H., Kennel, W. E., Mindon, C. S., Carl, R., Picornel, P. M., and Dew, J. E., 1949, "Heat Transfer to Water With Surface Boiling," Ind. Eng. Chem., **41**, pp. 1945–1953.
[35] Lockhart, R. W., and Martinelli, R. C., 1949, "Proposed Correlation of Data for Isothermal Two-Phase Two-Component Flow in Pipes," Chem. Eng. Prog., **45**(1), pp. 39–48.
[36] Rohsenow, W. M., 1952, "A Method of Correlating Heat Transfer Data for Surface Boiling of Liquids," Trans. ASME, **74**, pp. 969–976.
[37] Bergles, A. E., 1969, "Survey and Evaluation of Techniques to Augment Convective Heat Transfer," Prog. Heat Mass Transfer, **1**, pp. 331–424.
[38] Bergles, A. E., 2000, "New Frontiers in Enhanced Heat Transfer," in *Advances in Enhanced Heat Transfer*, R. M. Manglik, T. S. Ravigururajan, A. Muley, R. A. Papar, and J. Kim, eds., ASME, New York, pp. 1–8.
[39] Kenning, D. B. R., 1999, "What Do We Really Know About Nucleate Boiling," IMechE Trans., 6th UK National Heat Transfer Conference, Edinburgh, pp. 143–167.
[40] Nelson, R. A., 2001, "Do We Doubt Too Little? Examples From the Thermal Sciences," Exp. Therm. Fluid Sci., **25**, pp. 255–267.
[41] Dhir, V. K., 2001, "Numerical Simulation of Pool-Boiling Heat Transfer," AIChE J., **47**(4), pp. 813–834.
[42] Shoji, M., 2004, "Studies of Boiling Chaos: A Review," Int. J. Heat Mass Transfer, **47**(6–7), pp. 1105–1128.
[43] Zhang, J., and Manglik, R. M., 2004, "Effect of Ethoxylation and Molecular Weight of Cationic Surfactants on Nucleate Boiling in Aqueous Solutions," ASME J. Heat Transfer, **126**(1), pp. 34–42.
[44] Wasekar, V. M., and Manglik, R. M., 1999, "A Review of Enhanced Heat Transfer in Nucleate Pool Boiling of Aqueous Surfactant and Polymeric Solutions," J. Enhanced Heat Transfer, **6**(2–4), pp. 135–150.
[45] Zhang, J., and Manglik, R. M., 2005, "Additive Adsorption and Interfacial Characteristics of Nucleate Pool Boiling in Aqueous Surfactant Solutions," ASME J. Heat Transfer, **127**(7), pp. 684–691.
[46] Zhang, J., and Manglik, R. M., 2005, "Nucleate Pool Boiling of Aqueous Polymer Solutions on a Cylindrical Heater," J. Non-Newtonian Fluid Mech., **125**(2–3), pp. 185–196.
[47] Warrier, G. R., and Dhir, V. K., 2006, "Heat Transfer and Wall Heat Flux Partitioning during Subcooled Flow Nucleate Boiling—A Review," ASME J. Heat Transfer, **128**(12), pp. 1243–1256.
[48] Fuchs, T., Kern, J., and Stephan, P., 2006, "A Transient Nucleate Boiling Model Including Microscale Effects and Wall Heat Transfer," ASME J. Heat Transfer, **128**(12), pp. 1257–1265.
[49] Panchamgam, S. S., Plawsky, J. L., and Wayner, P. C. Jr., 2006, "Spreading Characteristics and Microscale Evaporative Heat Transfer in an Ultra-Thin Film Containing a Binary Mixture," ASME J. Heat Transfer, **128**(12), pp. 1266–1275.
[50] Carey, V. P., and Wemhoff, A. P., 2006, "Disjoining Pressure Effects in Ultra-Thin Liquid Films in Micropassages—Comparison of Thermodynamic Theory With Predictions of Molecular Dynamics Simulations," ASME J. Heat Transfer, **128**(12), pp. 1276–1284.
[51] Mukherjee, A., and Kandlikar, S. G., 2006, "Numerical Study of an Evaporating Meniscus on a Moving Heated Surface," ASME J. Heat Transfer, **128**(12), pp. 1285–1292.
[52] Bergles, A. E., 1999, "Enhanced Heat Transfer: Endless Frontier, or Mature

and Routine?," J. Enhanced Heat Transfer, **6**(2–4), pp. 79–88.

[53] Schneider, B., Kosar, A., Kuo, C.-J., Mishra, C., Cole, G. S., Scaringe, R. P., and Peles, Y., 2006, "Cavitation Enhanced Heat Transfer in Microchannels," ASME J. Heat Transfer, **128**(12), pp. 1293–1301.

[54] Ghiu, C.-D., and Joshi, Y. K., 2006, "Pool Boiling Using Thin Enhanced Structures Under Top-Confined Conditions," ASME J. Heat Transfer, **128**(12), pp. 1302–1311.

[55] Ahn, H. S., Sinha, N., Zhang, M., Fang, S., Banerjee, D., and Baughman, R. H., 2006, "Pool Boiling Experiments on Multi-Walled Carbon Nano Tube (MWCNT) Forests," ASME J. Heat Transfer, **128**(12), pp. 1335–1342.

[56] Li, C., Peterson, G. P., and Wang, Y., 2006, "Evaporation/Boiling in Thin Capillary Wicks I—Wick Thickness Effects," ASME J. Heat Transfer, **128**(12), pp. 1312–1319.

[57] Li, C., and Peterson, G. P, 2006, "Evaporation/Boiling in Thin Capillary Wicks II—Effects of Volumetric Porosity," ASME J. Heat Transfer, **128**(12), pp. 1320–1328.

[58] Cai, Q., Chen, C.-L., and Asfia, J. F., 2006, "Operating Characteristic Investigations in Pulsating Heat Pipe," ASME J. Heat Transfer, **128**(12), pp. 1329–1334.

[59] Thome, J. R., 2004, "Boiling in Microchannels: A Review of Experiment and Theory," Int. J. Heat Mass Transfer, **25**, pp. 128–139.

[60] Bergles, A. E., and Kandlikar, S. G., 2005, "On the Nature of Critical Heat Flux in Microchannels," ASME J. Heat Transfer, **127**(1), pp. 101–107.

[61] Ichimura, K., Oh, S.-K., and Nakagawa, M., 2000, "Light-Driven Motion of Liquids on a Photoresponsive Surface," Science, **288**, pp. 1624–1626.

[62] Lahann, J., Mitragotri, S., Tran, T.-N., Kaido, H., Sundaram, J., Choi, S., Hoffer, S., Somorjai, G. A., and Langer, R., 2003, "A Reversibly Switching Surface," Science, **299**, pp. 371–374.

[63] Wasekar, V. M., and Manglik, R. M., 2000, "Pool Boiling Heat Transfer in Aqueous Solutions of an Anionic Surfactant," ASME J. Heat Transfer, **122**(4), pp. 708–715.

Gopinath R. Warrier

Vijay K. Dhir[1]
e-mail: vdhir@seas.ucla.edu

Mechanical and Aerospace Engineering Department,
Henry Samueli School of Engineering and Applied Science,
University of California, Los Angeles,
Los Angeles, CA 90095-1597

Heat Transfer and Wall Heat Flux Partitioning During Subcooled Flow Nucleate Boiling—A Review

In this paper we provide a review of heat transfer and wall heat flux partitioning models/correlations applicable to subcooled forced flow nucleate boiling. Details of both empirical and mechanistic models that have been proposed in the literature are provided. A comparison of the experimental data with predictions from selected models is also included. [DOI: 10.1115/1.2349510]

Keywords: flow boiling, heat flux, prediction

Introduction

Subcooled flow boiling is characterized by the presence of thermodynamic nonequilibrium between the liquid and vapor phases. This increases the complexity of the process and makes the analysis of the process very challenging. During the last five decades, numerous models have been developed to predict the heat transfer rate during subcooled flow boiling. These models can be broadly classified into three categories: (i) empirical correlations for wall heat flux, (ii) empirical correlations for partitioning of wall heat flux, and (iii) mechanistic models for wall heat flux and partitioning. The empirical correlations for wall heat flux are generally limited to the prediction of total wall heat flux for a particular flow situation. They are merely correlations of experimental data and as such do not include modeling of the heat transfer mechanisms involved. As a result, these correlations cannot provide any information regarding the partitioning of wall heat flux between the liquid and vapor phases. However, in a number of applications, such as nuclear reactors, knowledge of only the overall heat transfer rate from the wall is insufficient. This is because the reactivity and two-phase thermal hydraulics is directly related to the void fraction in the reactor, which in turn depends on how the wall heat flux is partitioned between the liquid and vapor phases. In thermal hydraulic codes such as RELAP5, the void fraction is calculated using separate submodels for the vapor generation rate, vapor condensation rate, and interfacial drag. As such, the vapor generation and vapor condensation rates are the source and sink terms in these codes. Since vapor is generated at the heater surface, in order to predict the vapor generation rate, one has to know the fraction of the wall heat flux used for vapor generation. Also, since the vapor condensation rate depends on the local bulk liquid temperature, one also needs to know what fraction of the wall heat flux is utilized for heating the bulk liquid. This information can only be provided by the empirical correlations for wall heat flux partitioning and the mechanistic models. However, it is important to keep in mind that the empirical correlations for wall heat flux partitioning only provide information regarding how the wall heat flux is to be partitioned. They cannot be used for the prediction of the wall heat flux itself. On the other hand, the mechanistic models, which are based on the relevant heat transfer mechanisms occurring during the boiling process, have the capability of determining each of the relevant heat flux components individually. Hence the mechanistic models can be used for both the prediction of the wall heat flux and the partitioning of the wall heat flux between the liquid and vapor phases.

Figure 1 shows a schematic of a subcooled flow nucleate boiling process on a heated surface. Liquid is subcooled at the inlet. At some location downstream, when the wall temperature is high enough, bubble nucleation occurs. This location is referred to as Onset of Nucleate Boiling (ONB). Just downstream of ONB, the bubbles are still small enough that they remain attached to the heater surface. Farther downstream, as the bulk liquid temperature increases, the bubbles grow larger and begin to depart from their sites of origin. These bubbles then slide along the heater surface and eventually lift off from the wall. The location where the bubbles begin to lift off from the heated wall is called the location of Onset of Significant Voids (OSV). In the region between ONB and OSV, the void fraction is small but increases rapidly downstream of OSV.

A review of the various models/correlations developed for the prediction of heat transfer and wall heat flux partitioning is given in the following sections.

Empirical Correlations for Wall Heat Flux

Figure 2 shows a typical flow boiling curve. It consists of the single-phase forced convection region, the partial nucleate boiling region, and the fully developed boiling region. The location where fully developed boiling (FDB) begins is shown in Fig. 2. The empirical heat transfer models attempt to predict this boiling curve [i.e., predict the heat flux (q_w) given the wall superheat (ΔT_w) or vice versa] for a given flow condition. The most common approach used in the development of the empirical models is to assume that the total heat flux during subcooled flow boiling is a combination of the single-phase forced convection and saturated pool nucleate boiling heat fluxes. Since the focus of this review is only on subcooled flow boiling, only the partial and fully developed regions of nucleate boiling will be considered.

Partial Nucleate Boiling. Partial nucleate boiling is the transition region between single-phase forced convection and fully developed nucleate boiling. Bowring [1] used a superposition method to determine the partial nucleate boiling heat flux, as shown in Fig. 2. Note that Fig. 2 is for a prescribed axial location (z) and fixed system pressure (p). Important reference points are also shown in Fig. 2. According to Bowring's model,

$$q_{\mathrm{pb}} = q_{\mathrm{fc}} + q_{\mathrm{nb}} \tag{1}$$

where q_{pb} is the heat flux during partial boiling, q_{fc} is the single-phase forced convection heat flux, and q_{nb} is the fully developed pool boiling heat flux. The heat flux at which fully developed nucleate boiling begins (q_{fdb}) was assumed to be given by the relationship suggested by Engelberg-Forster and Greif [2], i.e.,

---

[1] Author to whom all correspondence should be addressed.

Contributed by the Heat Transfer Division of ASME for publication in the JOURNAL OF HEAT TRANSFER. Manuscript received January 5, 2006; final manuscript received February 23, 2006. Review conducted by Raj M. Manglik.

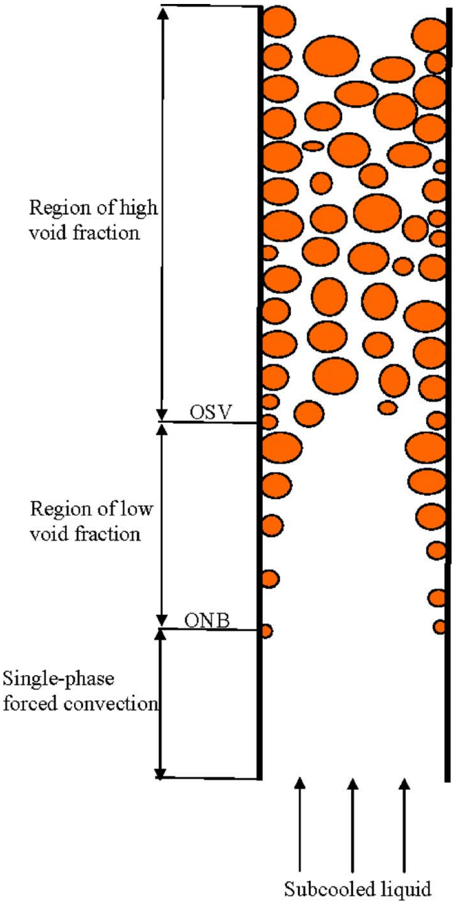

Fig. 1 Schematic of subcooled flow nucleate boiling

$q_{\mathrm{fdb}}=1.4q_{\mathrm{int}}$, where q_{int} is the heat flux at the intersection of the single-phase and fully developed nucleate boiling curves. It should be mentioned that in the single-phase region, the heat flux was calculated as,

$$q_{\mathrm{fc}}=h_{\mathrm{fc}}(T_{\mathrm{sat}}-T_l)=h_{\mathrm{fc}}\Delta T_{\mathrm{sub}} \tag{2}$$

with the single-phase heat transfer coefficient (h_{fc}) calculated using standard correlations. Thus, one can see that Eq. (1) provides a smooth transition between single-phase forced convection and fully developed nucleate boiling and satisfies the end conditions: $q_{\mathrm{pb}}=q_{\mathrm{fc}}$ at $T_w=T_{\mathrm{sat}}$ and $q_{\mathrm{pb}}=q_{\mathrm{fdb}}$ at $T_w=T_{w,\mathrm{fdb}}$. According to this model, $q_{\mathrm{fc}}>0$ for $T_w<T_{w,\mathrm{fdb}}$ and $q_{\mathrm{fc}}=0$ for $T_w=T_{w,\mathrm{fdb}}$.

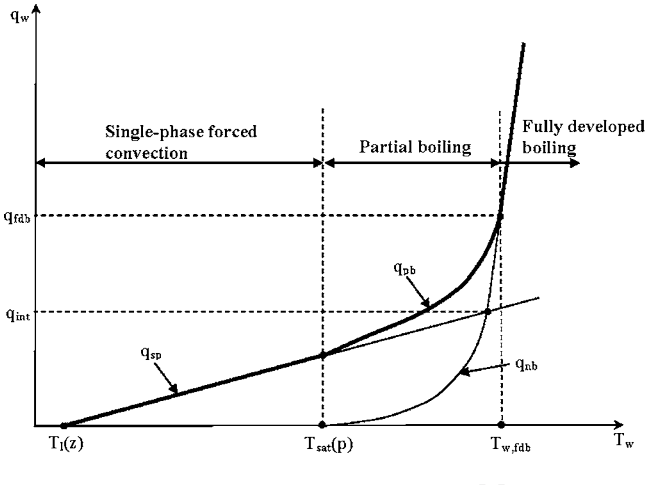

Fig. 2 Boiling curve from the Bowring [1] model

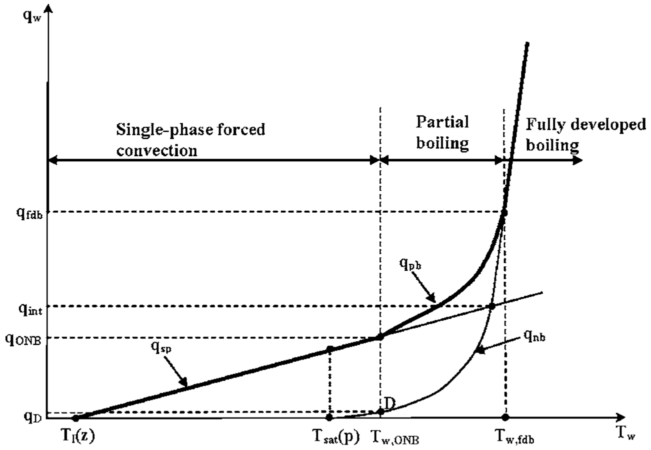

Fig. 3 Boiling curve for the Bergles and Rohsenow [5] model

Kutateladze [3] proposed the following interpolation formula,

$$h_{\mathrm{pb}}=\sqrt{h_{\mathrm{fc}}^2+h_{\mathrm{nb}}^2} \tag{3}$$

to determine the heat transfer coefficient during partial boiling (h_{pb}). In Eq. (3), h_{nb} is the heat transfer coefficient during fully developed pool nucleate boiling given by the relation,

$$h_{\mathrm{nb}}=C(p)q_w^{0.7} \tag{4}$$

where $C(p)$ is an empirical function that depends on pressure.

An approach similar to Bowring's was adopted by Rohsenow [4], except that in this model q_{fc} was calculated as,

$$q_{\mathrm{fc}}=h_{\mathrm{fc}}[T_w-T_l(z)]=h_{\mathrm{fc}}[\Delta T_w+\Delta T_{\mathrm{sub}}(z)] \tag{5}$$

The fully developed nucleate boiling curve is computed using the saturated pool nucleate boiling correlation,

$$q_{\mathrm{nb}}=\mu_l h_{\mathrm{fg}}\sqrt{\frac{g(\rho_l-\rho_v)}{\sigma}}\mathrm{Pr}_l^{-m/n}\left(\frac{c_{p,l}[T_w-T_{\mathrm{sat}}(p)]}{C_s h_{\mathrm{fg}}}\right)^{1/n} \tag{6}$$

where C_s is an empirical constant that depends on the fluid-solid combination, and m and n are empirical constants that depend on the fluid properties. Another interpolation method was later proposed by Bergles and Rohsenow [5]. In their model, single-phase forced convection was assumed to be the only mode of heat transfer until nucleation occurs. Once boiling begins, the partial nucleate boiling heat flux was assumed to be given by the relationship,

$$q_{\mathrm{pb}}=q_{\mathrm{fc}}\sqrt{1+\left[\left(\frac{q_{\mathrm{nb}}}{q_{\mathrm{fc}}}\right)\left(1-\frac{q_D}{q_{\mathrm{nb}}}\right)\right]} \tag{7}$$

where q_D is the heat flux computed from the fully developed boiling curve at $T_{w,\mathrm{ONB}}$ (see Fig. 3). In turn, the heat flux at which ONB (q_{ONB}) occurs was given by the empirical correlation,

$$q_{\mathrm{ONB}}=5.30p^{1.156}[1.80\,\Delta T_{w,\mathrm{ONB}}]^{2.41/p^{0.0234}} \tag{8}$$

where p is in kPa, $\Delta T_{w,\mathrm{ONB}}$ is in °C, and q_{ONB} is in $\mathrm{W/m^2}$. Based on the predicted results, Bergles and Rohsenow concluded that using a saturated pool boiling correlation to compute q_{nb} (and hence q_D) can result in significant errors in the predicted values of q_{pb}. They recommended using actual flow boiling curves to determine q_{nb}.

Bjorge et al. [6] suggested using the following correlation to predict the boiling curve during subcooled flow boiling,

$$q_{\mathrm{pb}}=\sqrt{q_{\mathrm{fc}}+q_{\mathrm{nb}}^2\left[1-\left(\frac{\Delta T_{w,\mathrm{ONB}}}{\Delta T_w}\right)^3\right]^2} \tag{9}$$

where q_{fc} is calculated using Eq. (5) with h_{fc} calculated from the Colburn [7] correlation. The wall superheat at ONB was deter-

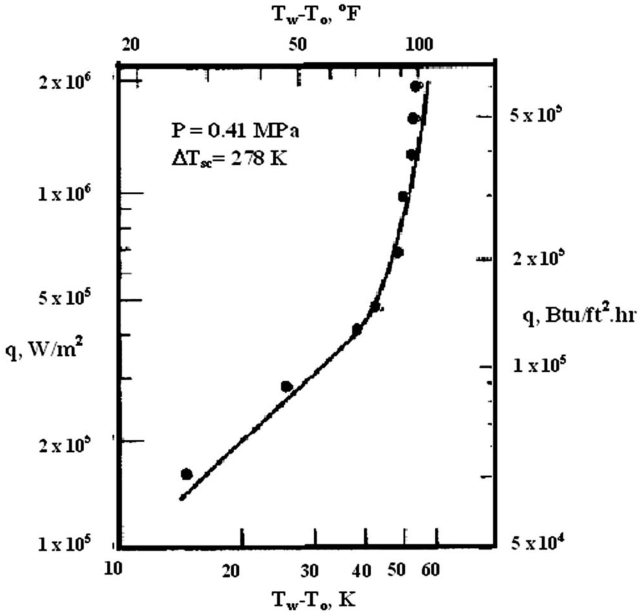

Fig. 4 A comparison of the Bjorge et al. [6] model predictions with experimental data of McAdams et al. [9]

mined using the Bergles and Rohsenow [5] correlation [Eq. (8)]. In Eq. (9), q_{nb} is the fully developed pool boiling heat flux given as (from Mikic and Rohsenow [8]),

$$q_{\text{nb}} = C\left(\frac{k_l^{1/2}\rho_l^{17/8}c_{p,l}^{19/8}\rho_v^{1/8}h_{\text{fg}}^{1/8}}{(\rho_l-\rho_v)^{9/8}\sigma^{5/8}T_{\text{sat}}^{1/8}}\sqrt{\frac{g(\rho_l-\rho_v)}{\sigma}}\right)\Delta T_w^3 \qquad (10)$$

where C is a dimensional constant that depends on the cavity size distribution and fluid properties. The model predictions compared well with the experimental data of McAdams et al. [9], as shown in Fig. 4.

Liu and Winterton [10] combined some of the concepts proposed by Kutateladze [3] and Chen [11] to develop a model to predict the subcooled flow boiling heat flux. The premise of this model is that total heat flux can be expressed as a combination of the single-phase forced convection heat transfer and the pool boiling heat transfer. However, the single-phase heat transfer is assumed to be enhanced by the increased liquid velocity during two-phase flow while the pool boiling heat transfer is suppressed due to a lower effective wall superheat in flow boiling compared to that in pool boiling (as a result of a thinner thermal boundary layer). Accordingly, the overall wall heat flux during subcooled flow boiling (q_w) was assumed to be given by the relationship,

$$q_w = \sqrt{(Fq_{\text{fc}})^2 + (Sq_{\text{nb}})^2} = \sqrt{(Fh_{\text{fc}}[\Delta T_w + \Delta T_{\text{sub}}])^2 + (Sh_{\text{pool}}\Delta T_w)^2} \qquad (11)$$

where F and S are the single-phase heat transfer enhancement factor and the pool boiling heat transfer suppression factor, respectively. In turn, the enhancement and suppression factors are calculated from the following equations,

$$F = \left[1 + \text{Pr}_l\left(\frac{\rho_l}{\rho_v} - 1\right)\right]^{0.35}$$

$$S = \frac{1}{1 + 0.055F^{0.1}\,\text{Re}_l^{0.16}} \qquad (12)$$

where Pr_l and Re_l are the Prandtl and Reynolds number based on the liquid properties. Figure 5 shows a comparison between the predicted and experimental heat transfer coefficients during subcooled flow boiling. The model predicts the experimental data to within ±40%.

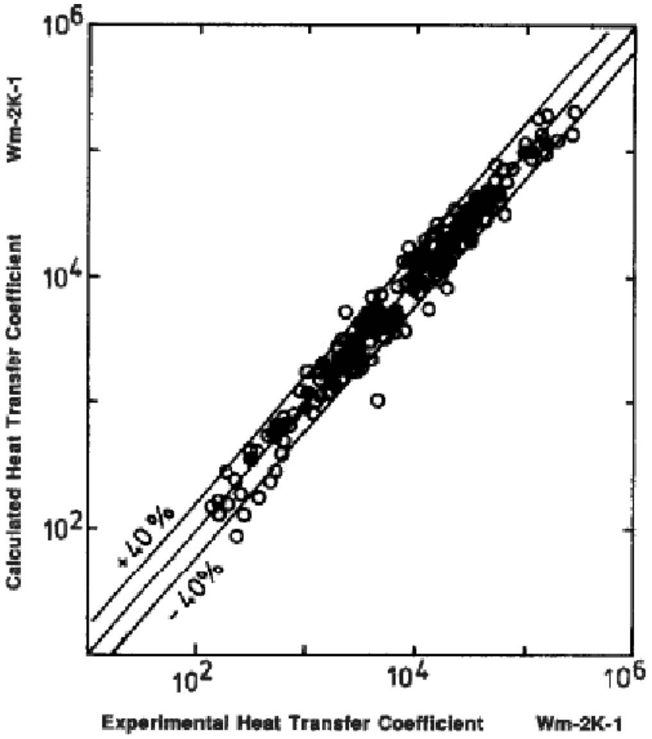

Fig. 5 A comparison of the Liu and Winterton [10] model predictions with experimental data

Boyd and Meng [12] suggested another interpolation method to predict q_{pb}. According to this model, q_{pb} was assumed to have the functional form,

$$q_{\text{pb}} = a + b(\Delta T_w)^m \qquad (13)$$

with the empirical parameters a, b, and m computed such that the following conditions are satisfied, namely,

$$q_{\text{pb}} = q_{\text{fc}} \quad at\ T_w = T_{\text{sat}}$$

$$q_{\text{pb}} = q_{\text{fdb}} \quad at\ \Delta T_w = \Delta T_{w,\text{fdb}} \qquad (14)$$

$$\frac{\partial q_{\text{pb}}}{\partial \Delta T_w} = \frac{\partial q_{\text{fdb}}}{\partial \Delta T_w} \quad at\ \text{fdb}$$

As such, the empirical parameters a, b, and m are not constants but change along the boiling curve. The location at which fully developed boiling begins (fdb) was determined using the Engelberg-Forster and Greif [2] method. A similar correlation has also been proposed by Kandlikar [13], with the empirical parameters a, b, and m assumed to be constant. Figure 6 shows the boiling curve predicted using Kandlikar's [13] model. The partial boiling curve was computed using the functional form given by Eq. (13), while the fully developed boiling curve is determined using Eq. (21), as described later.

A different approach was taken by Wadekar [14]. Wadekar assumed that in the partial boiling region, the total heat flux can be expressed as a combination of the area-averaged single-phase and pool nucleate boiling heat fluxes. This relationship can be written as,

$$q_{\text{pb}} = (1 - A_{\text{nb}})q_{\text{sp}} + q_{\text{nb}} \qquad (15)$$

where A_{nb} is the time-averaged fraction of the total heater surface area over which nucleate boiling occurs. Wadekar argued that q_{nb} should not be multiplied by A_{nb} since the pool boiling correlations were already based on the overall heat transfer area. For q_{nb}, Cooper's [15] pool boiling correlation is used, i.e.,

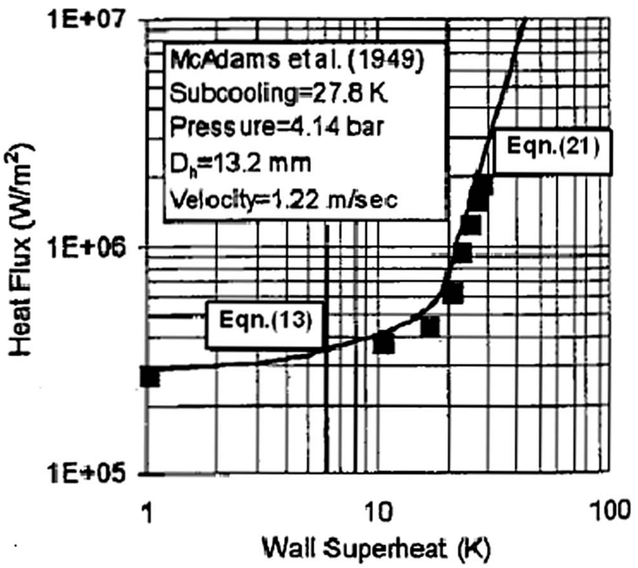

Fig. 6 A comparison of Kandlikar's [13] model predictions with experimental data of McAdams et al. [9]

$$q_{\mathrm{nb}} = [C_1 \Delta T_w p_r^{0.12} (-\log_{10} p_r)^{-0.55} M^{-0.5}]^3 \tag{16}$$

where C_1 is an empirical constant that is specific to the fluid, p_r is the reduced pressure, and M is the molecular weight of the fluid. In turn, A_{nb} was assumed to decrease as,

$$A_{\mathrm{nb}} = 1 - e^{\frac{177 C_1 \Delta T_w^{2.5} p_r}{\mathrm{Re}_{\mathrm{TP}}}} \tag{17}$$

where p_r is the reduced pressure, $\mathrm{Re}_{\mathrm{TP}}$ is the two-phase Reynolds number as defined by Chen [11], and C_1 is the lead constant in Cooper's correlation [Eq. (16)]. From Eqs. (15)–(17) it can be seen that A_{nb} increases as ΔT_w increases (due to the increase in the number of active nucleation sites) and vice versa. As a result, q_{pb} asymptotically approaches q_{fc} at low ΔT_w, while at large ΔT_w, q_{pb} approaches q_{nb}.

Fully Developed Nucleate Boiling. Several correlations have also been proposed for fully developed flow boiling heat flux (q_{fdb}). One of the earliest was proposed by McAdams et al. [9]. This power law relationship can be expressed as,

$$q_{\mathrm{fdb}} = C_2 (\Delta T_w)^{3.86} \tag{18}$$

where C_2 is an empirical constant that depends on the dissolved gas content, q_{fdb} is the heat flux in W/m^2, and ΔT_w is the wall superheat in °C. Jens and Lottes [16] proposed the following correlation for fully developed boiling of degassed water,

$$q_{\mathrm{fdb}} = \left(e^{p/62} \frac{\Delta T_w}{25} \right)^4 \tag{19}$$

where q_{fdb} is in MW/m^2, ΔT_w is in °C, and p is the absolute pressure in bars. Later, Thom et al. [17] proposed a modified form of Eq. (19). This relationship, which is only valid for water, was given as,

$$q_{\mathrm{fdb}} = \left(e^{p/87} \frac{\Delta T_w}{22.65} \right)^2 \tag{20}$$

Assuming that the two-phase convective heat transfer component is insignificant during fully developed nucleate boiling, Kandlikar [13] suggested using the following expression to compute q_{fdb},

$$q_{\mathrm{fdb}} = [1058(\dot{m} h_{\mathrm{fg}})^{0.7} F_{\mathrm{fl}} h_{\mathrm{lo}} (\Delta T_w + \Delta T_{\mathrm{sub}})]^{1/0.3} \tag{21}$$

where $\dot{m}$ is the total mass flux in kg/m^2 s, F_{fl} is a fluid-surface parameter, and h_{lo} is the single-phase heat transfer coefficient for liquid only flows (in W/m^2 K).

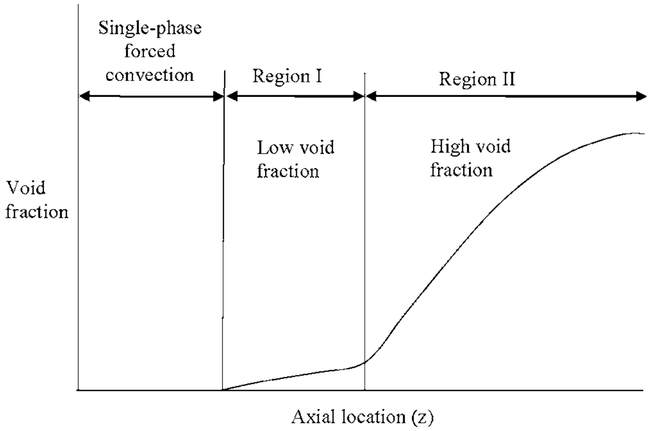

Fig. 7 Variation of void fraction with axial distance

Empirical Correlations for Partitioning of Wall Heat Flux

A survey of the literature shows that a number of correlations for wall heat flux partitioning have been proposed. These correlations differ from one another on two counts, namely, what heat transfer mechanisms are considered, and what fraction of the total heat flux is transferred by each of these mechanisms. It must be noted that since the primary goal of the correlations discussed in this section is to predict the bulk void fraction, the focus of these correlations is to determine how the given total wall heat flux is partitioned and not the prediction of the total wall heat flux itself.

One of the earliest models was developed by Griffith et al. [18]. Based on visual observation during experiments, they identified two distinct boiling regions (see Fig. 7): (i) a highly subcooled region with a low void fraction (region I); and (ii) a slightly subcooled region with a significant void fraction (region II). Region I includes the heater area between ONB and OSV locations, while region II begins at OSV and extends until bulk boiling begins. Single-phase forced convection occurs upstream of region I. In region I, small bubbles attached to the heater surface were observed, resulting in a stratified flow pattern. Hence, in this region, the total heat flux was partitioned into single-phase (q_{fc}) and boiling (q_{b}) components as follows,

$$q_w = q_{fc} + q_b \tag{22}$$

with $q_{\mathrm{fc}} = h_{\mathrm{fc}}(T_{\mathrm{sat}} - T_l)$, under the assumption that all of the heater surface area is subjected to forced convection. The average single-phase heat transfer coefficient (h_{fc}) is calculated from,

$$\mathrm{Nu}_z = \frac{h_{\mathrm{fc}} z}{k_l} = 0.036\, \mathrm{Re}_z^{0.8} \mathrm{Pr}_l^{1/3} \tag{23}$$

Additionally, since the void fraction was low and the bubbles were static in size, the condensation heat flux (q_c) from the top of the bubbles was assumed to exactly balance the boiling heat flux (q_b) (i.e., $q_b = q_c$). The condensation heat flux was expressed as,

$$q_c = q_b = q_w - q_{\mathrm{fc}} = B_0 h_{\mathrm{fc}} \frac{A_c}{A_h} \Delta T_{\mathrm{sub}} \tag{24}$$

where B_0 is an empirical constant, and A_c and A_h are the condensation and heater surface areas, respectively. Based on physical arguments, the ratio (A_c/A_h) was assumed to be proportional to

$\alpha_w(h_{fc}/k_l)/\mathrm{Pr}_l$, where αw is the wall voidage. Hence, q_c was given by the expression,

$$q_c = \frac{B_1 \alpha_w h_{fc}^2 \, \Delta T_{sub}}{k_l \, \mathrm{Pr}_l} \tag{25}$$

where B1 is an empirical constant (=1.07). Hence, in the highly subcooled region, condensation from the bubbles merely provides an alternate route for the transfer of wall energy to the bulk liquid. As a result, in this region, all the energy from the wall was assumed to be utilized for heating the bulk liquid (i.e, $q_w = q_l = q_{fc} + q_c$).

Based on experimental data, Griffith et al. found that when $q_b = 5q_{fc}$ (q_{fc} calculated as described above), the slope of the boiling curve did not change. This was assumed to signify the start of fully developed boiling and the beginning of region II. In this region, the heating surface was assumed to be covered by "several layers of bubbles," with all the energy from the wall being utilized for vapor generation ($q_b = q_w$). Condensation from the top layer of bubbles was the only energy added to the liquid (i.e., $q_l = q_c$). Assuming the condensation heat transfer coefficient to be equal to $5h_{fc}$, the condensation heat flux was expressed as,

$$q_c = 5h_{fc} \, \Delta T_{sub} \tag{26}$$

Since the entire heater surface was covered with bubbles, the area over which condensation occurs was assumed to be equal to the heater surface area. It must be mentioned that at the transition point between regions I and II, q_{fc} will be discontinuous (because $q_{fc} > 0$ in region I and then suddenly goes to zero at the start region II). In region II, the void fraction was calculated using $q_b (= q_w)$ as the source term.

Bowring [1] also utilized the "two-region" model developed by Griffith et al. [18]. However, he argued that the rapid increase in void fraction in the slightly subcooled region (region II) is not due to the "wall effect" (heater surface being covered by "layers of bubbles") as proposed by Griffith et al. [18]. He instead put forth the argument that, in region II, the increase in void fraction is due to the bubbles lifting off the heater surface and moving into the bulk liquid and is thus essentially a "bulk fluid effect." This location also denotes the OSV location. These bubbles are then assumed to slowly condense in the bulk liquid as they traveled downstream.

Upstream of region I, single-phase forced convection occurs with the heat transfer coefficient calculated using standard forced convection correlations. In region I, all the energy from the wall is assumed to be utilized for heating the bulk fluid and hence the Griffith et al. formulation is applicable. Based on experimental data, he developed an empirical correlation for the OSV location (the beginning of bubble liftoff). This can be expressed as,

$$\Delta T_{sub,OSV} = q_w \frac{(14 + 0.1p)}{U} \tag{27}$$

where the local subcooling (ΔT_{sub}) is in °C, q_w is in $\mathrm{W/cm^2}$, p is the pressure in atmospheres, and U is the fluid velocity in cm/s. Downstream of OSV, Bowring then developed a mechanistic model for subcooled flow boiling by modifying the model originally developed by Engelberg-Forster and Greif [2] for pool nucleate boiling. Bowring is the first one to consider bubble liftoff in region II. In this region, four heat transfer mechanisms were identified, namely (i) single-phase convection (q_{fc}) in regions not occupied by bubbles, (ii) evaporation (q_{ev}) at the bubble base, (iii) convection heat transfer due to bubble agitation of the thermal boundary layer, which Bowring termed "agitation heat flux" (q_a), and (iv) condensation (q_c) from the top of bubbles still attached to the heater surface. Neglecting q_c (based on the Engelberg-Foster and Greif analysis), the wall heat flux is given as,

$$q_w = q_{fc} + q_{ev} + q_a \tag{28}$$

The evaporation heat flux (q_{ev}) is defined as the amount of energy carried away by the bubbles per unit area of the heater surface and is given by the expression,

$$q_{ev} = \rho_v h_{fg} V_b f N_a, \tag{29}$$

where f is the bubble release frequency, N_a is the active nucleation site density, and V_b is the bubble volume at departure.

The agitation heat flux (q_a), which results from the disruption of the thermal boundary layer during bubble growth and liftoff and the subsequent heating of the cold liquid that replaces the volume vacated by the departed bubble, was expressed as,

$$q_a = N_a f V_b \rho_l c_{p,l} \, \Delta T \tag{30}$$

where ΔT was the effective temperature difference through which the liquid was heated. Equation (30) is derived assuming that the volume of cold liquid could be treated as a slug with a volume equal to the volume of the departing bubble (V_b). However, due to the lack of information regarding f, N_a, and V_b, Eqs. (29) and (30) could not be used. Instead, an empirical parameter, ε, defined as the ratio of agitation to evaporation heat flux was introduced. Based on the experimental data available, Bowring correlated the ratio ϵ by the expression,

$$\epsilon \equiv \frac{q_a}{q_{ev}} = \begin{cases} 1 + 3.2\dfrac{\rho_l c_{p,l}\Delta T}{\rho_g h_{fg}}, & 1 \le p \le 9.5 \\ 1.3, & 9.5 \le p \le 50 \\ 1.6, & p \ge 50 \end{cases} \tag{31}$$

where p is pressure in bar. Hence, the wall heat flux could be partitioned as,

$$q_w = q_{fc} + q_a + q_{ev} = h_{fc}(T_{sat} - T_l) + (1 + \epsilon) q_{ev} \tag{32}$$

From Eq. (32) knowing ϵ and q_{fc}, q_{ev} can be calculated. Then q_a can be calculated as $q_a = \varepsilon q_{ev}$. It must, however, be stressed that all three heat flux components are not calculated independently. Also, since the empirical parameter ϵ is only a function of pressure, for given flow situation, ϵ is independent of the axial location. In Eq. (32), q_{fc} is significant only until fully developed nucleate boiling is reached. In turn, fully developed nucleate boiling was assumed to occur when $\Delta T_{sub} \le \Delta T_{sub,fdb}$, where $\Delta T_{sub,fdb}$ is calculated as (from Engelberg-Foster and Greif [2]),

$$\Delta T_{sub,fdb} = \frac{0.7 q_w}{h_{fc}} - 7.8 \exp[-0.0163(p-1)](0.7 q_w)^{0.25} \tag{33}$$

As such, in region I, $q_l = q_{fc}$ and in region II, $q_l = q_{fc} + q_a$. The void fraction in region II was calculated using q_{ev} as the source term.

In their model, Rouhani and Axelsson [19] used some of the concepts from Bowring's earlier model. Their model again assumes two distinct boiling regions: regions I and II, as shown in Fig. 4. The transition between the first and second regions was defined as the location where the bubbles begin lifting off from the heater. The wall heat flux partitioning for both regions was expressed as,

$$q_w = q_{fc} + q_b \tag{34}$$

where q_b is the boiling heat flux. Based on the argument that the single-phase heat flux contribution should decrease as the number of bubbles on the heater surface increases, q_{fc} was expressed in terms of the void fraction. This implied that the single-phase heat transfer mechanism was only applicable until the surface is completely covered with vapor bubbles. As such, the single-phase component of heat flux was given as,

$$q_{\mathrm{fc}} = h_{\mathrm{fc}}\,\Delta T_{\mathrm{sub}}\left(1 - \frac{\alpha}{\alpha_c}\right), \tag{35}$$

where α is the bulk void fraction determined using the correlation of Zuber and Findlay [20] and α_c is the bulk void fraction at the transition point between the two regions determined using the correlation developed by Rouhani [21]. From Eq. (35), it can be seen that the magnitude of q_{fc} decreases steadily as the α increases and goes to zero when $\alpha = \alpha_c$ (i.e., at the transition point between the two regions, OSV location). Note that this model is based on the bulk void fraction, which is always less than the wall void fraction.

The boiling heat flux component (q_b) in Eq. (34) was, in turn, expressed as the sum of the agitation (q_a) and evaporation (q_{ev}) heat flux components. However, the agitation heat flux (q_a) was expressed independently based on the argument that the slug of cold liquid replacing the departing vapor bubble would be heated to the mean liquid subcooling through a temperature gradient. Based on this, their final model was,

$$q_w = q_{\mathrm{fc}} + q_b = q_{\mathrm{fc}} + q_a + q_{\mathrm{ev}} = h_{\mathrm{fc}}(T_{\mathrm{sat}} - T_l)\left(1 - \frac{\alpha}{\alpha_c}\right) + \frac{\dot{m}_s}{\rho_v} c_{p,l}\rho_l \Delta T_{\mathrm{sub}} + \dot{m}_s h_{\mathrm{fg}} \tag{36}$$

where $\dot{m}_s$ is the mass of liquid converted to vapor per unit area of the heated surface. Defining a heat flux ratio ϵ $(= q_a/q_{\mathrm{ev}} = c_{p,l}\rho_l\,\Delta T_{\mathrm{sub}}/\rho_v h_{\mathrm{fg}})$, Eq. (36) was rewritten as,

$$q_w = q_{fc} + q_a + q_{\mathrm{ev}} = h_{\mathrm{fc}}(T_{\mathrm{sat}} - T_l)\left(1 - \frac{\alpha}{\alpha_c}\right) + (1 + \epsilon) q_{\mathrm{ev}} \tag{37}$$

Note that ϵ can be explicitly calculated knowing the fluid properties and liquid subcooling. In contrast, in Bowring's model, ϵ had to be determined using the correlation given by Eq. (31). As such, the heat flux utilized for vapor generation (and hence to calculate the void fraction) is $q_a + q_{\mathrm{ev}}$. Rouhani and Axelsson only used the final void fraction predictions to validate their model. This is shown in Fig. 8. No information was provided regarding the heat transfer components.

Several other studies have used Bowring's model. However, many of them ignore the contribution of q_a and only consider q_{fc} and q_{ev}. The models of Dix [22], Larsen and Tong [23], Ahmad [24], Hancox and Nicoll [25], Maroti [26], Lahey [27], Chatoorgoon et al. [28], and Zeitoun [29] fall into this category. Most of these models do not calculate q_{ev} directly, but do so indirectly by knowing the supplied q_w and calculating q_{fc}. A few of these models are discussed below.

Dix's [22] model is very similar to that developed by Bowring [1]. The wall heat flux partitioning for regions I and II was expressed as,

$$q_w = q_{\mathrm{fc}} + q_{\mathrm{ev}} + q_a = h_{\mathrm{fc}}\,\Delta T_{\mathrm{sub}} + \dot{V}_b \rho_g h_{fg} + \dot{V}_b \rho_f (h_f - h_l)\left(c + (1 - c)\frac{\rho_g}{\rho_f}\right) \tag{38}$$

where $\dot{V}_b$ is the vapor generation rate per unit area of the heater surface and c is a constant ($c \leq 1$). In deriving Eq. (38), Dix assumed that q_{fc} acted over approximately the entire heater surface area (based on visual observation during experiments). The constant c in Eq. (38) was introduced based on the assumption that the effective enthalpy of the liquid (h_{ll}) displaced by the growing bubble lies in between the saturated liquid enthalpy (h_f) and the enthalpy of the subcooled liquid (h_l), i.e., $h_{ll} = c(h_f - h_l) + h_l$. The constant c had to be determined by matching the void fraction predictions with the experimental data. Note that the source term for the void fraction calculation is q_{ev}.

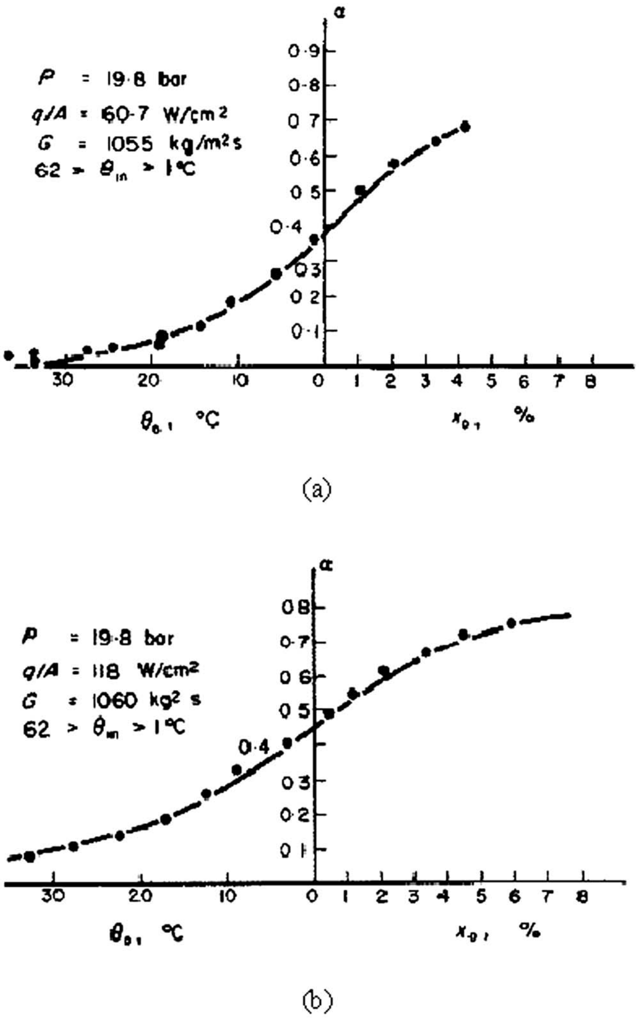

Fig. 8 Void fraction predicted using Rouhani and Axelsson's [19] model, (*a*) q_w=60.7 W/cm^2, and (*b*) q_w=118 W/cm^2

Dix's model also included a new empirical correlation for the OSV condition based on the following assumptions: (i) the size of the bubbles on the heater surface is inversely proportional to the condensation rate from the top of the bubbles, (ii) the size of the bubbles is directly proportional to the wall heat flux, (iii) the condensation rate is proportional to the product $h_{\mathrm{fc}}\,\Delta T_{\mathrm{sub}}$, and (iv) the bubble size at the OSV location is assumed to be proportional to the Reynolds number (i.e., $D_l \sim \mathrm{Re}^{-n}$), where Re $(= \rho_l V_l D_h/\mu_l)$ is based on saturated liquid conditions. Based on these assumptions, the liquid subcooling at OSV is given by the empirical relation,

$$\Delta T_{\mathrm{sub,OSV}} = \frac{0.00135 q_w\,\mathrm{Re}^{0.5}}{h_{\mathrm{fc}}} \tag{39}$$

One of the most commonly used models in thermal hydraulic codes is the one by Lahey [27]. The focus of this model is again on determining the wall heat flux partitioning and not the total wall heat flux itself. In the model developed by Lahey, the overall wall heat flux is partitioned into q_{fc}, q_a, and q_{ev} heat flux components. Defining the boiling heat flux (q_b) as the sum of q_a and q_{ev}, the wall heat flux is expressed as,

$$q_w = q_{\mathrm{fc}} + q_a + q_{\mathrm{ev}} = q_{\mathrm{fc}} + q_b = q_{\mathrm{fc}} + [1 + \epsilon(z)] q_{\mathrm{ev}} \tag{40}$$

In the above equation $\epsilon(z) = q_a/q_{\mathrm{ev}} = \rho_l(he_{l,\mathrm{sat}} - he_l)/\rho_v h_{\mathrm{fg}}$, where he_l and $he_{l,\mathrm{sat}}$ denote enthalpies of the subcooled and saturated liquid, respectively. Note that ϵ is a function of the axial distance

(z) and that $\epsilon=0$ when the liquid is saturated. In this model the following assumptions were made: (i) the void fraction was negligible in the highly subcooled region; and (ii) the OSV location coincides with the point where bubbles begin lifting off from the heater surface, which also signals the onset of fully developed nucleate boiling. Based on these assumptions, upstream of OSV (in region I), $q_w=q_{\mathrm{fc}}$ and downstream of OSV (in region II), $q_w=q_{\mathrm{fc}}+q_b$. In order to account for the fact that the void fraction was neglected upstream of OSV and to ensure that there was no discontinuity in the heat flux calculations, an effective single-phase heat flux component $(q_{\mathrm{fc,eff}})$ was defined as,

$$q_{\mathrm{fc,eff}} = q_w(z)\left(\frac{he_{l,\mathrm{sat}} - he_l(z)}{he_{l,\mathrm{sat}} - he_{l,\mathrm{OSV}}(z)}\right) \tag{41}$$

The boiling heat flux component could then be expressed as

$$q_b = \begin{cases} 0.0 & he_l \le he_{l,\mathrm{OSV}} \\ q_w(z) - q_{\mathrm{fc,eff}} = q_w(z)\left\{1 - \left[\dfrac{he_{l,\mathrm{sat}} - he_l(z)}{he_{l,\mathrm{sat}} - he_{l,\mathrm{OSV}}(z)}\right]\right\} & he_l > he_{l,\mathrm{OSV}} \end{cases} \tag{42}$$

where $he_{l,\mathrm{OSV}}$ is the enthalpy of the liquid at OSV while $he_l(z)$ denotes the enthalpy of the liquid at any axial location (z). The OSV location was calculated using the correlation of Saha and Zuber [30]. It should be noted that in this model, q_a is not calculated explicitly. Condensation of the bubbles in the bulk also provides an additional source of energy into the liquid and was given as,

$$q_c = H_0(\rho_l - \rho_v)h_{\mathrm{fg}}\alpha\frac{A_{\mathrm{cs}}}{P_h}\Delta T_{\mathrm{sub}} \tag{43}$$

where H_0 is a dimensional constant (=0.075) chosen such that the void fraction data was predicted accurately, α is the local void fraction, and A_{cs} and P_h are the cross-sectional area and heated perimeter of the channel, respectively. This model utilizes assumed functional forms for the parameters such as $\epsilon(z)$, z_{OSV}, $q_b(z)$, and $q_c(z)$. As such, upstream of OSV, $q_l=q_w$, and downstream of OSV, $q_l=q_{\mathrm{fc}}+q_a$. The validity of the model predictions was determined by comparing the predicted void fraction profile with experimentally measured values, as shown in Fig. 9. The predicted values closely match the experimental data. However, no information regarding the heat flux components was provided.

Zeitoun's [29] approach was similar to Bowring's, i.e.,

$$q_w = q_{\mathrm{fc}} + q_a + q_{\mathrm{ev}} = h_{\mathrm{fc}}(T_w - T_l) + (1+\epsilon)q_{\mathrm{ev}} \tag{44}$$

where $\epsilon=q_a/q_{\mathrm{ev}}$. The single-phase heat transfer coefficient was calculated using standard correlations. However, the energy carried away by the liquid as a result of bubble agitation was calculated based on the volume of the thermal boundary layer displaced and the mean temperature difference across the thermal boundary layer. As a result, he developed the following expression for ϵ,

$$\epsilon = \frac{A_b\ \delta_t\rho_l\ c_{p,l}\left(\dfrac{T_w+T_l}{2} - T_l\right)}{V_b\rho_v h_{\mathrm{fg}}} \tag{45}$$

where A_b and V_b are the bubble area and volume calculated using the mean Sauter diameter, respectively. It must be mentioned that the mean Sauter diameter used in this model is for bubbles in the bulk subcooled liquid and hence do not represent the bubble diameter at or close to the heated wall. The mean Sauter diameter $(D_{b,s})$ was given by the correlation,

$$D_{b,s} = 1.85\alpha^{0.243}\left(\frac{\sigma}{g\,\Delta\rho}\right)^{0.55}\left(\frac{G}{\mu_l}\right)^{0.1} \tag{46}$$

where α is the bulk void fraction, σ is the surface tension, and G is the total mass flux. The thermal boundary layer thickness (δ_t) was calculated as $\delta_t=k_l(T_w-T_l)/q_w$. Zeitoun, however, did not calculate q_{ev} independently. Instead he calculated ϵ and then from Eq. (44) calculated q_{ev}. Then, knowing ϵ and q_{ev}, q_a can be calculated. Thus, $q_l=q_{\mathrm{fc}}+q_a$, and $q_{\mathrm{ev}}=q_w-q_l$. The void fraction profile was calculated using q_{ev} as the source term.

Mechanistic Models for Prediction of Wall Heat Flux and Partitioning

The mechanistic models described in this section determine the relevant heat flux components independently. Hence these models can be used to predict both the wall heat flux partitioning and the overall wall heat flux.

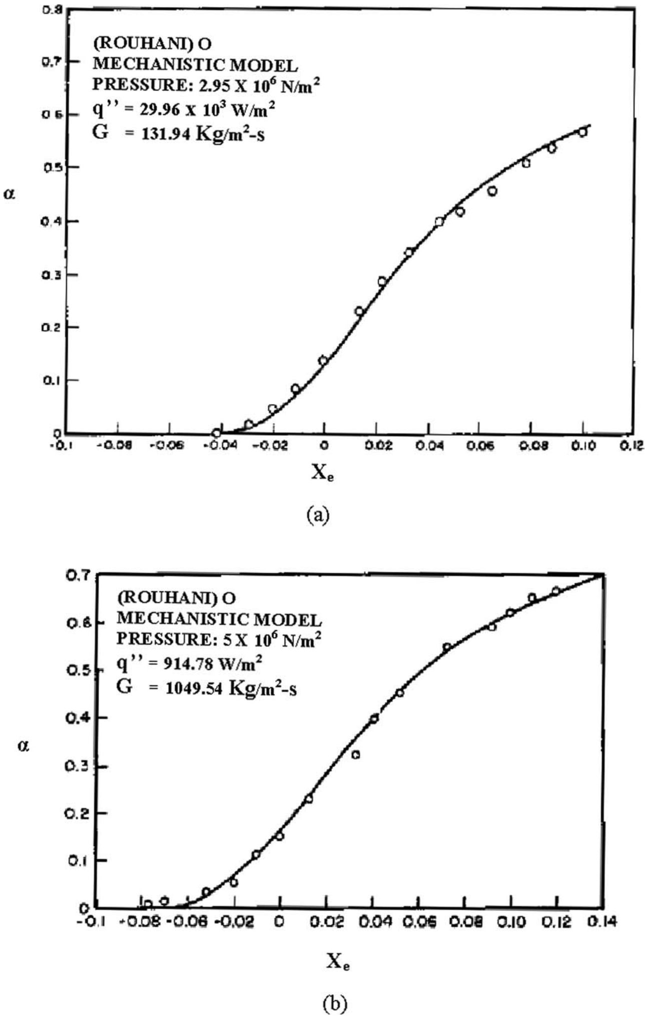

Fig. 9 Lahey's [27] model predictions (*a*) low heat flux; (*b*) high heat flux

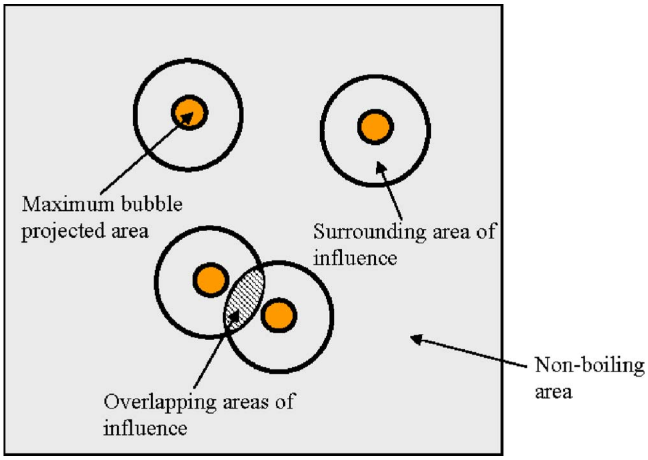

Fig. 10 Heat transfer regions considered by Del Valle and Kenning [31]

Del Valle and Kenning [31] developed a mechanistic model for subcooled flow nucleating boiling, taking into consideration the bubble dynamics at the heated wall. This model used some of the concepts developed earlier by Graham and Hendricks [32] for wall heat flux partitioning during pool nucleate boiling. In the Del Valle and Kenning model, it was assumed that, once boiling begins, the heated wall could be divided into four regions namely, maximum bubble projected area, surrounding area of influence, overlapping areas of influence, and nonboiling area, with different heat transfer mechanisms in each region (see Fig. 10). Assuming the bubbles to be hemispherical in shape, the maximum bubble projected area (A_b), per bubble, was given by $A_b = \pi R_m^2$, where R_m is the maximum bubble radius. For a heater surface with an active nucleation site density of N_a, the fraction (F) of the heater surface covered by the maximum bubble projected area was $F = A_b N_a = \pi R_m^2 N_a$. The active nucleation site density (N_a) was not correlated but instead was tabulated as a function of wall superheat. Note that R_m was assumed to be the same for all the sites. The nominal area of the heater surface over which boiling was assumed to occur was KF, where K is an empirical constant that accounts for the ratio of the area of influence to the maximum bubble projected area. However, to account for the fact that the true area over which boiling occurs will be reduced due to significant overlapping of the areas of influence, an additional empirical parameter (X) was introduced. Hence the true boiling area was given as XKF. Thus the nonboiling area fraction was $1 - XKF$. Additionally, based on the analysis of Kenning and Del Valle [33], the overlapping area of influence was given as $(1-X)KF$ while the area of influence without overlap was given as $(2X-1)KF - F$.

Under the assumption that the temperature profile in the microlayer is linear and that the energy conducted through the microlayer is utilized for evaporation at the liquid-vapor interface (as a result the thickness of the microlayer decreases with time), the instantaneous heat transfer rate in the microlayer was calculated using the following set of equations:

$$q_m = \frac{k_l \, \Delta T_w}{\delta_m} \tag{47}$$

$$\delta_m = \sqrt{\delta_{m,0}^2 - \frac{2 k_l \, \Delta T_w \, t}{\rho_l h_{\mathrm{fg}}}} \tag{48}$$

In Eq. (48) the initial microlayer thickness ($\delta_{m,0}$) was obtained from the correlation of Cooper et al. [34]. The energy utilized for microlayer evaporation was then obtained by integrating Eq. (47) over the appropriate time interval and area. The time-averaged heat flux during quenching (or transient conduction) q_{tc} was given as,

$$q_{\mathrm{tc}} = t_{\mathrm{tc}} f \frac{2 k_l (\Delta T_w + \Delta T_{\mathrm{sub}})}{\sqrt{\pi \alpha_l t_{\mathrm{tc}}}} \tag{49}$$

where t_{tc} is the time for transient conduction [=bubble waiting time (t_w)] determined from visual observations during experiments. The quenching heat flux was assumed to occur in the surrounding areas of influence over the time period t_{tc}. The heat flux experienced by the overlapping areas of influence was determined to be $4/3 q_{\mathrm{tc}}$ and acted for a time interval $1/f$. As such, the total heat flux was then sum of the heat flux contributions from these four areas. It should be noted that the empirical constant K was varied from 5.8 to 7.5 so as to match the predicted heat flux values with the experimental data. Table 1 shows the heat flux components and total heat flux predicted for experiments with water as the test fluid. Based on the predicted values, they concluded that the microlayer evaporation contribution was only about 2–3%, while single-phase heat transfer accounted for about 10% of the total heat flux at low heat fluxes and about 5% at high heat fluxes. The quenching heat flux in the areas of influence was the largest component of the total heat flux.

Kurul and Podowski [35] also developed a mechanistic model, wherein the wall heat flux was partitioned into three heat flux components; single-phase (q_{fc}), transient conduction (q_{tc}), and evaporation (q_{ev}). Since the heat flux supplied to the liquid is the sum of q_{fc} and q_{tc}, the wall heat flux partitioning can be written as,

$$q_w = q_{\mathrm{fc}} + q_{\mathrm{tc}} + q_{\mathrm{ev}} = q_l + q_{\mathrm{ev}} \tag{50}$$

Single-phase heat transfer was assumed to occur in areas of the heater surface not influenced by the bubbles. Accordingly, assuming turbulent forced convection and using Reynolds analogy, q_{fc} is expressed as,

$$q_{\mathrm{sp}} = A_{\mathrm{fc}} \rho_l c_{p,l} U_l \, \mathrm{St}(T_w - T_l) \tag{51}$$

where A_{fc} is the fraction of the heater surface area not influenced by bubbles and St is the Stanton number. The quenching heat flux component is the same as that used by Del Valle and Kenning [31], while q_{ev} is given by Eq. (30). The area of the heater surface influenced by bubbles (A_{tc}) and over which transient conduction occurs is given as,

Table 1 Predicted heat flux components (from Del Valle and Kenning [31])

CHF (%)	K	KF	KFX	Microlayer evaporation (W/cm^2)	Quenching under bubble (W/cm^2)	Quenching in area of influence (W/cm^2)	Convection (W/cm^2)	q_w predicted (W/cm^2)	q_w experimental (W/cm^2)
70	7.5	0.94	0.67	6	49	264	28	347	344
80	7.3	1.08	0.73	8	62	303	23	396	394
90	6.7	1.19	0.74	10	80	329	23	442	443
95	5.8	1.10	0.73	13	93	338	24	468	467

$$A_{\text{tc}} = K\frac{\pi D_l^2}{4}N_a \tag{52}$$

where the empirical constant K was used to account for the area of the heater surface influenced by the bubble (a value of $K=4$ was used in this study), and N_a is the calculated using the correlation (based on Del Valle and Kenning's [31] data),

$$N_a = (210\,\Delta T_w)^{1.8} \tag{53}$$

Additionally, since the overlapping of bubble influence areas was neglected, the minimum spacing between nucleation sites was equal to twice the bubble departure diameter. In this model, q_{fc} acts over the area $(1-A_{\text{tc}})$, while q_{tc} acts over the area A_{tc}. Moreover, q_{tc} was assumed to act only during the time interval 0.8/f. In Eq. (52), the bubble diameter at lift off (D_l) is calculated from the correlation (based on Unal's [36] data),

$$D_l = 0.0014 + 10^{-4}\,\Delta T_{\text{sub}} \tag{54}$$

where D_l is in m and ΔT_{sub} is in °C. Additionally, the bubble release frequency is calculated from Cole's [37] correlation for pool nucleate boiling,

$$f = \sqrt{\frac{4g\,\Delta\rho}{3D_l\rho_l}} \tag{55}$$

Though the Kurul and Podowski model can be used to predict the wall heat flux (since the individual heat flux components are calculated independently), this has not been reported. The validation of their model was only done by comparing the void fraction prediction with the experimentally obtained data.

The mechanistic model of Kurul and Podowski has also been used more recently by Tu and Yeoh [38], Kumar et al. [39], Končar et al. [40], and Wintterle et al. [41] as heat transfer closure models for modeling the thermal hydraulics in nuclear reactor geometries. It must be noted that a number of different correlations for N_a, D_l, and f have been adopted in these follow on studies.

More recently, a new approach to the partitioning of the wall heat flux was proposed by Basu et al. [42,43]. The fundamental idea of this model is that the all the energy from the wall is transferred to the liquid layer adjacent to the heated wall. Thereafter, a fraction of the energy from this superheated liquid layer is transferred to the vapor bubbles by evaporation while the remainder goes into the bulk liquid. As in previous models, this model also assumes that once boiling begins, the heating surface can be split into two regions, namely, (i) the region between ONB and OSV (region I) and (ii) the region downstream of OSV (region II). In each region, various heat transfer mechanisms were considered depending on the physical processes involved.

As in previous models, upstream of ONB, all the energy is transferred from the wall to the bulk liquid by single-phase forced convection (Q_{fc}), i.e.,

$$q_w = \frac{Q_w}{A_h} = \frac{Q_{fc}}{A_h} = h_{fc}(\Delta T_w + \Delta T_{sub}) = \frac{Q_l}{A_h} = q_l \tag{56}$$

where h_{fc} is the single-phase forced convection heat transfer coefficient determined from standard correlations and A_h is the total heater area.

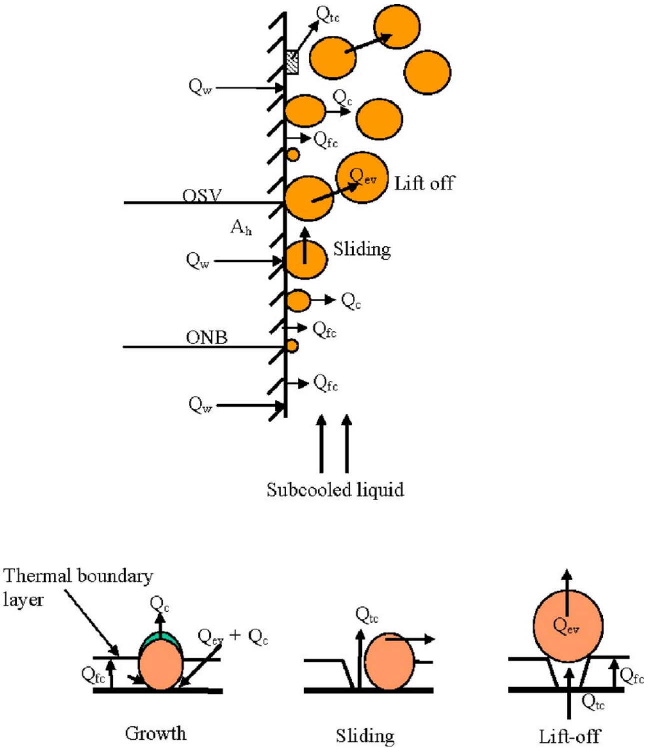

Fig. 11 Heat transfer mechanisms considered by Basu et al. [42,43]

In the region between ONB and OSV, small bubbles were assumed to be attached to the heater surface, as shown in Fig. 11. In the regions not occupied by bubbles, all the energy from the wall is directly transferred to the liquid by single-phase forced convection (Q_{fc}). In turn, a fraction of the energy from the superheated liquid layer adjacent to the wall is utilized for evaporation (Q_{ev}). Additionally, condensation heat transfer (Q_c) was assumed to occur from the top of the attached bubbles which are exposed to the subcooled liquid. Since the bubbles do not grow in size and remain attached to the heated wall, $Q_c=Q_{\text{ev}}$. As such, condensation from the bubbles attached to the surface merely provides an alternate route for heat transfer from the wall to the liquid. Hence, the wall heat flux partitioning was expressed as,

$$q_w = \frac{Q_w}{A_h} = \frac{Q_{fc}}{A_h} = h^*_{\text{fc}}(\Delta T_w + \Delta T_{\text{sub}}) = \frac{Q_l}{A_h} \tag{57}$$

where h^*_{fc} is the enhanced forced convection heat transfer coefficient. The enhancement is due to the additional surface roughness due to presence of the bubbles and the oscillations at the liquid-vapor interface. In Eq. (57), Q_l is the energy transferred to the bulk subcooled liquid.

In the region downstream of OSV, as the bulk liquid subcooling decreases, the bubbles grow to a size D_d (called the departure diameter), depart from their sites of origin, slide along the heater surface and eventually lift off when they reach a size D_l (called the liftoff diameter). Figure 11 shows the various heat transfer mechanisms considered. Transient conduction (Q_{tc}) occurs when the thermal boundary layer is disrupted due to bubble growth and/or bubble sliding. In this model, it was assumed that when the boundary layer is disrupted, q_{tc} initially occurs for a time interval t^*, followed by q_{fc}. In other words, this implies that since q_{tc} decreases as the square root of time while q_{fc} is independent of time, the heater surface always experiences the large to the two heat fluxes. The time interval t^* was determined by equating q_{tc} and q_{fc} and was expressed as,

$$t^* = \left(\frac{k_l}{h_{fc}}\right)^2 \frac{1}{\pi\alpha} \tag{58}$$

Since condensation heat transfer (Q_c) occurs at the top of the bubbles attached to the heater surface and the energy carried away by a bubble during liftoff was Q_{ev}, the total energy input into the bubble from the superheated liquid layer is $Q_{\text{ev}}+Q_c$. The rest of the energy from the superheated layer goes toward heating of the bulk liquid (Q_{bulk}). Condensation was again assumed to be an alternate path for heat transfer to the liquid. As such, the wall heat flux was partitioned as,

$$q_w = \frac{Q_w}{A_h} = \frac{Q_{\mathrm{fc}}}{A_h} + \frac{Q_{\mathrm{tc}}}{A_h} = \frac{Q_{\mathrm{bulk}}}{A_h} + \frac{Q_c}{A_h} + \frac{Q_{\mathrm{ev}}}{A_h} = \frac{Q_l}{A_h} + \frac{Q_{\mathrm{ev}}}{A_h} \tag{59}$$

Basu et al. noted that since Eq. (59) implied that Q_c was not an independent component of the wall heat flux, this information was not necessary for modeling the wall heat flux partitioning. It must be noted that Q_l consists of the energy gained directly from the wall and energy gained due to the condensation of vapor bubbles in the bulk liquid.

In the region downstream of OSV, with the increase in the bubble number density with an increase in the wall temperature, situations where bubble merger can occur were also identified. Fully developed boiling was assumed to begin when the spacing between the nucleation sites (s) was small enough that the bubbles could merge laterally without sliding. On the other hand, for large values of s, the bubbles will slide along the surface before lifting off. For simplicity, the Basu et al. model assumed that the nucleation sites were distributed in a square grid, and hence $s=1/\sqrt{N_a}$. Further, it was assumed that the bubbles only slide in the flow direction. Based on these assumptions, they considered situations where the bubbles slide and situations where they did not. A summary of this is given below.

Bubble Sliding and Merger: Bubble sliding was assumed to occur when s was greater than both D_d and D_l. The model also accounted for bubble growth while sliding. Additionally, once a bubble began to slide, two possible scenarios were considered: (i) the bubble will not encounter other bubbles before liftoff; and (ii) the bubble will encounter one or more bubbles along its sliding path and merge with them before liftoff. Defining l_0 as the distance a bubble will travel as it grows from D_d to D_l, when no other sites are active or the sites are widely spaced, they argued that merger will only occur when $s \le l_0$. When merger did occur, the primary bubble was assumed to gain the vapor volume of the secondary bubble. Hence, the actual distance (l) that the primary bubble will slide before liftoff will be less than l_0. These situations are shown in Fig. 12. Basu et al. argued that as a result of bubble mergers, the actual number of bubbles lifting off the heater surface will be less than N_a and accounted for this using a reduction factor (R_f). The reduction factor was defined as the ratio of the actual number of bubbles lifting off per unit area of the heater surface to the number of active nucleation sites per unit area and was given as,

$$R_f = \frac{1}{l/s} = \frac{1}{l\sqrt{N_a}} \tag{60}$$

Note that for $s > l_0$, $l=l_0$ and $R_f=1$.

Figure 12 also shows the bubble waiting time (t_w) and bubble growth time (t_g). The bubble waiting time is defined as the time period between bubble departure and the inception of the next bubble at a given site, while the growth time (t_g) is the time required for bubble growth from inception to the maximum size (D_d), at its site of origin. In Fig. 12 it should also be noted that though the bubble continues to grow while sliding, the time of growth at the site of origin along with the waiting time represents the periodicity. Thus the time period (t_w+t_g) was taken as the appropriate time period for averaging all the heat transfer components. As such, the frequency of bubble release (f) is given by $1/(t_w+t_g)$. Additionally, at steady state a continuous train of bubbles slide and lift off, hence f represented both the bubble departure rate as well as the bubble lift off rate from the heater surface.

Transient conduction (Q_{tc}) occurs in the regions swept by the sliding bubble. Since the duration for which it will occur is governed by the magnitude of t^*, Q_{tc} was given by,

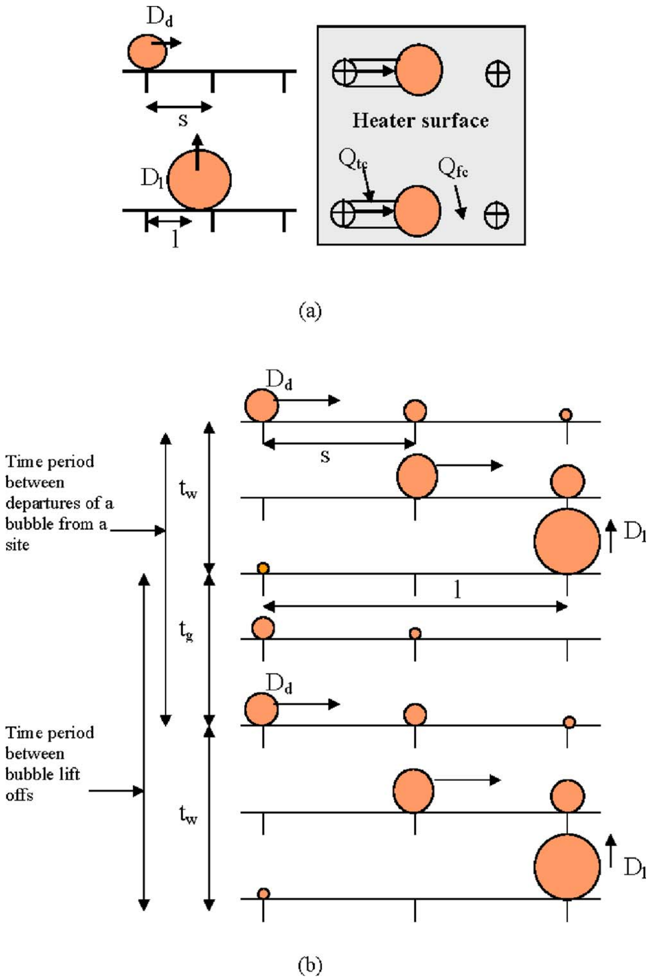

Fig. 12 Bubble sliding cases (*a*) sliding without merger (*b*) sliding with merger (Basu et al. [42,43])

$$\frac{Q_{\mathrm{tc}}}{A_h} = \frac{1}{t_w + t_g}\int_0^t \frac{k_l}{\sqrt{\pi \alpha_l t}}(\Delta T_w + \Delta T_{\mathrm{sub}})(A_{sl})R_f N_a \, dt \tag{61}$$

where $t=t^*$ when $t^* < (t_w+t_g)$ and $t=(t_w+t_g)$ when $t^* \ge (t_w+t_g)$ and A_{sl} is the sliding area.

Forced convection (Q_{fc}) prevails at all times in the areas of the heater surface not influenced by sliding bubbles. The fraction of the heater area not influenced by sliding bubbles was given by $(1-A_{\mathrm{sl}}R_f N_a)$. It should be noted that if $t^* < (t_w+t_g)$, the heater area influenced by sliding will experience Q_{tc} followed by Q_{fc}. As such, the forced convection component was expressed as,

$$\frac{Q_{\mathrm{fc}}}{A_h} = h^*_{\mathrm{fc}}(\Delta T_w + \Delta T_{\mathrm{sub}})[1 - A_{\mathrm{sl}}R_f N_a] + h^*_{\mathrm{fc}}(\Delta T_w + \Delta T_{\mathrm{sub}})A_{\mathrm{sl}}R_f N_a\left(1 - \frac{t^*}{t_w + t_g}\right) \tag{62}$$

where h^*_{fc} is the area-averaged enhanced heat transfer coefficient.

Since the evaporative component (Q_{ev}) of the wall heat transfer is the energy of vaporization required to produce a bubble of size D_l, it was expressed as,

$$\frac{Q_{\mathrm{ev}}}{A_h} = \rho_v h_{\mathrm{fg}} \frac{\pi}{6} D_l^3 R_f N_a f \tag{63}$$

As such, $q_l = q_w - q_{\mathrm{ev}}$.

Bubble Merger Without Sliding: This was assumed to occur at high superheats. As N_a, D_d and D_l increase, the bubbles tend to

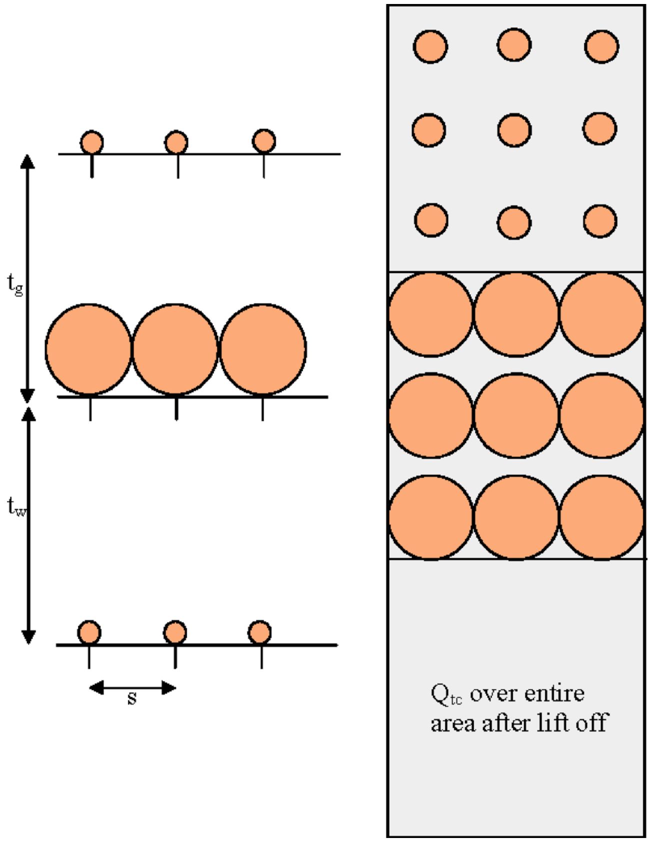

Fig. 13 Sliding without merger (Basu et al. [42,43])

merge with each other in all directions, while growing at their sites of origin. This is shown in Fig. 13. In this situation, the maximum size that the bubble can grow to is the average spacing between sites (s). Thereafter they will merge together to form a bubble of size D_l, which then lifts off from the heater surface. In this case, the growth time (t_g) corresponds to the time required for a bubble to grow to size s. The number of bubbles that will merge together to yield one liftoff diameter bubble was obtained from volume considerations. Hence, the reduction factor was expressed as,

$$R_f = \frac{s^3}{D_l^3} \tag{64}$$

Transient conduction occurs over the entire heater surface after bubble merger and liftoff, as shown in Fig. 13. Depending on the relative magnitudes of t_w, t_g, and t^*, several possibilities were considered, as given below.

(i) $t^* \leq t_w$: Transient conduction will occur on the entire heater surface for a time interval t^*, i.e.,

$$\frac{Q_{\rm tc}}{A_h} = \frac{1}{t_w + t_g}\int_0^{t^*} \frac{k_l}{\sqrt{\pi\alpha_l t}}(\Delta T_w + \Delta T_{\rm sub})dt \tag{65}$$

Following transient conduction, forced convection will take place on the entire heater surface area until time t_w and thereafter in regions not occupied by bubbles during time t_g. This was expressed as,

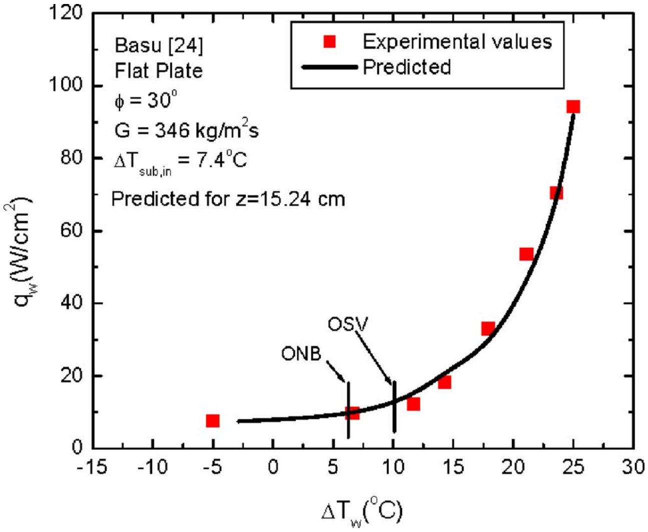

Fig. 14 Predicted boiling curve for flat plate test case (Basu et al. [43])

$$\frac{Q_{\rm fc}}{A_h} = h_{\rm fc}^*(\Delta T_w + \Delta T_{\rm sub})\frac{t_w - t^*}{(t_g + t_w)} + h_{\rm fc}^*(\Delta T_w + \Delta T_{sub}) \times [1 - A_b N_a]\frac{t_g}{(t_g + t_w)} \tag{66}$$

where A_b is the base area of the bubble.

(ii) $t^* > t_w$: Transient conduction occurs over the entire heater surface for time t_w. It then also continues for time t_g in regions not occupied by bubbles until time t^* or $(t_w + t_g)$, whichever is smaller. In this case, $q_{\rm tc}$ was expressed as,

$$\frac{Q_{\rm tc}}{A_h} = \frac{1}{t_w + t_g}\left[\begin{array}{l} \displaystyle\int_0^{t_w} \frac{k_l}{\sqrt{\pi\alpha_l t}}(\Delta T_w + \Delta T_{\rm sub})dt \\ \displaystyle + \int_{t_w}^{t} \frac{k_l}{\sqrt{\pi\alpha_l t}}(\Delta T_w + \Delta T_{\rm sub})[1 - A_b N_a]dt \end{array}\right] \tag{67}$$

where $t = (t_w + t_g)$, if $t^* > (t_w + t_g)$, otherwise $t = t^*$. Forced convection will occur after transient conduction only if $t^* < (t_w + t_g)$. In the case where $t^* \geq (t_w + t_g)$, $q_{\rm fc}$ will be zero (i.e., $q_{\rm tc}$ will prevail at all times). As such, $q_{\rm fc}$ can be expressed as,

$$\frac{Q_{\rm fc}}{A_h} = \begin{array}{ll} h_{\rm fc}^*(\Delta T_w + \Delta T_{\rm sub})[1 - A_b N_a]\dfrac{t_w + t_g - t^*}{(t_w + t_g)} & t_w < t^* < (t_w + t_g) \\ 0 & t^* \geq (t_w + t_g) \end{array} \tag{68}$$

The evaporative component ($q_{\rm ev}$) is given by Eq. (63) with the R_f obtained from Eq. (64). Thus the evaporative component was given as,

$$\frac{Q_{\rm ev}}{A_h} = \rho_v h_{\rm fg}\frac{\pi}{6}D_l^3 R_f N_a f = \rho_v h_{\rm fg}\frac{\pi}{6}s^3 N_a f \tag{69}$$

The total wall heat flux can then be partitioned into that going into the liquid and vapor phases using Eq. (59).

Due to the additional subprocesses considered in the Basu et al. model, in order to apply this model additional submodels for various parameters such as the location of ONB, the location of OSV, N_a, D_d, D_l, t_w, t_g, $h_{\rm fc}^*$, sliding distance (l), and ratio of the bubble base to bubble diameter (C) are required. Basu et al. developed models/correlations for each of these parameters based on the experimental data obtained from their experiments (see Basu

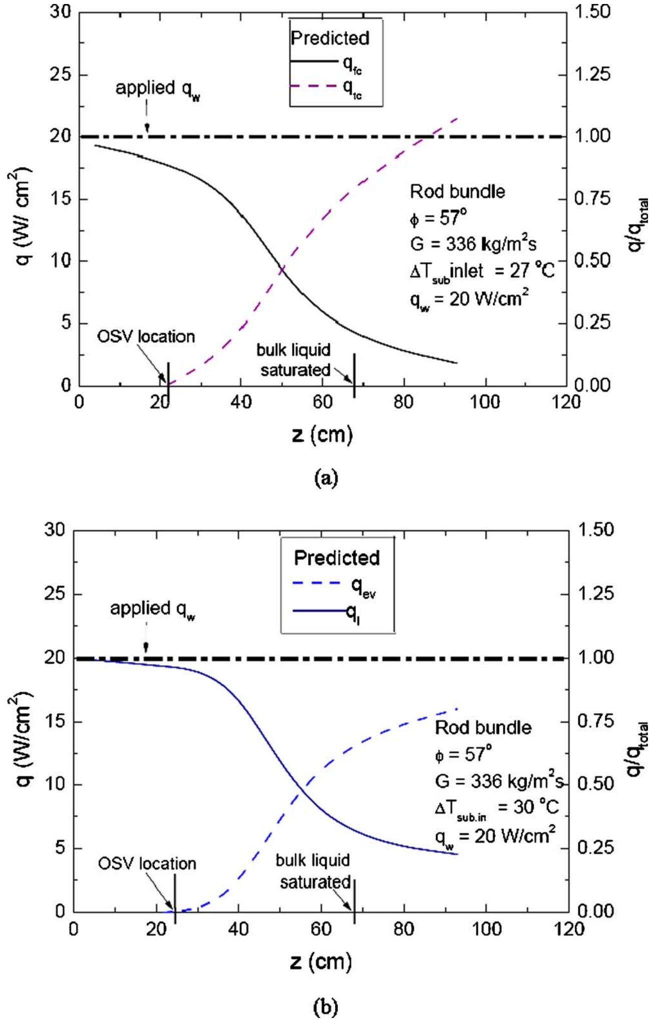

Fig. 15 Predicted heat flux components for rod bundle geometry (*a*) q_{fc} and q_{tc}, (*b*) q_l and q_{ev} (Basu et al. [43])

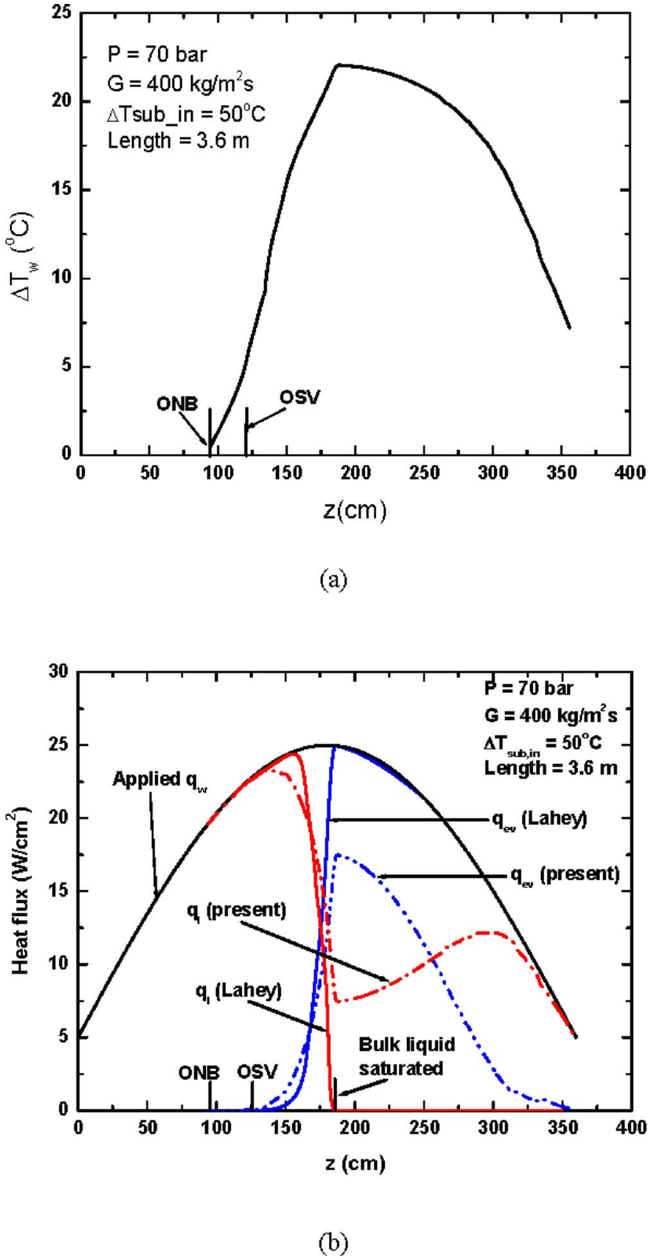

Fig. 16 A comparison between the Basu et al. [42] and Lahey's [27] model

[42,44]) and from those available in the literature. It should be noted that the submodels for the various parameters is only valid for the vertical upflow of water.

The subcooled flow boiling curve predicted using this model shows good agreement with experimental data for a vertical flat plate, as shown in Fig. 14. The q_{fc} and q_{tc} heat flux components calculated using this model for a nine-rod bundle is shown in Fig. 15(*a*). The corresponding q_l and q_{ev} components are shown in Fig. 15(*b*). Note that these components are plotted as a function of the axial direction. In these figures, the difference between the predicted and imposed total heat fluxes varied between −2.5% to +5.5%. In Fig. 15(*b*), it is interesting to note that at the exit only 80% of the total heat flux is utilized for evaporation though the liquid is already saturated. Thus, 20% of the wall heat flux is still used to superheat the liquid. Figure 16(*a*) shows the computed wall temperature profile for subcooled boiling of water in a vertical pipe when the imposed heat flux has a sine profile. Figure 16(*b*) shows the corresponding q_l and q_{ev} heat flux components computed using the mechanistic wall heat flux partitioning models of Basu et al. [42,43] and Lahey [27]. The ONB, OSV, and the location where the bulk liquid attains saturation are also shown in Fig. 16. Lahey's model predicts that as long as the liquid is subcooled, all the energy is utilized for heating the bulk liquid ($q_{ev} \approx 0, q_l \approx q_w$). However, once the liquid is saturated, $q_{ev} \approx q_w$ and hence $q_l \approx 0$. The Basu et al. model predicts that upstream of OSV, all the energy goes to the liquid ($q_l \approx q_w$). However, downstream of OSV, q_{ev} increases rapidly with a corresponding decrease in q_l. It should be noted that even when the liquid is saturated, a fraction of the wall heat flux is utilized for superheating the liquid.

Summary

A review of both empirical correlations and mechanistic heat transfer models has been presented. The empirical correlations for wall heat flux are based on curve fitting experimental datasets and hence are only capable of predicting the total wall heat flux. Since they do not account for the physical mechanisms involved, significant differences between the predictions and experimental data can occur when the conditions for which they were developed is not duplicated. This is a major drawback of these models. Moreover, they cannot be used to partition the wall heat flux. On the other hand, the empirical correlations that are based on the relevant heat transfer mechanisms can be used to determine how the wall heat flux is partitioned. However, since all the heat flux components are not calculated independently, these correlations cannot be used to predict the wall heat flux itself. The mechanistic wall heat flux partitioning models attempt to predict the wall heat flux based on the individual heat transfer mechanisms involved. Since each heat flux component is calculated independently, these models can also be used to predict the overall wall heat flux. However, due to fact that the relevant heat transfer mechanisms are modeled, additional submodels or correlations are required for the parameters involved (such as N_a, D_d, D_l, t_w, t_g, etc.). This in turn means that well controlled experiments will need to be performed to gather the data and validate the model predictions.

Acknowledgment

This work received support from the United States Nuclear Regulatory Commission (USNRC).

Nomenclature

A_b = Base area of influence of a bubble
A_{nb} = Fractional area over which nucleate boiling occurs
A_{sl} = Area swept by a sliding bubble
A_{tc} = Area experiencing transient conduction
c_p = Specific heat capacity
C = Ratio of bubble base diameter to bubble diameter
D = Diameter
f = Bubble release frequency
g = Gravitational acceleration
h = Heat transfer coefficient
he = Enthalpy
h_{fg} = Latent heat of vaporization
k = Thermal conductivity
l = Sliding distance
l_0 = Sliding distance for a single cavity on the surface
M = Molecular weight
N_a = Nucleation site density
p = Pressure
Pr = Prandtl number
Q = Energy
q = Heat flux
Re = Reynolds number
St = Stanton number
t = Time
T = Temperature
ΔT = Temperature difference
U = Bulk velocity
V = Volume
z = Axial direction (along the flow direction)

Greek

α = Thermal diffusivity or void fraction
δ_{t} = Thermal boundary layer thickness
ρ = Density
σ = Surface tension
μ = Viscosity

Subscripts

b = Bubble
c = Condensation
d = Departure diameter
ev = Evaporation
fc = Forced convection
fdb = Fully developed boiling
g = Growth
l = Liquid, liftoff diameter when used with D
nb = Pool nucleate boiling
ONB = Onset of nucleate boiling
OSV = Onset of significant void
pb = Partial nucleate boiling
sat = Saturation
sub = Subcooled
tc = Transient conduction
v = Vapor
w = Wall, waiting when used with t

References

[1] Bowring, R. W., 1962, "Physical Model Based on Bubble Detachment and Calculation of Steam Voidage in the Subcooled Region of a Heated Channel," HPR-10, Institutt for Atomenergi, Halden, Norway.
[2] Engelberg-Forster, K., and Greif, R., 1959, "Heat Transfer to a Boiling Liquid—Mechanism and Correlation," Trans. ASME, Ser. C: J. Heat Transfer, **81**, pp. 43–53.
[3] Kutateladze, S. S., 1961, "Boiling Heat Transfer," Int. J. Heat Mass Transfer, **4**, pp. 31–45.
[4] Rohsenow, W. M., 1953, "Heat Transfer with Evaporation," *Proceedings of Heat Transfer—A Symposium Held at the University of Michigan During the Summer of 1952*, University of Michigan Press, Ann Arbor, pp. 101–150.
[5] Bergles, A. E., and Rohsenow, W. M., 1964, "The Determination of Forced Convection, Surface Boiling Heat Transfer," ASME J. Heat Transfer, **86**, pp. 365–372.
[6] Bjorge, R. W., Hall, G. R., and Rohsenow, W. M., 1982, "Correlation of Forced Convection Boiling Heat Transfer Data," Int. J. Heat Mass Transfer, **25**, pp. 753–757.
[7] Colburn, A. P., 1933, "A Method of Correlating Forced Convection Heat Transfer Data and a Comparison with Fluid Friction Data," Trans. Am. Inst. Chem. Eng., **29**, p. 174.
[8] Mikic, B. B., and Rohsenow, W. M., 1969, "A New Correlation of Pool Boiling Data Including the Effect of Heating Surface Characteristics," ASME J. Heat Transfer, **91**, pp. 245–256.
[9] McAdams, W. H., Kennel, W. E., Minden, C. S., Carl, R., Picornell, P. M., and Dew, J. E., 1949, "Heat Transfer at High Rates to Water with Surface Boiling," Ind. Eng. Chem., **41**, pp. 1945–1953.
[10] Liu, Z., and Winterton, R. H. S., 1991, "A General Correlation for Saturated and Subcooled Flow Boiling in Tubes and Annuli, Based on a Nucleate Pool Boiling Equation," Int. J. Heat Mass Transfer, **34**, pp. 2759–2766.
[11] Chen, J. C., 1966, "A Correlation for Boiling Heat Transfer to Saturated Fluids in Convective Flows," Ind. Eng. Chem. Process Des. Dev., **5**, pp. 322–329.
[12] Boyd, R. D., and Meng, X., 1996, "Boiling Curve Correlation for Subcooled Flow Boiling," Int. J. Heat Mass Transfer, **38**, pp. 758–760.
[13] Kandlikar, S. G., 1998, "Heat Transfer Characteristics in Partial Boiling, Fully Developed Boiling, and Significant Void Flow Regions of Subcooled Flow Boiling," ASME J. Heat Transfer, **120**, pp. 395–401.
[14] Wadekar, V. V., 1996, "An Alternative Model for Flow Boiling Heat Transfer," *Convective Flow Boiling*, edited by J. C. Chen, Taylor and Francis, Washington, DC, pp. 187–192.
[15] Cooper, M. G., 1984, "Saturation Nucleation Boiling—A Simple Correlation," IChemE Symp. Ser., **86**, pp. 786–793.
[16] Jens, W. H., and Lottes, P. A., 1951, "An Analysis of Heat Transfer, Burnout, Pressure Drop, and Density Data for High Pressure Water," Argonne Natl. Lab Report No. ANL-4627-1951.
[17] Thom, J. R. S., Walker, W. M., Fallon, T. A., and Reising, G. F. S., 1965, "Boiling in Subcooled Water During Flow up Heated Tubes or Annuli," presented at the Symposium on Boiling Heat Transfer in Steam Generating Units and Heat Exchangers, Institute of Mechanical Engineers, London.
[18] Griffith, P., Clark, J. A., and Rohsenow, W. M., 1958, "Void Volumes in Subcooled Boiling," ASME Paper 58-HT-19, U.S. National Heat Transfer Conference, Chicago.
[19] Rouhani, S. Z., and Axelsson, E., 1970, "Calculation of Void Volume Fraction in the Subcooled and Quality Boiling Regions," Int. J. Heat Mass Transfer, **13**, pp. 383–393.
[20] Zuber, N., and Findlay, J., 1965, "Average Volumetric Concentration in Two-Phase Flow Systems," ASME J. Heat Transfer, **87**, pp. 453–462.
[21] Rouhani, S. Z., 1968, "Calculation of Steam Volume Fraction in Subcooled Boiling," ASME J. Heat Transfer, **90**, pp. 158–164.
[22] Dix, G. E., 1971, "Vapor Void Fraction For Forced Convection with Subcooled Boiling at Low Flow Rates," Ph.D. thesis, University of California, Berkeley.
[23] Larsen, P. S., and Tong, L. S., 1969, "Void Fractions in Subcooled Flow Boiling," ASME J. Heat Transfer, **91**, pp. 471–476.
[24] Ahmad, S. Y., 1970, "Axial Distribution of Bulk Temperature and Void Fraction in a Heater Channel With Inlet Subcooling," ASME J. Heat Transfer, **92**, pp. 595–609.
[25] Hancox, W. T., and Nicoll, W. B., 1971, "A General Technique for the Prediction of Void Distributions in Non-Steady Two-Phase Forced Convection," Int. J. Heat Mass Transfer, **14**, pp. 1377–1394.
[26] Maroti, L., 1977, "Axial Distribution of Void Fraction in Subcooled Boiling," Nucl. Technol., **34**, pp. 8–17.
[27] Lahey, R. T., 1978, "A Mechanistic Subcooled Boiling Model," *Proceedings of the 6th International Heat Transfer Conference*, Toronto, Canada, Hemisphere Publishing Corporation, Washington, Vol. 1, pp. 293–297.
[28] Chatoorgoon, V., Dimmick, G. R., Carver, M. B., Selander, W. N., and Shoukri, M., 1992, "Application of Generation and Condensation Models to

Predict Subcooled Boiling Void at Low Pressures," Nucl. Technol., **98**, pp. 366–378.

[29] Zeitoun, O., 1994, "Subcooled Flow Boiling and Condensation," Ph.D. thesis, McMaster, University, Hamilton, Ontario, Canada.

[30] Saha, P., and Zuber, N., 1974, "Point of net vapor generation and vapor void fraction in subcooled boiling," *Proceedings of the 5th International Heat Transfer Conference, Tokyo, Japan*, Hemisphere Publishing Corporation, Washington, Vol. 4, pp. 175–179.

[31] Del Valle, V. H. M., and Kenning, D. B. R., 1985, "Subcooled Flow Boiling at High Heat Flux," Int. J. Heat Mass Transfer, **28**, pp. 1907–1920.

[32] Graham, R. W., and Hendricks, R. C., 1967, "Assessment of Convection, Conduction and Evaporation in Nucleate Boiling," NASA TND-3943.

[33] Kenning, D. B. R., and Del Valle, V. H. M., 1981, "Fully Developed Nucleate Boiling: Overlap of Areas of Influence and Interference between Bubble Sites," Int. J. Heat Mass Transfer, **21**, pp. 1025–1032.

[34] Cooper, M. G., Judd, A. M., and Pike, R. A., 1978, "Shape and Departure of Single Bubbles Growing at a Wall," *Proceedings of the 6th International Heat Transfer Conference*, Toronto, Hemisphere Publishing Corporation, Washington, Vol. 1, pp. 115–120.

[35] Kurul, N., and Podowski, M. Z., 1990, "Multidimensional Effects in Forced Convection Subcooled Boiling," *Proceedings of the 9th International Heat Transfer Conference*, Jerusalem, Israel, Hemisphere Publishing Corporation, Vol. 2, pp. 21–26.

[36] Unal, H. C., 1976, "Maximum Bubble Diameter, Maximum Bubble Growth Time and Bubble Growth Rate During Subcooled Nucleate Flow Boiling of Water up to 17.7 $\mathrm{MN/m^2}$," Int. J. Heat Mass Transfer, **19**, pp. 643–649.

[37] Cole, R., 1960, "Photographic Study of Boiling in the Region of Critical Heat Flux," AIChE J., **6**, pp. 533–542.

[38] Tu, J. Y., and Yeoh, G. H., 2002, "On Numerical Modeling of Low-Pressure Subcooled Boiling Flows," Int. J. Heat Mass Transfer, **45**, pp. 1197–1209.

[39] Kumar, R., Maneri, C. C., and Strayer, T. D., 2004, "Modeling and Numerical Prediction of Flow Boiling in a Thin Geometry," ASME J. Heat Transfer, **126**, pp. 23–33.

[40] Končar, B., Kljenak, I., and Mavko, B., 2004, "Modeling of Local Two-Phase Parameters in Upward Subcooled Flow Boiling at Low Pressures," Int. J. Heat Mass Transfer, **47**, pp. 1499–1513.

[41] Wintterle, T., Laurien, E., Egorov, Y. E., and Menter, F. R., 2005, "Numerical Simulation of a Subcooled Boiling Flow in a Nuclear Reactor Rod Bundle Assembly," *Proceedings of the 11th Workshop on Two-Phase Flow Predictions*, Merseburg, Germany.

[42] Basu, N., Warrier, G. R., and Dhir, V. K., 2005, "Wall Heat Flux Partitioning During Subcooled Flow Boiling: Part I—Model Development," ASME J. Heat Transfer, **127**, pp. 131–140.

[43] Basu, N., Warrier, G. R., and Dhir, V. K., 2005, "Wall Heat Flux Partitioning During Subcooled Flow Boiling: Part II—Model Validation," ASME J. Heat Transfer, **127**, pp. 141–148.

[44] Basu, N., 2003, "Modeling and Experiments For Wall Heat Flux Partitioning During Subcooled Flow Boiling of Water at Low Pressures," Ph.D. thesis, University of California, Los Angeles.

A Transient Nucleate Boiling Model Including Microscale Effects and Wall Heat Transfer

Thomas Fuchs

Jürgen Kern

Peter Stephan
e-mail: pstephan@ttd.tu-darmstadt.de

Chair of Technical Thermodynamics,
Darmstadt University of Technology,
Petersenstrasse 30,
64287 Darmstadt, Germany

A new model is presented to compute nucleate boiling heat and mass transfer. It is based on a previous one (Kern, J., and Stephan, P., 2003, ASME J. Heat Transfer, 125, pp. 1106–1115) for quasi-stationary heat transfer to single vapor bubbles. In contrast to the preceding model, fully transient heat and fluid flow is computed with a free surface of the rising bubble and a periodic calculation of repeated cycles of bubble growth, detachment, and rise, requiring only specification of the waiting time between successive bubbles. Additionally, microscopic effects at the foot of the bubble are considered. The model is verified by comparing computed with measured heat transfer coefficients. Typical results for heat and mass transfer to a single vapor bubble are shown at all time steps of the bubble cycle. By means of the model the transient heat flow through different interfaces, e.g., wall/liquid or liquid/vapor, is computed for the whole bubble cycle. Thus, it was possible to evaluate the influence of transient heat conduction, heat storage, and convection in liquid as well as heat transfer in the wall on overall heat transfer performance.
[DOI: 10.1115/1.2349502]

Keywords: nucleate boiling, transient, free surface, arbitrary Lagrangian Eulerian method, microscale, micro region

1 Introduction

In spite of numerous investigations, nucleate boiling heat and mass transfer is still not fully understood. To study heat and mass transfer, experiments with single vapor bubbles have been carried out. One of the pioneering investigations was done by Beer [1] who measured the interferometric pattern around a growing and rising vapor bubble. In recent experimental investigations progress is mainly made

- by a miniaturization of measurement devices, e.g., Auracher and co-workers [2] use micro-thermocouples and an optical probe to measure heat and mass transfer to single vapor bubbles,
- by means of microtechnology, e.g., Kim and co-workers [3,4] use a microheater array that provides local surface heat flux and temperature measurements, and
- by new measurement technologies, e.g., thermochromic liquid crystals that show a high local temperature resolution and thus are used to determine the time evolution of the spatial temperature distribution on the heater surface [5–7].

Besides experimental investigations, in the last decade theoretical models have been developed to compute numerically nucleate boiling heat and mass transfer. Fundamentally, they are all based on a thin film evaporation concept of Wayner and co-workers [8]. They investigated the evaporation of a liquid meniscus in a tiny area where the liquid-vapor interface approaches the wall. In spite of the small spatial dimensions (about one micrometer), a considerable amount of the supplied heat at the evaporator wall flows through the so-called "micro region." In this region, microscale effects such as adhesion forces and interfacial thermal resistance in combination with a strong curvature change of the liquid-vapor interface significantly influence local heat and mass transfer. The micro region model was implemented into macroscopic vapor bubble growth models by several authors using different assumptions and simplifications [9–12]. Stephan and Hammer [9] introduced a nucleate boiling model for pure substances that was extended to binary mixtures by Kern and Stephan [10]. This model considers heat conduction in liquid and wall as well as evaporation of the liquid for quasi-stationary bubble growth. A transient nucleate boiling model was presented by Dhir and co-workers [11]. They computed nucleate boiling heat and mass transfer for the whole bubble cycle of a growing, departing, and rising vapor bubble. Fujita and Bai [12] introduced a transient nucleate boiling model for bubble growth and departure. They assumed a constant contact angle during the whole bubble growth and departure process. Dhir and co-workers [11] as well as Fujita and Bai [12] assumed a constant wall temperature and therefore neglected the influence of transient heat conduction in the wall on the boiling process.

In the present work a new nucleate boiling model is presented. It is based on the previous model of Kern and Stephan [10]. In contrast to the preceding model, fully transient heat and fluid flow is computed including wall heat transfer with a free surface of the rising bubble and a periodic calculation of repeated cycles of bubble growth, detachment, and rise, requiring only specification of the waiting time between successive bubbles. In Sec. 2, a detailed description of the new model is given including modeling strategy, governing equations, boundary conditions, and numerical treatment. Typical results of a single bubble cycle are shown in Sec. 3. Additionally, the transient heat flow to wall, bubble, and liquid is discussed. Furthermore, the accuracy of the model is assessed by comparing computed with measured heat transfer coefficients.

2 Numerical Model

2.1 Modeling Strategy. As long as neighboring bubbles do not interact, the boiling system can be divided into subsystems, each of them containing a single nucleation site (Fig. 1). This is fulfilled for low and intermediate heat fluxes. The subsystem consists of a single nucleation site, surrounding liquid, and a part of the heated wall (Fig. 1). Using cylindrical coordinates (ξ, η), the

---

Contributed by the Heat Transfer Division of ASME for publication in the JOURNAL OF HEAT TRANSFER. Manuscript received July 27, 2005; final manuscript received April 5, 2006. Review conducted by Raj M. Manglik.

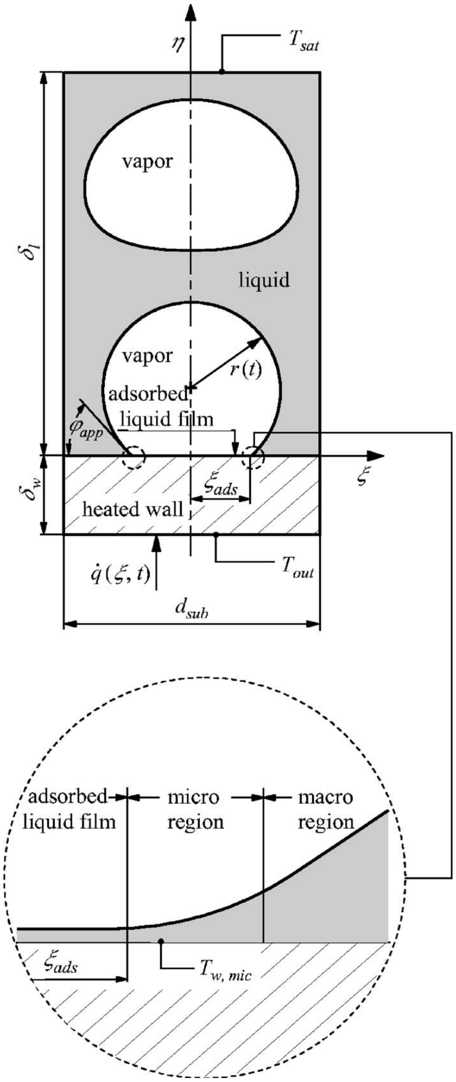

Fig. 1 Subsystem and computational domains

radius r_{sub} of the single bubble subsystems corresponds to the bubble site density (N_b). The thickness δ_l of the liquid layer is chosen to be greater than the thickness of the thermal boundary layer, which is calculated by the model. The subsystem includes a part of the heated wall because in experiments thermocouples are placed at a distance δ_w below the boiler surface. Furthermore, the wall is included in the subsystem because the effect of wall heat transfer on nucleate boiling is the subject of the present investigation.

Boundary conditions (Fig. 1) are the outside wall temperature T_{out} and the saturation temperature of the bulk fluid T_{sat} (upper boundary contacts a perfectly mixed pool). Regarding the constant outside wall temperature T_{out}, current calculations [13] with a corresponding constant heat flux $\dot{q}_{out}$ at the outside of the heater wall approve the equivalence of both boundary conditions in the case of the presented copper heater. Using a constant heat flux boundary condition causes a temperature variation of less than 0.04 K at the outside of the heater wall during a bubble cycle. The model describes heat and mass transfer in this subsystem for the time period when the bubble grows from a tiny size to the departure radius, detaches, and rises towards the upper boundary of the subsystem until the next bubble is formed at the nucleation site and a new cycle starts. The shape of the bubble is assumed to be spherical during bubble growth and departure. For the rising bubble a free surface is considered. As input parameters only values for the bubble site density and waiting time, respectively, bubble frequency, are required. These data can either be taken from measurements or from correlations for the bubble site density, e.g., [14–16], and for the bubble frequency, e.g., [17].

In contrast to the preceding model of Kern and Stephan [10] the new model provides a periodic calculation of repeated cycles of bubble growth, detachment, and rise. The transient computation yields the time-dependent local distribution of the heat flux $\dot{q}(\xi,t)$. Averaging the local heat flux $\dot{q}(\xi,t)$ with respect to the radius r_{sub} of the subsystem and the time period of the bubble cycle t_b, which is a result of the computation, yields the mean heat flux,

$$\dot{q}_m = \frac{2}{t_b r_{sub}^2}\int_0^{t_b}\int_0^{r_{sub}} \dot{q}(\xi,t)\xi\, d\xi\, dt \tag{1}$$

From that the mean heat transfer coefficient is obtained,

$$\alpha_m = \frac{\dot{q}_m}{T_{out}-T_{sat}} \tag{2}$$

The local heat flux $\dot{q}(\xi,t)$ is also used to predict the evaporative mass flux, which yields the bubble growth rate, by solving

$$\dot{m}_{evap}(t) = \frac{\lambda_l}{\Delta h_{lv}} \iint_{A_{\mathrm{int}}} \left.\frac{dT}{dn}\right|_{\mathrm{int}} dA_{\mathrm{int}} \tag{3}$$

at the phase interface of the bubble.

To calculate the heat flux $\dot{q}(\xi,t)$ the computational domain is divided into two regions (Fig. 1):

- the tiny thin film area, called the micro region, where the bubble is attached to the wall
- and the liquid adjacent to the micro region as well as the wall, called the macro region.

Transport phenomena within the vapor bubble are insignificant for overall heat transfer coefficients [18]. Therefore, the vapor is not included into one of these regions during bubble growth and departure. The model considers a very thin, nonevaporating liquid film, which is adsorbed at the wall underneath the vapor bubble. Governing equations, boundary conditions, and numerical treatment of both regions are explained in the succeeding sections.

2.2 Governing Equations and Boundary Conditions

2.2.1 Micro Region. In Fig. 2 the micro region is plotted on a larger scale. In this region the curvature of the liquid-vapor interface differs strongly from the mean curvature in the macro region. High local heat fluxes induce a transverse liquid flow into the micro region. The following effects are considered in the micro region (see also spheres of influence in Fig. 2): Surface tension and adhesion forces influence the mechanical equilibrium at the liquid-vapor interface of the thin curved liquid film. Due to the very thin liquid film and high heat fluxes, the interfacial thermal resistance becomes important. If a binary mixture is boiled, one component evaporates preferentially. Therefore, strong concentration gradients and thus diffusive mass transfer as well as Marangoni convection occur. Furthermore, the high local curvature of the liquid-vapor interface, the adhesion forces, and the change of concentration strongly influence the thermodynamic equilibrium at the liquid-vapor interface. Considering the described effects in standard equations of continuity and a scale analysis yields a set of six nonlinear ordinary differential equations as described in a preceding paper [10]. Even if the equations in this paper [10] are derived for a quasi-stationary solution, estimations of Stephan [19] and Mann [20] show that these equations are still valid for transient problems if the heater wall material features a high thermal conductivity. The modeling equations are solved numerically in an iterative process with the macro region equations (Sec. 2.3). As a result, for a given radius $r(t)$, one gets the heat flux $\dot{q}_{mic}(\xi)$,

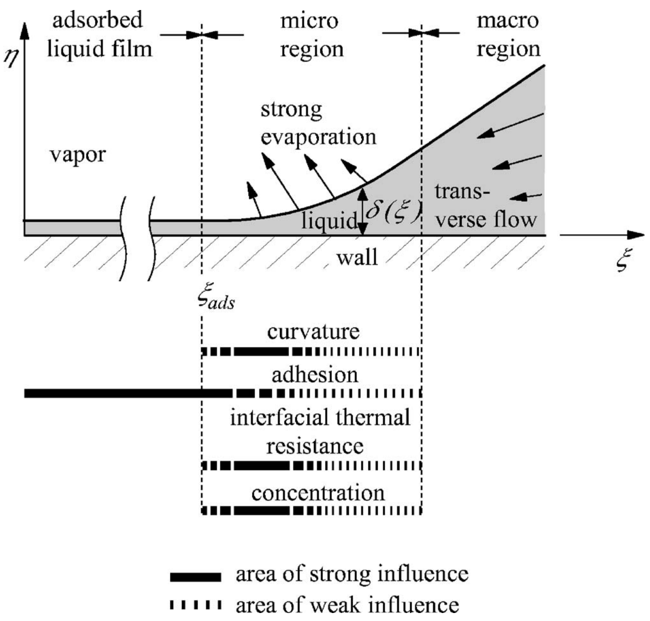

Fig. 2 Significant phenomena in the micro region

the meniscus shape $\delta(\xi)$, and the liquid composition as well as the apparent contact angle φ_{app} shown in Fig. 1 [10].

2.2.2 Macro Region. In the macro region the standard equations of conservation with the following assumptions are used:

- incompressible fluid, $D\rho/Dt=0$ (except for the Boussinesq term)
- symmetry with respect to normal co-ordinate $\eta, (\partial/\partial\xi)|_{\xi=0,\xi=r_{sub}}=0$
- laminar flow without vortices around normal coordinate η, $u_\theta=0$
- only gravity acts as volume force, $\mathbf{f}=(0,-g)$
- dissipation can be neglected in the energy equation.

Thus, the conservation equations can be written for
mass

$$\frac{1}{\xi}\frac{\partial}{\partial\xi}(\xi u_\xi)+\frac{\partial}{\partial\eta}(u_\eta)=0 \tag{4}$$

momentum (ξ):

$$\rho\left(\frac{\partial u_\xi}{\partial t}+(u_\xi-u_{\xi m})\frac{\partial u_\xi}{\partial\xi}+(u_\eta-u_{\eta m})\frac{\partial u_\xi}{\partial\eta}\right)=\frac{-\partial p}{\partial\xi}+\frac{\partial}{\partial\xi}\left(\frac{\rho\nu}{\xi}\frac{\partial(\xi u_\xi)}{\partial\xi}\right)+\frac{\partial}{\partial\eta}\left(\rho\nu\frac{\partial u_\xi}{\partial\eta}\right) \tag{5}$$

momentum (η):

$$\rho\left(\frac{\partial u_\eta}{\partial t}+(u_\xi-u_{\xi m})\frac{\partial u_\eta}{\partial\xi}+(u_\eta-u_{\eta m})\frac{\partial u_\eta}{\partial\eta}\right)=\frac{-\partial p}{\partial\eta}+\frac{1}{\xi}\frac{\partial}{\partial\xi}\left(\xi\rho\nu\frac{\partial u_\eta}{\partial\xi}\right)+\frac{\partial}{\partial\eta}\left(\rho\nu\frac{\partial u_\eta}{\partial\eta}\right)+\rho f_\eta+\rho g\beta_{ref}(T-T_{ref}) \tag{6}$$

energy:

$$\rho c\left(\frac{\partial T}{\partial t}+(u_\xi-u_{\xi m})\frac{\partial T}{\partial\xi}+(u_\eta-u_{\eta m})\frac{\partial T}{\partial\eta}\right)=\frac{1}{\xi}\frac{\partial}{\partial\xi}\left(\xi\lambda\frac{\partial T}{\partial\xi}\right)+\frac{\partial}{\partial\eta}\left(\lambda\frac{\partial T}{\partial\eta}\right) \tag{7}$$

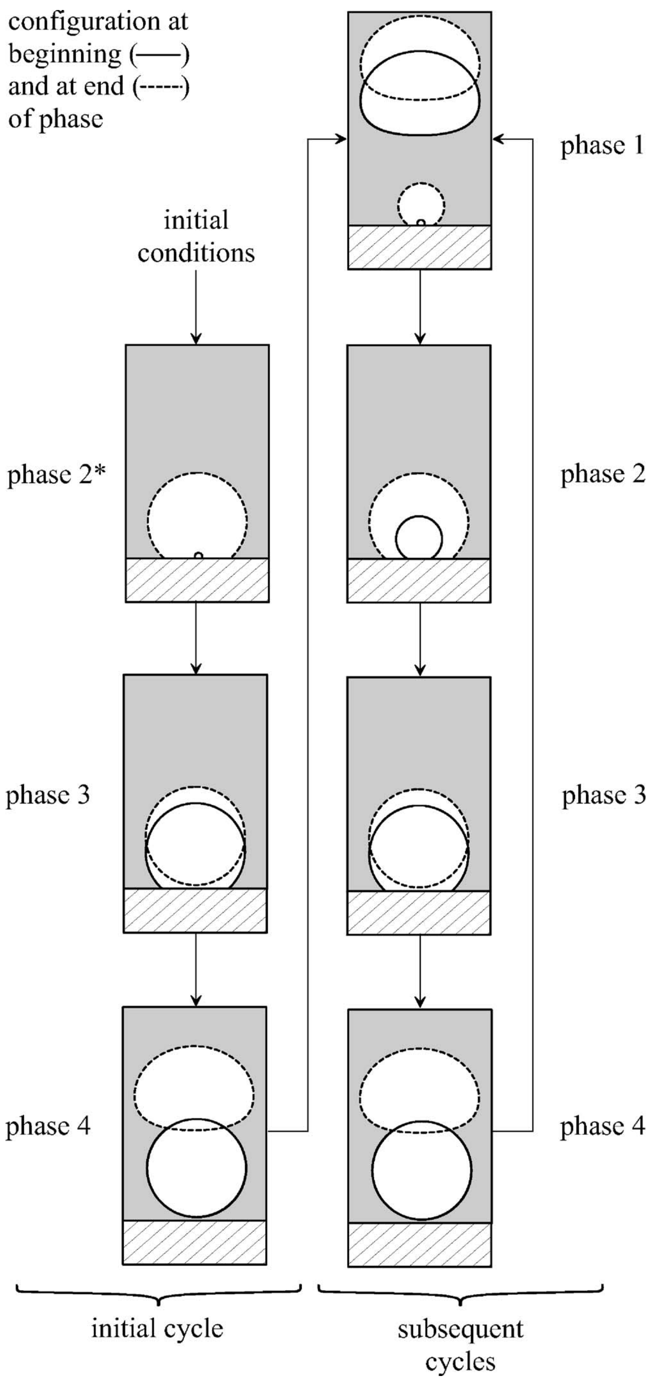

Fig. 3 Definition of phases for the initial bubble cycle and subsequent bubble cycles

Since the influence of mass diffusion of each component on local heat transfer and liquid properties is negligible at the outer liquid boundary of the micro region [21], the effect of mass diffusion in the macro region is not considered in the modeling equations.

For numerical reasons the bubble cycle is divided into phases. The initial cycle consists of three phases (see also Fig. 3):

- Phase 2^* (growing bubble): Period when a bubble is

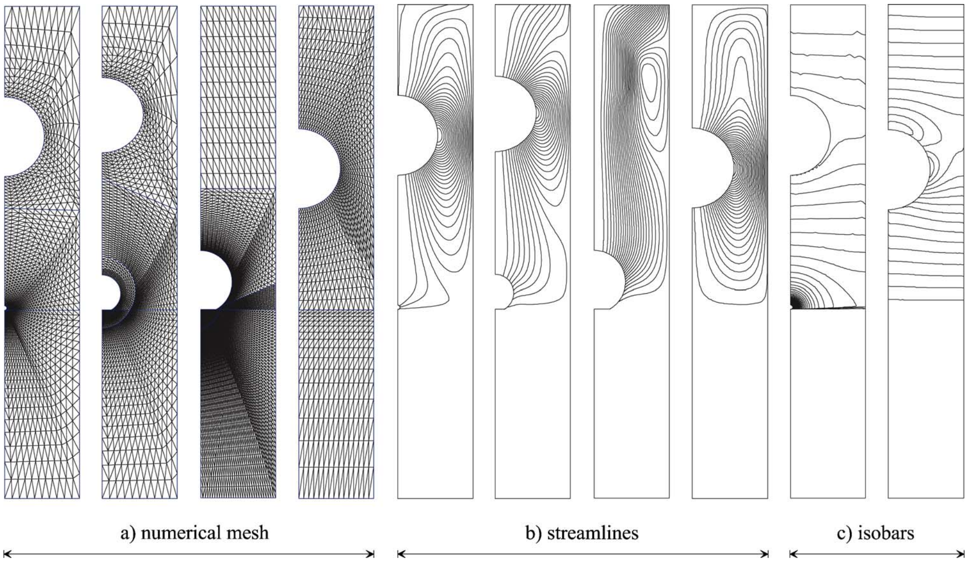

Fig. 4 Finite element grid (*a*), streamlines (*b*), and isobars (*c*) at different stages of the bubble cycle (propane/*n*-butane, $p^*=0.2$, $T_{out}-T_{sat}=8.7$ K, $x_{L,1}=0.245$, $d_{sub}=0.4$ mm)

growing from a tiny size, $r_{ini}=3$ μm (not infinitesimally-small due to numerical reasons), to the radius where the bubble starts to detach.

- Phase 3 (detaching bubble): Period of bubble detachment.
- Phase 4 (rising bubble): Period of the rising bubble until a new bubble is formed at the cavity.

As soon as a new bubble is formed at the cavity, the next bubble cycle starts. In contrast to the first cycle, now two bubbles are considered in the subsystem. Therefore, starting with the second bubble cycle, phase 2^* is subdivided into phases 1 and 2:

- Phase 1 (rising bubble and subsequent growing bubble): The new bubble is growing at the heater surface and the rising bubble is still calculated in the same system. This phase ends when the rising bubble is far away from the thermal boundary layer or reaches the upper part of the subsystem.
- Phase 2 (growing bubble): The growing bubble is considered as in phase 2^*, but at the beginning of phase 2 the bubble radius corresponds to the radius of the growing vapor bubble at the end of phase 1.

At the end of phase 1, when the upper (rising) bubble reaches the top of the considered domain and the numerical mesh gets to distort, the vapor volume of this bubble is filled with saturated liquid (see Figs. 4, 5(*a*), and 5(*b*)). The restrictions of the boundary fitted mesh that is used (see succeeding section) do not allow the surface of the rising bubble to intersect the upper boundary. Neither the kinetic energy nor the shape of the liquid that replaces the vapor has a significant influence on the heat transfer (even if the vortex around the former vapor bubble changes slightly in Fig. 4(*b*)) since the liquid is far away from the thermal boundary layer and drifts with the bubbles constant velocity through the upper boundary like the vapor bubble actually would do. Calculations with a diversifying liquid column approve this. In addition, shape and velocity of the liquid bubble correspond to shape and velocity of the vapor bubble.

By definition, the model is valid for liquids and boiling conditions ensuring small bubble departure diameters. At these special conditions, liquids like propane/*n*-butane hold a nearly spherical bubble shape. Therefore, during phases 1, 2, 2^*, and 3, a spherical shape can be assumed for the growing and detaching bubble. This is necessary to match the macro and micro regions. Due to the very high heat flux density in between and adjacent to the micro region a precise geometrical description of this area is necessary. Using instead a free surface for the growing bubble would induce a phase interface that approaches the wall from a special angle (apparent contact angle) and contacts it in one point. This would be in opposition to the theory of the micro region and would avoid a physical adjustment of this area and cause defective heat fluxes. During phases 4 and 1, the liquid-vapor interface of the rising bubble is treated as a free surface. It ensures the calculation of an accurate rising velocity depending on the bubble's shape. This is important as long as the bubble is located in the thermal boundary layer due to the coherence of rising velocity and convective heat transfer.

To state the boundary conditions, Fig. 6, a definition of the following interfaces is given:

- interface 1: outer surface of the heater wall
- interface 2: surface between the wall and bulk liquid
- interface 3: surface between the wall and liquid in the micro region
- interface 4: surface between the wall and adsorbed liquid film
- interface 5: surface between the bulk liquid and vapor of the bubble during bubble growth and detachment
- interface 6: surface between the bulk liquid and vapor of the bubble during bubble rise
- interface 7: upper surface of the liquid bulk

The boundary conditions of the Navier-Stokes equations and the continuity equation are given in Table 1 for each phase of the bubble cycle. The kinematic description of the liquid-vapor interface during bubble growth and detachment ($u_\xi(\xi,\eta)$, $u_\eta(\xi,\eta)$, interface 5) is determined by the contact angle calculated at the transition from micro to macro region, the assumption of a spherical shape of the bubble, and the evaporating mass. The boundary conditions of the energy equation are shown in Table 2.

Initial conditions of the energy equation are as follows: The temperature of the whole wall corresponds to the outside wall temperature (T_{out}) and a linear temperature distribution is assumed in the thermal boundary layer. The initial thickness of the thermal boundary layer is estimated using a correlation for free convection [22]. The initial condition of the Navier-Stokes equations and the continuity equation is a motionless liquid. Any initial mismatches of heat flux due to these assumptions are not relevant

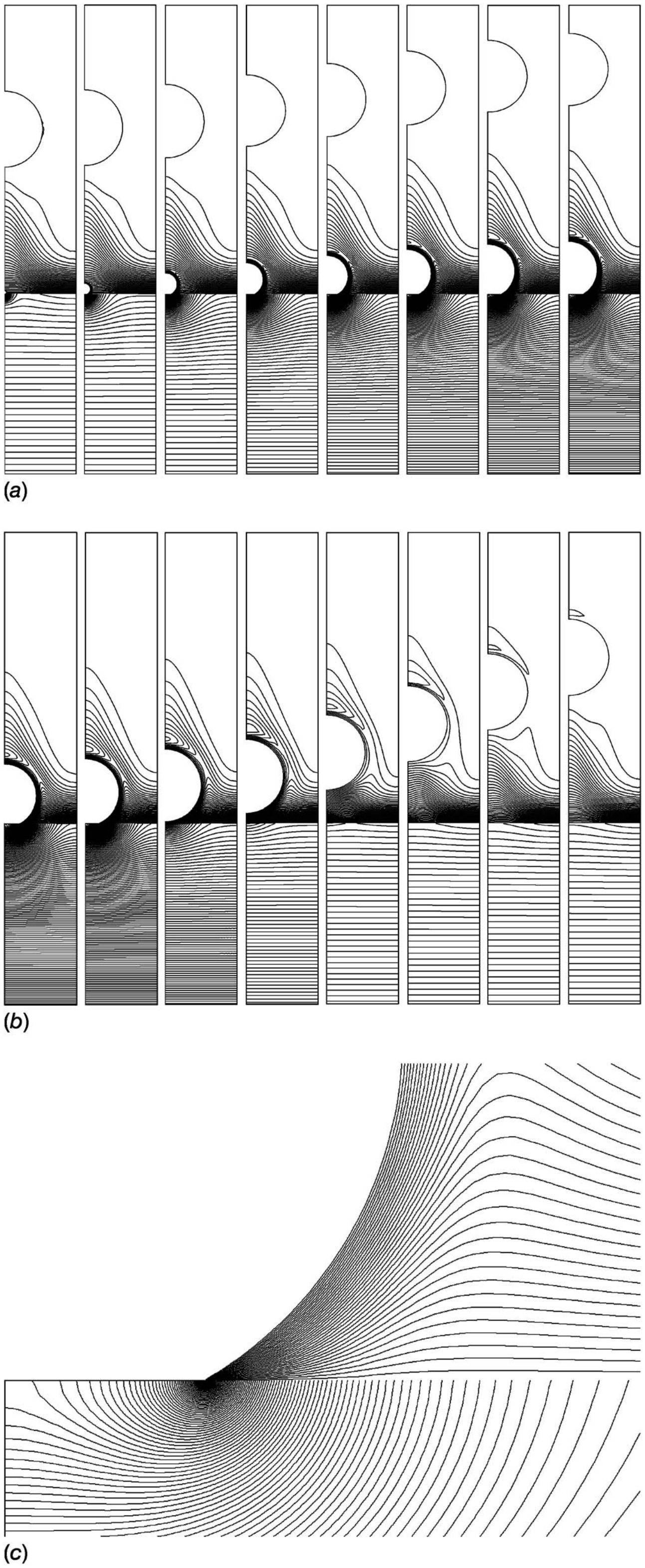

Fig. 5 (*a*) and (*b*) Isotherms ($\Delta T_{iso,w}=5^{*}10^{-4}$ K, $\Delta T_{iso,l}=0.17$ K), (*c*) magnification of isotherms near the micro region ($\Delta T_{iso,w}=5^{*}10^{-4}$ K, $\Delta T_{iso,l}=0.17$ K)

since the simulation settles into a stable cycle. Calculations with different initial conditions concerning the temperature distribution in fluid and heater show the same periodically stationary solution. For each subsequent bubble cycle the thermal and flow conditions at the end of the preceding cycle are used.

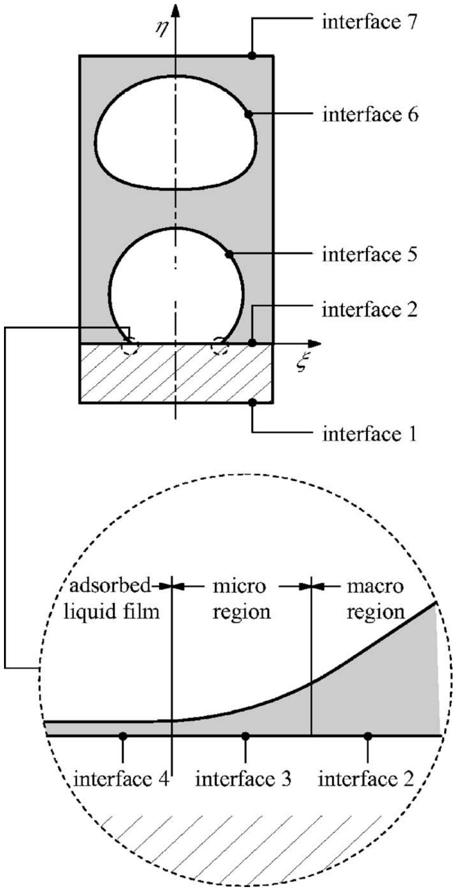

Fig. 6 Definition of interfaces of the subsystem

2.3 Numerical Treatment. During bubble growth and departure the modeling equations of micro and macro regions are solved in an iterative process since heat is transferred from the heater wall (macro region) through the micro region into the vapor. The time-dependent numerical computation starts by calculating the temperature distribution within the subsystem for a bubble of finite size. From the calculated temperature distribution the increase of the bubble volume due to evaporation is determined. Taking into account the apparent contact angle φ_{app}, which is a result of the micro region model, the bubble growth rate $r=f(t)$ is obtained.

To consider the micro region and to avoid diffusion of the phase interface due to strong surface tension effects, a mixed Euler Lagrange method is used. Numerical codes based on discontinu-

Table 1 Boundary conditions of Navier-Stokes equations and continuity equation for each phase of the bubble cycle

Phase no.	Interface no.				
	$\xi=0,\ \xi=r_{sub}$	3, 4	5	6	7
1	$u_\xi=0$ $\frac{\partial u_\eta}{\partial \xi}=0$	$u_\xi=0$ $u_\eta=0$	$u_\xi(\xi,\eta)$ $u_\eta(\xi,\eta)$	$\sigma_n=\gamma\left(\frac{1}{R_1}+\frac{1}{R_2}\right)$ $\sigma_t=0$	$\frac{\partial u_\xi}{\partial \eta}=0$ $u_\eta(\dot{m}_{evap})$
2, 2*	$u_\xi=0$ $\frac{\partial u_\eta}{\partial \xi}=0$	$u_\xi=0$ $u_\eta=0$	$u_\xi(\xi,\eta)$ $u_\eta(\xi,\eta)$		$\frac{\partial u_\xi}{\partial \eta}=0$ $\frac{\partial u_\eta}{\partial \eta}=0$
3	$u_\xi=0$ $\frac{\partial u_\eta}{\partial \xi}=0$	$u_\xi=0$ $u_\eta=0$	$u_\xi(\xi,\eta)$ $u_\eta(\xi,\eta)$	$\sigma_n=\gamma\left(\frac{1}{R_1}+\frac{1}{R_2}\right)$ $\sigma_t=0$	$\frac{\partial u_\xi}{\partial \eta}=0$ $\frac{\partial u_\eta}{\partial \eta}=0$
4	$u_\xi=0$ $\frac{\partial u_\eta}{\partial \xi}=0$	$u_\xi=0$ $u_\eta=0$	$\sigma_n=\gamma\left(\frac{1}{R_1}+\frac{1}{R_2}\right)$ $\sigma_t=0$	$\sigma_n=\gamma\left(\frac{1}{R_1}+\frac{1}{R_2}\right)$ $\sigma_t=0$	$\frac{\partial u_\xi}{\partial \eta}=0$ $u_\eta(\dot{m}_{evap})$

Table 2 Boundary conditions of the energy equation for the whole bubble cycle

	Interface no.				
$\xi=0,\ \xi=r_{sub}$	1	3	4	5, 6	7
$\frac{\partial T}{\partial \xi}=0$	$T=T_{out}$	$T=T_{w,mic}$	$\frac{\partial T}{\partial \eta}=0$	$T=T_{sat}$	$T=T_{sat}$

ous interface capturing methods, e.g., a volume of fluid (VOF) method, turned out to be not useful due to problems at the interface reconstruction and sharpening algorithms (parasitic currents induced by surface tension). Therefore, an arbitrary Lagrangian-Eulerian (ALE) kinematic description is chosen. Using the ALE method, computational meshes may be fixed in space (Eulerian description), may move with the fluid velocity (Lagrangian description), or may move in any other arbitrary way. Thus, between the boundaries of the calculated area, the mesh can be moved in any arbitrary way depending on time and space ($u_m=u_m(\xi,\eta,t)$). A detailed introduction into the ALE theory and the derivations of numerical implementations are given by Frank et al. [23], Noh [24], Hirt et al. [25], Hughes et al. [26], and Donea [27]. For the macro region calculation the finite-element package SEPRAN [28] is used. This modular open source code is modified to fulfill our requirements. The governing equations are discretized in space using a Galerkin finite element method in combination with extended quadratic triangle elements according to Crouzeix-Raviart. The finite elements are distributed depending on the temperature gradient in the macro region. Hence, the grid width in the neighborhood of the micro region and close to the liquid-vapor interface is extremely small (Fig. 4) and the number of elements therefore becomes very high. In order to decouple pressure and velocity, a penalty function method is applied. Girault and Raviart [29] provide a detailed derivation and a convergence proof of this method. The nonlinear (convective) terms in the momentum equations are treated by a Newton or alternatively by a Picard linearization and the time integration is approximated by an implicit Euler scheme. To prevent problems with the free surface implementation a slow but stable direct solver is chosen. The numerical accuracy of this model is estimated by a variation of mesh size and time-step size. To verify the free surface implementation, different test cases, e.g., the broken dam problem [30–33], terminal velocity calculations of rising bubbles by Raymond [34], and shape analyses of growing vapor bubbles by Dhir [11], were performed. The results confirm the validity of the free surface model. To prove the overall heat balance, a spatial and temporal integration of the heat flux for one bubble cycle is performed. We thereby estimate the accuracy of the calculated heat transfer coefficients to 2–3%.

3 Results

As input parameters the model needs the bubble site density and waiting time, which are reported in a very few publications only. Therefore, experimental values are taken from Bednar and Bier [35] as well as Schmidt [17]. Bednar and Bier [35] measured wall superheat and heat transfer coefficients on copper tubes and determined bubble site densities for various hydrocarbons simultaneously. Additionally, Schmidt [17] observed bubble behavior in nucleate boiling of the same liquids photographically and determined the waiting time.

3.1 Bubble Cycle. Using data for the bubble site density from Bednar and Bier [35] as the input parameter, nucleate boiling heat and mass transfer of propane/*n*-butane on copper is calculated. In Figs. 5(*a*)–5(*c*) the isotherms and in Fig. 4 the streamlines are shown at different phases of the bubble cycle, i.e., at the beginning of phase1 (nucleation), during phase 2 (growth), at the end of phase 3 (departure), and during phase 4 (rise). As can be seen from the isotherms in Figs. 5(*a*)–5(*c*), during bubble growth heat flow is concentrated towards the micro region due to the high heat flux in the micro region. Therefore, heat conduction in the wall becomes two-dimensional. After departure and during subsequent rise of the bubble (when no micro region occurs), wall heat flow to the heater surface immediately becomes nearly one-dimensional. Thus, the effect of thermal inertia on the temperature distribution in the wall is weak. Furthermore, it can be stated that the effect of the micro region on wall heat flow during bubble growth and departure is very strong. Due to the streamlines liquid is displaced by the growing bubble. Each bubble induces a single vortex. Although a free surface is assumed for the rising bubble, the bubble still deviates only little from a spherical shape because the bubble is very small. The model was also tested for lower surface tension fluids. In that case the typical mushroom-like shape was obtained.

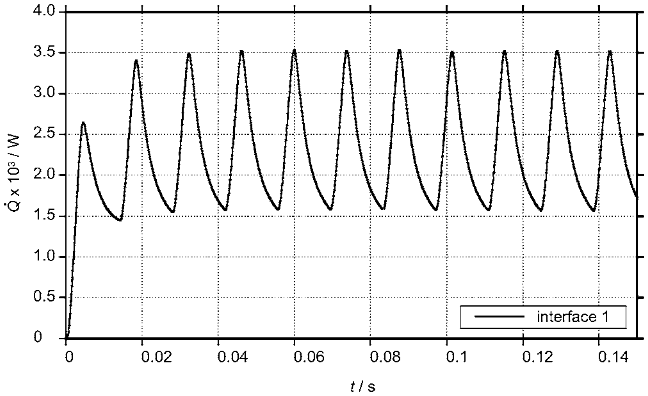

Fig. 7 Time-dependent heat flow through interface 1 (propane/*n*-butane, $p^*=0.2$, $T_{out}-T_{sat}=8.7$ K, $x_{L,1}=0.245$, $d_{sub}=0.4$ mm)

3.2 Transient Heat Flow to Wall, Bubble, and Liquid. To investigate the influence of transient heat conduction, heat storage, and convection in liquid as well as heat transfer in the wall on overall heat transfer performance, the transient heat flow through different interfaces is computed as a function of time. In Fig. 7 the calculated heat flow through interface 1, i.e., through the outer surface of the wall (Fig. 6), is plotted versus time for 11 bubble cycles. At the beginning of the calculation a constant temperature in the wall is assumed and the thickness of the thermal boundary layer is estimated using a correlation for free convection. As can be seen from the heat flow through interface 1 (Fig. 7), the assumed temperature distribution at the beginning corresponds to a stored heat in the system that is too high. Therefore, the mean heat flow per cycle through interface 1 increases during the first cycles until a periodically stationary heat flow is obtained (approximately at the fourth bubble cycle).

In Fig. 8 the calculated heat flow through interfaces 2, 3, and 5 (Fig. 6) is plotted versus time for the seventh and eigth bubble cycles. No heat is transferred through the adsorbed liquid film (interface 4). The heat flow through interface 3, i.e., through the micro region, increases during bubble growth, decreases during bubble departure, and equals to zero during bubble rise. Increase and decrease of heat flow through the micro region is roughly proportional to the variation of the circular interface area between micro region and wall that increases with increasing bubble radius. The heat flow to the bubble cap (interface 5) also increases during bubble growth and departure due to an increase of the bubble surface. During bubble rise this heat flow decreases since the bubble removes from the superheated thermal boundary layer. The heat flow through interface 2, i.e., through the heater surface to the liquid of the macro region, also increases during bubble growth and departure due to the vicinity of the bubble that acts as a heat sink. After departure heat flow through interface 2 rapidly decreases, indicating that single phase heat transfer to the liquid is very low.

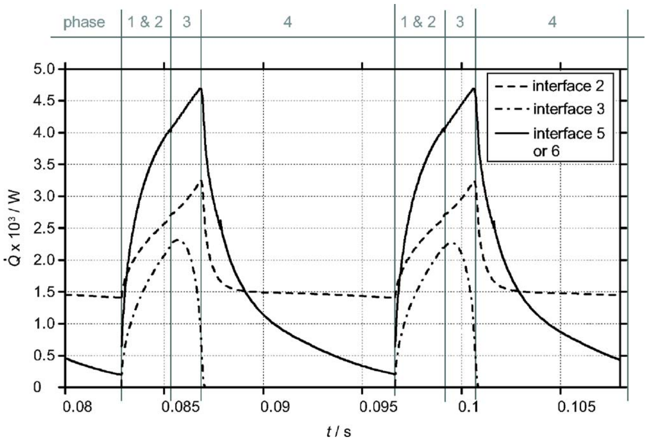

Fig. 8 Time-dependent heat flow through interfaces 2, 3, and 5 (propane/*n*-butane, $p^*=0.2$, $T_{out}-T_{sat}=8.7$ K, $x_{L,1}=0.245$, $d_{sub}=0.4$ mm)

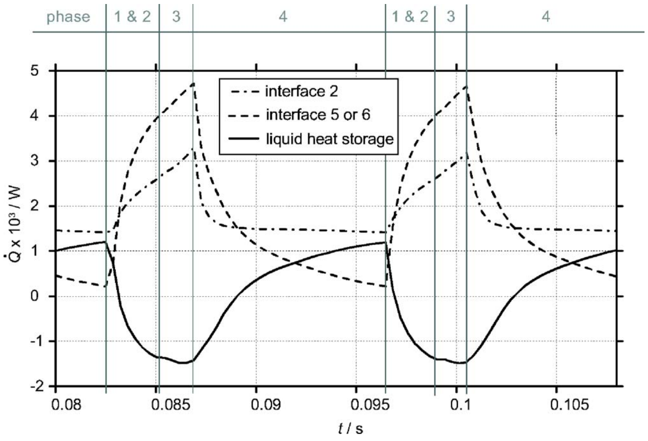

Fig. 10 Time-dependent heat flow through interfaces 2 and 5 or 6 as well as heat storage in the liquid (propane/*n*-butane, $p^*=0.2$, $T_{out}-T_{sat}=8.7$ K, $x_{L,1}=0.245$, $d_{sub}=0.4$ mm)

Additionally, the heat flow through interface 1 and the total heat flow through interfaces 2 + 3 are shown in Fig. 9. Moreover, the difference between these two heat flows, i.e., the time-dependent variation of heat storage in the wall, is shown in that figure. It decreases during bubble growth due to a very high heat transfer through micro and macro regions (Fig. 9, interfaces 2 + 3) and increases during bubble detachment and rise since one phase heat transfer to the liquid is very low. In spite of this significant variation of heat stored in the wall, the thermal inertia of the wall is small because heat flow through interface 1 starts to vary immediately after a change of heat flow through interfaces 2 + 3 as can be seen from Fig. 9: At the beginning of bubble growth, i.e., at the beginning of phase 1 ($t \cong 0.0825$ s), heat flow through interfaces 2 + 3 increases strongly, and heat flow through interface 1 starts to increase only about 0.001 s later (Fig. 9). Although thermal inertia is small, heat transfer in the wall is essential for a correct modeling of nucleate boiling due to a strong variation of heat transfer at the heater surface (Fig. 9, interfaces 2 + 3). In addition heat flow in the micro region strongly depends on the micro region wall temperature and this temperature cannot be obtained without considering the wall.

In Fig. 10 the heat flow through interface 2, i.e., through the heater surface to the liquid of the macro region, is plotted versus time for the seventh and eigth bubble cycles. Furthermore, the heat flow through interface 5 or 6, i.e., through the bubbles cap, and the difference between them, i.e., the liquid heat storage, are shown. The heat flow through interface 5 increases strongly when the bubble starts to grow (phases 1 and 2) and decreases after bubble detachment (phase 4). The heat flow through interface 2 varies in the same way without delay, i.e., it also starts to increase at the beginning of phase 1 and decreases as soon as the bubble has detached. In contrast to the conclusions drawn based on Fig. 9 concerning thermal inertia of the wall, in this case it is not possible to derive a statement about the thermal inertia of the liquid. This is due to the fact that in the liquid phase two-dimensional heat conduction and additionally convective heat transfer take place. The reason for the strong coupling between the heat flow through interface 2 and interface 5 or 6 is based upon the geometry of the area close to the micro region. In this area the liquid film is very thin and hence thermal resistance and inertia are very low. Thus, a variation of heat flow through interface 5 or 6 immediately affects heat flow through interface 2.

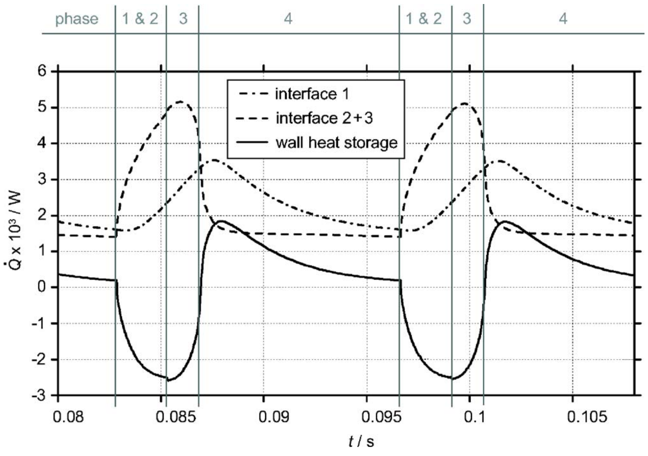

Fig. 9 Time-dependent heat flow through interfaces 1–3 as well as heat storage in the wall (propane/*n*-butane, $p^*=0.2$, $T_{out}-T_{sat}=8.7$ K, $x_{L,1}=0.245$, $d_{sub}=0.4$ mm)

The moment when the "heat storage" curve changes its sign is also of special interest. Whereas the wall heat storage (see Fig. 9) changes its sign very close to the transition of the different phases, i.e., growing/detaching and rising, the liquid heat storage changes its sign later. The quick response of wall heat storage is due to the very high heat transfer at the bubble foot, i.e., within and close to the micro region. During phases 1–3 heat is extracted from the wall and after detachment storage of heat in the wall starts without delay. For the liquid heat storage (Fig. 10) the distinct delay between the beginning of phase 4 and the change of sign indicates that in this time period most of the heat that is transferred to the bubble is supplied from the liquid and not from the wall.

Table 3 contains the integrated heat flow through each interface (columns) and during each phase (rows). To compare the amount of heat transferred to the vapor bubble during bubble growth and detachment (phases 1–3) to the total heat transferred to the bubble during one bubble cycle, one has to proceed as follows. To calculate the total heat transferred during one bubble cycle, the values of column 3 (interface 3) and column 4 (interface 5 or 6) have to be summed for all phases. The heat transferred to the vapor

Table 3 Integrated heat flow through each interface during all phases (propane/*n*-butane, $p^*=0.2$, $T_{out}-T_{sat}=8.7$ K, $x_{L,1}=0.245$)

Phase no.	Interface no.			
	1	2	3	5 or 6
1+2	4.47×10^{-6} W	5.47×10^{-6} W	3.71×10^{-6} W	7.49×10^{-6} W
3	4.67×10^{-6} W	4.83×10^{-6} W	3.14×10^{-6} W	7.14×10^{-6} W
4	26.01×10^{-6} W	16.81×10^{-6} W	0 W	12.87×10^{-6} W

bubble during bubble growth and detachment (phases 1–3) is calculated by summing the values of rows 1 and 2 of columns 3 and 4. Thus during bubble growth and detachment approximately 63% of the total heat is transferred to the bubble. The remaining 37% is transferred through the thermal boundary layer and the liquid bulk during bubble rise. In some experimental and theoretical investigations [36,37] researchers subdivided the total heat transfer by nucleate boiling into

1. evaporative heat transfer, which corresponds to the latent heat required to form a vapor bubble with the size of a detaching vapor bubble, and
2. convective and diffusive heat transfer (without specifying whether the heat is transferred to the bubble while it is rising or if it is transferred to the liquid bulk).

In the present model the second point equals to that part of the heat that completely flows from the wall through the liquid into the rising vapor bubble (phase 4), i.e., 37% of the total heat in the present example. Thus, no heat is transferred through the liquid into the far field of the liquid bulk, i.e., to the upper boundary of the single bubble subsystem, except for the heat transferred with the bubble itself. This characteristic is not based on modeling restrictions. Generally convective heat transport over the upper boundary is possible. When the bubble leaves the thermal boundary layer (Fig. 5(*b*), last five plots) the bubble entrains an amount of hot liquid and shifts it in higher regions (wedge-shaped isotherms above the bubble). However, during the rising period this heat is likewise used for evaporation, so that no heat reaches the upper boundary.

As shown in Table 3 during bubble growth and detachment, 32% of the heat passes through the micro region, i.e., interface 3, although this region is tiny compared to the size of the subsystem.

3.3 Heat Transfer Coefficients. In order to compare computational to experimental results, the mean heat transfer coefficient for a propane/*n*-butane mixture ($p^*=0.2$, $T_{out}-T_{sat}=8.7$ K, $x_{L,1}=0.245$) is calculated according to Eqs. (1) and (2). It amounts to 2190 W/m^{2}K. Comparing this value to the measured heat transfer coefficient of Bednar and Bier [35], which amounts to 2490 W/m^2 K, in the present example the deviation between experimental and numerical values is less than 12%, if the error of the measured data (in the range of ±10%) is not considered. The reason that the calculated heat transfer coefficient is lower than the measured one might be that the single bubble model does not yet account for convection and flow effects around tubes induced by other rising bubbles and natural convection. This explanation is strengthened by a study of the influence of convection on nucleate boiling heat transfer of pure substances around horizontal tubes [36] using the micro region model.

Compared to the preceding model of Kern and Stephan [10] the computed heat transfer coefficients are somewhat higher and thus closer to the experimental data. Nevertheless, it is very difficult to compare the results of both models due to the reason that the preceding model only considered the bubble growth without departure and subsequent rising (waiting time). Additionally, there is a variation concerning the arrangement of interface 7, i.e., the upper boundary of the bubble cell. Whereas in the old model this interface assigns the top of the temperature boundary layer, in the new one this interface is explicitly located in the saturated bulk liquid, i.e., far from the thermal boundary layer. So the average heat flow over this interface turns from approximately 20% of the average input heat flow in the preceding model to nearly 0% in the present model. The heat input through interface 1 is also not comparable due to the reason that the new model calculates — compared to the old one — twice the time for an overall bubble cycle and only half the time for the growing part (phases 1 and 2). Therefore, the heat flow (calculated by the actual model) over interface 1 is always smaller and the heat flow over interface 5 or 6 is mostly higher compared to the results of the preceding model.

4 Summary and Conclusions

A new model is introduced to compute nucleate boiling heat and mass transfer. Fully transient heat and fluid flow is modeled with a free surface of the rising bubble and a periodic calculation of the whole cycle of a growing, detaching, and rising bubble including waiting time between two successive bubbles. To verify the model, computed heat transfer coefficients are compared with measured heat transfer coefficients from the literature. Good agreement is found. To evaluate the influence of transient heat conduction, heat storage, and convection in liquid and wall on overall heat transfer, heat flow through different interfaces of the single bubble subsystem is calculated. Due to the assumptions of the model, the calculations are true for low and moderate heat fluxes, as long as bubbles do not interact. By means of the computations the following conclusions are drawn:

- If the ratio between the thickness of the thermal boundary layer and the filling height is rather small (which is the case for almost all technical applications), the heat supplied at the evaporator wall is almost totally transferred to the liquid-vapor interface of the bubble. The part of the heat that is transferred over the top of the thermal boundary layer to the bulk liquid by conduction and convection is eventually also transferred to the vapor bubble. Therefore, considering bubble rise is important for a correct modeling of heat and mass transfer during nucleate boiling.
- Heat flow to the vapor bubble can be divided into heat transfer in micro and macro regions. In the tiny micro region at the bubble foot heat is transferred from the wall to the liquid-vapor interface of the bubble only by one-dimensional heat conduction in the liquid [10]. In the macro region heat is transferred from the wall to the liquid-vapor interface of the bubble cap by two-dimensional heat conduction and convection in the liquid. Although the micro region is far smaller than the macro region, in the present example 32% of the heat passes through the micro region during bubble growth and detachment. No heat is transferred through the adsorbed liquid film underneath the bubble.
- Due to the high heat flux in the micro region during bubble growth and departure, heat flow in the wall is concentrated towards the micro region and therefore heat conduction in the wall becomes two-dimensional. After departure and during subsequent rise of the bubble, wall heat flow to the heater surface immediately becomes one-dimensional.
- Although the thermal inertia of the wall is rather small, the variation of heat stored in the wall is significant as calculated by the model. Therefore, considering heat transfer in the wall is essential for a correct modeling of nucleate boiling. In addition heat flow in the micro region strongly depends on the micro region wall temperature and this temperature cannot be obtained without considering the wall.

There is no evidence of strong cooling of the wall by the induced vortex behind the bubble over a certain influence area greater than the bubble contact area.

Acknowledgment

The authors are indebted to Deutsche Forschungsgemeinschaft, Bonn, for financial support.

Nomenclature

A = area (m^2)
c = specific heat capacity (J/(kg K))
g = acceleration of gravity (m/s^2)

Δh_{lv} = latent heat of evaporation (J/kg)
$\dot{m}$ = mass flux (kg/s)
N_b = bubble site density ($1/\mathrm{m}^2$)
p = pressure ($\mathrm{N/m}^2$)
p^* = reduced pressure (p/p_c)
p_c = critical pressure ($\mathrm{N/m}^2$)
$\dot{Q}$ = heat flow (W)
$\dot{q}$ = heat flux ($\mathrm{W/m}^2$)
$\dot{q}_m$ = time- and area-averaged heat flux ($\mathrm{W/m}^2$)
R_1 = radius of curvature (m)
R_2 = radius of curvature (m)
r = radius (m)
T = temperature (K)
ΔT_{iso} = temperature difference of isotherms (K)
t = time (s)
t_b = time period of one bubble cycle (s)
u = velocity (m/s)
$x_{L,1}$ = liquid mole fraction of the more volatile component

Greek Symbols

α_m = time- and area-averaged heat transfer coefficient ($\mathrm{W/(m^2\,K)}$)
β = coefficient of thermal expansion (1/K)
δ = liquid film thickness (m)
δ_l = thickness of liquid layer (m)
δ_w = wall thickness (m)
η = coordinate normal to the wall (m)
φ_{app} = apparent contact angle (deg)
λ = thermal conductivity (W/(m K))
ν = kinematic viscosity ($\mathrm{m^2/s}$)
ξ = coordinate parallel to the wall (m)
ρ = density ($\mathrm{kg/m^3}$)
Θ = angle (deg)

Subscripts

ads = adsorbed film
$evap$ = evaporation
η = vertical direction
ini = initial
int = interface
l = liquid
m = mesh
mic = micro region
out = outer surface of the wall
ref = reference property in bulk
sat = saturation
sub = subsystem
w = wall
ξ = radial direction
$1-7$ = interfaces

References

[1] Beer, H., 1971, "Das dynamische Blasenwachstum beim Sieden von Flüssigkeiten an Heizflächen," Forsch. Ingenieurwes., **37**, pp. 85–90.
[2] Buchholz, M., Auracher, H., Lüttich, T., and Marquardt, W., 2004, "Experimental Investigation of Local Processes in Pool Boiling Along the Entire Boiling Curve," Int. J. Heat Fluid Flow, **25**, pp. 243–261.
[3] Bae, S., Kim, M., and Kim, J., 1999, "Improved Technique to Measure Time- and Space-Resolved Heat Transfer Under Single Bubbles During Saturated Pool Boiling of FC-72," Exp. Heat Transfer, **12**, pp. 265–278.
[4] Demiray, F., and Kim, J., 2004, "Microscale Heat Transfer Measurements During Pool Boiling of FC-72: Effect of Subcooling," Int. J. Heat Mass Transfer, **47**, pp. 3257–3268.
[5] Kenning, D. B. R., and Yan, Y., 1996, "Pool Boiling Heat Transfer on a Thin Plate: Features Revealed by Liquid Crystal Technology," Int. J. Heat Mass Transfer, **39**, pp. 3117–3137.
[6] Höhmann, C., and Stephan, P., 2002, "Microscale Temperature Measurement at an Evaporating Liquid Meniscus," Exp. Therm. Fluid Sci., **26**, pp. 157–162.
[7] Sodtke, C., Kern, J., and Stephan, P., 2006, "High Resolution Measurements of Wall Temperature Distribution Underneath a Single Vapor Bubble Under Microgravity Conditions," Int. J. Heat Mass Transfer, **49**, pp. 1100–1106.
[8] Wayner, P. C., Kao, Y. K., and La Croix, L. V., 1976, "The Interline Heat Transfer Coefficient on an Evaporating Wetting Film," Int. J. Heat Mass Transfer, **19**, pp. 487–492.
[9] Stephan, P., and Hammer, J., 1994, "A New Model for Nucleate Boiling Heat Transfer," Heat Mass Transfer, **30**, pp. 119–125.
[10] Kern, J., and Stephan, P., 2003, "Theoretical Model for Nucleate Boiling Heat and Mass Transfer of Binary Mixtures," ASME J. Heat Transfer, **125**, pp. 1106–1115.
[11] Dhir, V. K., 2001, "Numerical Simulations of Pool-Boiling Heat Transfer," AIChE J., **47**, pp. 813–834.
[12] Fujita, Y., and Bai, Q., 1998, "Numerical Simulation of the Growth for an Isolated Bubble in Nucleate Boiling," in Proceedings of the Eleventh Heat Transfer Conference, J. S. Lee (Ed.), Taylor & Francis, Philadelphia, PA, pp. 437–442.
[13] Fuchs, T., Kern, J., and Stephan, P., 2006, "Transient Simulations of the Heat Transfer in the Liquid Boundary Layer and the Heater Wall for Nucleate Pool Boiling," in *Proceedings of the 13th International Heat Transfer Conference*, Sydney, BOI-26.
[14] Wang, C. H., and Dhir, V., 1993, "On the Gas Entrapment and Nucleation Site Density During Pool Boiling of Saturated Water," ASME J. Heat Transfer, **115**, pp. 670–679.
[15] Hibiki, T., and Ishii, M., 2001, "Active Nucleation Site Density in Boiling Systems," Int. J. Heat Mass Transfer, **46**, pp. 2587–2601.
[16] Benjamin, R. J., and Balakrishnan, A. R., 1997, "Nucleation Site Density in Pool Boiling of Binary Mixtures: Effect of Surface Micro-Roughness and Surface and Liquid Physical Properties," Can. J. Chem. Eng., **75**, pp. 1080–1089.
[17] Schmidt, J. G., 1995, "Blasenbildung beim Sieden von Stoffgemischen," Ph.D. thesis, Universität Karlsruhe (TH), Germany.
[18] Krupiczka, R., Rotkegel, A., and Ziobrowski, Z., 2000, "The Influence of Mass Transfer on the Heat Transfer Coefficients During the Boiling of Multicomponent Mixtures," Int. J. Therm. Sci., **39**, pp. 667–672.
[19] Stephan, P., 1992, "Wärmedurchgang bei der Verdampfung aus Kapillarrillen in Wärmerohren," Fortschr.-Ber. VDI, Reihe 6, **19**(59), VDI Verlag, Düsseldorf.
[20] Mann, M., 2001, "Ein Mikrozonenmodell zur Beschreibung der Blasenbildung und des Wärmeübergangs beim Sieden," Fortschr.-Ber. VDI, Reihe 6, **3**(708), VDI Verlag, Düsseldorf.
[21] Kern, J., and Stephan, P., 2003, "Investigation of Decisive Mixture Effects in Nucleate Boiling of Binary Mixtures Using a Theoretical Model," ASME J. Heat Transfer, **125**, pp. 1116–1122.
[22] Stephan, K., 1992, *Heat Transfer in Condensation and Boiling*, Springer-Verlag, Berlin.
[23] Frank, M. R., and Lazarus, R. B., 1964, "Mixed Euler-Lagrange Method," Methods Comput. Phys., **3**, pp. 47–67.
[24] Noh, W. F., Adler, B., Fernbach, S., and Rothenberger, M. (eds.), 1964, "CEL: A Time-Dependent Two-Space-Dimensional Coupled Eulerian-Lagrangian Code," Methods Comput. Phys., **3**, pp. 117–180.
[25] Hirt, C. W., Amsden, A. A., and Cook, J. L., 1974, "An Arbitrary Lagrangian-Eulerian Computing Method for All Speeds," J. Comput. Phys., **14**, pp. 227–253.
[26] Hughes, T. J. R., Liu, W. K., and Zimmermann, T. K., 1981, "Lagrangian-Eulerian Finite Element Formulation for Incompressible Viscous Flows," Comput. Methods Appl. Mech. Eng., **29**, pp. 329–349.
[27] Donea, J., and Huerta, A., 2003, *Finite Element Methods for Flow Problems*, Wiley, New York.
[28] Ingenieursbureau Sepra, 1993, "SEPRAN, A Finite Element Code. User Manual," (http://ta.twi.tudelft.nl/NW/sepran/um.pdf).
[29] Girault, V., and Raviart, P. A., 1979, *Finite Element Approximation of the Navier-Stokes Equations*, Lecture Notes in Mathematics, Vol. 749, Springer Verlag, Berlin.
[30] Martin, J. C., and Moyce, W. J., 1952, "An Experimental Study of the Collapse of Liquid Columns on a Rigid Horizontal Plane," Philos. Trans. R. Soc. London, Ser. A, **224**, pp. 312–334.
[31] Harlow, F., and Welch, J., 1965, "Numerical Calculation of Time-Dependent Viscous Incompressible Flow of Fluid with Free Surface," Phys. Fluids, **8**, pp. 2182–2189.
[32] Hirt, C., and Nichols, B., 1981, "Volume of Fluid (VOF) Method for the Dynamics of Free Boundaries," J. Comput. Phys., **39**, pp. 201–225.
[33] Griebel, M., Dornseifer, T., and Neunhoeffer, T., 1995, *Numerische Simulation in der Strömungsmechanik*, Vieweg, Wiesbaden.
[34] Raymond, F., and Rosant, J.-M., 2000, "A Numerical and Experimental Study of the Terminal Velocity and Shape of Bubbles in Viscous Liquids," Chem. Eng. Sci., **55**, pp. 943–955.
[35] Bednar, W. H., and Bier, K., 1994, "Wärmeübergang beim Blasensieden von binären Kohlenwasserstoffgemischen," Fortschr.-Ber. VDI, Reihe 6, **3**(357), VDI Verlag, Düsseldorf.
[36] Mann, M., and Stephan, K., 2000, "Influence of Convection on Nucleate Boiling Heat Transfer Around Horizontal Tubes," Multiphase Sci. Technol., **12**, pp. 1–13.
[37] Stephan, K., 1964, *Beitrag zur Thermodynamik des Wärmeübergangs beim Sieden*, Verlag C.F. Müller, Karlsruhe.

Spreading Characteristics and Microscale Evaporative Heat Transfer in an Ultrathin Film Containing a Binary Mixture

Sashidhar S. Panchamgam

Joel L. Plawsky

Peter C. Wayner, Jr.[1]
e-mail: wayner@rpi.edu

The Isermann Department of Chemical and
Biological Engineering,
Rensselaer Polytechnic Institute,
Troy, NY 12180

Using image-analyzing interferometry, the thickness profile, in the range of δ_0 (adsorbed thickness) $<\delta<3$ μm, at the leading edge of a moving ultrathin film with phase change, was measured for a mixture of pentane-octane and compared to that of pure pentane. An improved data-analysis procedure was used to enhance the use of the measured thickness profile. There were significant differences between these two systems, demonstrating the presence of large Marangoni interfacial shear stresses with the mixture. A control volume model was developed to evaluate the differences between the pure fluid and the mixture. The disjoining pressure at the leading edge was found to control fluid flow in the evaporating pure system. However, due to Marangoni stresses, the effect of disjoining pressure on the mixture was found to be small at steady state for the fluxes studied. With an upstream bulk mixture of 2% octane and 98% pentane, a shear stress due to the gradient of the liquid-vapor interfacial surface tension resulting from distillation controlled fluid flow in the contact line region. The average curvature of the evaporating pseudo-steady state pure system was significantly larger (smaller length and larger apparent contact angle at $\delta=0.1$ μm) than the isothermal value, whereas the reverse occurred for the mixture. Using a continuum model, a comparison of numerically obtained Marangoni stresses and local evaporative heat flux profiles between the two systems was also made. [DOI: 10.1115/1.2349506]

Keywords: binary evaporation, contact line, disjoining pressure, evaporating meniscus, evaporating ultra thin film, Marangoni stresses

Introduction

In many liquid-vapor systems, such as the microlayer at the base of a bubble in boiling [1–8] and the similar meniscus in heat pipes [9–11], interfacial phenomena control the phase-change process. Herein, we are concerned with the microscopic details of the phase-change process at the leading edge of a curved liquid film on a solid substrate (the generic meniscus) where large heat fluxes and shear stresses occur because of the extremely small thickness of the liquid film. These films are at the leading edge of the microlayer in boiling [2–8]. Fluid flows as a result of the pressure gradient and the shear stress at the liquid-vapor interface due to capillary and intermolecular forces (disjoining pressure), which are a function of the temperature, concentration, and film thickness profiles. One of the objectives of our efforts has been to improve the optical resolution in our experiments on the microscopic details of the transport processes (e.g., [12–15]). An example of a more macroscopic approach is the experimental study of an evaporating meniscus formed at the exit of a capillary tube by Pratt and Khim [16]. The details of the evaporating meniscus have also been studied using numerical solutions to the applicable differential equations (e.g., [2–9,11,17–21]), and control volume models (e.g., [14,15,22]). Although numerical solutions have been presented for mixtures (e.g., [23,24]), very little experimental data have been obtained on the details of the phase change process in the contact line region using a mixture (e.g., [13,16]). However, there have been many macroscopic studies of boiling using various experimental techniques. An example of a recent study of nucleate boiling on a cylindrical heater in aqueous solutions, which includes a map of the complicated conjugate problem, is given in [25]. There is further rich literature on the fundamentals of the physicochemical processes occurring at the contact line and the measurement thereof. However, to save space, the extensive literature review given on these topics in Refs. [14,22,25] will not be repeated here.

Herein, we present data on the microscopic details of the phase change process for a moving extended pentane-octane meniscus where the thickness is $\delta_0<\delta<3$ μm, which were obtained using the improved techniques described in [14]. The results are based on the changes in the thickness profile associated with phase change. The thickness, δ_0, is the adsorbed, nonevaporating thickness at the leading edge controlled by disjoining pressure in the pure completely wetting case and affected by Marangoni stresses with a mixture (contact line boundary condition). The major result is the comparison of the effect of the significantly different profile data obtained for a mixture with the results obtained previously for a pure fluid [15]. The understanding of the experimental results is enhanced theoretically using both a control volume model, which was previously used successfully with a pure fluid [14,15], and a continuum model. Herein, this control volume model is extended to include the Marangoni stress. The control volume model demonstrates the significant effect that the second component has on fluid flow and the relative size of the disjoining pressure. We also found that the length of the control volume reached a steady-state value for the pure system but not for the mixture. However, we find that the use of the control volume model is limited by the lack of data on the details of the concentration gradient with the mixture. Therefore, additional numerical results

---

[1] Corresponding author.

Contributed by the Heat Transfer Division of ASME for publication in the JOURNAL OF HEAT TRANSFER. Manuscript received August 23, 2005; final manuscript received March 26, 2006. Review conducted by Raj M. Manglik.

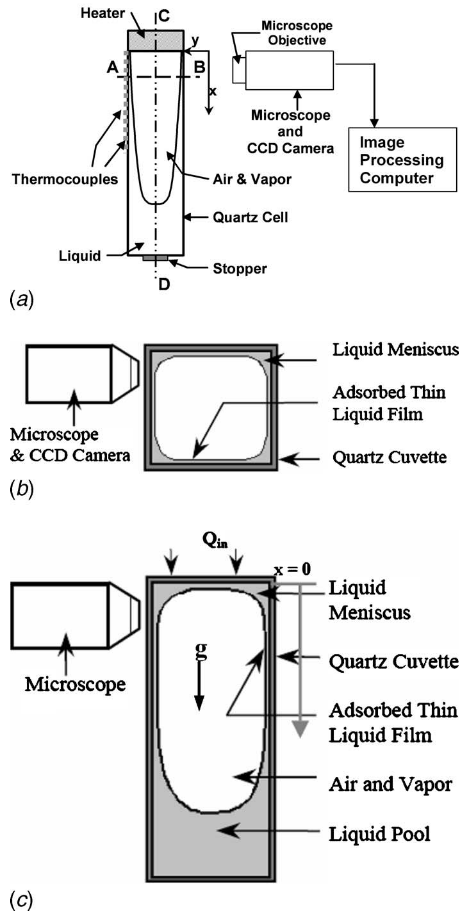

Fig. 1 (*a*) **Schematic diagram of the experimental setup,** (*b*) **cross-sectional view (line AB in (*a*)) of the quartz cuvette with inside dimensions 3 mm × 3 mm. Gravity *g* is acting perpendicular to the cross section, and (*c*) cross-sectional view (line CD in (*a*)) of the quartz cuvette (inside dimensions 3 mm × 43 mm).**

from the solution of a continuum model [26] on the details of the transport processes are included to complement the experimental study.

Experimental Setup

The experimental system in Refs. [14,22] was complicated, which included attaching by fusion the quartz cuvette to pyrex tubing. Fusion is done at a high temperature (1000 °C) in an unclean environment, and as a result, the properties of the quartz surface may have changed due to the added impurities inside the experimental system. To avoid such contaminants, a simple clean quartz cuvette system was used without fusion (see Fig. 1), which eliminated the pressure transducer and vacuum inside the cuvette. The evaporation process for the extremely small region studied would not be strongly affected by the convenience of the nonvacuum. In Fig. 1(*a*), line AB represents a square cross section of inside dimensions 3 mm × 3 mm (Fig. 1(*b*)) and line CD represents a rectangular cross section of inside dimensions 3 mm × 43 mm (Fig. 1(*c*)). The cuvette was filled partially with a working fluid inside a glove bag under an ultrafine nitrogen environment. A thermoelectric heater was attached at the top end of the cuvette (see Fig. 1(*a*)). The cuvette was closed using a Teflon® stopper at the bottom of the cuvette. Therefore, the working liquid was in contact with a mixture of its vapor and noncondensable gases at atmospheric pressure forming a constrained vapor bubble (CVB). From the perspective of microscale heat transfer, this allows the contact line region to be isolated and studied more conveniently. We note that, without the noncondensables, the total system is also an effective wickless heat pipe designed for microgravity because of the large size with sharp corners where the radius of curvature can become extremely small. A series of thermocouples, to measure the axial temperature profile, were attached along the length of the quartz cuvette. The entire cuvette assembly was mounted on an aluminum base plate, and the base plate was attached to a precision, three-way translation stage on an air-buffered vibration control bench. The translation stage allowed us to focus the microscope at any desired position along the extended meniscus formed in the corners of the cuvette.

Table 1 Physical properties of pentane and octane [27,28]

Properties @ 25 °C	Pentane (1)	Octane (2)
Boiling point, °C	36	126
n (refractive index)	1.358	1.398
ρ (density), kg/m^3	621	699
σ (surface tension), N/m	0.0155	0.0211
k_l (thermal conductivity), W/mK	0.113	0.128
ν (kinematic viscosity), m^2/s	3.61×10^{-7}	7.28×10^{-7}

Experimental Procedure

In the experimental system, liquid from the pool at the bottom of the cuvette rises along the corners of the cuvette due to capillary and disjoining pressure forces and thereby forms a continuous extended meniscus in the four corners of the cuvette cross section (see Fig. 1(*b*)). Also, it forms extended menisci at the top end of the cuvette (see Fig. 1(*c*)). To study the fluid flow and evaporation in a binary mixture meniscus (bulk concentration of 98% pentane and 2% octane by volume) and compare it to that of relatively pure pentane, we used a change in the heater power input from the isothermal (reference state) to $Q_{\text{in}}=0.076$ W. The resulting movement of a portion of the meniscus due to evaporation was captured and analyzed. A comparison of the physical properties of pentane and octane is given in Table 1. Initially, the meniscus receded toward the corner of the cuvette (transient state), then advanced away from the corner. This was followed by slow advancement (pseudo-steady state). The reader should note that the meniscus is not a rigid body and its dimensions change with the meniscus movement. Therefore, the "overall" movement of the meniscus was quantified by monitoring the distance traveled by the zeroth dark fringe ($\delta=0.1$ μm) with respect to its position in the isothermal reference state. Since the thermocouples were large compared to the microscopic region studied using the microscope, only an estimate of the power input to the meniscus region was measured. For the mixture, the power input per unit length of the meniscus was $P_{T,\text{mixture}}=2.5$ W/m.

In the current study, monochromatic light ($\lambda=546$ nm) from a mercury light source was used to illuminate the cuvette through the objective of the microscope. Naturally occurring interference fringes appeared (see Fig. 2), which were due to the reflection of light from the liquid-vapor and the liquid-solid interfaces. A charged couple diode (CCD) camera with a maximum frame rate of 30 frames per second was used to capture reflectivity images of the receding and advancing menisci. The captured images were digitized using a data acquisition card (DT3155—MACH Series Frame Grabber) and analyzed as described in Refs. [14,15] to give the film thickness. Each pixel measured the reflectivity over a length of 0.177 μm.

Observations

Receding and Advancing Menisci and Interfacial Velocity. Two types of liquids, pure pentane and a mixture of pentane and octane (bulk concentration of 98% pentane and 2% octane by

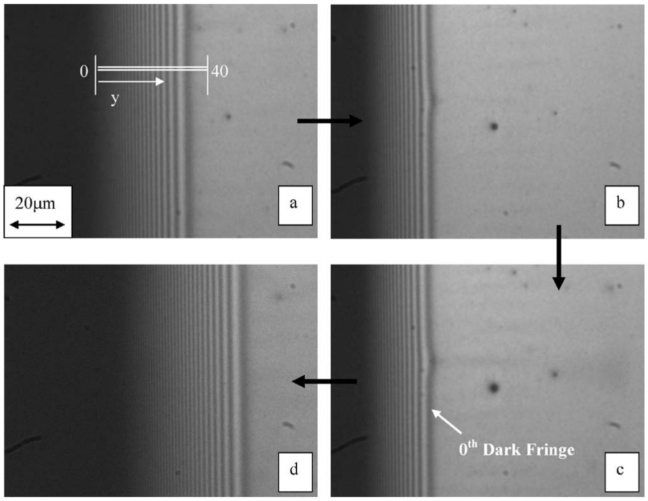

Fig. 2 Reflectivity images illustrating the movement of the binary mixture meniscus due to change in the heater power: (*a*) isothermal state ($t=2.86$ s), (*b*) receding state ($t=8.64$ s), (*c*) advancing state ($t=20.54$ s), and (*d*) pseudo-steady state ($t=336.1$ s). Reflectivity images were captured at an axial location of $x\approx 0$ (near the heater).

volume), were used as the working fluids in the experimental system. The reason for choosing a bulk composition of 98% pentane and 2% octane was to study the effect of a high boiling impurity (octane) on the wetting characteristics of a relatively pure evaporating meniscus (pentane). Distillation gives an interfacial shear stress due to a surface tension gradient, which is important in boiling. The pure pentane data are from our Ref. [15].

For both the working fluids, a stationary isothermal meniscus was considered as the reference state (Fig. 2(*a*) and I I′ in Fig. 3). The thermoelectric heater at the top end of the cuvette was turned on at time $t=3.26$ s, with a power input of $Q_{\text{in}}=0.076$ W. The power input per unit length of the meniscus region was estimated to be 2.5 W/m. Figure 2 shows the reflectivity images of the meniscus movement of the binary mixture captured at an axial location, $x\approx 0$, during different regimes of the evaporation cycle. The movement of the meniscus due to evaporation, starting from the isothermal reference state to a new steady state, was monitored by observing the distance traveled ($\Psi_{0.1\ \mu\text{m}}$) by the zeroth dark fringe (thickness, $\delta=0.1\ \mu$m, see Fig. 2(*c*)) with respect to its position in the isothermal reference state. The sign convention for the distance traveled is shown in Fig. 3, where a negative distance implies the meniscus is in a region "behind" the reference state (between I I′ and the cuvette corner) and a positive distance implies the meniscus is in a region in "front" (ahead) of the reference state (region on right side of I I′). The interfacial velocity of the meniscus (U_i) was calculated from the change in the measured distance ($\Psi_{0.1\ \mu\text{m}}$) between t_{i-1} and t_i by

$$U_i = \frac{\Psi_{0.1\ \mu\text{m}}|_i - \Psi_{0.1\ \mu\text{m}}|_{i-1}}{t_i - t_{i-1}} \tag{1}$$

The maximum relative error associated with U_i is estimated to be ±2.6% and that with $\Psi_{0.1\ \mu m}$ is ±1.8%. Figure 4 shows the comparison of the profiles of the distance traveled by the pentane and the binary mixture menisci as a function of time, and Fig. 5 shows the comparison of the interfacial velocity profiles as a function of time. Based on the distance traveled and the interfacial velocity, the meniscus movement for both the working fluids can be classified into different regimes. The reader should note that for both the working fluids, i.e., pure pentane and the binary mixture, the trend in the meniscus movement was similar and the description given below is mainly with reference to the binary mixture.

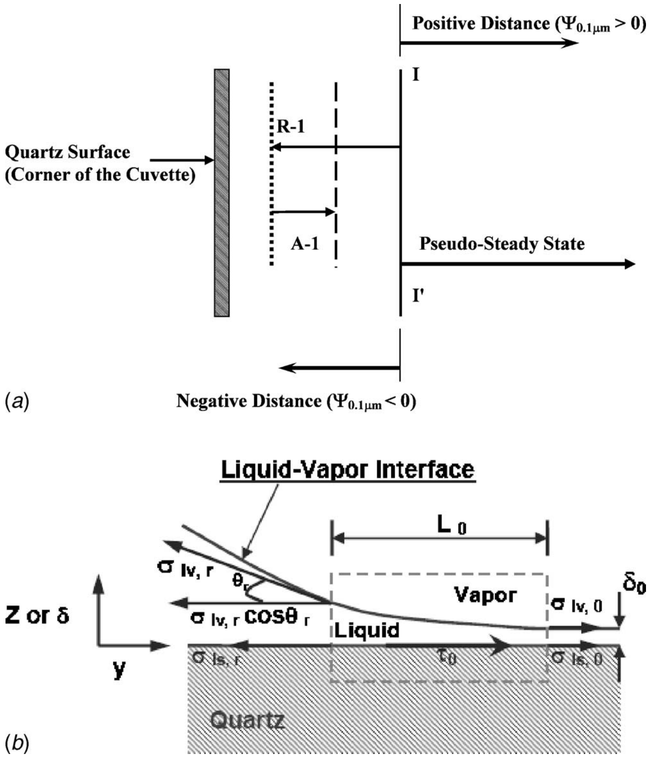

Fig. 3 Illustration of the meniscus movement due to change in the heater power. I I′: Isothermal reference state, R-1: Receding cycle, and A-1: Advancing cycle, and a schematic of the control volume of an evaporating corner meniscus used for macroscopic interfacial force balance and continuum model.

1. Isothermal state, $0<t<3.26$ s (segment AB in Figs. 4 and 5(*b*) for the binary mixture meniscus and segment A_1B_1 in Figs. 4 and 5(*a*) for the pure pentane meniscus)

   During this period, the pentane and the binary mixture menisci were stationary ($\Psi_{0.1\ \mu\text{m}}=0$) and at isothermal conditions ($Q_{\text{in}}=0$). Hence, the interfacial velocity was zero ($U_i=0$). Figure 2(*a*) represents the reflectivity image of the binary mixture meniscus in the isothermal state at time $t=2.86$ s.
2. Receding cycle (segment BC in Figs. 4 and 5(*b*) for the binary mixture meniscus and segment B_1C_1 in Figs. 4 and 5(*a*) for the pure pentane meniscus). At $t=3.26$ s, the heater power was changed from $Q_{\text{in}}=0$ to 0.076 W. Because of the relatively large heat flux entering the system, and subsequent evaporation, the pentane and the binary mixture menisci receded toward the corner of the quartz cuvette as shown in

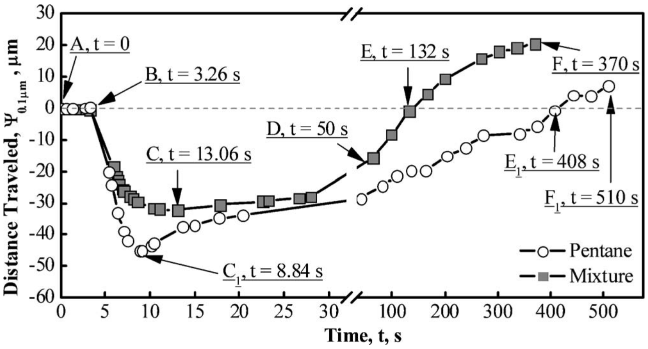

Fig. 4 Comparison of profiles of the distance traveled as a function of time of the pentane and the binary mixture menisci

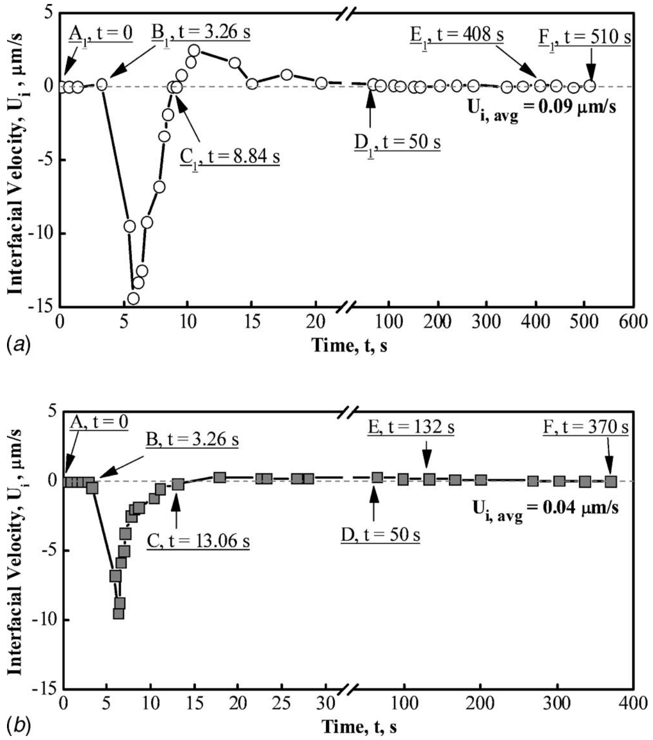

Fig. 5 Comparison of interfacial velocity profiles as a function of time of (*a*) the pentane meniscus and (*b*) the binary mixture meniscus

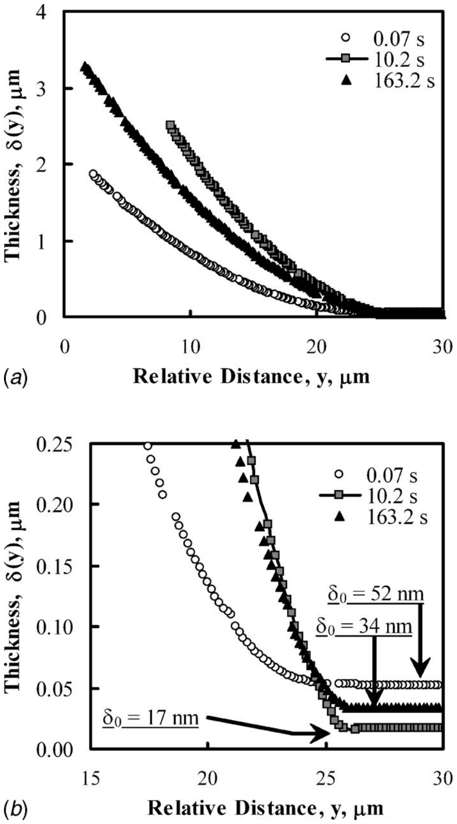

Fig. 6 (*a*) Comparison of thickness profiles of the pentane meniscus at (1) isothermal state (*t*=0.07 s), (2) advancing state (*t*=10.2 s), and (3) pseudo-steady state (*t*=163.2 s), and (*b*) expanded for contact line region [15]

Fig. 4. The pentane meniscus attained maximum recession at $t=8.84$ s, whereas the binary mixture meniscus attained maximum recession at $t=13.06$ s. From Fig. 5(*b*), we see that for the time interval, $3.26<t<6.25$ s, the binary mixture meniscus accelerated toward the corner and for the time interval, $6.25<t<13.06$ s, the meniscus decelerated toward the corner. For pentane (Fig. 5(*a*)), in the time interval $3.26<t<5.71$ s, the meniscus accelerated towards the corner and in the time interval $5.71<t<8.84$ s, the meniscus decelerated towards the corner. The difference in the time instants is due to higher volatility and purity of pentane compared to that of the mixture. Figure 2(*b*) represents the reflectivity image of the binary mixture meniscus during recession at $t=8.64$ s.

3. Advancing cycle (segment CD in Figs. 4 and 5(*b*) for the binary mixture meniscus and segment C_1D_1 in Figs. 4 and 5(*a*) for the pure pentane meniscus). At $t=13.06$ s, the binary mixture meniscus stopped receding. The reader should note that, at this time instance, the heater power was still on at 0.076 W and the meniscus was still being evaporated. During this cycle, the meniscus advanced slowly (or moved away from the corner of the cuvette). Figure 2(*c*) represents the reflectivity image of the binary mixture meniscus during advancement at $t=20.54$ s. For pentane, the meniscus stopped receding at $t=8.84$ s, followed by slow advancement similar to that of the mixture.
4. Pseudo-steady state, $t>50$ s (segment DF in Figs. 4 and 5(*b*) for the binary mixture meniscus and segment D_1F_1 in Figs. 4 and 5(*a*) for the pure pentane meniscus). For $t>50$ s, the meniscus slowly advanced with negligible velocities (average velocities of the pentane and the binary mixture menisci for this segment were 0.09 μm/s and 0.04 μm/s, respectively). For $t>408$ s, the location of the pentane meniscus surpassed the isothermal reference state, i.e., $\Psi_{0.1\ \mu\text{m}}=0$ (see Fig. 4). For pentane, the pseudo-steady-state regime is due to an imbalance in the capillary pressure in the thicker region and the disjoining pressure in the thinner region, which results in a net force acting toward the adsorbed film region. For the mixture (Fig. 4), for $t>132$ s, the location of the meniscus has surpassed the isothermal reference state. In this case, the pseudo-steady-state regime is probably due to the Marangoni flow directed toward the adsorbed film region. Figure 2(*d*) represents the reflectivity image of the binary mixture meniscus at $t=366.1$ s.

Data Analysis

The film-thickness profiles of the pentane and the binary mixture menisci during the different regimes of evaporation were obtained from the reflectivity images. A detailed description of the determination of the meniscus thickness from the meniscus reflectivity image is given in Refs. [14,15]. Figure 6 shows the comparison of thickness profiles of the pentane meniscus at the isothermal state ($t=0.07$ s), advancing state ($t=10.2$ s), and pseudo-steady state ($t=163.2$ s). Figure 7 shows the comparison of thickness profiles of the binary mixture meniscus at the isothermal state ($t=2.86$ s), receding state ($t=8.64$ s), and pseudo-steady state ($t=366.1$ s). We note that $\delta_0(t=366.1\ \text{s})>\delta_0(t=2.86\ \text{s})$. The reverse is true for the pure fluid. The significance of the time instants and respective adsorbed film thickness values (δ_0) at these instants is mentioned later.

To calculate the pressure gradient and the evaporative heat flux existing along the length of an evaporating meniscus, we need to determine the first (δ'), second (δ''), third (δ'''), and fourth (δ'''') derivatives of the thickness profiles ($\delta(y)$). The thickness profile obtained from the technique described in Ref. [14] contains noise. Therefore, a smoothing spline function with tolerance f_{tol} given by

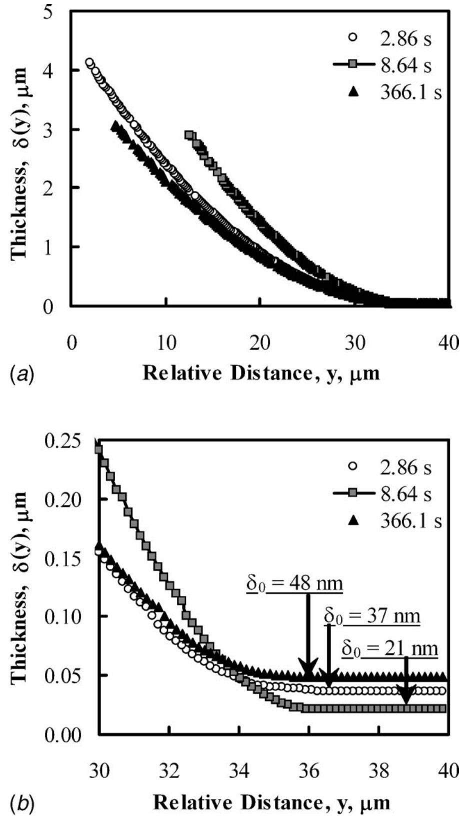

Fig. 7 (***a***) **Comparison of thickness profiles of the binary mixture meniscus at** (**1**) **isothermal state** (***t*=2.86 s**), (**2**) **receding state** (***t*=8.64 s**), **and** (**3**) **pseudo-steady state** (***t*=366.1 s**), **and** (***b***) **expanded for contact line region**

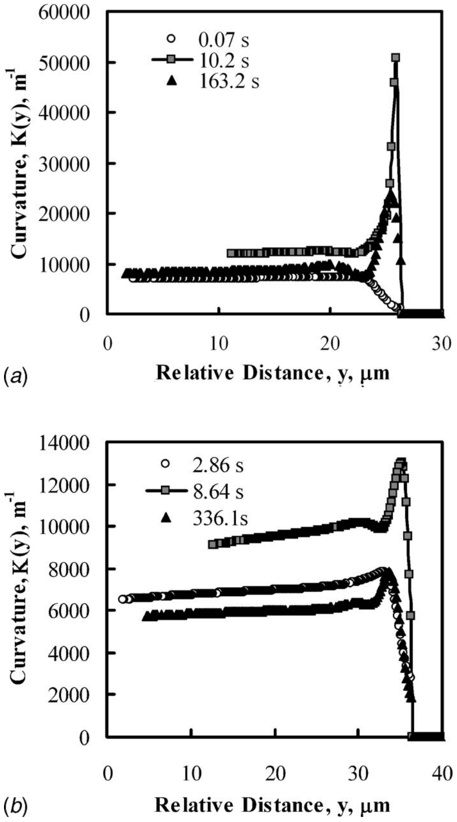

Fig. 8 Comparison of curvature profiles of (***a***) **the pentane meniscus and** (***b***) **the binary mixture meniscus**

$f_{\text{tol}}=a\delta^4$ was used to remove noise in the thickness profile and derive its successive derivatives. The value of a is determined such that the absolute error in the curve fitting is within 3% and δ''', δ'''' are piecewise continuous.

The curvature profiles for the thickness profiles presented in Figs. 6 and 7 are shown in Figs. 8(*a*) and 8(*b*), respectively. In Fig. 8, we see that the curvature is zero in the adsorbed thin film region (large relative distance). For the isothermal state, the curvature increased to a constant maximum value (K_T) as the thickness increased (or as the relative distance decreased). Using the values of K_T and the adsorbed film thickness (δ_0), we characterized the surface with respect to the working fluid by estimating the retarded dispersion constant of the quartz-liquid-air/vapor system. A detailed explanation on the determination of the retarded dispersion constant is given in Ref. [14]. The average dispersion constant of the system with pentane as the working fluid was -8.71×10^{-28} Jm ($\mathrm{B}_{\text{avg,pentane}}$), and with the mixture as the working fluid was -2.22×10^{-28} Jm ($\mathrm{B}_{\text{avg,mixture}}$). The experimental values of the retarded dispersion constants obtained for both the systems are useful in estimating the disjoining pressure contribution to the pressure jump across the interface during the isothermal and nonisothermal states of the meniscus movements. As the disjoining pressure for thicker films, $\Pi_0=-\mathrm{B}_{\text{avg}}/\delta_0^4$, we see that a small error in the measured adsorbed film thickness could result in a larger than expected value of the dispersion constant. An error in the adsorbed film thickness could be due to (i) presence of solid particles in the liquid and/or on the solid surface and (ii) an uncontrollable interfacial temperature jump of the order of 10^{-4} K could cause changes in δ_0 [14]. Although further studies are needed to quantify these effects and so achieve a better understanding of the value of the dispersion constant, we emphasize that an error incorporated in the value of the dispersion constant does not effect the conclusions given below because they depend on the relative change of Π during the nonisothermal state with respect to the isothermal reference state.

Results and Discussion

Adsorbed Film Thickness, δ_0. Plots of the variation of the adsorbed film thickness with time for both the pentane from [15] and the binary mixture menisci are shown in Figs. 9(*a*) and 9(*b*), respectively. For pentane, during the isothermal state, the adsorbed film thickness was constant at 52 nm (see Fig. 9(*a*)). During recession, the adsorbed film thickness decreased due to the relatively large heat flux entering the system. During initial advancement, the adsorbed film thickness decreased further to a minimum value of 17 nm at $t=10.2$ s. As the meniscus advanced further, $10.2<t<50$ s, the adsorbed film thickness increased. During the pseudo-steady state, $t>50$ s, the adsorbed film thickness remained nearly constant at 34 nm, which is less than the isothermal value. This implies that the disjoining pressure ($-\mathrm{B}_{\text{avg,pentane}}/\delta_0^4$) in the adsorbed film region during the pseudo-steady state was higher than that during the isothermal state. Since the capillary pressures (σK) in the thicker regions are nearly constant and equal for the isothermal and the pseudo-steady states (as shown in Fig. 8(*a*)), there is an imbalance between the disjoining pressure in the thin film region and the capillary pressure in the thicker region that causes fluid flow and the pentane meniscus to advance forward during evaporation and, hence, results in the pseudo-steady state for pure pentane meniscus.

For the mixture, during the isothermal state, the adsorbed film thickness was constant at 37 nm (see Fig. 9(*b*)). During recession, the adsorbed film thickness decreased until it reached a minimum of 21 nm at $t=8.64$ s. For $8.64\text{ s}<t<50$ s, the adsorbed film thickness increased. During the pseudo-steady state, $t>50$ s, the adsorbed film thickness remained nearly constant at 48 nm, which

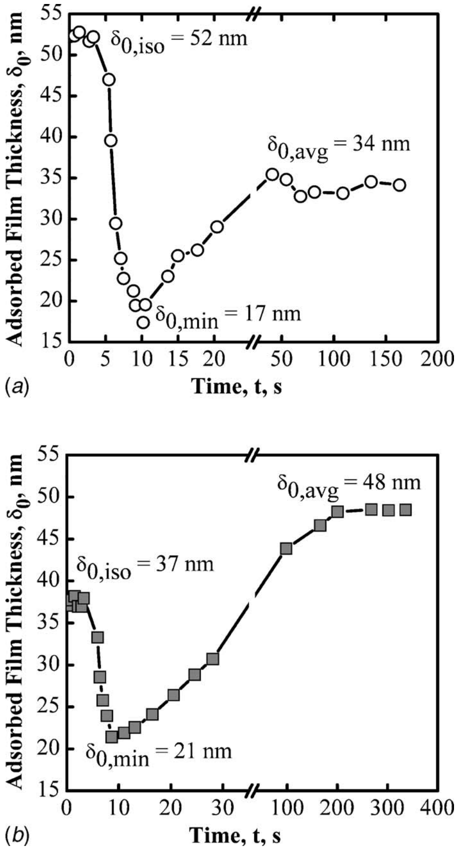

Fig. 9 Comparison of adsorbed film-thickness profiles as a function of time of (*a*) the pentane meniscus and (*b*) the binary mixture meniscus. iso represents isothermal meniscus, min represents minimum, and avg represents an average value over the pseudo-steady-state regime

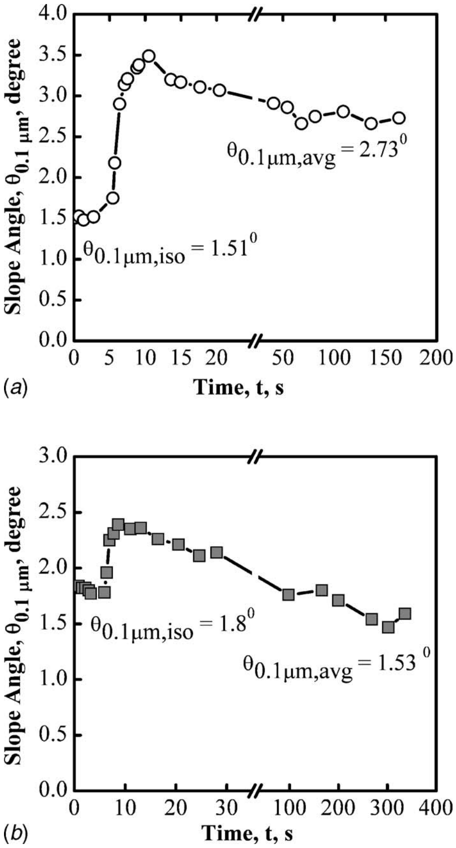

Fig. 10 Comparison of profiles of the slope angle at $\delta=0.1\ \mu$m as a function of time of (*a*) the pentane meniscus and (*b*) the binary mixture meniscus

is larger than the value obtained for the isothermal system. This implies that the disjoining pressure $(-B_{\mathrm{avg,mixture}}/\delta_0^4)$ in the adsorbed film region during the pseudo-steady state was lower than that during the isothermal state. However, as the working fluid is a mixture, existence of surface tension gradients at the interface due to distillation would result in Marangoni flow toward the thin film region. Because of Marangoni flow, the mixture meniscus advances forward, and hence, the observed results in pseudo-steady state for the binary mixture meniscus.

Slope Angle at 0.1 μm, $\theta_{0.1\ \mu m}$. Slope angle of a liquid on a solid surface is an indication of the wetting characteristics of the fluid over the solid surface. For a completely wetting system, slope angles are quite often measured at a thickness of 0.1 μm (or the zeroth dark fringe in the interference pattern; see Fig. 2(*c*)). A zero slope angle of a liquid on a solid surface $(\theta_{0.1\ \mu m}=0)$ implies the liquid completely wets the solid surface. In the current experimental system, the shape of the corner meniscus gives a finite value to the apparent contact angle at $\delta=0.1\ \mu$m. Plots of the variation of slope angle profiles of the pentane and the binary mixture menisci with the evaporation cycles are shown in Figs. 10(*a*) and 10(*b*), respectively. For pentane, due to increased curvature, the average slope angle during the pseudo-steady state is higher than that during the isothermal state. For the mixture, the average slope angle during the pseudo-steady state is lower than that during the isothermal state. From Fig. 10, we find that a mixture of pentane and octane spreads over the quartz surface better than pure pentane upon evaporation. This difference in the behavior between the pure system and the mixture is attributed to Marangoni stresses existing at the interface of the mixture.

Curvature Profiles. The curvature profiles for the nonisothermal states were different from the isothermal states. Herein, we observed a maximum in the curvature $(K_{\max})$ in the transition region $(\delta_0<\delta<0.1\ \mu\mathrm{m})$. For pentane (see Fig. 8(*a*)), the maximum curvature was highest for the film thickness profile with lowest adsorbed film thickness ($\delta_0=17$ nm; advancing state; $t=10.2$ s). As shown in Fig. 11(*a*), the maximum curvature decreased as the meniscus advanced. During the pseudo-steady state, $t>50$ s, the maximum curvature remained constant at 23,801 m^{-1}, which is higher than the maximum curvature during the isothermal state (7383 m^{-1}). As discussed in [7,9,13,14], this curvature gradient causes the liquid to flow toward the thinner region. The curvature then decreases as disjoining pressure becomes more important with a decrease in thickness.

For the mixture (see Fig. 8(*b*)), the maximum curvature was highest for the film thickness profile with lowest adsorbed film thickness ($\delta_0=21$ nm; receding state; $t=8.64$ s). As shown in Fig. 11(*b*), the maximum curvature decreased as the meniscus advanced. During the pseudo-steady state, the maximum curvature remained constant at 7018 m^{-1}, which is slightly less than the maximum curvature (7839 m^{-1}) during the isothermal state ($K_{\max,\mathrm{iso}}=7839\ \mathrm{m}^{-1}$). The difference in the trends for the adsorbed film thickness, slope angle at 0.1 μm, and maximum curvature between the pure pentane and the mixture indicate that Marangoni stresses at the interface govern the fluid flow and spreading characteristics of an evaporating binary mixture. As described next, to estimate the Marangoni stresses at the interface of the binary mixture, we need to obtain the temperature and the composition gradient along the meniscus length, using the experimental thickness and curvature profiles presented herein, from the numerical solutions of the differential equations governing the transport processes.

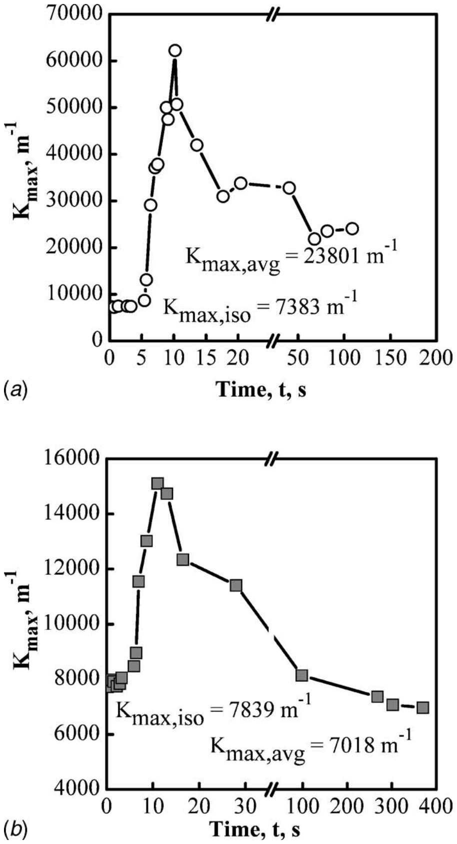

Fig. 11 Comparison of the maximum curvature profiles as a function of time of (*a*) the pentane meniscus and (*b*) the binary mixture meniscus

Continuum Model. A continuum model based on the theoretical formulation discussed in Refs. [23,26] was used to describe the isothermal and nonisothermal (pseudo-steady) states of the liquid meniscus (pentane and binary mixture). Using this model, we could obtain the numerical solution for σ (surface tension), T_i (interfacial temperature), Γ (mass flow rate per unit width), and q'' (local evaporative heat flux) as a function of the meniscus length. The model uses the experimental values of thickness (δ), slope (δ'), curvature (K), curvature gradient (K') and wall temperature (T_w). However, the unknown value of the composition ($x_1(L)$) of the binary mixture at the contact line is an adjustable parameter.

Equation (2) from Ref. [26] relates the mass flow rate per unit width (Γ) of an evaporating meniscus in terms of the surface tension gradient, σ' (Term I: A-D), the curvature gradient K' (Term II: E and F), and the disjoining pressure (Term III: G and H).

$$\Gamma = \underbrace{\left[\overbrace{\frac{1.5\delta^2\sigma'}{3\upsilon}}^{\text{A}} + \overbrace{\frac{K\delta^3\sigma'}{3\upsilon}}^{\text{B}} + \overbrace{\frac{3\beta K\delta^2\sigma'}{3\upsilon}}^{\text{C}} + \overbrace{\frac{3\beta\delta\sigma'}{3\upsilon}}^{\text{D}} \right]}_{\substack{\text{Term I} \\ \text{Marangoni}}} + \underbrace{\left[\overbrace{\frac{\sigma\delta^3 K'}{3\upsilon}}^{\text{E}} + \overbrace{\frac{3\sigma\delta^2\beta K'}{3\upsilon}}^{\text{F}} \right]}_{\substack{\text{Term II} \\ \text{Capillarity}}} + \underbrace{\left[-\overbrace{\frac{4(-\text{B}_{\text{avg}})\delta'}{3\upsilon\delta^2}}^{\text{G}} - \overbrace{\frac{12\beta(-\text{B}_{\text{avg}})\delta'}{3\upsilon\delta^3}}^{\text{H}} \right]}_{\substack{\text{Term III} \\ \text{Disjoining Pressure}}} \quad (2)$$

The parameter β (or the slip coefficient) is related to the slip at the solid-liquid interface, which arises due to the existence of the interfacial surface energy gradient and the pressure gradient. The interfacial surface energy gradient is due to the variations in the interfacial temperature (T_i) and the concentration of pentane (x_1) for the binary mixture meniscus, and due to the variation in the interfacial temperature for the pure pentane meniscus. In Eq. (2), υ is the kinematic viscosity of the working liquid. As described in Refs. [23,26], we could obtain the numerical solution of Γ for the evaporating pentane and binary mixture menisci during the nonisothermal (pseudo-steady) state and the result for $x_1(L) = 0.94$ is shown in Fig. 12. A discussion of the effect of $x_1(L)$ is given in Ref. [26]. Figures 12(*a*) and 12(*b*) show the comparison of various terms in Eq. (2) for the evaporating pentane and the binary mixture menisci, respectively. For pure pentane, terms A, D, F, and H and for the binary mixture, terms A, D, E, and F are significant and contribute to the fluid flow. A positive value of these terms is favorable for fluid flow toward the adsorbed film region. By definition, we see that the sign of these terms depend on the sign of δ', K', and σ'. For a completely wetting meniscus (i.e., pentane and mixture of pentane and octane on the quartz surface), δ' is negative. Hence the contribution of the disjoining pressure terms, represented by G and H in Eq. (2), is positive for both the menisci and favorable for fluid flow toward the adsorbed film region. However, for the binary mixture, both G and H are insignificant due to higher values of δ_0 and lower values of δ' compared to the pentane meniscus.

The liquid flow rate contribution from terms E and F depends on the sign of K'. For the pentane and the binary mixture menisci, K' is negative in the transition region. For the pentane meniscus, K' is significantly negative due to the large increase in the curvature because of evaporation (Fig. 8(*a*)). However, for the binary mixture meniscus, the negative value of K' in the transition region is insignificant due to Marangoni flow.

Terms A and D depend mainly on the sign of the surface tension gradient, σ'. A positive σ' assists and a negative σ' hinders fluid flow towards the adsorbed film region. Figure 13(*a*) shows the comparison of σ' of the pentane and the binary mixture menisci as a function of meniscus length during the nonisothermal (pseudo-steady) state. For pentane, σ' is relatively more negative in the transition region (large y) and is almost zero in the thicker meniscus region (small y), whereas, for the binary mixture, σ' is positive for the majority of the meniscus length except for a small portion in the thicker meniscus region. The differences in the σ' profiles between the two fluids are due to the temperature gradient and the concentration gradient along the interface. For pentane, Marangoni stresses (σ') depend on the interfacial temperature alone and σ' is negative in the transition region. For the mixture, Marangoni stresses depend on both the interface temperature and the concentration gradients. The concentration of pentane along the meniscus (mole fraction, x_1) is shown in Fig. 13(*b*). In Fig. 13(*b*), we see that, for the binary mixture, as we go toward the thicker meniscus region, the concentration of pentane increased relative to the thin film region. As a result, the surface tension due to the concentration gradient, in the adsorbed film region was higher than in the thicker meniscus region, whereas, the surface tension, due to the interfacial temperature gradient, in the adsorbed film region was lower than in the thicker meniscus region. However, the net surface tension gradient is positive. Hence, for the mixture, Marangoni stresses (σ') assist the fluid flow and for pentane, Marangoni stresses hinder the fluid flow.

The local evaporative heat flux of an evaporating meniscus can be obtained using

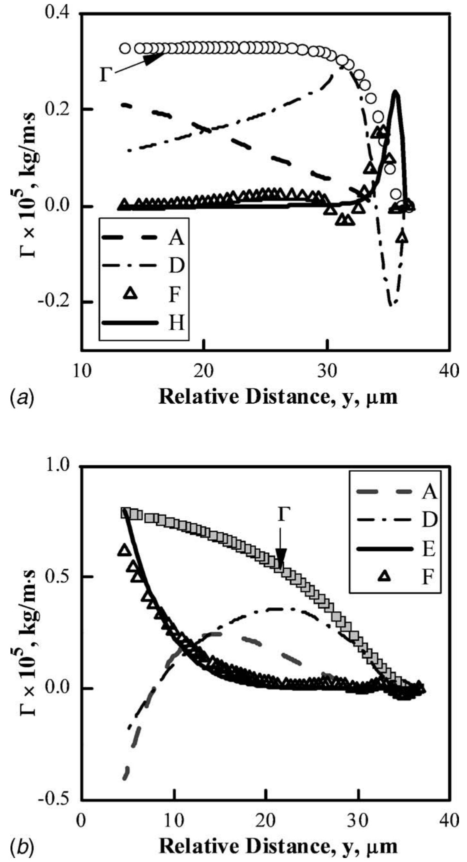

Fig. 12 Comparison of various terms in Eq. (2) [A: $1.5\delta^2\sigma'/3\nu$, D: $3\beta\delta\sigma'/3\nu$, E: $\sigma\delta^3K'/3\nu$, F: $3\sigma\delta^2\beta K'/3\nu$, and H: $-12\beta(-B_{avg})\times\delta'/3\nu\delta^3$] for the mass flow rate equation for (*a*) the pentane and (*b*) the binary mixture menisci during nonisothermal (pseudo-steady) state for the adsorbed film region concentration, $x_1(L)=0.94$

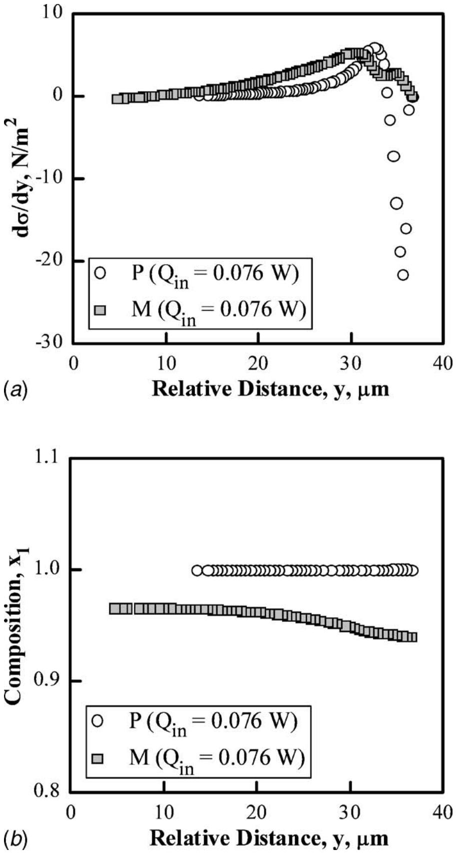

Fig. 13 (*a*) $d\sigma/dy$ and (*b*) mole fraction of pentane (x_1) as a function of meniscus length for the pentane (*P*) and the binary mixture (*M*) menisci during nonisothermal (pseudo-steady) state. x_1 and σ' profiles for the binary mixture meniscus in nonisothermal state were evaluated for the adsorbed film region concentration, $x_1(L)=0.94$

$$q'' = -h_{fg}\frac{d\Gamma}{dy} \tag{3}$$

A comparison of the local evaporative heat flux profiles, for isothermal and nonisothermal states of the pentane and the binary mixture menisci is shown in Fig. 14. For the "isothermal" state, we see that the evaporative heat flux is insignificant with slight phase change compared to the nonisothermal state. This small flux is either a measure of numerical error or due to a small temperature variation. For the nonisothermal profiles, we see a maximum in the evaporative heat flux near the transition region. For the pentane meniscus, the maximum in the evaporative heat flux ($q''_{\mathrm{max,pentane}}=4.21\times10^5$ W/m^2) occurs at a thickness of 56 nm, which is close to the adsorbed film region. In the case of a mixture, the maximum in the evaporative heat flux ($q''_{\mathrm{max,mixture}}=1.83\times10^5$ W/m^2) occurs at a thickness of 0.16 μm. However, for the binary mixture meniscus, due to favorable Marangoni stresses at the liquid-vapor interface, the region of maximum evaporation (or the transition region) has expanded with an increase in the average value of q'' ($q''_{\mathrm{avg.,pentane}}=5.18\times10^4$ W/m^2 and $q''_{\mathrm{avg.,mixture}}=9.11\times10^4$ W/m^2). We find that the evaporative heat flux of pure pentane can be improved by adding octane in small quantities. The complementary change in the temperature is discussed in Ref. [26].

Control Volume Model. The following force balance for the control volume of an oscillating pentane-octane film that includes the Marangoni stresses is an extension of previous work for a pure fluid [14]. Figure 3 illustrates the macroscopic interfacial force balance that relates viscous losses to interfacial forces and the local apparent contact angle in an evaporating meniscus for the control volume between δ_0 and δ_r. Because of the extremely small momentum of the system, we can assume that the sum of the forces acting on the interfaces of the control volume is balanced. Using a uniform vertical thickness for the control volume equal to

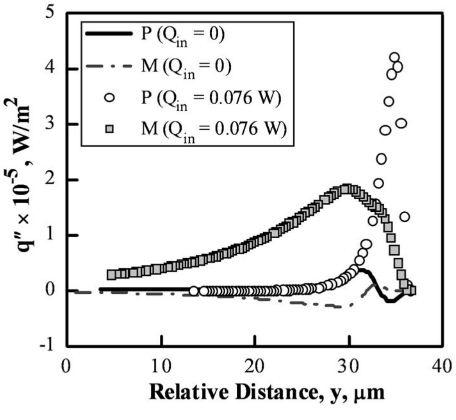

Fig. 14 Comparison of evaporative heat flux (q'') profiles of the pentane (*P*) and the binary mixture (*M*) menisci in isothermal and nonisothermal (pseudo-steady) states. The evaporative heat flux for the binary mixture meniscus in nonisothermal state was evaluated for the adsorbed film region concentration, $x_1(L)=0.94$

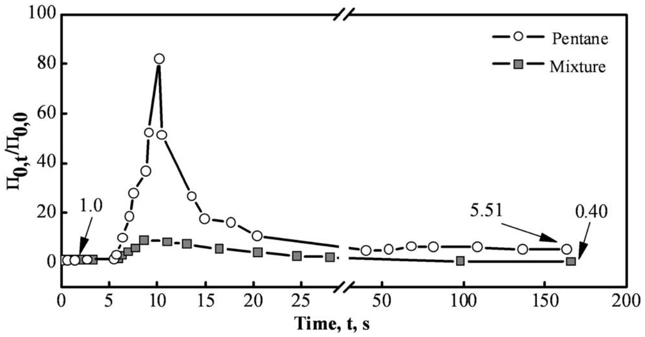

Fig. 15 Comparison of $\Pi_{0,t}/\Pi_{0,0}$ between the pentane and the binary mixture menisci

δ_r, the cause of the liquid-vapor interfacial stress is included in the difference in the surface tensions at the ends of the control volume. Using the augmented Young-Laplace equation for the interfacial pressure jump, the horizontal component of the interfacial force balance between δ_r (measured at $\delta_r = 0.1\ \mu$m), and the flat liquid film on the quartz surface (at δ_0) is

$$\sigma_{\mathrm{lv},r}\cos\theta_r + \sigma_{\mathrm{ls},r} + (\sigma_{\mathrm{lv},r}K_r + \Pi_r)\delta_r = \tau_0 L_0 + \sigma_{\mathrm{lv},0} + \sigma_{\mathrm{ls},0} + (\sigma_{\mathrm{lv},0}K_0 + \Pi_0)\delta_0 \qquad (4)$$

Where τ_0 is the average shear stress that the solid exerts on the fluid over the length L_0. The product $\tau_0 L_0$ represents a shear force per unit contact line length perpendicular to L_0 and is assumed to be positive toward the adsorbed thin film. Π_0 is the disjoining pressure at δ_0 and θ_r is the value of the apparent contact angle at a reference point r in the thicker meniscus region. The sum $(\Pi_0\delta_0 + \sigma_{\mathrm{lv},0}K_0\delta_0)$ represents the "suction" at δ_0 due to interfacial forces. The disjoining pressure or free energy per unit volume, Π_0, represents the force per unit area at the contact line and is positive for a completely wetting fluid. The value of the apparent contact angle is a function of the location because of the curvature, K. To overcome the difficulty of measuring the disjoining pressure at the thicker end of the control volume, the film thickness, δ_r, is taken where the disjoining pressure, Π_r, is negligible.

Assuming that $\sigma_{\mathrm{lv},0} = \sigma_{\mathrm{lv},r} + \Delta\sigma_{\mathrm{lv}}$; $\sigma_{\mathrm{ls},0} = \sigma_{\mathrm{ls},r} + \Delta\sigma_{\mathrm{ls}}$, and dividing by $\sigma_{\mathrm{lv},r}$ Eq. (4) becomes

$$\frac{\tau_0 L_0}{\sigma_{\mathrm{lv},r}} = -\frac{\Pi_0\delta_0}{\sigma_{\mathrm{lv},r}} + K_r\delta_r + \cos\theta_r - 1 - \left(\frac{\Delta\sigma_{\mathrm{ls}}}{\sigma_{\mathrm{lv},r}} + \frac{\Delta\sigma_{\mathrm{lv}}}{\sigma_{\mathrm{lv},r}}\right) \qquad (5)$$

Using $\tau_M L_0 = \Delta\sigma_{\mathrm{lv}} + \Delta\sigma_{\mathrm{ls}}$ to model the Marangoni shear stress over the control volume width, L_0, gives

$$\frac{\tau_0 L_0}{\sigma_{\mathrm{lv},r}} = -\frac{\Pi_0\delta_0}{\sigma_{\mathrm{lv},r}} - \frac{\tau_{\mathrm{M}} L_0}{\sigma_{\mathrm{lv},r}} + [K_r\delta_r + \cos\theta_r - 1] \qquad (6)$$

In both the study of the pure system and the current study, we found experimentally that the group in the bracket at the end of Eq. (6) was small for the fluxes used. Therefore,

$$\frac{\tau_0 L_0}{\sigma_{\mathrm{lv},r}} \approx -\left(\frac{\Pi_0\delta_0}{\sigma_{\mathrm{lv},r}} + \frac{\tau_{\mathrm{M}} L_0}{\sigma_{\mathrm{lv},r}}\right) \qquad (7)$$

Also, we found in Refs. [14,15] and Fig. 12(*a*) that the first term on the right-hand side of Eq. (7) (disjoining pressure) controlled the process for pure pentane. For the mixture, the results in Fig. 12(*b*) and Fig. 15 demonstrate experimentally that the disjoining pressure effect is considerably less than that in the pure fluid system because of the difference in the change in the values of the adsorbed film thickness (see Fig. 9). In Fig. 15, $\Pi_{0,t}$ represents the disjoining pressure in the adsorbed film region at t and $\Pi_{0,0}$ represents the disjoining pressure in the adsorbed film region during the isothermal state. We note that the disjoining pressure is inversely proportional to the adsorbed film thickness raised to a power of 3 or 4. Herein, as δ_0 is relatively large, the use of the power 4 and the retarded dispersion constant is required.

Using Fig. 13(*a*) and ignoring the surface tension stresses at the solid-liquid interface, we can obtain a rough estimate for τ_{M} using Eq. (8)

$$\tau_{\mathrm{M}} = \frac{1}{L}\int_0^L \sigma' dy \qquad (8)$$

In Eq. (8), the numerical integration of σ' is carried over the entire meniscus length L. Using Eq. (8), we find $\tau_{\mathrm{M}} = 1.989\ \mathrm{N/m^2}$ for the binary mixture meniscus and $\tau_{\mathrm{M}} = 0.148\ \mathrm{N/m^2}$ for the pure pentane meniscus. The Marangoni stresses for the binary mixture are an order of magnitude higher than for pure pentane. Therefore, we demonstrate that fluid flow with the mixture is caused primarily by a substantial increase in the Marangoni shear stress, $\tau_{\mathrm{M}} > 0$, due to evaporation of the component with the higher vapor pressure (lower surface tension). In the limit of $\Pi \approx 0$, $\tau_0 = -\tau_M$

A Marangoni shear stress, $\tau_{\mathrm{M}} > 0$ implies a higher surface tension in the adsorbed film region compared to the reference state in the thicker meniscus region. If the resulting mass flow rate of liquid toward the adsorbed film region for the mixture due to distillation (surface tension gradient) is not balanced by evaporation, the length of the binary mixture meniscus should change with evaporation during the pseudo-steady-state regime as presented in Fig. 4.

Conclusions

1. There were significant differences between the two systems demonstrating the presence of Marangoni shear stresses in the mixture at the liquid-vapor interface.
2. The disjoining pressure at the leading edge controlled the evaporating pure system, whereas its effect on the mixture was small for the fluxes studied.
3. The Marangoni shear stresses due to the gradient of the liquid-vapor interfacial surface tension resulting from distillation controlled fluid flow in the contact line region.
4. The average curvature of the evaporating pseudo-steady-state pure system was significantly larger (smaller length) than the isothermal value, whereas the reverse occurred for the mixture.
5. A maximum in the mass flux and evaporative heat flux was observed for both the menisci in the transition region, where the resistance for phase change due to the liquid thickness and intermolecular interactions are smaller.
6. A comparison of heat flux profiles between the pure pentane and the binary mixture menisci showed that, for the binary mixture, the region of maximum evaporation expanded giving an increase in the overall heat flux compared to that of pure pentane due to favorable Marangoni stresses for the mixture.

Acknowledgment

This material is based on the work supported by the National Aeronautics and Space Administration under Grant No. NNC05GA27G. Any opinions, findings, and conclusions or recommendations expressed in this publication are those of the authors and do not necessarily reflect the view of NASA.

Nomenclature

B_{avg} = average dispersion constant (Jm)
f_{tol} = smoothing spline tolerance function
K = curvature ($\mathrm{m^{-1}}$)
L = meniscus length (m)
L_0 = control volume length (m)
P_{l} = liquid pressure ($\mathrm{N/m^2}$)

$P_{\mathrm{T,mixture}}$ = power input per unit length of the meniscus (W/m)
q'' = local evaporative heat flux ($\mathrm{W/m^2}$)
Q_{in} = heat input (W)
t = time (s)
U_i = interfacial velocity (m/s)
x = axial location (mm)
y = relative distance (μm)
z = axis perpendicular to y (along the thickness)

Greek Symbols

β = slip coefficient (m)
δ = film thickness (μm)
δ_0 = adsorbed thin film thickness (nm)
Δ = difference
Γ = mass flow rate per unit width of the meniscus (kg/m s)
λ = Wavelength (nm)
ν = kinematic viscosity ($\mathrm{m^2/s}$)
Π = disjoining pressure ($\mathrm{N/m^2}$)
$\Psi_{0.1\ \mu\mathrm{m}}$ = distance traveled by the meniscus (μm)
σ = surface tension of the liquid (N/m)
θ_r = apparent contact angle (tangent angle) at $\delta = 0.1\ \mu$m (deg)
τ_0 = average shear stress ($\mathrm{N/m^2}$)
τ_M = Marangoni shear stress ($\mathrm{N/m^2}$)

Subscripts

avg = average
i = ith instant
iso = isothermal reference state
ls = liquid-solid interface
lv = liquid-vapor interface
M = Marangoni stresses
max = maximum
min = minimum
mixture = the binary mixture
pentane = pentane
r = reference state
T = thicker portion
x = axial distance (mm)
v = vapor
0 = adsorbed film region
0,0 = adsorbed film region at $t=0$
$0,t$ = adsorbed film region at t

Superscript

$'$ = derivative with respect to length of the meniscus (y)

References

[1] Snyder, N. R., and Edwards, D. K., 1956, "Summary of Conference on Bubble Dynamics and Boiling Heat Transfer," Jet Propulsion Lab, Pasadena, Memo No. 20–137.

[2] Cooper, M. G., and Lloyd, A. J. P., 1969, "The Microlayer in Nucleate Pool Boiling," Int. J. Heat Mass Transfer, **12**, pp. 895–913.

[3] Judd, R. L., and Hwang, K. S., 1976, "A Comprehensive Model for Nucleate Pool Boiling Heat Transfer Including Microlayer Evaporation," ASME J. Heat Transfer, **98**, pp. 623–629.

[4] Dhir, V. K., 2001, "Numerical Simulations of Pool-Boiling Heat Transfer," AIChE J., **47**, pp. 813–834.

[5] Wayner, P. C., Jr., 1992, "Evaporation and Stress in the Contact Line Region," *Proc. Conference on Pool and External Flow Boiling*, Santa Barbara, V. K. Dhir, and A. E. Bergles, eds., Engineering Foundation, New York, pp. 251–256.

[6] Stephan, P., and Hammer, J., 1994, "New Model for Nucleate Boiling Heat Transfer," Heat Mass Transfer, **30**, pp. 119–125.

[7] Wayner, P. C., Jr., 1994, "Thermal and Mechanical Effects in the Spreading of a Liquid Film Due to a Change in the Apparent Finite Contact Angle," ASME J. Heat Transfer, **116**, pp. 938–945.

[8] Luttich, T., Marquardt, W., Buchholz, M., and Auracher, H., 2004, "Towards a Unifying Heat Transfer Correlation for the Entire Boiling Curve," Int. J. Therm. Sci., **43**, pp. 1125–1139.

[9] Potash, M., Jr., and Wayner, P. C., Jr., 1972, "Evaporation From a Two-dimensional Extended Meniscus," Int. J. Heat Mass Transfer, **15**, pp. 1851–1863.

[10] Raiff, R. J., and Wayner, P. C., Jr., 1973, "Evaporation From a Porous Flow Control Element on a Porous Heat Source," Int. J. Heat Mass Transfer, **16**, pp. 1919–1929.

[11] Khrustalev, D., and Faghri, A., 1996, "Fluid Flow Effects in Evaporation From Liquid/Vapor Meniscus," ASME J. Heat Transfer, **118**, pp. 725–730.

[12] Renk, F. J., and Wayner, P. C., Jr., 1979, "An Evaporating Ethanol Meniscus, Part I: Experimental Studies," ASME J. Heat Transfer, **101**, pp. 55–58.

[13] Wayner, P. C., Jr., Tung, C. Y., Tirumala, M., and Yang, J. H., 1985, "Experimental Study of Evaporation in the Contact Line Region of a Thin Film of Hexane," ASME J. Heat Transfer, **107**, pp. 182–189.

[14] Panchamgam, S. S., Gokhale, S. J., DasGupta, S., Plawsky, J. L., and Wayner, P. C., Jr., 2005, "Experimental Determination of the Effect of Disjoining Pressure on Shear in the Contact Line Region of a Moving Evaporating Thin Film," ASME J. Heat Transfer, **127**(3), pp. 231–243.

[15] Panchamgam, S. S., Plawsky, J. L., and Wayner, P. C., Jr., 2006, "Microscale Heat Transfer in an Evaporating Moving Extended Meniscus," Exp. Therm. Fluid Sci., **30**, pp. 745–754.

[16] Pratt, D. M., and Kihm, K. D., 2003, "Binary Fluid Mixture and Thermocapillary Effects on the Wetting Characteristics of a Heated Curved Meniscus," ASME J. Heat Transfer, **125**, pp. 867–874.

[17] Renk, F. J., and Wayner, P. C., Jr., 1979, "An Evaporating Ethanol Meniscus, Part II: Analytical Studies," ASME J. Heat Transfer, **101**, pp. 59–62.

[18] Hammer, J., and Stephan, P., 1996, "The Role of Micro Region Phenomena on Nucleate Boiling Heat Transfer," *Proc. 2nd European Thermal Sciences and 14th UIT National Heat Transfer Conference*, May 29–31, Rome, Edizioni ETS, Pisa, Italy, pp. 467–474.

[19] Ajaev, V. S., Homsy, G. M., and Morris, S. J. S., 2002, "Dynamic Response of Geometrically Constrained Vapor Bubbles," J. Colloid Interface Sci., **254**, pp. 346–354.

[20] Anand, S., De, S., and DasGupta, S., 2002, "Experimental and Theoretical Study of Axial Dryout Point for Evaporation From V-shaped Microgrooves," Int. J. Heat Mass Transfer, **45**, pp. 1535–1543.

[21] Suman, B., and Kumar, P., 2005, "An Analytical Model for Fluid Flow and Heat Transfer in a Micro-Heat Pipe of Polygonal Shape," Int. J. Heat Mass Transfer, **48**, pp. 4498–4509.

[22] Zheng, L., Plawsky, J. L., Wayner, P. C., Jr., and DasGupta, S., 2004, "Stability and Oscillations in an Evaporating Corner Meniscus," ASME J. Heat Transfer, **126**, pp. 169–178.

[23] Parks, C. J., and Wayner, P. C., Jr., 1987, "Surface Shear Near the Contact Line of a Binary Evaporating Curved Thin Film," AIChE J., **33**, pp. 1–10.

[24] Kern, J., and Stephan, P., 2003, "Theoretical Model for Nucleate Boiling Heat and Mass Transfer of Binary Mixtures," ASME J. Heat Transfer, **125**, pp. 1106–1115.

[25] Zhang, J., and Manglik, R. M., 2004, "Effect o Ethoxylation and Molecular Weight of Cationic Surfactants on Nucleate Boiling in Aqueous Solutions," ASME J. Heat Transfer, **126**, pp. 34–42.

[26] Panchamgam, S. S., Plawsky, J. L., and Wayner, P. C., Jr., 2006, "Influence of Marangoni Stresses and Slip on Spreading Characteristics of an Evaporating Binary Mixture Meniscus," *9th Joint AIAA/ASME Thermophysics and Heat Transfer Conference*, San Francisco, June 5–8.

[27] *CRC Handbook of Chemistry and Physics*, 2003, 84th ed., CRC Press, Boca Raton.

[28] *Perry's Chemical Engineers' Handbook*, 1997, 7th ed., McGraw-Hill, New York.

Disjoining Pressure Effects in Ultra-Thin Liquid Films in Micropassages—Comparison of Thermodynamic Theory With Predictions of Molecular Dynamics Simulations

V. P. Carey
e-mail: vcarey@me.berkeley.edu

A. P. Wemhoff
e-mail: wemhoff2@llnl.gov

Mechanical Engineering Department,
University of California,
Berkeley, CA 94720-1740

The concept of disjoining pressure, developed from thermodynamic and hydrodynamic analysis, has been widely used as a means of modeling the liquid-solid molecular force interactions in an ultra-thin liquid film on a solid surface. In particular, this approach has been extensively used in models of thin film transport in passages in micro evaporators and micro heat pipes. In this investigation, hybrid μPT molecular dynamics (MD) simulations were used to predict the pressure field and film thermophysics for an argon film on a metal surface. The results of the simulations are compared with predictions of the classic thermodynamic disjoining pressure model and the Born-Green-Yvon (BGY) equation. The thermodynamic model provides only a prediction of the relation between vapor pressure and film thickness for a specified temperature. The MD simulations provide a detailed prediction of the density and pressure variation in the liquid film, as well as a prediction of the variation of the equilibrium vapor pressure variation with temperature and film thickness. Comparisons indicate that the predicted variations of vapor pressure with thickness for the three models are in close agreement. In addition, the density profile layering predicted by the MD simulations is in qualitative agreement with BGY results, however the exact density profile is dependent upon simulation parameters. Furthermore, the disjoining pressure effect predicted by MD simulations is strongly influenced by the allowable propagation time of injected molecules through the vapor region in the simulation domain. A modified thermodynamic model is developed that suggests that presence of a wall-affected layer tends to enhance the reduction of the equilibrium vapor pressure. However, the MD simulation results imply that presence of a wall layer has little effect on the vapor pressure. Implications of the MD simulation predictions for thin film transport in micro evaporators and heat pipes are also discussed.

[DOI: 10.1115/1.2349504]

Keywords: thin film, wall effects, disjoining pressure, molecular dynamics, vapor pressure

Introduction

The concept of disjoining pressure has become a well-established formalism for treating the effect of wall-fluid force interaction in thin liquid films [1]. A typical situation of interest is shown in Fig. 1. This figure shows a cross section of a passage carrying a stratified flow of liquid and vapor flow. A deeper central portion of the passage (location A) carries most of the liquid while the lateral portions (location B) carry a thin liquid film flow with film thickness δ_f. Since most of the interface is flat and separates the deeper liquid flow from the vapor, at equilibrium we expect that

$$P_{ve} = P_{l0} \tag{1}$$

where P_{l0} is the liquid pressure at the interface in the absence of wall attractive forces and P_{ve} is the vapor pressure.

In the thin liquid film at location B, the pressure in the liquid film is altered by force interactions between liquid molecules and atoms or molecules in the solid. Although Israelachvili [1] provides the general disjoining pressure relation for a film of specified thickness, we derive the same relation here using the potential energy due to the forces that the solid wall molecules exert on each fluid molecule. To determine the resulting pressure variation in the film, we considered the system shown in Fig. 2. Fluid and metallic solid interactions are modeled with a Lennard-Jones interaction potential having the form

$$\phi_{fs}(r) = -\frac{C_{\phi,fs}}{r^6}\left(1 - \frac{D_m^6}{r^6}\right) \tag{2}$$

We further assume that a similar form, with different constants, models the long-range attraction between a pair of two fluid molecules.

$$\phi_{ff}(r) = -\frac{C_{\phi,ff}}{r^6}\left(1 - \frac{D_f^6}{r^6}\right) \tag{3}$$

In the liquid and solid phases of interest here, the interactions between pairs of molecules are treated as independent and addi-

---

Contributed by the Heat Transfer Division of ASME for publication in the JOURNAL OF HEAT TRANSFER. Manuscript received August 26, 2005; final manuscript received March 1, 2006. Review conducted by Raj M. Manglik. Paper presented at the 2005 ASME International Mechanical Engineering Congress (IMECE2005), November 5–11, 2005, Orlando, Florida, USA.

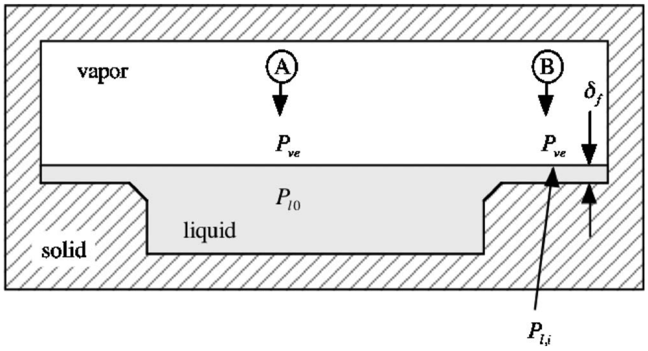

Fig. 1 Cross section of a micropassage containing thin liquid films

tive. D_m is the closest approach distance of fluid to solid molecules, and D_f is the closest approach distance of two fluid molecules. D_m and D_f are on the order of mean diameters for the molecular species involved. To get the total effect of all the solid metallic molecules on a given free fluid molecule, we integrate the product of the density and molecular potential to sum the contributions of all the solid molecules. It follows that the mean-field potential energy felt by the free fluid molecule due to interactions with all the metallic solid molecules is

$$\Phi_{fmf} = \int_{z_s=z}^{\infty} \int_{x=0}^{\infty} \rho_s \phi_{fs} (2\pi x)\, dx\, dz_s \tag{4}$$

Substituting the relation (2) above for the molecular potential, substituting x^2+z^2 for r^2, and integrating yields

$$\Phi_{fmf} = -\frac{\pi \rho_s C_{\phi,fs}}{6z^3} + \frac{\pi \rho_s C_{\phi,fs} D_m^6}{45 z^9} \tag{5}$$

For convenience, we reorganize the relation above in terms of a modified Hamaker constant A_{ls} defined as

$$A_{ls} = \pi^2 \rho_f \rho_s C_{\phi,fs} \tag{6}$$

Using these definitions converts Eq. (5) to the form

$$\Phi_{fmf} = \frac{A_{ls}}{6\pi \rho_f D_m^3} \left[\frac{2}{15} \left(\frac{D_m}{z} \right)^9 - \left(\frac{D_m}{z} \right)^3 \right] \tag{7}$$

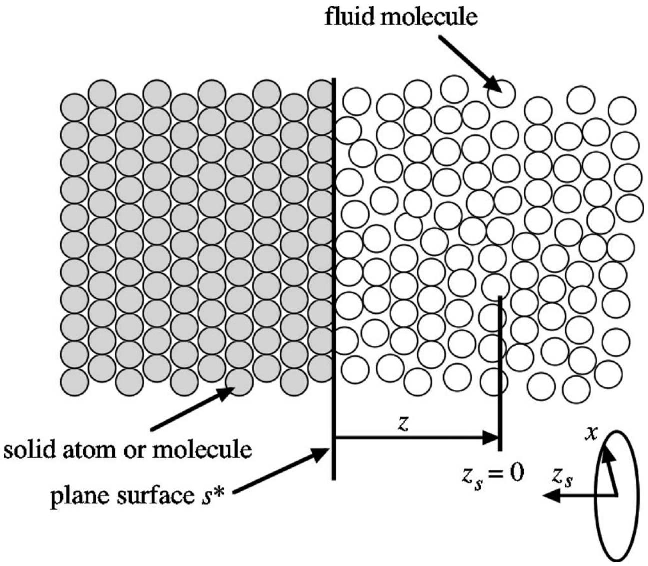

Fig. 2 Schematic used for derivation of disjoining pressure

This potential is equivalent to a body force that produces a hydrostatic variation of pressure similar to that produced by gravity. We determine the pressure field by using the wall potential to determine the body force in the Navier-Stokes equations with no velocity terms,

$$0 = -\frac{1}{(\rho_f M/N_A)} \nabla P + \boldsymbol{f}_{fs} \tag{8}$$

In the above equation, $\boldsymbol{f}_{fs}$ is the force per unit mass on the fluid system. The force exerted on a single molecule by the entire wall is given by

$$\boldsymbol{F}_{fs} = -\nabla \Phi_{fmf} = \frac{A_{ls}}{2\pi \rho_f D_m^4} \left[\frac{2}{5} \left(\frac{D_m}{z} \right)^{10} - \left(\frac{D_m}{z} \right)^4 \right] \boldsymbol{z} \tag{9}$$

where $\boldsymbol{z}$ is the unit vector in the z direction, and the corresponding force per unit mass is

$$\boldsymbol{f}_{fs} = \frac{N_A \boldsymbol{F}_{fs}}{M} = \frac{N_A A_{ls}}{2\pi M \rho_f D_m^4} \left[\frac{2}{5} \left(\frac{D_m}{z} \right)^{10} - \left(\frac{D_m}{z} \right)^4 \right] \boldsymbol{z} \tag{10}$$

The force per unit mass specified by Eq. (10) is substituted into Eq. (8), and since the force only acts in the z direction, the relation simplifies to

$$\frac{dP}{dz} = \frac{A_{ls}}{2\pi D_m^4} \left[\frac{2}{5} \left(\frac{D_m}{z} \right)^{10} - \left(\frac{D_m}{z} \right)^4 \right] \tag{11}$$

Integrating both sides of Eq. (11) from a position z to ∞, and taking the pressure at ∞ to be P_{l0}, the resultant expression for the pressure profile close to the wall is

$$P(z) = P_{l0} - \frac{A_{ls}}{6\pi D_m^3} \left[\frac{2}{15} \left(\frac{D_m}{z} \right)^9 - \left(\frac{D_m}{z} \right)^3 \right] \tag{12}$$

Because D_m is on the order of a molecular diameter, and we are interested in z values larger than that, the z^{-9} term in Eq. (12) may be neglected. The relation for the pressure profile then simplifies to

$$P(z) = P_{l0} + \frac{A_{ls}}{6\pi z^3} \tag{13}$$

In the thin liquid film at location B in Fig. 1, we therefore expect the pressure to vary with distance from the lower wall according to Eq. (13). It follows that at the interface ($z = \delta_f$), the pressure in the liquid $P_{l,i}$ must be

$$P_{l,i} = P(\delta_f) = P_{l0} + \frac{A_{ls}}{6\pi \delta_f^3} \tag{14}$$

Combining Eqs. (1) and (14) and solving for $P_{ve} - P_{l,i}$ yields

$$P_{ve} - P_{l,i} = -\frac{A_{ls}}{6\pi \delta_f^3} \tag{15}$$

The amount by which P_{ve} differs from $P_{l,i}$ is the disjoining pressure P_d

$$P_d = -\frac{A_{ls}}{6\pi \delta_f^3} \tag{16}$$

Thus, for the circumstances depicted in Fig. 1, the pressure difference across the interface is equal to the disjoining pressure, which increases rapidly in magnitude as the film grows thinner. The result provided by Eq. (16) is also given in many texts (e.g., [1]).

The alteration of the equilibrium vapor pressure and liquid pressure in the film associated with disjoining pressure effects has been shown to alter the thermodynamic equilibrium conditions at the liquid-vapor interface of thin liquid films. The resulting shift in the vapor-pressure versus temperature relation must be taken into account when modeling thin film evaporation or condensation processes in micropassages of micro heat pipes and micro capillary-pumped loops. Consequently, the effects of disjoining pressure have been explored in a variety of circumstances typically encountered in these types of applications [2–13]. While the concept of disjoining pressure provides a framework for analyzing the effects of wall-fluid attractive forces, it ignores many of the detailed features of the liquid film. In the work summarized here, molecular dynamics simulations were used to explore the detailed features of the structure and thermophysics of thin liquid films on a solid surface. The predicted film features and equilibrium vapor pressure were examined for films of varying thickness and the results were compared to predictions of the conventional disjoining pressure treatment. These comparisons are described in the following sections of this paper.

MD Simulation of Thin Liquid Films

As a means of assessing the validity of the pressure profile predicted by our thermodynamic model, we also modeled the molecular level behavior of liquid argon near a solid gold (metallic) wall using a classical molecular dynamics (MD) simulation. The hybrid molecular dynamics simulation technique used here combines traditional *NVE*-type MD simulation techniques with a stochastic boundary condition used for the equilibration of pressure. Several aspects of the methodology presented here have been previously described [14]. However, some adjustments have been made in this study to obtain as accurate a value of saturation pressure as possible. This methodology allows for the implementation of monatomic fluids that interact via the well-known Lennard-Jones 6-12 potential,

$$\phi_{LJ}(r) = 4\varepsilon_{LJ}\left[\left(\frac{\sigma_{LJ}}{r}\right)^{12} - \left(\frac{\sigma_{LJ}}{r}\right)^{6}\right] \tag{17}$$

where σ_{LJ} and ε_{LJ} are the Lennard-Jones length and energy parameters, respectively, and r is the distance between two molecules. For this methodology, the particles are initialized in either a face-centered-cubic (fcc) lattice or in a cubic lattice whose densities matched the values for bulk phases at the desired equilibrium temperature (the cubic lattice is used in lieu of the standard fcc lattice for placement of individual layers of molecules for modeling ultra-thin films). The molecules are also initialized with velocities matching the Boltzmann distribution for a low initial temperature ($T_r = T/T_c = 0.1$) using the Box-Mueller algorithm [15]. The system equilibrates by raising the system temperature from the initially low value to the desired equilibrium temperature via velocity rescaling such that the system kinetic energy adheres to the relation

$$\frac{1}{2}m\sum_{i=1}^{N} c_i^2 = \frac{3}{2}Nk_BT \tag{18}$$

This rescaling is executed for 30,000 steps, and then the system was allowed to equilibrate with the rescaling turned off for an additional 20,000 steps. Upon equilibration, the simulation domain is evenly divided into 100 bins along the z axis for collection of mean density values during subsequent time steps.

The hybrid MD simulation domain utilized in this study, depicted in Fig. 3, features three types of boundaries: periodic, wall, and flux. Periodic boundaries exist at all four boundaries in the x and y directions. The $z = 0$ boundary represents the solid surface and features a wall potential, Φ_{fmf}, which binds the liquid film to a semi-infinite metal solid. The wall potential (7) was used here with the constant values

$$A_{ls} = 1.01 \times 10^{-19}\ \text{J} \tag{19a}$$

$$D_m = 0.304\ \text{nm} \tag{19b}$$

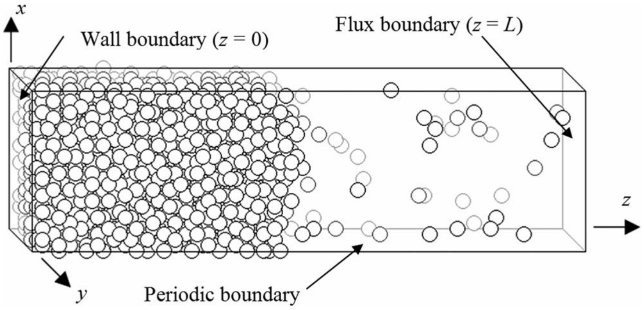

Fig. 3 MD simulation domain

$$\rho_f = 2.08 \times 10^{28}\ \text{m}^{-3} \tag{19c}$$

which are appropriate for argon on a metal surface. Note that this 9-3 version of the wall potential (7) is slightly different than the 10-4 model given by Toxvaerd [16] for an fcc Lennard-Jones solid lattice. However, a 9-3 potential has been previously used in some studies of Lennard-Jones molecules interacting with a surface (e.g., [17,18]).

A flux boundary at $z = L$ is used to adjust the system pressure to an equilibrium value. For an ideal gas, the flux J (in molecules/m^2s) is related to the system pressure P and temperature T by the kinetic theory relation [19]

$$J = \sqrt{\frac{k_BT}{2\pi m}}\left(\frac{P}{k_BT}\right) \tag{20}$$

where m is the molecular mass of the injected species. Note that the flux boundary borders on the vapor region of the simulation domain as shown in Fig. 3, allowing for the ideal gas approximation in the derivation of Eq. (20). The concept behind the flux condition is similar to that provided by an Andersen thermostat [20], where system molecules randomly collide with a fictitious surrounding infinite heat bath to maintain a constant system temperature. In the hybrid simulation, the flux boundary separates the simulation domain from an infinite vapor bath, and the flux supplied by Eq. (20) represents an equilibrium value for the vapor bath of specified temperature and pressure. Frenkel and Smit discuss this concept further for a Monte Carlo simulation [21]. The treatment of the vapor as an ideal gas is not completely accurate for a vapor at saturation. However, we adopt this idealization here since it is a good approximation at low vapor densities, and it is consistent with idealizations made in formulation of conventional disjoining pressure, as discussed in the next section.

The flux boundary acts to inject a molecule stochastically into the simulation domain at a desired interval. During the initial 50,000 steps of the simulation, the boundary acts to preserve mass, hence when a molecule leaves the $z = L$ boundary, another molecule is injected directly into the simulation domain through that same boundary. After the kinetic energy equilibration period, molecules are injected corresponding to a desired pressure using Eq. (20). When a molecule is injected, the position of the molecule is chosen randomly on the flux boundary plane. The x and y velocities adhere to the Boltzmann distribution for a bulk gas, while the z velocity is sampled from the distribution [22]

$$f(v_z)dv_z = \frac{mv_z}{k_BT}e^{-mv_z^2/2k_BT}dv_z \tag{21}$$

where $f(v_z)$ represents the fraction of molecules of a large sample with z-velocity components between v_z and $v_z + dv_z$. Sampling of the x- and y-velocity distributions is performed via the Box-Mueller algorithm [15], while the z velocity is sampled using the relation

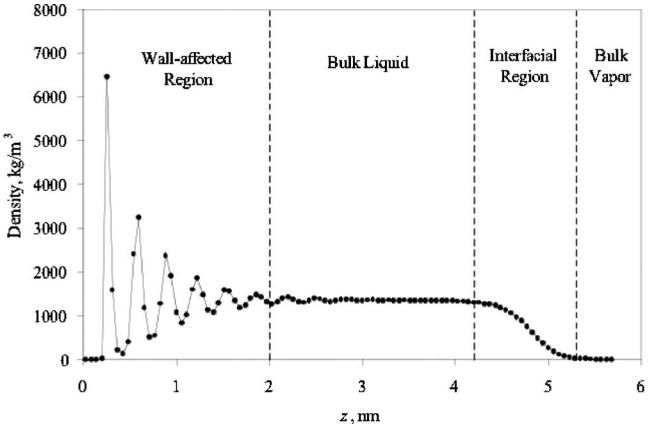

Fig. 4 Argon liquid film mass density profile: $T_r = 0.57$, 100 collection bins, and 400,000 time steps

$$v_{z,i} = -\sqrt{-\log(\mathfrak{R})\left(\frac{2k_BT}{m}\right)} \tag{22}$$

where $\mathfrak{R}$ is a random number between 0 and 1.

The system is equilibrated by adjusting the input flux every 50,000 time steps to force the loss of molecules from the simulation domain to match the gain from the flux boundary. The adjustment is performed by determining the net outflux of molecules per time step over the 50,000-step period by applying a fit curve to the system molecule count variation with time. Unlike previous work [14], however, the injected flux value was adjusted via the equation

$$J_{\text{new}} = \frac{1}{2}(J_{\text{old}} - J_{\text{slope}}) \tag{23}$$

where J_{new} is the updated flux, J_{old} is the previous flux, and J_{slope} is the average net influx of molecules over the previous 50,000 steps determined using the fit curve, and the factor of one-half was used to prevent overshoot.

For this study, a simulation of argon molecules was used, where values of σ_{LJ} and ε_{LJ} were taken to be 0.34 nm and 1.67×10^{-21} J ($\varepsilon_{LJ}/k_B = 121$ K), respectively. Both the forces and intermolecular potentials were smoothly truncated at the cutoff radius of $5.0\sigma_{LJ}$ using standard truncation algorithms for short-ranged forces [23]. The time step used in the simulations was 5 fs, and the configuration was updated at each step by the velocity Verlet algorithm [23]. The initial liquid film lattice consisted of $c_Z \times 6 \times 6$ primitive fcc cells, where c_Z is the number of cells in the z direction. The initial vapor lattice size depended on the system temperature.

A typical average mass density profile through the simulation domain is shown in Fig. 4. The attraction of the wall potential causes an ordering of molecules in the wall-affected region of the liquid that results in peaks in the density profile. These peaks rapidly diminish where the wall potential becomes repulsive ($z < (2/5)^{1/6}D_m$). A similar wall-region profile for argon was exhibited in the MD simulation of Liu [24], and in the application of the Born-Green-Yvon equation for argon on graphite [18] and for binary Lennard-Jones fluids on a surface [25], although these comparisons are qualitative and are strongly dependent upon the parameters used in the wall potential [18]. At a value of approximately 2.0 nm from the wall, the density profile becomes approximately uniform, suggesting the transition to a bulk liquid region. At 4.2 nm from the wall the rapid decrease in the density profile suggests an interfacial region, while beyond 5.3 nm the uniform low density profile indicates a bulk vapor region. Values of the bulk liquid density as a function of temperature compared well with ASHRAE recommended values [26].

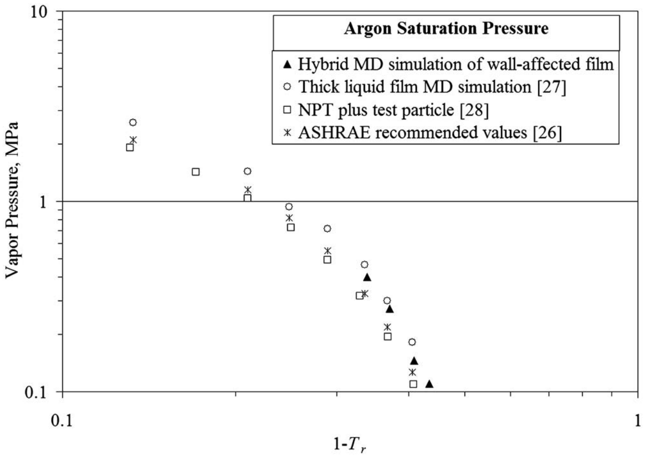

Fig. 5 Simulated argon vapor pressure values from the hybrid MD simulation of the wall-affected film compared to results for a simulated thick liquid film, the NPT plus test particle method, and ASHRAE recommended values. Simulations were run for 400,000 time steps for this study.

Once the equilibrium flux at the $z = L$ boundary was found, the value of pressure was determined from Eq. (20). Figure 5 shows the mean pressure values derived from the hybrid MD method for a thick argon film ($\delta_f > 15$ nm) compared to values given by ASHRAE tables [26] as a function of the departure from the critical point, 1-T_r. Also shown in Fig. 5 are the thick film values from argon simulations by Dunikov et al. [27] for a cutoff of $3.5\sigma_{LJ}$ and values taken from vapor phase equilibria MD simulations by Lotfi et al. using the NPT plus test particle method [28]; the cited data were adjusted using the values of σ_{LJ} and ε_{LJ} for this study. The figure depicts that, for thick films, the predicted vapor pressure variation for our hybrid model is comparable to the ASHRAE data and results of other MD simulations, regardless of the inhomogeneity of the fluid.

For any equilibrium saturation pressure value shown in Fig. 5, the resultant local pressure profile can be determined from MD simulations using the modified virial calculation by Weng et al. [29] and by fixing the external pressure to the specified value. One example of this is shown in Fig. 6 for $T_r = 0.6$, where the pressure

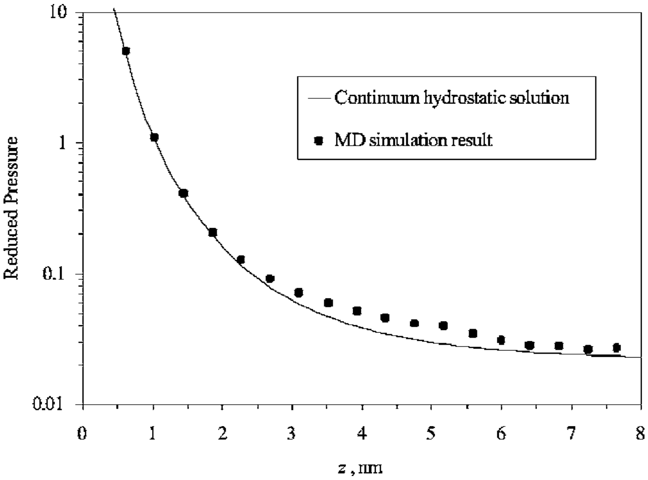

Fig. 6 Calculated local pressure profile for argon on a metallic solid surface using MD and hydrostatic analyses; external conditions match saturation data for argon at 1 atm. Simulation featured 300,000 time steps, 50 collection bins, and approximately 1980 molecules.

profile in the film was also predicted by the hydrostatic model in Eq. (12) using A_{ls} and D_m values similar to those in Eqs. (19*a*) and (19*b*).

It should be noted that equilibrium mean local pressure values extracted from the simulation domain far from the wall compared well with the applied external vapor pressure values for the simulations in this study. Therefore, the flux boundary method provides a viable alternative to traditional domain volume rescaling methods for system pressure management. Furthermore, since the hybrid method allows for system readjustment towards equilibrium (as described above), then the equilibrium system by definition would have a constant chemical potential in both phases, and thus a grand canonical system (μPT) is simulated.

Theoretical analyses of thin films on solid surfaces suggest that the saturation pressure decreases with thickness for very thin films [30]. The results described above indicate that the hybrid MD simulation scheme predicts the equilibrium vapor pressure with reasonable accuracy for thick films. It is therefore plausible to expect that it will provide physically realistic predictions of how the vapor pressure varies with film thickness. Exploration of the effects of film thickness on equilibrium vapor pressure is described in the following sections.

Comparison to Disjoining Pressure Theory

Variation of the liquid film thickness produces disjoining pressure effects that alter the equilibrium vapor pressure from the normal bulk-fluid equilibrium value in standard saturation tables. The conventional thermodynamic analysis of these effects begins by integrating the Gibbs-Duhem equation

$$d\hat{\mu} = -\hat{s}dT + \hat{v}dP \tag{24}$$

at constant temperature from saturation conditions to an arbitrary state in the liquid and vapor phases. In doing so, we follow the usual conventions of treating the liquid as incompressible and the vapor as an ideal gas. This yields the following relations for the vapor and liquid chemical potentials in the absence of wall attraction effects:

$$\hat{\mu}_v = \hat{\mu}_{v,sat} + \overline{R}T \ln (P_{ve}/P_{sat}) \tag{25}$$

$$\hat{\mu}_l = \hat{\mu}_{l,sat} + \hat{v}_l(P_l - P_{sat}) \tag{26}$$

For a pure fluid, the chemical potential is equivalent to the specific Gibbs function

$$\hat{\mu}_l = \hat{g}_l$$

In the presence of wall attraction effects in the liquid film, the Gibbs function is augmented by the potential energy associated with interaction between fluid molecules and surface molecules or atoms. Denoting the potential energy per fluid molecule due to interaction with the wall as a whole as Φ_{fmf}, the expression for the liquid chemical potential becomes

$$\hat{\mu}_l = \hat{\mu}_{l,sat} + \hat{v}_l(P_l - P_{sat}) + N_A\Phi_{fmf} \tag{27}$$

For the system to be in equilibrium at the interface, the liquid pressure must equal the equilibrium vapor pressure

$$P_{l,i} = P_{ve} \tag{28}$$

and the chemical potentials must be equal there. Equating the right sides of Eqs. (25) and (27), and setting P_l equal to P_{ve} as dictated by Eq. (28), yields

$$\overline{R}T \ln (P_{ve}/P_{sat}) = \hat{v}_l(P_{ve} - P_{sat}) + N_A\Phi_{fmf} \tag{29}$$

which can be rearranged to the form

$$\frac{P_{ve}}{P_{sat}} = \exp\left\{\frac{P_{sat}\hat{v}_l}{\overline{R}T}\left(\frac{P_{ve}}{P_{sat}} - 1\right) + \frac{N_A\Phi_{fmf}}{\overline{R}T}\right\} \tag{30}$$

For the circumstances of interest here, P_{ve} is close to P_{sat} and $P_{sat}\hat{v}_l/\overline{R}T$ is small, with the net result that the first term in the curly brackets above is negligible compared to the second. Neglecting the first term simplifies Eq. (30) to the form

$$\frac{P_{ve}}{P_{sat}} = \exp\left\{\frac{\Phi_{fmf}}{k_BT}\right\} \tag{31}$$

Substituting the relation (7) derived previously for the wall potential, neglecting the z^{-9} term, and setting z equal to δ_f at the interface, the following relation is obtained

$$\frac{P_{ve}}{P_{sat}} = \exp\left\{-\frac{A_{ls}}{6\pi\rho_f\delta_f^3k_BT}\right\} \tag{32}$$

A key objective of this investigation was to determine if the MD simulation model predictions agreed with the variation of saturation pressure with film thickness indicated by Eq. (32).

To explore the predicted effect of film thickness on equilibrium saturation pressure, MD simulations of argon were performed at $T_r = 0.6$ for films of various thicknesses. The parameters for the simulations were set at the values described in the previous section. In these runs, the initial thickness of the film was specified via the number of fcc cells in the z direction, and the initial thickness of the vapor region was kept constant at 2.0 fcc lattice parameters. It should be noted that the size of the vapor region has a significant effect on the calculated saturation pressure values due to the time required for molecular propagation across the vapor region during the 50,000-step sampling period. The thickness of the equilibrated film was calculated as the distance from the wall ($z=0$) to the center of the interfacial region, corresponding to

$$\rho = \rho_{m,\infty} = \frac{1}{2}(\rho_{l,\infty} + \rho_{v,\infty})$$

where $\rho_{l,\infty}$ and $\rho_{v,\infty}$ are the values of liquid and vapor bulk densities for films thick enough that disjoining effects are not present. The runs were performed for 500,000 time steps, over a range of film thickness from 0.7 to 4.9 nm. Figure 7 is a plot of the density profile for a thickness value of 2.6 nm, where one can observe that for this thickness value, very little bulk liquid density region is present. For $T_r = 0.6$, the density transition associated with the interfacial region occupies a thickness of approximately 0.7 nm, and the wall-affected region has a thickness of about 2 nm, so the size

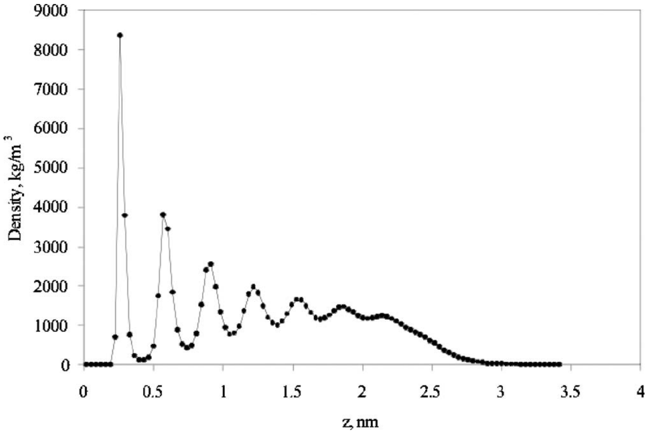

Fig. 7 Mass density profile for argon film on solid surface, $T_r = 0.6$. Film thickness was calculated as 2.6 nm. Simulation was run with lateral dimensions of $10.0\sigma_{LJ} \times 10.0\sigma_{LJ}$ and 500,000 time steps.

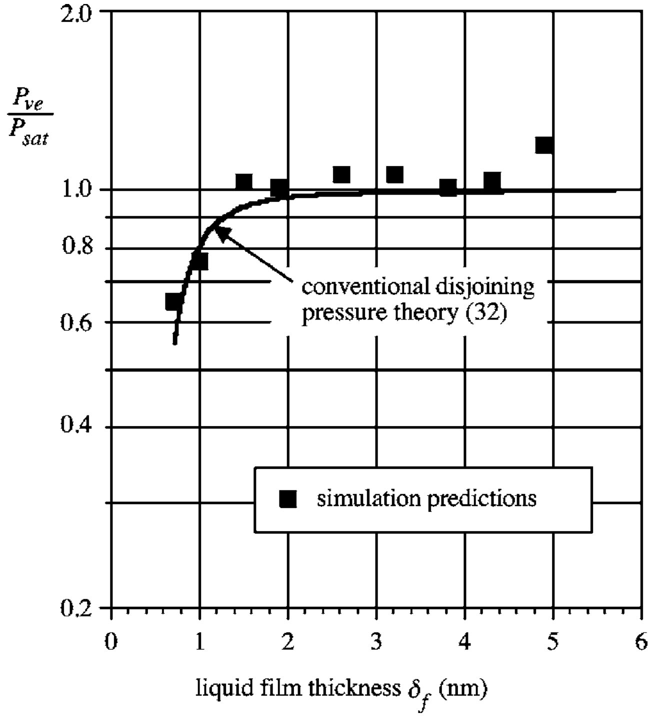

Fig. 8 Comparison of MD results with conventional theory

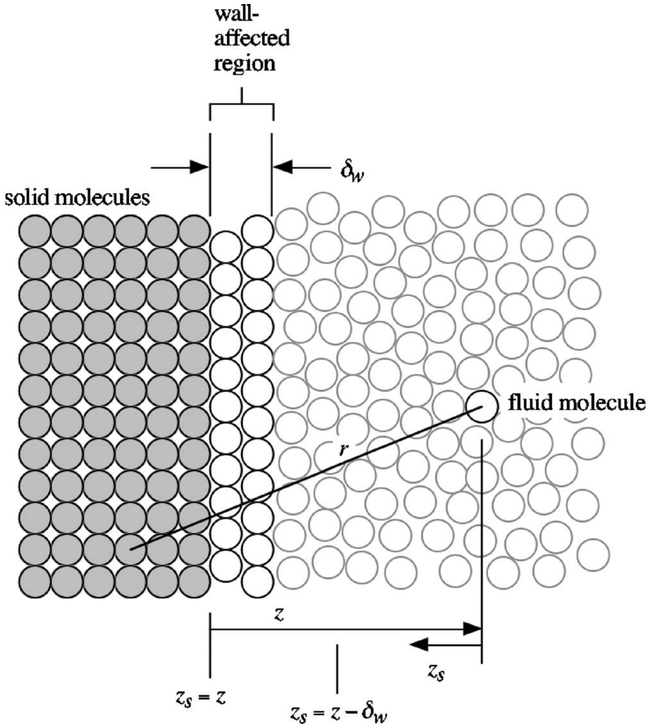

Fig. 9 Wall layer model

of the bulk liquid region tends to zero as the film thickness falls below 2.7 nm.

For films with thicknesses above 1.5 nm, the predicted vapor pressure agrees fairly well with the corresponding ASHRAE value [26]. Figure 8 presents the variation of P_{ve}/P_{sat} with film thickness predicted by our hybrid MD simulations for film thicknesses below 6 nm. In these results, the average of the final six calculated pressure values (step 250,000 through step 500,000) were used as data points. Also shown is the variation predicted by the theoretical relation (32) derived from conventional disjoining pressure theory. It can be seen in Fig. 8 that the MD simulation predictions generally agree with the tabulated bulk saturation pressure within about 10% at film thicknesses greater than 1.5 nm, with the exception of the film with thickness of 4.9 nm. Below 1.5 nm, the simulation vapor pressure predictions drop well below the equilibrium saturation pressure for the bulk phases at $T_r=0.6$. As indicated in Fig. 8, overall, the variation of equilibrium vapor pressure agrees well with the variation predicted by the conventional disjoining pressure theory.

As noted above, we found that the simulation predictions of equilibrium pressure were sensitive to vapor region thickness. Our initial simulation efforts were found to predict a vapor pressure variation with film thickness that differed significantly from conventional theory. We subsequently found that the periods between external flux adjustments were not long enough to fully equilibrate molecular exchange at the interface with the imposed flux boundary condition at the outer boundary of the simulation. The MD simulation results in Fig. 8 were obtained from simulation runs in which the simulation was run long enough that molecular exchange at the interface is in equilibrium with the outer boundary flux condition for the specified vapor region thickness.

While the agreement of the simulation predictions with conventional theory is reassuring, it is interesting that the MD simulations that include the effect of the wall-affected region produce a prediction that agrees so well with a thermodynamic theory that largely ignores such effects. The next section explores this issue further.

A Wall Layer Model

The peaks in the local mean density indicated in Figs. 4 and 7 reflect a layered order in the fluid molecules near the surface. The decreasing magnitude of the peaks with increasing distance from the solid wall indicates that the degree of organization in the layered structure of the fluid diminishes with distance from the wall. In a recent study of this type of liquid layering near a liquid-solid interface, Xue et al. [31] quantified this in terms of a planar structure factor that varied from 1 for a perfect fcc plane of molecules to 0 for molecules in random positions. The planar structure factor varies from close to 1 at the solid-liquid interface to close to 0 at larger distances from the wall. Xue et al. [31] found that for a wetting fluid, the planar structure factor decreased to 0 about two fluid molecular diameters away from the wall.

To explore how the liquid layering near the solid wall affects the disjoining pressure, a model is adopted here in which the fluid within two molecular diameters of the wall is treated as a solid phase of planar layers, and the fluid beyond two molecular diameters is treated as bulk fluid. This is obviously a crude approximation to the gradually diminishing layered structure in the fluid near the surface, but it captures the main features of the layering, and it is consistent with the results of Xue et al. [31] in that it limits the strongest layering effects to the region within two molecular diameters of the wall.

To develop this model with wall effects included, we consider the system shown in Fig. 9 in which fluid molecules interact with a composite wall structure. The composite wall is a semi-infinite region of solid metal wall molecules or atoms covered with a layer of fluid molecules that are modeled as being in a solid phase. The layer of fluid molecules has thickness δ_w. Because they are more localized in their position than molecules in the bulk liquid, molecules in the wall-affected region behave almost like a solid layer attached to the metal surface. The wall layer model proposed here is based on the reasoning that the presence of this layer causes molecules in the bulk liquid to behave as though they are interacting with a composite wall structure consisting of the metal substrate plus the strongly wall-affected layer. The molecules in the bulk fluid layer are presumed to behave as predicted by the bulk-fluid analysis in the previous section except that they are closer to the effective solid-liquid interface than would be the case if the wall-affected region were not considered to be part of the composite solid in Fig. 9. Although this model is simplistic, it accomplishes the objective of predicting the effect of the quasi-solid wall-affected layer on the force interaction potential Φ_{fmf} at the interface, which affects the vapor pressure as predicted by Eq. (31).

In this model, consistent with the reasoning above, we take δ_w to be two molecular diameters D_m. As in the first section of this paper, the fluid and metallic solid interactions and the interactions between fluid molecules are modeled with Lennard-Jones potentials (2) and (3). The interactions between pairs of molecules are treated as independent and additive. To get the total effect of all the solid metallic molecules and the solid layer molecules on a given free fluid molecule, we integrate the product of the density and molecular potential to sum the contributions of all the solid and layer molecules.

It follows that the mean-field potential energy felt by the free fluid molecule due to interactions with all the metallic solid molecules and the solid layer molecules is

$$\Phi_{fmf} = \int_{z_s=z-\delta_w}^{z_s=z} \int_{x=0}^{\infty} \rho_f \phi_{ff}(2\pi x)\, dx\, dz_s + \int_{z_s=z}^{\infty} \int_{x=0}^{\infty} \rho_s \phi_{fs}(2\pi x)\, dx\, dz_s \tag{33}$$

Substituting the relations (2) and (3) above for the molecular potentials, substituting x^2+z^2 for r^2, and integrating yields

$$\Phi_{fmf} = \frac{\pi\rho_f C_{\phi,ff}}{6}\left(\frac{1}{z^3} - \frac{1}{(z-\delta_w)^3}\right) - \frac{\pi\rho_f C_{\phi,ff} D_f^6}{45}\left(\frac{1}{z^9} - \frac{1}{(z-\delta_w)^9}\right) - \frac{\pi\rho_s C_{\phi,fs}}{6z^3} + \frac{\pi\rho_s C_{\phi,fs} D_m^6}{45z^9} \tag{34}$$

For $z > D_f$ or D_m, terms involving D_f and D_m are small and can be neglected. The potential is then well approximated as

$$\Phi_{fmf} = \frac{\pi\rho_f C_{\phi,ff}}{6}\left(\frac{1}{z^3} - \frac{1}{(z-\delta_w)^3}\right) - \frac{\pi\rho_f C_{\phi,fs}}{6z^3} \tag{35}$$

For convenience, we reorganize the relation above in terms of modified Hamaker constants A_{ls} defined by Eq. (6) and A_{ll} defined as

$$A_{ll} = \pi^2 \rho_f^2 C_{\phi,ff} \tag{36}$$

Using these definitions converts Eq. (35) to the form

$$\Phi_{fmf} = -\frac{A_{ls}}{6\pi\rho_f(z-\delta_w)^3}\left[\frac{(z-\delta_w)^3}{z^3}\left(1 - \frac{A_{ll}}{A_{ls}}\right) + \frac{A_{ll}}{A_{ls}}\right] \tag{37}$$

In this model, Eq. (31) from the thermodynamic analysis above still applies, with Φ_{fmf} evaluated at the interface z location, which is $z=\delta_f$. Using (37) to evaluate Φ_{fmf} with $z=\delta_f$, and neglecting $P_{sat}\hat{v}_l/RT$ compared to terms of order one, we convert Eq. (31) to

$$\frac{P_{ve}}{P_{sat}} = \exp\left\{-\frac{A_{ls}}{6\pi(N_A/\hat{v}_l)(\delta_f-\delta_w)^3 k_B T}\left[\frac{(\delta_f-\delta_w)^3}{\delta_f^3}\left(1-\frac{A_{ll}}{A_{ls}}\right) + \frac{A_{ll}}{A_{ls}}\right]\right\} \tag{38}$$

Figure 10 compares the MD simulation values of P_{ve}/P_{sat} with the profiles predicted using the conventional disjoining pressure theory (32) and the wall layer model (38). For our analysis, A_{ll} for argon was taken to be 2.57×10^{-20} J. This value was obtained using the relation for A_{ll} recommended by Israelachvili [1] with the value of surface tension for argon recommended by Ref. [26] at $T_r=0.6$.

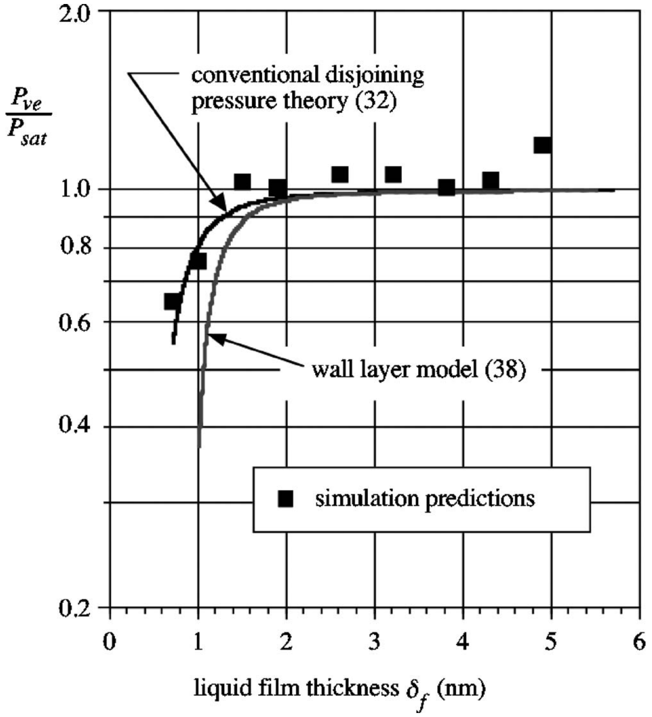

Fig. 10 Comparison of MD simulation results with predictions of conventional theory and the wall layer model

In this model, we have taken the density in the wall-affected region to be equal to the bulk liquid density. Because of the layered structure, the density may actually be slightly different in the wall-affected region. The density in this region would affect the A_{ll} value, as dictated by Eq. (36). Sensitivity calculations using Eq. (38) indicate that a 10% change in density in the wall-affected region would produce about a 20% change in A_{ll}, but only about an 8% change in P_{ve}/P_{sat}. Thus, taking the wall region density to equal the bulk density may produce some inaccuracy, but the effect on the vapor pressure prediction is estimated to be on the order of about 8%.

In comparing the different model predictions in Fig. 10, it should be noted that the MD simulation points for $\delta_f \leq 1.5$ nm correspond to a film with no bulk fluid region. Since the conventional theory applies to bulk fluid interacting with a wall, there is reason to expect that the vapor pressure predicted by the MD simulation may not agree with the conventional model prediction for these points. The MD simulation is expected to be a better prediction for such cases. As noted in the previous section, the conventional theory actually agrees well with the MD simulation predictions, even for $\delta_f \leq 1.5$ nm, where no conventional bulk liquid region exists in the film.

Figure 10 indicates that, relative to the predictions of the MD simulations, the wall layer model predicts a more rapid decrease of vapor pressure with decreasing film thickness. Hence, the wall layer model, which was expected to better model the impact of liquid layering near the wall, actually does not agree as well with the simulation predictions as the conventional theory. The wall layer model developed here assumes the extreme case in which the layers of fluid molecules closest to the wall behave as a solid, strongly resisting the forces of molecules farther from the surface. Even for this extreme case, the effect on vapor pressure is small, as indicated in Fig. 10. Our results suggest that when the fluid molecules in the layers near the wall are allowed some limited motion, as is the case in the MD simulations, the effect of their limited capability to move may have little influence on their force interaction with molecules further from the wall. The liquid film may then behave essentially as if the film were all bulk liquid with no layering near the wall. Overall, the results of our models and these observations suggest that liquid layering near the wall does not strongly influence the impact of wall attractive forces on the equilibrium vapor pressure in thin liquid films on solid surfaces.

Concluding Remarks

The hybrid MD simulations used in this investigation of thin liquid films predict vapor pressure values for thick films that agree well with tabulated values for saturated liquids. This agreement suggests that the predictions of this type of simulation for very thin films should be physically realistic. This lends some credibility to MD simulation prediction of equilibrium vapor pressure predictions for thin liquid films on solid surfaces. The MD simulations are particularly useful for modeling extremely thin films where the thickness of the bulk liquid region is of the same order of magnitude or smaller than that for the layered wall-affected region and the interfacial region. In such cases, the MD simulations directly account for the effects of layering and the density variation in the interfacial region.

The use of conventional disjoining pressure theory is suspect in such cases because it is generally constructed using relations derived for equilibrium of coexisting bulk phases. The conventional theory thus does not account for potential effects of direct interaction of a layered region with the interfacial region in ultra thin films. Despite the expected limitations of the conventional theory, its predictions of equilibrium vapor pressure were found to agree well with the MD simulation predictions, even for extremely thin film thicknesses where no bulk liquid region separates the wall-affected region from the interfacial region.

The model analysis developed here to explore the effects of liquid layering at the solid-liquid interface predicts that layering tends to slightly reduce the vapor pressure below that predicted by the conventional disjoining theory for a specified film thickness. The modified theory was found to not agree as well as the conventional theory with vapor pressure predictions of our MD simulations for the same film thickness. Because this modified theory adopts an extreme treatment of the near-wall layered region as a solid phase, it is expected to provide an upper bound for the effect of layering on the equilibrium vapor pressure. Even for this extreme model, the effect on vapor pressure is small, suggesting that for a real system, in which the wall region molecules have some mobility, the effects of the wall layer would be even less. Overall, the results imply that liquid layering has little, if any, effect on the equilibrium vapor pressure.

Accurate prediction of the effects of intermolecular attractive forces and associated disjoining pressure effects on equilibrium saturation properties is an important element of the analysis of transport for thin liquid films on the passage walls in micro evaporators, micro condensers, and micro heat pipes. Because of the linkage between vapor pressure and saturation temperature, the variation of vapor pressure with liquid film thickness strongly impacts the effectiveness of transport during vaporization or condensation at the interface of thin liquid films in micropassages.

Although conventional disjoining pressure theory is based on a simplistic treatment that ignores the presence of the wall-affected region and the interfacial region in the film, the results of our MD simulations and analysis indicate that, for extremely thin liquid films, conventional disjoining pressure theory nevertheless provides a prediction of the variation of vapor pressure with film thickness that is consistent with MD simulation predictions. These results enhance the credibility of models of transport in micro evaporators and micro condensers that make use of conventional disjoining pressure theory to predict local saturation conditions.

Acknowledgment

Support for this research under NSF Grant No. CTS-0456982 is gratefully acknowledged. MD simulations were performed using the Millennium workstation cluster at UC Berkeley.

Nomenclature

A_{ll} = liquid-liquid Hamaker constant
A_{ls} = liquid-solid Hamaker constant
c_i = speed of molecule i
$C_{\phi,ff}$ = fluid-fluid attractive force potential coefficient
$C_{\phi,sf}$ = solid-fluid attractive force potential coefficient
D_f = fluid molecule effective diameter
D_m = mean effective molecular diameter
D_s = solid molecule effective diameter
$\boldsymbol{F}$ = molecular force vector
$\hat{g}_l$ = molar specific Gibbs function of liquid
J = vapor boundary molecular flux
k_B = Boltzmann constant
m = molecular mass
N = number of molecules in system
N_A = Avogadro's number
P = pressure
P_d = disjoining pressure
P_l = liquid pressure
P_{ve} = vapor pressure
P_{sat} = saturation pressure for bulk equilibrium
$\overline{R}$ = universal gas constant
$\hat{s}$ = molar entropy
T = temperature
T_c = critical temperature
T_r = reduced temperature$=T/T_c$
δ_f = liquid film thickness
δ_w = wall-affected region thickness
$\hat{v}_l$ = liquid molar specific volume
v_z = z-direction molecular velocity component
Φ_{fmf} = potential energy for one fluid molecule interacting with all wall molecules
ϕ_{ff} = fluid-fluid intermolecular potential
ϕ_{LJ} = Lennard-Jones 6-12 intermolecular potential
ϕ_{sf} = solid-fluid intermolecular potential
$\hat{\rho}$ = molar density
ρ_f = Fluid molecular number density
$\rho_{l,\infty}$ = molecular number density of bulk saturated liquid
$\rho_{v,\infty}$ = molecular number density of bulk saturated vapor
ρ_s = solid wall molecular number density
$\sigma_{LJ}, \varepsilon_{LJ}$ = Lennard-Jones 6-12 potential length and energy parameters
$\hat{\mu}_l$ = liquid molar chemical potential
$\hat{\mu}_{l,sat}$ = molar chemical potential of bulk liquid at saturation
$\hat{\mu}_v$ = vapor molar chemical potential
$\hat{\mu}_{v,sat}$ = molar chemical potential of bulk vapor at saturation

References

[1] Israelachvili, J., 1992, *Intermolecular & Surface Forces*, 2nd ed., Academic, London.
[2] Kandlikar, S. G., 2002, "Fundamental Issues Related to Flow Boiling in Minichannels and Microchannels," Exp. Therm. Fluid Sci., **26**, pp. 389–407.
[3] Peterson, G. P., Duncan, A. B., and Weichold, M. H., 1993, "Experimental Investigation of Micro Heat Pipes Fabricated in Silicone Wafers," ASME J. Heat Transfer, **115**, pp. 751–756.
[4] Gerner, F. M., Badran, B., Henderson, H. T., and Ramadas, P., 1994, "Silicon-Water Micro Heat Pipes," Photochemistry, **2**, pp. 90–97.
[5] Pettersen, J., 2004, "Flow Vaporization of CO_2 in Microchannel Tubes," Exp. Therm. Fluid Sci., **28**, pp. 111–121.
[6] Park, K., and Lee, K-S., 2003, "Flow and Heat Transfer Characteristics of the Evaporating Extended Meniscus in a Micro-Capillary Channel," Int. J. Heat Mass Transfer, **46**, pp. 4587–4594.
[7] Wayner, P. C., Jr., Kao, Y. K., and LaCroix, L. V., 1976, "The Interline Heat-Transfer Coefficient of an Evaporating Wetting Film," Int. J. Heat Mass Transfer, **19**, pp. 487–492.
[8] Xu, X., and Carey, V. P., 1991, "Film Evaporation From a Micro-Grooved

Surface — An Approximate Heat Transfer Model and Its Comparison With Experimental Data," J. Thermophys. Heat Transfer, **4**, pp. 512–520.

[9] Stephan, P., and Busse, C. A., 1992, "Analysis of the Heat Transfer Coefficient of Grooved Heat Pipe Evaporator Walls," Int. J. Heat Mass Transfer, **35**, pp. 383–391.

[10] Swanson, L., and Herdt, G. C., 1992, "Model of the Evaporating Meniscus in a Capillary Tube," ASME J. Heat Transfer, **114**, pp. 434–441.

[11] Swanson, L., and Peterson, G. P., 1994, "The Evaporating Extended Meniscus in a V-Shaped Channel," J. Thermophys. Heat Transfer, **8**, pp. 172–181.

[12] Hallinan, K. P., Chebaro, H. C., Kim, S. J., and Change, W. S., 1994, "Evaporation From an Extended Meniscus for Nonisothermal Interfacial Conditions," J. Thermophys. Heat Transfer, **8**, pp. 709–716.

[13] Khrustalev, D., and Faghri, A., 1995, "Heat Transfer During Evaporation on Capillary Grooved Structures of Heat Pipes," ASME J. Heat Transfer, **117**, pp. 740–747.

[14] Wemhoff, A. P., and Carey, V. P., 2004, "Exploration of Nanoscale Features of Thin Liquid Films on Solid Surfaces Using Molecular Dynamics Simulations," Paper No. IMECE2004-59429, *Proceedings of the 2004 ASME International Mechanical Engineering Conference and RD&D Exposition*.

[15] Box, G. E. P., and Mueller, M. E., 1958, "A Note on the Generation of Random Normal Deviates," Ann. Math. Stat., **29**, pp. 610–611.

[16] Toxvaerd, S., 1981, "The Structure and Thermodynamics of a Solid-Fluid Interface," J. Chem. Phys., **74**, pp. 1998–2005.

[17] Rowley, L. A., Nicholson, D., and Parsonage, N. G., 1976, "Grand Ensemble Monte Carlo Studies of Physical Adsorption. I. Results for Multilayer Adsorption of 12-6 Argon in the Field of a Plane Homogeneous Solid," Mol. Phys., **31**, pp. 365–387.

[18] Wendland, M., Salzmann, S., Heinbuch, U., and Fischer, J., 1989, "Born-Green-Yvon Results for Adsorption of a Simple Fluid on Plane Walls," Mol. Phys., **67**, pp. 161–172.

[19] Carey, V. P., 1999, *Statistical Thermodynamics and Microscale Thermophysics*, Cambridge U. P., Cambridge.

[20] Andersen, H. C., 1980, "Molecular Dynamics at Constant Pressure and/or Temperature," J. Chem. Phys., **72**, pp. 2384–2393.

[21] Frenkel, D., and Smit, B., 2002, *Understanding Molecular Simulation; From Algorithms to Applications*, 2nd ed., Academic, San Diego.

[22] Carey, V. P., and Hawks, N. E., 1995, "Stochastic Modeling of Molecular Transport to an Evaporating Microdroplet in a Superheated Gas," ASME J. Heat Transfer, **117**, pp. 432–439.

[23] Allen, M. P., and Tildesley, D. J., 1987, *Computer Simulation of Liquids*, Clarendon, Oxford.

[24] Liu, K. S., 1974, "Phase Separation of Lennard-Jones Systems: A Film in Equilibrium with Vapor," J. Chem. Phys., **60**, pp. 4226–4230.

[25] Wendland, M., Heinbuch, U., and Fischer, J., 1989, "Adsorption of Simple Gas Mixtures on a Plane Wall: Born-Green-Yvon Results for Structure, Adsorption Isotherms and Selectivity," Fluid Phase Equilib., **48**, pp. 259–277.

[26] American Society of Heating, Refrigerating, and Air-conditioning Engineers, 2001, *ASHRAE Fundamentals Handbook*, ASHRAE, Atlanta.

[27] Dunikov, D. O., Malyshenko, S. P., and Zhakhovskii, V. V., 2001, "Corresponding States Law and Molecular Dynamics Simulations of the Lennard-Jones Fluid," J. Chem. Phys., **115**, pp. 6623–6631.

[28] Lotfi, A., Vrabec, J., and Fischer, J., 1992, "Vapour Liquid Equilibria of the Lennard-Jones Fluid from the NPT Plus Test Particle Method," Mol. Phys., **76**, pp. 1319–1333.

[29] Weng, J. G., Park, S., Lukes, J. R., and Tien, C. L., 2000, "Molecular Dynamics Investigation of Thickness Effect on Liquid Films," J. Chem. Phys., **113**, pp. 5917–5923.

[30] Carey, V. P., 1992, *Liquid-Vapor Phase Change Phenomena*, Taylor and Francis, New York.

[31] Xue, L., Keblinski, P., Phillpot, S. R., Choi, S. U.-S., and Eastman, J. A., 2004, "Effect of Liquid Layering at the Liquid-Solid Interface on Thermal Transport," Int. J. Heat Mass Transfer, **47**, pp. 4277–4284.

Numerical Study of an Evaporating Meniscus on a Moving Heated Surface

Abhijit Mukherjee[1]
e-mail: mukherje@mtu.edu

Satish G. Kandlikar

Thermal Analysis and Microfluidics Laboratory,
Department of Mechanical Engineering,
Rochester Institute of Technology,
Rochester, NY 14623

The present study is performed to numerically analyze an evaporating meniscus bounded between the advancing and receding interfaces on a moving heated surface. The numerical scheme developed for analyzing interface motion during bubble growth in pool boiling has been applied. A column of liquid is placed between a nozzle outlet and a moving wall, and calculations are done in two dimensions with a fixed distance between the nozzle and the wall. The results show that the wall velocity creates a circulation near the meniscus base, resulting in transient heat conduction. The local wall heat transfer is found to vary significantly along the meniscus base, the highest being near the advancing contact line. The heat transfer coefficient is found to depend on the advancing contact angle and wall velocity but is independent of the wall superheat. Reasonable agreement is observed when the meniscus profile and heat transfer results obtained from the numerical simulation are compared to the experimental data. [DOI: 10.1115/1.2397093]

Keywords: meniscus, boiling

Introduction

Stationary Evaporating Meniscus. Figure 1 shows the details of an extended evaporating meniscus on a heated surface. Three regions are identified here:

1. *Non-Evaporating Adsorbed Thin-Film Region*. In this region, liquid is adsorbed on the heater surface and forms a nonevaporating layer. The molecular forces have controlling influence, and the disjoining pressure reduces the pressure in the liquid and enables it to reside in a supersaturated liquid state.
2. *Evaporating Thin-Film Region*. Evaporation occurs at the liquid-vapor interface, and liquid is fed from the bulk liquid through the intrinsic meniscus region. Here both the disjoining pressure and the capillary forces play a role. It is often referred to as the "microlayer."
3. *Intrinsic Meniscus Region*. The fluid mechanics in this region is governed by the conventional equation of capillarity.

Derjaguin [1] provided the basis of the thin film behavior by showing that the net effect, at the macroscopic level, of solid-liquid interactions is a reduction of pressure of the liquid interface relative to the pressure of the equilibrium vapor phase. He argued that the disjoining action could explain the deviation from the laws of hydrostatics that exists in a thin wetting film. Later Derjaguin et al. [2] developed an analytical theory to show that the rate of evaporation from a capillary does not depend only on the vapor diffusion through the gas but also on the film transport caused by the film thickness gradient. Potash and Wayner [3] studied the transport processes occurring in a two-dimensional evaporating extended meniscus, where the fluid flow resulted from both capillarity and disjoining pressure and calculated the heat flux profile for a given plate superheat. The results showed that the heat flux reached maximum in the evaporating thin film portion of the extended meniscus.

Nucleate Boiling. Nucleate pool boiling is typically characterized by the growth and departure of vapor bubbles on a heated surface. During its growth cycle, the bubble base expands initially, stays constant for some time, and then contracts as the bubble departs. The high heat flux during nucleate boiling is often attributed to the wall heat transfer near the bubble base, which includes conduction to the liquid and its subsequent evaporation at the liquid-vapor interface. Investigators have extensively studied wall heat transfer near the bubble base by measuring the local transient surface temperatures and confirmed the existence of very high local wall heat flux. Moore and Mesler [4] measured the surface temperatures during nucleate boiling with a special thermocouple having an extremely rapid response time. The fluid boiled was water at atmospheric pressure and at saturation temperature. During nucleate boiling, the surface temperature was observed to fluctuate with time. Occasionally, the surface temperature would drop rapidly and then return to its previous level. The authors argued that only the theory of existence of a vaporizing microlayer at the base of the bubbles could explain these observations. Labunstov [5] proposed an analytical model explaining the mechanism of growth of vapor bubbles on a heated surface. He argued that the growth of bubbles developing on the heated surface must depend primarily on the heat flux supplied by the heated surface to the bubble surface close to the base of the bubble. He also developed a vapor bubble growth expression and compared it to available experimental data. The model had limited success. Mikic and Rohsenow [6] developed a correlation for pool boiling. The correlation assumed that the main mechanism of heat transfer in nucleate boiling was transient heat conduction to, and subsequent replacement of, the superheated layer around nucleation sites associated with bubble departure. The transient conduction problem was modeled as conduction to a semi-infinite plate with a step change in temperature at the surface. The correlation was checked with available experimental data and the results were found to be satisfactory. Koffman and Plesset [7] obtained microlayer thickness measurements in water, for small, short-lived bubbles characteristic of highly subcooled nucleate boiling. The detailed measurements were obtained using laser interferometry, combined with high-speed video. The authors concluded that microlayer evaporation alone cannot account for the increased heat transfer rates observed in highly subcooled nucleate boiling, and microconvection must play at least an equal role.

---

[1] Corresponding author.

Contributed by the Heat Transfer Division of ASME for publication in the JOURNAL OF HEAT TRANSFER. Manuscript received August 31, 2005; final manuscript received August 3, 2006. Review conducted by Raj M. Manglik.

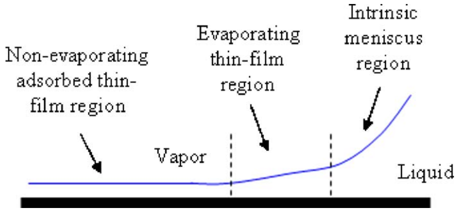

Fig. 1 Details of a stationary evaporating meniscus region

Moving Evaporating Meniscus. Kandlikar et al. [8] developed a new meniscus configuration to visualize the advancing and receding fronts of a liquid vapor interface. It consists of a circular evaporating meniscus on a smooth heated moving copper surface. The meniscus profile is very similar to the contact region at the base of a growing vapor bubble as explained in Fig. 2. Figure 2(*a*) shows a typical nucleating bubble on a heated surface, and Fig. 2(*b*) shows an evaporating meniscus on a moving wall. When the bubble base of a nucleating bubble expands, it is similar to the receding contact line of the meniscus, and when the bubble base shrinks, it is comparable to the advancing contact region of the meniscus. Kandlikar et al. [8] obtained the meniscus shape and heat transfer rates as functions of heater temperature and surface velocity. They found that at lower velocities, the heat flux was relatively insensitive to velocity, but it increased almost linearly with velocity at higher velocities. The results indicated that transient heat conduction played a major role in the heat transfer process to a moving meniscus. Photographs of the meniscus were taken with high-speed cameras using microscopic lens, and no presence of thin films was detected at the edge of either the advancing or the receding contact regions.

Objective

The present numerical study is performed to obtain the velocity and temperature field inside an evaporating meniscus on a moving heated surface. Calculations are done for different values of wall velocity, wall superheat, and advancing and receding contact angles. The main objective is to ascertain the wall heat transfer mechanism in the moving and evaporating meniscus and evaluate its dependence on the above parameters.

The numerical calculations have been done in two dimensions. It was observed from experiments that the moving evaporating meniscus was primarily a two-dimensional (2D) phenomenon since the predominant motion in the liquid was in the plane that corresponded to the movement of the heated plate. Preliminary numerical calculations were run with both 2D and three-dimensional (3D) considerations. The 2D numerical results were found to agree well with the experimental data. Thus, 3D simulations were not pursued because they required more computation time and did not provide any significant additional information.

Numerical Model

Son et al. [9] developed a two-dimensional numerical model of growth and departure of single vapor bubbles during nucleate pool boiling. They used the level-set technique to implicitly capture the liquid vapor interface. Mukherjee and Dhir [10] extended the model to three dimensions and studied merger and departure of multiple bubbles during nucleate pool boiling. The present calculations are done using a similar model, to study the evaporating meniscus on a moving heated plate.

Method. The numerical analysis is done by solving the complete incompressible Navier-Stokes equations and using the SIMPLER method [11], which stands for semi-implicit method for pressure-linked equations revised. A pressure field is extracted from the given velocity field. The continuity equation is turned into an equation for the pressure correction. During each iteration, the velocities are corrected using velocity-correction formulas. The computations proceed to convergence via a series of continuity satisfying velocity fields. The algebraic equations are solved using the line-by-line technique, which uses TDMA (tridiagonal matrix algorithm) as the basic unit. The speed of convergence of the line-by-line technique is further increased by supplementing it with the block-correction procedure [12]. A multigrid technique is used to solve the pressure fields.

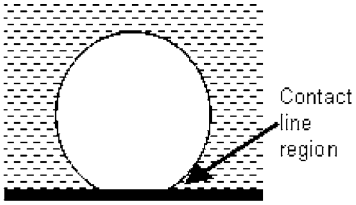

(a) Nucleating bubble

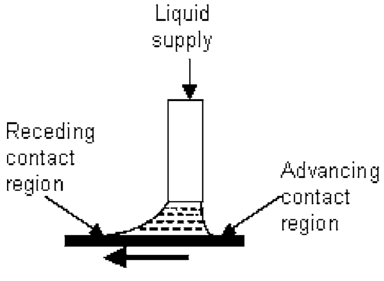

(b) Evaporating and moving meniscus

Fig. 2 Similarity between a nucleating bubble and a moving evaporating meniscus in the contact line region

Sussman et al. [13] developed a level set approach where the interface was captured implicitly as the zero level set of a smooth distance function. The level-set function was typically a smooth function, denoted as ϕ. This formulation eliminated the problems of adding/subtracting points to a moving grid and automatically took care of merging and breaking of the interface. The present analysis is done using this level-set technique.

The liquid vapor interface is identified as the zero level set of a smooth distance function ϕ. The level-set function ϕ is negative outside the meniscus and positive inside the meniscus. The interface is located by solving the level-set equation. A fifth-order WENO (weighted, essentially nonoscillatory) scheme is used for left-sided and right-sided discretization of ϕ [14]. Although ϕ is initially a distance function, it will not remain so after solving the level-set equation. Maintaining ϕ as a distance function is essential for providing the interface with a width fixed in time. This is achieved by reinitialization of ϕ. A modification of Godunov's method is used to determine the upwind directions. The reinitialization equation is solved in fictitious time after each fully complete time step. With $\Delta\tau = d/2u_0$, ten τ steps are taken with a third-order TVD (total variation diminishing) Runge Kutta method.

Governing Equations. Momentum equation:

$$\rho\left(\frac{\partial \vec{u}}{\partial t} + \vec{u}\cdot\nabla\vec{u}\right) = -\nabla p + \rho\vec{g} - \rho\beta_T(T - T_{\text{sat}})\vec{g} - \sigma\kappa\nabla H + \nabla\cdot\mu\nabla\vec{u} + \nabla\cdot\mu\nabla\vec{u}^T \tag{1}$$

Energy equation:

$$\rho C_p\left(\frac{\partial T}{\partial t} + \vec{u}\cdot\nabla T\right) = \nabla\cdot k\nabla T \quad \text{for} \quad \phi > 0$$

$$T = T_{\text{sat}} \quad \text{for} \quad \phi \leqslant 0 \tag{2}$$

Continuity equation:

$$\nabla \cdot \vec{u} = \frac{\vec{m}}{\rho^2} \cdot \nabla \rho \tag{3}$$

The curvature of the interface is defined in terms of level-set distance function as

$$\kappa(\phi) = \nabla \cdot \left(\frac{\nabla \phi}{|\nabla \phi|} \right) \tag{4}$$

The mass flux of liquid evaporating at the interface is given by

$$\vec{m} = \frac{k_l \nabla T}{h_{fg}} \tag{5}$$

The vapor velocity at the interface due to evaporation is calculated as

$$\vec{u}_{\text{evp}} = \frac{\vec{m}}{\rho_v} = \frac{k_l \nabla T}{\rho_v h_{fg}} \tag{6}$$

To prevent instabilities at the interface [13], the density and viscosity are defined as

$$\rho = \rho_v + (\rho_l - \rho_v) H \tag{7}$$

$$\mu = \mu_v + (\mu_l - \mu_v) H \tag{8}$$

H is the Heaviside function

$$H = 1 \quad \text{if} \quad \phi \geqslant +1.5d$$

$$H = 0 \quad \text{if} \quad \phi \leqslant -1.5d$$

$$H = 0.5 + \frac{\phi}{3d} + \frac{\sin\left(\frac{2\pi\phi}{3d}\right)}{2\pi} \quad \text{if} \quad |\phi| \leqslant 1.5d \tag{9}$$

where d is the grid spacing.

Since the vapor is assumed to remain at saturation temperature, the thermal conductivity is given by

$$k = k_l H^{-1} \tag{10}$$

Level set equation is solved as

$$\phi_t + (\vec{u} + \vec{u}_{\text{evp}}) \cdot \nabla \phi = 0 \tag{11}$$

After every time step, the level-set function ϕ is reinitialized as

$$\phi_t = S(\phi_0)(1 - |\nabla \phi|) u_0$$

$$\phi(x,0) = \phi_0(x) \tag{12}$$

S is the sign function which is calculated as

$$S(\phi_0) = \frac{\phi_0}{\sqrt{\phi_0^2 + d^2}} \tag{13}$$

Computational Domain. Figure 3 shows the computational domain. The domain is 4.95 × 0.99 nondimensional units in size. Cartesian coordinates are used with uniform grid.

The domain consists of two parallel plates with an opening in the top wall for the liquid to enter. The bottom wall moves in the positive x direction. The two other sides are outlets. The number of computational cells in the domain are 400 × 80 (i.e., 80 grids are used per $0.99 l_0$).

The working fluid is saturated water at atmospheric pressure. The liquid and vapor properties are taken at 373 K.

Scaling Factors. The distance and velocities are nondimensionalized with the length scale l_0 and the velocity scale u_0. For all calculations, l_0 is assumed 1 mm, since 0.99 mm is taken to be the height of the meniscus and also the width of the liquid inlet. The nondimensional temperature is defined as

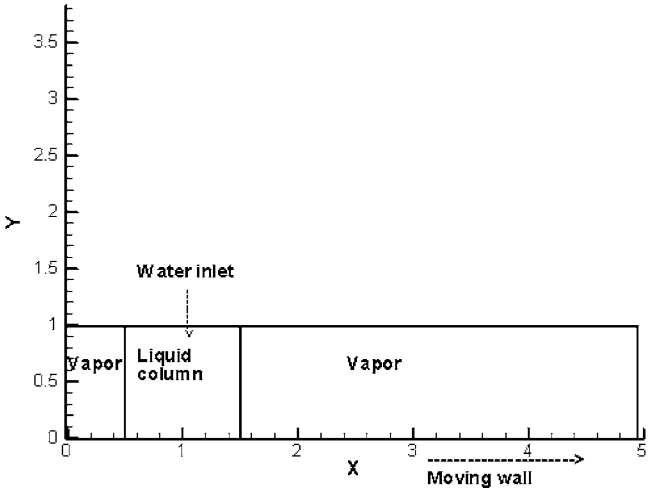

Fig. 3 Computational domain

$$T^* = \frac{T - T_{\text{sat}}}{T_w - T_{\text{sat}}} \tag{14}$$

Initial Conditions. The liquid column is initially placed with center at $x^* = 1$ and a width of 0.99 mm. Thus, the initial width of the liquid column is the same as the distance between the plates. Saturated vapor fills the rest of the domain and this is specified to simulate nucleate boiling conditions where evaporation takes place in the presence of pure vapor. All initial velocities inside the domain are set to zero. The liquid and vapor temperatures are set to the saturation temperature ($T^* = 0$). The wall temperature is set to the specified superheat ($T^* = 1$).

Boundary Conditions. At the bottom wall ($y^* = 0$),

$$v^* = 0$$

$$u^* = 1$$

$$T^* = 1; \quad \phi_y = -\cos \varphi \tag{15}$$

where φ is the contact angle.

At the top of the domain ($y^* = 0.99$),

$$v^* = -V_{\text{in}}^* \quad \text{if} \quad \phi > 0$$

$$v^* = 0 \quad \text{if} \quad \phi \leqslant 0$$

$$u^* = 0; \quad T^* = 0; \quad \phi_y = 0 \tag{16}$$

At the outlets ($x^* = 0$ and $x^* = 4.95$),

$$u_x^* = 0; \quad v_x^* = 0; \quad T_x^* = 0; \quad \phi_x = 0 \tag{17}$$

The inlet liquid velocity V_{in} for all cases is set to 0.00034 m/s. The simulation conditions were chosen to correspond to the experimental data presented by Kandlikar et al. [8]. Constant wall temperature is assumed at the bottom wall; it has been shown by Kandlikar et al. [8] that it is a reasonable assumption for a surface with high thermal diffusivity, such as copper.

Microlayer Evaporation. Several previous studies [9,10] of single or multiple vapor bubbles growing on a heated wall have included the effect of microlayer evaporation. Son et al. [9] reported microlayer contribution to be ~20% for a certain set of calculations. Recently, Dhir [15] reported that 50% of the energy from the wall is transferred by transient conduction, 35% by natu-

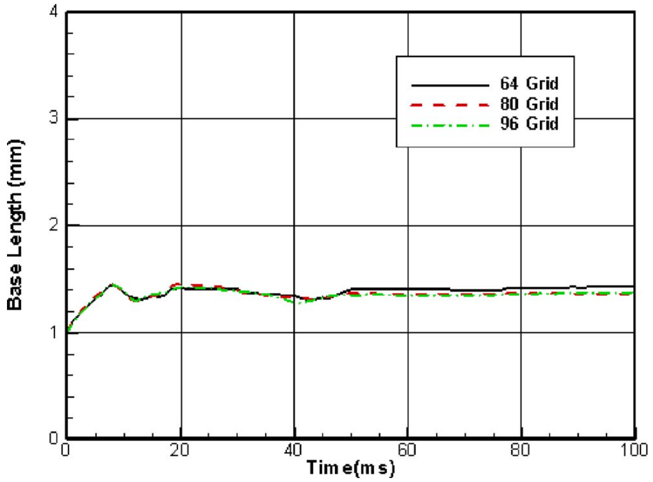

Fig. 4 Variation of meniscus base length with time and grid independence check (ACA—61; RCA—48; SH—5 K; WV—0.1 m/s)

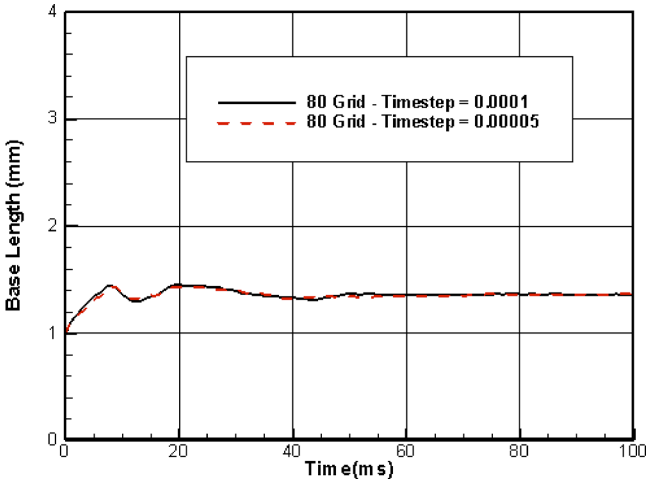

Fig. 5 Time-step independence check (ACA—61; RCA—48; SH—5 K; WV—0.1 m/s)

ral convection and 15% by microlayer evaporation. Since the effect of microlayer is seen to be small and no reliable experimental data on microlayer thickness under a bubble base are available, the present simulation is carried out to highlight the effect of liquid motion and transient conduction at the base of the meniscus. Hence, the effect of microlayer evaporation has been excluded from the calculations.

Results

Numerical simulation is carried out for different values of advancing and receding contact angles, wall superheat (SH) and wall velocity (WV). The mean value of contact angle used are advancing contact angle (ACA)=61 deg and receding contact angle (RCA)=48 deg, corresponding to experimental conditions during nucleate pool boiling [16]. Calculations are carried out by increasing ACA to 80 deg and decreasing RCA to 30 deg. The wall superheat is varied as 2 K, 5 K, and 8 K, which is typical during partial nucleate pool boiling. The wall velocity is varied as 0.05 m/s, 0.1 m/s, and 0.15 m/s, which are again observed rate of change of bubble base diameter with time during partial nucleate pool boiling [16].

Base Case. Figure 4 shows the variation of meniscus base length as a function of time for the case with ACA=61 deg, RCA=48 deg, SH=5 K, and WV=0.1 m/s. We will term this case as the *base case*. At time 0 ms, the base length is 0.99 mm, which is specified as the initial condition. The plot shows initial fluctuation of the meniscus base length as the calculations proceed, which becomes steady after 50 ms attaining a length of 1.4 mm.

A convergence check is carried out with various grid sizes to demonstrate grid independence. To optimize computation costs 80 grids per unit length is chosen for all calculations. Figure 4 shows the variation of meniscus base length with time for 64, 80, and 96 grids. After initial fluctuations subside around 50 ms, the results for 80 and 96 grids show very little difference. This confirms that the calculations with 80 grids provide sufficient resolution to capture details of high heat transfer region near the wall.

Figure 5 demonstrates the time-step independence. The *base case* with 80 grids per unit length is calculated with two different time steps of 0.0001 and 0.00005. The plot of meniscus base length against time shows little difference in the results. Thus, the time step of 0.0001 is used for all the calculations.

Figure 6 shows the velocity field in the meniscus for the *base case*. The wall velocity has caused the meniscus to become extended in one direction. The velocity vectors in the vapor are much larger than in the liquid due to the density difference. The streamlines in the liquid show a circulating flow inside the meniscus. Evaporation takes place at the liquid-vapor interface indicated by the jets of vapor leaving the interface. However, this evaporation is comparatively much more intense at the receding contact line region. Calculations show that more than 99% of the total evaporation takes place on the receding side. The reason for this can be explained by analyzing the temperature field inside the meniscus.

The thermal boundary layer inside the meniscus for the *base case* is shown in Fig. 7. Temperature contours are plotted for T^* at intervals of 0.1. The plot shows more superheated liquid near the receding liquid-vapor interface compared to the advancing interface. The liquid is dragged in the positive *x* direction near the wall due to the wall movement and gets heated up due to heat transfer from the wall. The circulation of liquid (shown in Fig. 6) causes the hotter liquid to move up along the receding interface near the receding contact line, increasing evaporation along the interface. The incoming cooler saturated liquid comes down near the advancing contact line suppressing evaporation at the interface in that region. The crowding of isotherms near the wall at the advancing contact region indicates area of high wall heat transfer. A part of the superheated liquid circulates near the wall at the reced-

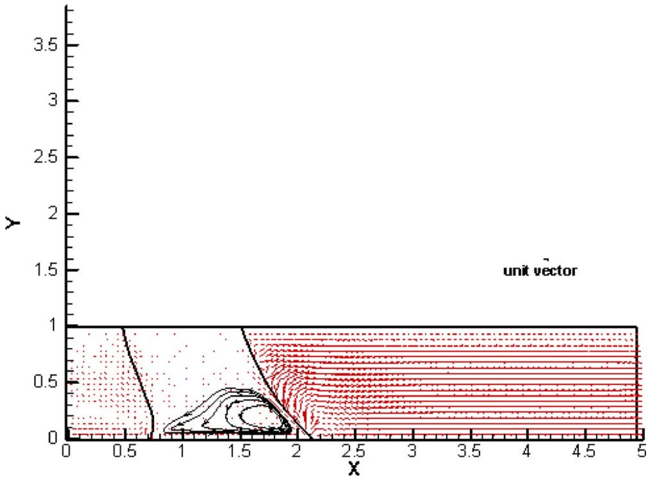

Fig. 6 Liquid circulation inside meniscus (ACA—61; RCA—48; SH—5 K; WV—0.1 m/s)

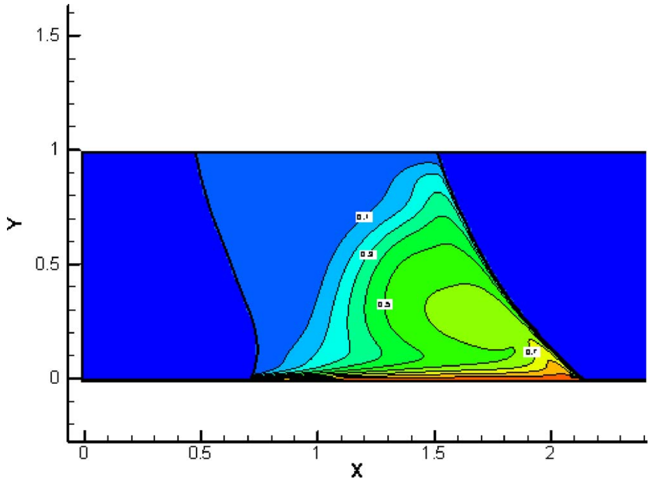

Fig. 7 Temperature field inside meniscus (ACA—61; RCA—48; SH—5 K; WV—0.1 m/s)

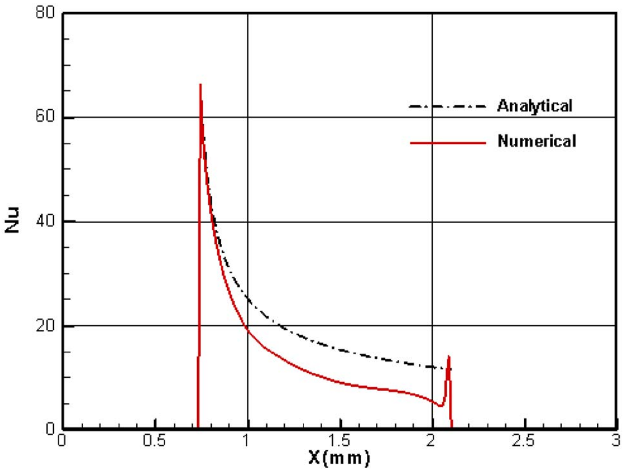

Fig. 8 Variation of heat transfer coefficient along the meniscus base (ACA—61; RCA—48; SH—5 K; WV—0.1 m/s)

ing contact region thereby hindering local wall heat transfer.

Figure 8 shows the local Nu variation along the meniscus base for the *base case*.

The local heat transfer coefficient h is obtained from

$$h = \frac{-k_l \left.\dfrac{\partial T}{\partial y}\right|_{\text{wall}}}{T_w - T_{\text{sat}}} \text{ at the meniscus base} \tag{18}$$

The local Nusselt number at the meniscus base is defined as

$$\text{Nu} = \frac{hl_0}{k_l} \tag{19}$$

The solid line shows the results obtained from the numerical calculations. The highest heat transfer is seen to occur at the advancing contact region. This is due to transient conduction as cooler saturated liquid comes down along the advancing interface near the heated wall. The heat transfer steadily decreases from that end until it reaches the receding contact line. There is a jump in wall heat transfer at the receding contact line. This is where the distance between the liquid-vapor interface and the wall becomes small, causing a steep temperature gradient at the wall.

The heat transfer near the advancing edge of the meniscus can be calculated analytically using a transient heat conduction model. The heater surface comes in contact with the liquid, which can be assumed to be a semi-infinite medium during the initial contact with the heater surface. In the present modeling, a constant heater wall temperature is assumed. The instantaneous heat flux following the initial contact with a semi-infinite medium (assuming water at saturation temperature) under the constant surface temperature case is given by

$$q'' = \frac{k(T_w - T_{\text{sat}})}{\sqrt{\pi \alpha t}} \tag{20}$$

The heat transfer coefficient h is calculated as

$$h = \frac{k}{\sqrt{\pi \alpha t}} \tag{21}$$

The instantaneous value of the Nusselt number near the advancing edge of the meniscus is calculated using

$$\text{Nu} = \frac{hl_0}{k} = \frac{l_0}{\sqrt{\pi \alpha t}} \tag{22}$$

$$t = \frac{x}{u_{\text{wall}}} \tag{23}$$

The distance along the meniscus base x is calculated starting from the location of the advancing contact region.

The analytical results for the base case are plotted in Fig. 8 as a dashed line along with the numerical results discussed earlier. It is seen that the numerical results and the results from the transient conduction model are in excellent agreement at the advancing contact region. This confirms that transient conduction is, indeed, the primary mechanism of heat transfer from the wall at the leading edge of the meniscus base. However, with increase in distance from the leading edge, the calculated heat transfer is found to be less than the analytical results. This is due to the fact that the circulation of liquid inside the meniscus causes a mixing effect. This mixing increases the average temperature of the liquid, which, in turn, reduces the wall heat transfer.

Comparison to Experimental Data. Figure 9 compares the meniscus shape obtained from numerical calculations to experimental data. Figure 9(*a*) shows the experimental observation of Kandlikar et al. [8]. The measured experimental parameters are as follows: ACA=110 deg, RCA=25 deg, SH=5.5 K, WV =0.241 m/s. The nozzle inside and outside diameters are 1.08 mm and 1.65 mm, respectively; the distance between the nozzle and the moving copper block is 0.9 mm, and the nozzle liquid flow rate is 0.016 mL/min. Numerical simulation was carried out for the moving and evaporating meniscus with the above conditions and the resultant meniscus profile is shown in Fig. 9(*b*).

In the experiment, even though the water flows through 1.08 mm i.d. of the nozzle, the meniscus clings to the nozzle mouth and the effective diameter becomes equal to the outside diameter of 1.65 mm. This can be clearly seen in Fig. 9(*a*). In the simulation, the liquid inlet was specified as 1.08 mm wide, which is the same as in the experiment, but the liquid interfaces at the top wall were not anchored to any particular location. At steady state, the liquid spread on the top wall and reached a width of 1.8 mm, as seen in Fig. 9(*b*).

Comparing Figs. 9(*a*) and 9(*b*), it can be seen that the meniscus profiles agree well between the numerical simulation and the experimental observation. The base length of the meniscus in the experiment is 2.9 mm, whereas the base length obtained from the numerical simulation is 3.1 mm.

Effect of Advancing and Receding Contact Angles. Figure 10 plots the averaged Nusselt number at the base of the meniscus as a function of time for different values of advancing and receding contact angles. Three cases are compared in the plot: (i) the *base case*, (ii) an increased advancing contact angle (80 deg) from the base case, and (iii) a decreased receding contact angle (30 deg)

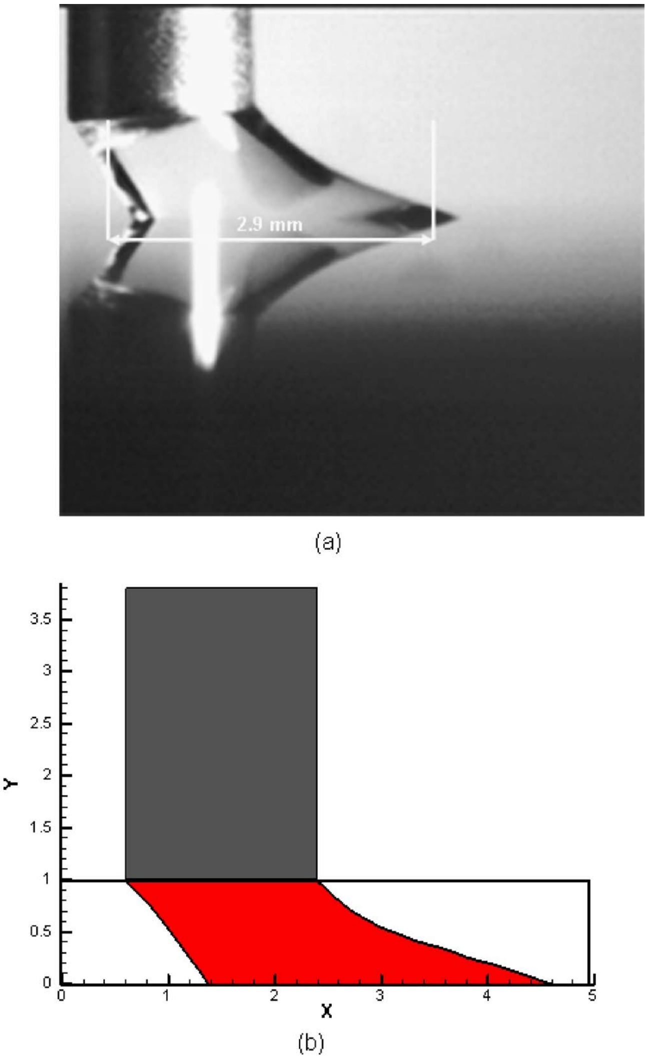

Fig. 9 Comparison of moving meniscus shapes: (*a*) Experiment and (*b*) numerical simulation

from the base case. The averaged Nusselt number $(\overline{\mathrm{Nu}})$ is calculated based on the line-averaged heat transfer coefficient $(\bar{h})$ at the wall given by

$$\bar{h} = \frac{1}{L}\int_0^L h\,dL \tag{24}$$

where L is the meniscus base length and local h is obtained from Eq. (18).

The average Nusselt number at the meniscus base is defined as

$$\overline{\mathrm{Nu}} = \frac{\bar{h} l_0}{k_l} \tag{25}$$

The $\overline{\mathrm{Nu}}$ is very high initially as the saturated liquid is in contact with the superheated wall. The wall heat transfer decreases as the thermal boundary layer thickens inside the liquid with time and reaches a steady value for all three cases after 60 ms. It can be seen that the $\overline{\mathrm{Nu}}$ increases with increase in advancing contact angle but is unaffected with the change in the receding contact angle. As the advancing contact angle is increased from 61 deg to 80 deg, it becomes easier for the cooler incoming saturated liquid to reach the superheated wall thereby facilitating transient heat conduction at the advancing contact region. However, the layer of trapped superheated liquid in the receding contact region has remained largely unaffected by change in the contact angle from 48 deg to 30 deg. Since bulk of the heat transfer at the meniscus base takes place at the advancing contact region as explained earlier in the paper, overall heat transfer at the meniscus base has improved with an increase in the advancing contact angle but has remained unaffected by the change in the receding contact angle.

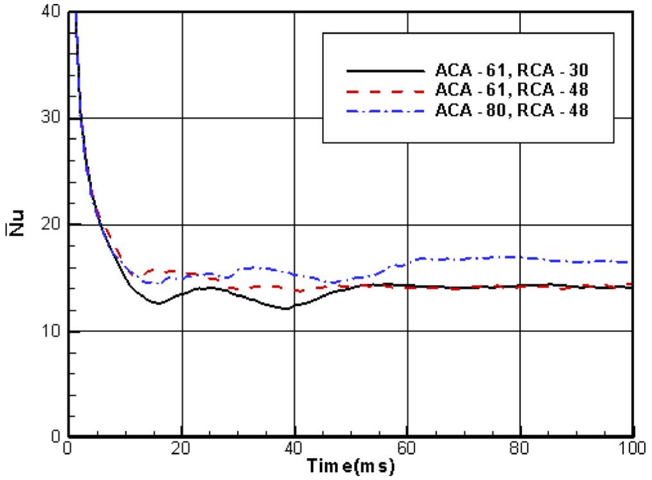

Fig. 10 Comparison of average heat transfer coefficient at the meniscus base as a function of contact angle (SH—5 K; WV—0.1 m/s)

Effect of Wall Superheat. Figure 11 compares the $\overline{\mathrm{Nu}}$ at the meniscus base for different values of wall superheat. Three cases are plotted: (i) the *base case*, (ii) increased wall superheat of 8 K, and (iii) decreased wall superheat of 2 K. The results show that the wall heat transfer coefficient remains unaffected with changes in the wall superheat, with constant properties assumed in the calculations.

Effect of Wall Velocity. Figure 12 shows the effect of the wall velocity on the average wall heat transfer coefficient. Results from three cases are plotted: (i) the *base case*, (ii) increased wall velocity of 0.15 m/s, and (iii) decreased wall velocity of 0.05 m/s. The nondimensional averaged wall heat transfer coefficient $\overline{\mathrm{Nu}}$ is found to increase with increase in the surface velocity, which

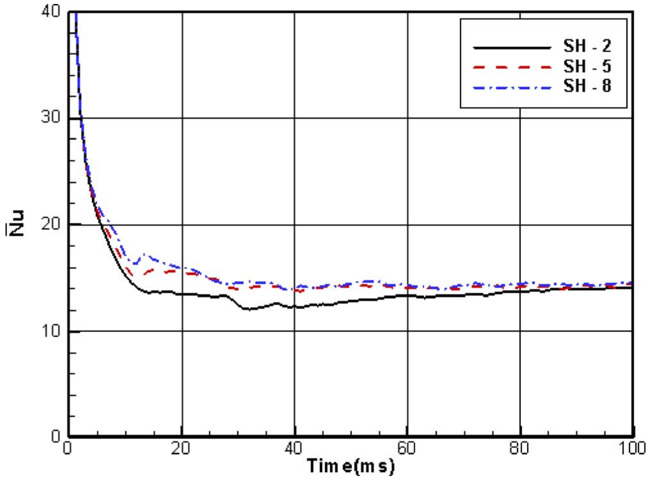

Fig. 11 Comparison of average heat transfer coefficient at the meniscus base as a function of wall superheat (ACA—61; RCA—48; WV—0.1 m/s)

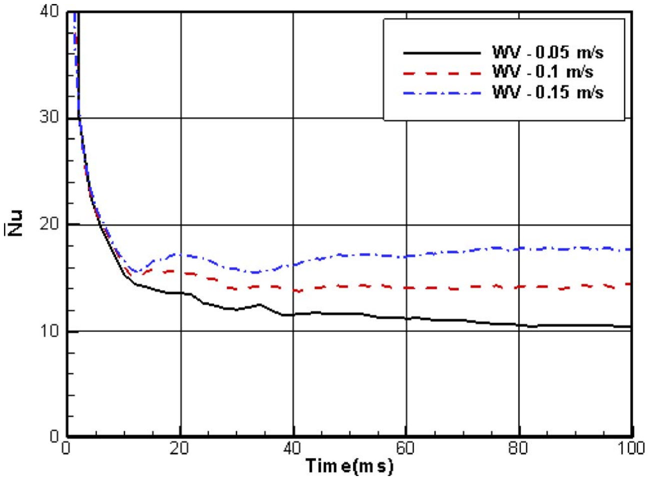

Fig. 12 Comparison of average heat transfer coefficient at the meniscus base as a function of wall velocity (ACA—61; RCA—48; SH—5 K)

makes the liquid circulation inside the meniscus more effective and enhances transient heat conduction from the wall.

Comparison to Nucleate Boiling

The $\overline{\text{Nu}}$ at the meniscus base obtained from the numerical simulation for the *base case* is 14; the corresponding wall heat flux with 5 K wall superheat is 47.6 kW/m^2. The nucleate boiling wall heat flux at 5 K wall superheat is 10 kW/m^2 [17]. Thus the numerical simulation predicts higher wall heat flux for the moving and evaporating meniscus as compared to partial nucleate pool boiling. However, it must be noted that the present wall heat flux calculations are carried out at the meniscus base in the liquid, whereas in nucleate boiling the heat flux is measured over the entire heater surface covered with isolated vapor bubbles (at 5 K wall superheat) and natural convection heat transfer present at locations away from the active nucleation sites.

It is difficult to specify a value for nucleation site density since it depends on the surface condition. However, as a first-order approximation, we assume that at 5 K superheat bubbles do not interfere and are located on a square grid 2D apart where D is the departure diameter. The area influenced by the meniscus is assumed to be the area under the departure diameter D, which is 19.6% of the heater area, whereas natural convection exists on the remaining 80.4% of the heater area. The natural convection heat flux for hot surfaces facing up is calculated to be 4.6 kW/m^2 from the correlation [17]

$$\overline{\text{Nu}}_L = 0.15\text{Ra}_L^{1/3} \tag{26}$$

Thus, the meniscus region heat flux of 47.6 kW/m^2 translates into an average pool boiling heat flux of 13 kW/m^2, which compares favorably with the pool boiling value of 10 kW/m^2 at 5 K superheat.

It must be noted here that the present work is not intended to predict the pool-boiling heat transfer rates but to provide a more in-depth look into the contact region heat transfer. The local velocity and temperature fields provide insight into the heat transfer mechanisms at the advancing and receding contact regions. The study confirms that the dominant heat transfer mechanism at the bubble base to be transient conduction and illustrates the importance of the advancing contact angle on the wall heat transfer as compared to the receding contact angle. In order to simulate the pool-boiling heat transfer, much more comprehensive approach will be needed as shown by Dhir [15].

Conclusions

1. A steady evaporating meniscus on a moving heated wall is numerically simulated in two dimensions, and the velocity and temperature fields are obtained.
2. Circulation of liquid is observed inside the meniscus on the moving wall. More than 99% of the evaporation is found to take place through the receding interface as compared to the advancing interface.
3. The local wall heat transfer varies significantly along the meniscus base. The advancing contact region shows the highest heat transfer due to transient conduction in the liquid from the heated wall.
4. The wall heat transfer coefficient is found to increase with increase in wall velocity and the advancing contact angle but remains unaffected with changes in wall superheat or the receding contact angle.
5. Reasonable agreement is observed when meniscus profiles and wall heat transfer are compared between numerical simulation and experimental observations.

Acknowledgment

This work was conducted in the Thermal Analysis and Microfluidics Laboratory at RIT.

Nomenclature

C_p = specific heat at constant pressure, J/kg K
d = grid spacing, m
D = departure diameter of single bubble, m
g = gravity vector, m^2/s
H = Heaviside function
h = heat transfer coefficient, W/m^2 K
h_{fg} = latent heat of evaporation, J/kg
k = thermal conductivity, W/m K
l_0 = length scale, m
L = meniscus base length, m
m = mass transfer rate at interface, kg/m^2 s
ms = milliseconds
Nu = Nusselt number
p = pressure, N/m^2
Re = Reynolds number
Ra = Rayleigh number
r = radius, m
T = temperature, °C
ΔT = temperature difference, $T_w - T_{\text{sat}}$, °C
t = time, s
u = x direction velocity, m/s
u_0 = velocity scale, m/s
V_{in} = inlet liquid velocity, m/s
v = y direction velocity, m/s
w = z direction velocity, m/s
x = distance in x direction, m
y = distance in y direction, m
z = distance in z direction, m
α = thermal diffusivity, m^2/s
β_T = coefficient of thermal expansion, K^{-1}
κ = interfacial curvature, m^{-1}
μ = dynamic viscosity, N s/m^2
ν = kinematic viscosity, m^2/s
ρ = density, kg/m^3
σ = surface tension, N/m
τ = time period, s
ϕ = level set function, m
φ = contact angle, deg

Subscripts

evp = evaporation
l = liquid

sat = saturation
v = vapor
w = wall
x = $\partial/\partial x$
y = $\partial/\partial y$
z = $\partial/\partial z$

Superscripts

* = nondimensional quantity
$\rightarrow$ = vector quantity

References

[1] Derjaguin, B. V., 1940, "A Theory of Capillary Condensation in the Pores of Sorbents and Other Capillary Phenomena Taking Into Account the Disjoining Action of Polymolecular Liquid Films," Acta Physicochim. URSS, **12**(1), pp. 181–200.
[2] Derjaguin, B. V., Nerpin, S. V., and Churayev, N. V., 1965, "Effect of Film Transfer Upon Evaporating Liquids From Capillaries," RILEM Bull., **29**(1), pp. 93–98.
[3] Potash, M., Jr., and Wayner, P. C., Jr., 1972, "Evaporation From A Two-Dimensional Extended Meniscus," Int. J. Heat Mass Transfer, **15**, pp. 1851–1863.
[4] Moore, F. D., and Mesler, R. B., 1961, "The Measurement of Rapid Surface Temperature Fluctuations During Nucleate Boiling of Water," AIChE J., **7**(4), pp. 620–624.
[5] Labunstov, D. A., 1963, "Mechanism of Vapor Bubble Growth in Boiling on the Heating Surface," J. Eng. Phys., **6**(4), pp. 33–39.
[6] Mikic, B. B., and Rohsenow, W. M., 1969, "A New Correlation of Pool-Boiling Data Including the Effect of Heating Surface Characteristics," ASME J. Heat Transfer, **9**, pp. 245–250.
[7] Koffman, L. D., and Plesset, M. S., 1983, "Experimental Observations of the Microlayer in Vapor Bubble Growth on a Heated Solid," ASME J. Heat Transfer, **105**, pp. 625–632.
[8] Kandlikar, S. G., Kuan, W. K., and Mukherjee, A., 2005, "Experimental Study of Heat Transfer in an Evaporating Meniscus on a Moving Heated Surface," ASME J. Heat Transfer, **127**, pp. 244–252.
[9] Son, G., Dhir, V. K., and Ramanujapu, N. K., 1999, "Dynamics and Heat Transfer Associated With a Single Bubble During Nucleate Boiling on a Horizontal Surface," ASME J. Heat Transfer, **121**, pp. 623–631.
[10] Mukherjee, A., and Dhir, V. K., 2004, "Study of Lateral Merger of Vapor Bubbles During Nucleate Pool Boiling," ASME J. Heat Transfer, **126**, pp. 1023–1039.
[11] Patankar, S. V., 1980, *Numerical Heat Transfer and Fluid Flow*, Hemisphere, Washington DC.
[12] Patankar, S. V., 1981, "A Calculation Procedure for Two-Dimensional Elliptic Situations," Numer. Heat Transfer, **4**, pp. 409–425.
[13] Sussman, M., Smereka, P., and Osher, S., 1994, "A Level Set Approach for Computing Solutions to Incompressible Two-Phase Flow," J. Comput. Phys., **114**, pp. 146–159.
[14] Fedkiw, R. P., Aslam, T., Merriman, B., and Osher, S., 1998, "A Non-Oscillatory Eulerian Approach to Interfaces in Multimaterial Flows (The Ghost Fluid Method)," Department of Mathematics, UCLA, CAM Report No. 98–17, Los Angeles, CA.
[15] Dhir, V. K., 2006, "Mechanistic Prediction of Nucleate Boiling Heat Transfer-Achievable or a Hopeless Task," ASME J. Heat Transfer, **128**, pp. 1–12.
[16] Ramanujapu, N., and Dhir, V. K., 1999, "Dynamics of Contact Angle During Growth and Detachment of a Vapor Bubble at a Single Nucleation Site," *Proceedings of 5th ASME/JSME Joint Thermal Engineering Conference*, San Diego, CA, Paper No. AJTE99/6277, ASME, New York.
[17] Incropera, F. P., and DeWitt, D. P., 2002, *Fundamentals of Heat and Mass Transfer*, Wiley, New York, Chap. 10, Fig. 10.4.

Brandon Schneider

Ali Koşar

Chih-Jung Kuo

Department of Mechanical, Aerospace and
Nuclear Engineering,
Rensselaer Polytechnic Institute,
Troy, NY 12180

Chandan Mishra
Intel Corporation,
2200 Mission College Boulevard,
Santa Clara, CA 95052

Gregory S. Cole

Robert P. Scaringe

Mainstream Engineering Corporation,
200 Yellow Place,
Rockledge, FL 32955

Yoav Peles[1]
Department of Mechanical, Aerospace and
Nuclear Engineering,
Rensselaer Polytechnic Institute,
Troy, NY 12180
e-mail: pelesy@rpi.edu

Cavitation Enhanced Heat Transfer in Microchannels

Heat transfer has been investigated in the presence of hydrodynamic cavitation instigated by 20-μm *wide inlet micro-orifices entrenched inside* 227-μm *hydraulic diameter microchannels. Average surface temperatures, heat transfer coefficients, and pressure drops have been obtained over effective heat fluxes ranging from 39 to* 558 W/cm^2 *at mass flux of* 1814 kg/m^2 s *under noncavitating and three cavitating conditions. Significant heat transfer enhancement has been recorded during supercavitating flow conditions in comparison to noncavitating flows with minimal pressure drop penalty. Once supercavitating conditions were reached, no apparent heat transfer augmentation was detected with the reduction of the cavitation index. Visualization of the flow morphology and the heat transfer coefficient characteristics aided in the evaluation of the dominant heat transfer mechanism under various thermal-hydraulic conditions.*

[DOI: 10.1115/1.2349505]

1 Introduction

Hydrodynamic cavitation, the formation of vapor or air pockets in flowing liquids as a result of local static pressure reduction below a critical value, has seldom been studied in the context of heat transfer enhancement. Studies on hydrodynamic cavitation in microchannels [1–5] have revealed unique two-phase flow patterns, which by conventional macroworld criteria can be used to enhance heat transfer. However, the lack of sufficient experimental evidence is hindering the practical realization of this cooling technique.

Exploitation of ultrasonic (not hydrodynamic) cavitation or induced vibration to augment natural convection [6–10], pool boiling [9–11], and forced convection boiling [12,13]/nonboiling [13] heat transfer has been a topic of some interest since the mid-1960s. Several independent studies have shown that heat transfer in the presence of ultrasonic cavitation may be enhanced, reduced, or have a negligible effect depending on the thermal-hydraulic conditions and ultrasonic characteristics. Various aspects affecting the thermal field were investigated, including wave generator intensity, location and frequency, geometrical configuration of heater, and liquid properties.

Recently, unique cavitating flow patterns in microchannels generated by an upstream microconstriction element have been visualized by Mishra and Peles [3]. Under supercavitating conditions several distinct flow patterns have been detected. Twin vapor/gas cavities have been observed to emanate from the orifice boundaries. The twin cavities continue to stretch downstream upon reducing the cavitation index and merge in a transition region, which is characterized by exceedingly agitated flow (rapid mixing). The downstream flow pattern either assumes an annular or a bubbly flow pattern depending on the prevalent hydrodynamic conditions. Since the presence of an annular flow pattern and/or rapid mixing are known to result in very high heat transfer coefficients, it has been speculated that thermal augmentation can be achieved by operating convective flow under certain cavitating flow morphologies.

Cavitation in microchannel boiling/heat transfer systems is also important from the design perspective. With the ever-increasing demand for high-power electronics, flow velocities in cooling microchannels are steadily rising. At sufficiently high dynamic heads, the flow becomes susceptible to cavitation [14]. Thus thermal engineers will need to carefully design microchannel cooling systems to avoid the pernicious effects of cavitation, or endorse and exploit the phenomenon. Regardless, it is essential to obtain better knowledge of the hydrodynamic conditions leading to cavitation and the subsequent thermal performance following cavitation inception.

The present investigation studied heat transfer in the presence of hydrodynamic cavitation instigated by inlet micro-orifices entrenched inside microchannels. The objectives of this work were as follows:

(a) To visualize the flow morphology under various adiabatic and diabatic conditions and to identify differences (if any) between various thermal loads.
(b) To assess the potential heat transfer enhancement of

---

[1] Corresponding author.

Contributed by the Heat Transfer Division of ASME for publication in the JOURNAL OF HEAT TRANSFER. Manuscript received September 1, 2005; final manuscript received February 21, 2006. Review conducted by Raj M. Manglik.

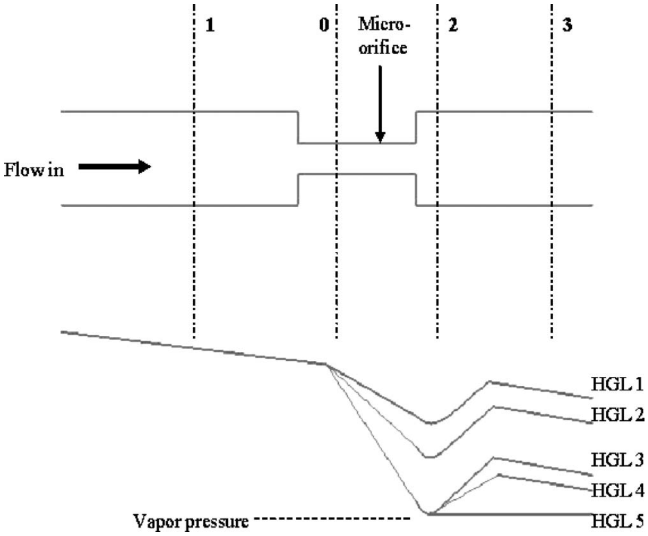

Fig. 1 Hydraulic Grade Line (HGL) for fluid flow through a micro-orifice

cavitating flows in microchannels in comparison to noncavitating flow conditions.

(c) To infer the predominate heat transfer mechanism governing various hydrodynamic cavitating flow conditions.
(d) To evaluate the pressure drop penalty required to generate cavitating flows.

This study is also meant to act as a stimulus for further research on cavitation that develops in microfluidic systems and as a prospective heat transfer enhancement technique.

A concise review on cavitating flow through orifices is provided in Sec. 2. An elaborate discussion of the device design and microfabrication is presented in Sec. 3, while the experimental setup development and experimental procedure are discussed in Sec. 4. Section 5 is devoted to the discussion of experimental results, and in Sec. 6 we present the conclusions of this work.

2 Background

The rudimentary requirement for hydrodynamic cavitation to appear is the reduction of static pressure to a critical value. This can be achieved by a dramatic change in the area of a microchannel brought about by placing a micro-orifice in the flow field. A characteristic pressure drop is observed in response to the sudden reduction in flow area. The reduction in static pressure is accompanied by an acceleration of the fluid and a consequent increase in the fluid velocity between points 1 and 2 (Fig. 1). The Hydraulic Grade Line (HGL) 1 shown in Fig. 1 captures this phenomenon. The location (point 2) where the static pressure drops to its minimum and the velocity rises to its maximum is termed the *Vena Contracta*. The static pressure recovers downstream of the orifice as the submerged jet is dissipated by viscous shear. Any further static pressure losses are primarily due to friction because the channel area remains constant.

A further reduction of the exit pressure causes the static pressure at the *Vena Contracta* to fall and produces an increase in the discharge (HGL 2). The discharge is directly proportional to the square root of the pressure difference between points 1 and 2. At some critical pressure in the *Vena Contracta*, the dissolved gas starts diffusing into the nuclei (submicron bubbles) and promotes their growth. The static pressure is still above the vapor pressure of the liquid; therefore, the mechanism of bubble growth is dominated by gaseous cavitation. A further reduction in the exit pressure succeeds in dropping the static pressure at the *Vena Contracta* to the vapor pressure of the liquid (HGL 3). Once this physical limit is reached, any attempt to increase the discharge by reducing the exit pressure is futile [14,15]. This is defined as choked flow or choked cavitation, and the exit pressure loses its control over the discharge. The micro-orifice produces its maximum discharge under these conditions. A reduction in the exit pressure only results in the elongation of the vapor cavity (HGL 4, HGL 5), and the orifice is termed to be supercavitating.

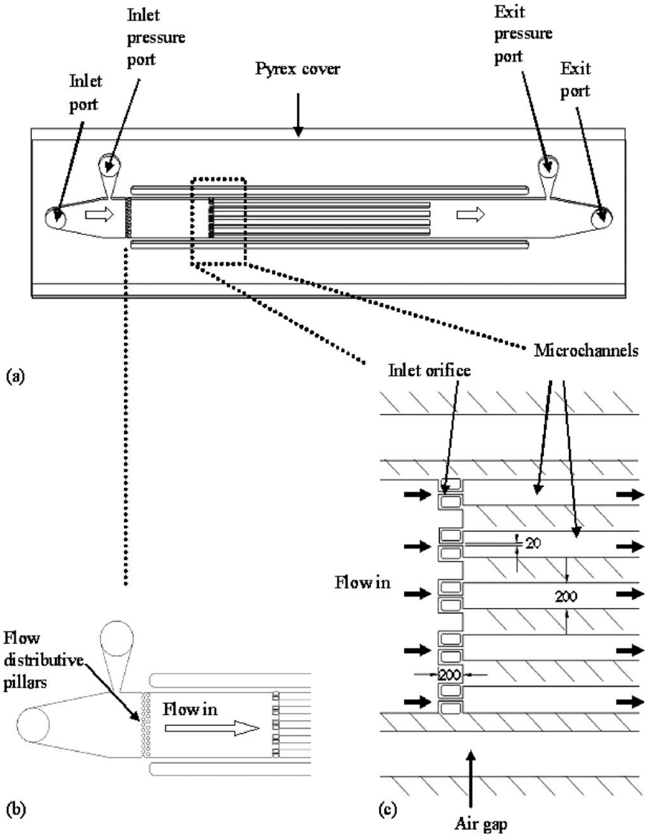

Fig. 2 (*a*) CAD model of the microchannel device; (*b*) flow distributive pillars; (*c*) geometry of the inlet region (dimensions in μm)

3 Device Overview and Fabrication

Figure 2(*a*) displays the microchannel device consisting of five 1-cm long, 200-μm wide and 264-μm deep parallel microchannels, spaced 200 μm apart. To minimize ambient heat losses, an air gap was formed on the two ends of the sidewalls, and an inlet and exit plenum were etched on the thin silicon substrate ($\sim$150 μm). A heater was deposited on the backside to deliver the heating power and also to serve as a thermistor for temperature measurements. The device is sealed from the top with a Pyrex substrate that also allows flow visualization. Flow distributive pillars were used to provide homogeneous distribution of flow in the inlet [Fig. 2(*b*)]. These pillars were arranged in 2 columns of 12 circular pillars having a diameter of 100 μm. The transverse pitch between the pillars was 150 μm and equal to the longitudinal pitch. Five 20-μm wide, 200-μm long orifices were also installed [Fig. 2(*c*)] at the entrance of each channel to promote/encourage cavitation events.

3.1 Microchannel Fabrication Method. The MEMS (Micro-ElectroMechanical Systems) device was micromachined on a polished double-sided *n*-type ⟨100⟩ single crystal silicon wafer using techniques adapted from integrated circuit (IC) manufacturing. The device was equipped with pressure ports at the inlet and the

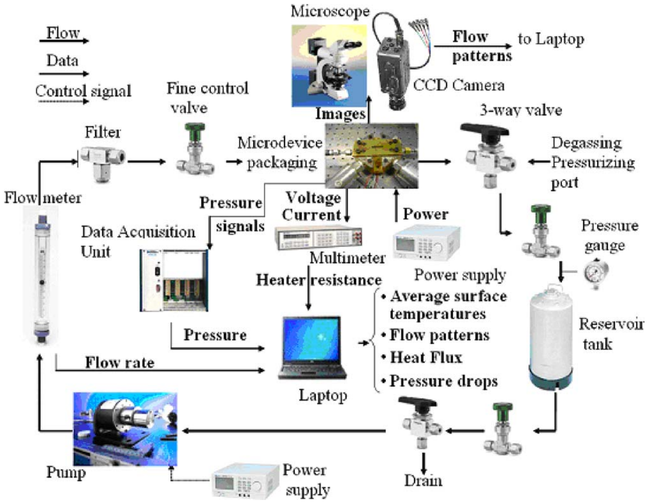

Fig. 3 Experimental setup

exit to obtain accurate measurements of the static pressures.

A 1-μm thick high-quality oxide film was deposited on both sides of the silicon wafer to shield the bare wafer surface during processing. This film also served as an electrical insulator during testing. The heater and the vias were formed on the backside of the wafer (on top of the thermistors) by sputtering. A 70-Å thick layer of titanium was initially deposited to enhance adhesion characteristics and was followed by sputtering a 1-μm thick layer of aluminum containing 1% silicon and 4% copper. Subsequent photolithography and concomitant wet bench processing created the heater on the backside of the wafer. A 1-μm thick Plasma Enhanced Chemical Vapor Deposition (PECVD) oxide was deposited to protect the heater during further processing.

Next, the microchannels were formed on the top side of the wafer. The wafer was taken through a photolithography step and a reactive ion etching (RIE) oxide removal process to mask certain areas on the wafer, which would not be etched during the deep reactive ion etching (DRIE) process. The wafer was consequently etched in a DRIE process, and silicon was removed from places not protected by the photoresist/oxide mask. The DRIE process formed deep vertical trenches on the silicon wafer with a characteristic scalloped sidewall that had a peak-to-peak roughness of ~0.3 μm. A profilometer and SEM were used to measure and record various dimensions of the device.

The wafer was flipped and the backside was then processed to create an inlet, outlet, side air gap, and pressure port taps for the transducers. A photolithography followed by a buffer oxide etching (BOE) (6:1) oxide removal process was carried out to create a pattern mask. The wafer was then etched through in a DRIE process to create the fluidic ports. Next, electrical contacts/pads were opened on the backside of the wafer by performing another round of photolithography and RIE processing. Finally, the processed wafer was stripped of any remaining resist or oxide layers and anodically bonded to a 1-mm thick polished Pyrex (glass) wafer to form a sealed device. After successful completion of the bonding process, the processed stack was die-sawed to separate the devices from the parent wafer.

The MEMS device was packaged by sandwiching it between two plates. The fluidic seals were forged using miniature "o rings," while the external electrical connections to the heater were achieved from beneath through spring-loaded pins, which connected the heater and thermistors to electrical pads residing away from the main microchannel body.

4 Experimental Test Rig and Procedure

4.1 Experimental Test Rig. The setup, shown in Fig. 3, consisted of three primary subsystems: the flow loop section, the instrumentation, and a data acquisition system. The test section housed the MEMS-based microchannel devices and its fluidic and thermal packaging module. The microchannel device was mounted on the fluidic packaging module through o rings to ensure a completely leak-free system. The fluidic packaging delivered the working fluid and provided access to the pressure transducers. The heater, which was fabricated on the device backside, was wired (through electric pads) to the power supply.

The main flow loop included the microchannel device, a pulseless gear pump, a reservoir consisting of a deaerator unit, and a heating element to control the inlet temperature, a flow meter, and a dissolved-oxygen meter (for use with water). The microheater was connected to a power supply with an adjustable dc current to provide power to the device. The inlet pressure and test-section pressure drop were collected, and the flow patterns at cavitating conditions along the microchannels were recorded by a Phantom V4.2 high-speed camera (maximum frame rate of 90 000 frames/sec, and 10-μs exposure time) mounted over a Leica DMLM microscope.

4.2 Experimental Procedures and Data Reduction. The deionized water flow rate was fixed, and the exit pressure was reduced until the desired cavitating conditions were obtained. A Dissolved Oxygen Concentration (DOC) level of 8.7 ppm was maintained during all experiments, which is the saturation concentration of water at atmospheric conditions. The measurements were performed through an Omega DOB-215 dissolved-oxygen sensor. Experiments were conducted after steady flow conditions were attained at exit pressures corresponding to the desired cavitating condition. First, the electrical resistance of the device was measured at room temperature. Thereafter, voltage was applied in 2-V increments to the heater, and the current/voltage data were recorded, along with pressure data from the inlet and exit pressure ports once steady state was reached. The power was switched off when the temperature difference between the average heater surface temperature and the ambient temperature exceeded ~100°C. Flow visualization through the high-speed camera and microscope complemented the measured data and enabled the characterization of flow patterns prevailing along the microchannels. Images of flow patterns were recorded at both adiabatic and diabatic tests for each operating condition.

Data obtained from the voltage, current, and pressure measurements were used to calculate the cavitation indices, heat transfer coefficients, and Euler numbers.

The pressure data from the inlet and outlet were used to obtain the dimensionless cavitation index, which is a prime parameter in the study of cavitation, using the following expressions:

$$\sigma = \frac{p_e - p_v}{\frac{1}{2}\rho u^2} \tag{1}$$

The electrical input power and heater resistance, respectively, were determined with

$$P = V \times I \tag{2}$$

and

$$R = V/I \tag{3}$$

The heater electrical resistance—temperature calibration curve (Fig. 4) was used for determining the heater temperature ($\overline{T}_{\text{heater}}$). To calculate the heat transfer coefficient, the wall temperature adjacent to the water at the base of the microchannel must be known, and therefore was calculated as follows:

$$\overline{T} = \overline{T}_{\text{heater}} - \frac{(P - \dot{Q}_{\text{loss}})t}{k_s A_p} \tag{4}$$

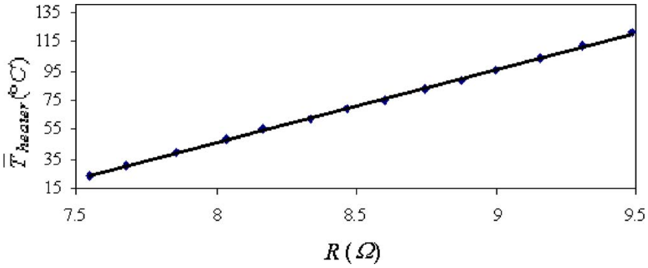

Fig. 4 Heater electrical resistance-temperature calibration curve

The exit single-phase fluid temperature was calculated with a calorimetric balance, and the average fluid temperature is expressed as:

$$\overline{T}_F = \frac{T_i + T_e}{2} \tag{5}$$

Assuming that the walls of the channels behaved as one-dimensional fins with an adiabatic tip, the power input was related to the average heat transfer coefficient in the channel:

$$P - \dot{Q}_{\text{loss}} = \eta_0 A_t \overline{h}(\overline{T} - \overline{T}_F) \tag{6}$$

where η_0 is the overall surface effectiveness of the microchannel configuration:

$$\eta_o = \frac{N\eta_f A_f + (A_t - NA_f)}{A_t} \tag{7}$$

where

$$\eta_f = \frac{\tanh(mH)}{mH} \qquad m = \sqrt{\frac{\overline{h}2(L+W)}{k_s WL}} \qquad A_f = 2HL \tag{8}$$

Equations (5)–(7) were used to evaluate $\overline{h}$ by performing an iterative scheme.

The exit quality was calculated using a caloric balance:

$$x_e = \frac{(P - \dot{Q}_{\text{loss}}) - \dot{m}c_p(T_{\text{sat}} - T_i)}{\dot{m}h_{\text{fg}}} \tag{9}$$

The uncertainties of the measured values, which are provided in Table 1, were obtained from the manufacturer's specification sheets, while the uncertainties of the derived parameters were calculated using the method developed by Kline and McClintock [16].

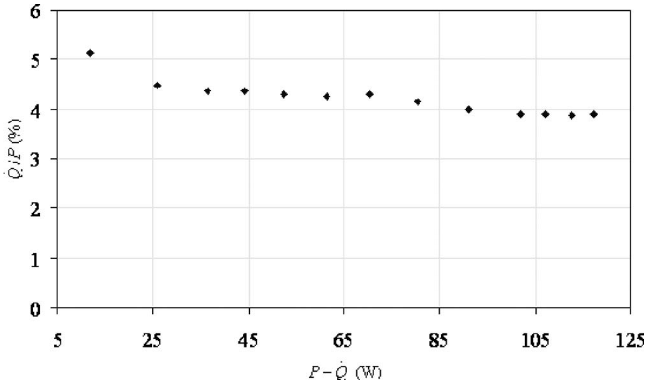

Fig. 5 Heat loss curve for cavitating conditions

4.3 Heat Losses. One-dimensional fin analysis on the inlet and exit plenum was performed to estimate heat losses from the microheat sink. Heat loss from the bottom surface was estimated by assuming one-dimensional conduction through a 2-mm air gap (the gap between the chip bottom and the top electrical probe pin block). Heat losses from the top surface were estimated from thermal losses comprised of conduction through the Pyrex substrate and natural convection. Maximum heat losses from the top and bottom surfaces yielded ~0.02 and ~0.01 W, respectively, which were considerably smaller than the applied heater power (10–117 W). Thus, heat losses from the top and bottom surfaces were neglected.

Table 1 Uncertainties in variables used in uncertainty analysis

Uncertainty	Error
Flow rate, Q (for each reading)	1.0%
Voltage supplied by power source, V	0.5%
Current supplied by power source, I	0.5%
Ambient temperature, T_{amb}	0.1°C
Electrical power, P	0.7%
Electrical resistance, R	0.7%
Average temperature, $\overline{T}$	1.0°C
Exit pressure, p_e	0.8 kPa
Cavitation index, σ	2.4%
Heat transfer coefficient, $\overline{h}$	4.5%

On the other hand, heat losses to the inlet and exit plenum through conduction could not be completely neglected. To verify the estimated heat loss, electrical power was applied to the test section after evacuating the water from the test loop. Once the temperature of the test section reached steady-state conditions, the temperature difference between the ambient and test section was recorded at the corresponding power. The temperature difference versus the power curve was plotted and used to compare the heat loss associated with each experimental data point to the fin analysis. The results from this comparison showed very good agreement. Thus, the measured heat loss was subtracted from the total heat supplied to the heat sink under forced flow conditions, and

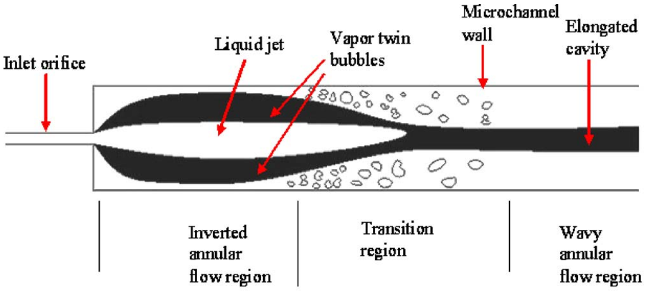

(a) Microchannel inlet

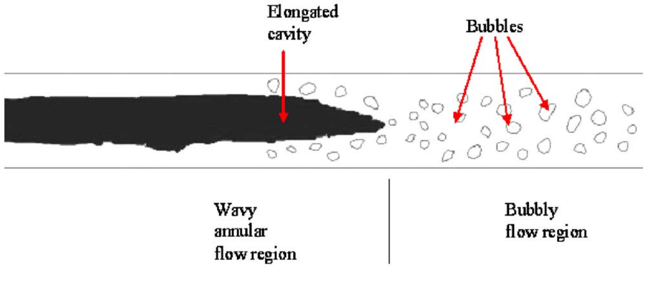

(b) Collapse of elongated bubble

Fig. 6 CAD drawing of flow patterns

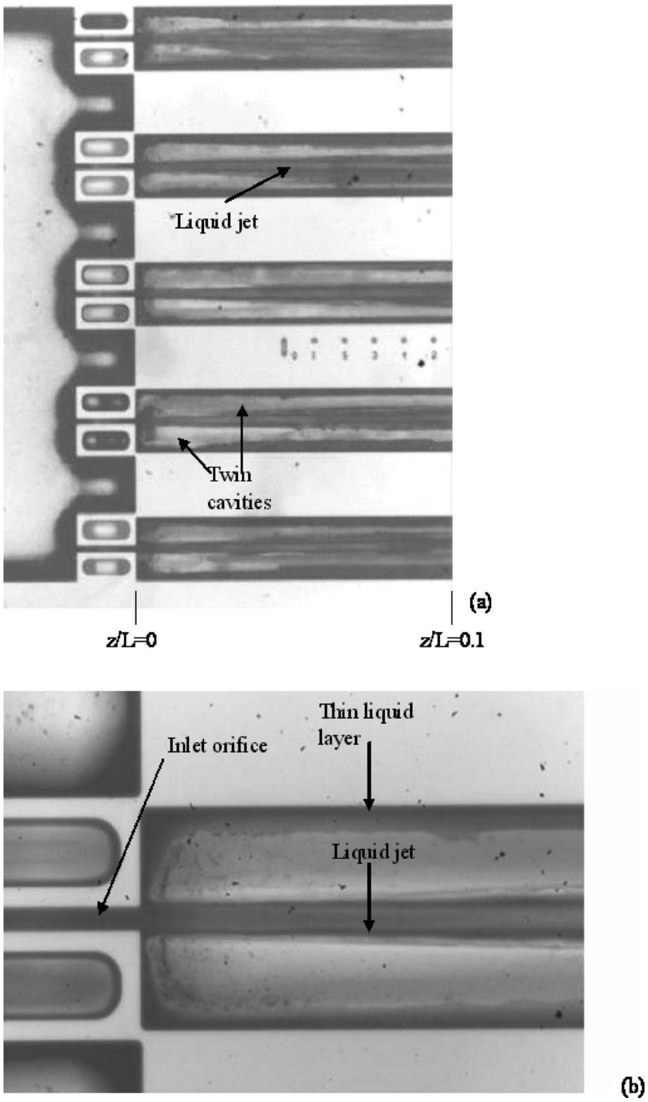

Fig. 7 (*a*) **Liquid jets at the inlet region for intermediate size cavities** (σ=**0.11**). (*b*) **Zoom in to the inlet region for intermediate size cavities** (σ=**0.11**).

the corresponding values were used in subsequent analyses of the data reduction. A heat loss curve for the cavitating flow conditions is shown as a sample in Fig. 5.

5 Results and Discussion

5.1 Adiabatic Flow. Single-phase flow and three assorted cavitating conditions corresponding to different cavitation numbers were investigated in the current study. The cavitation number was modulated by adjusting the exit pressures to 101 kPa (single-phase), 40, 21.4, and 7.8 kPa. With the decrease in cavitation index, the system becomes more susceptible to cavitation, and at a critical cavitation number (incipient cavitation number) of 0.253 inchoate bubbles emerge. Thereafter, any further reduction in the cavitation number only serves to provide cavitating flows of increasing intensity.

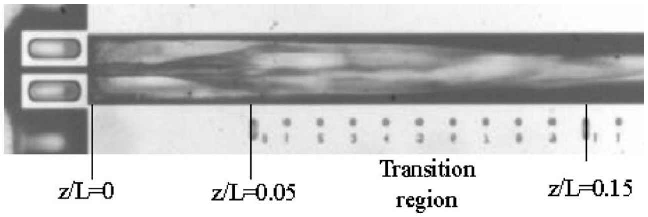

Fig. 8 Short cavity at the inlet region (σ=**0.223**)

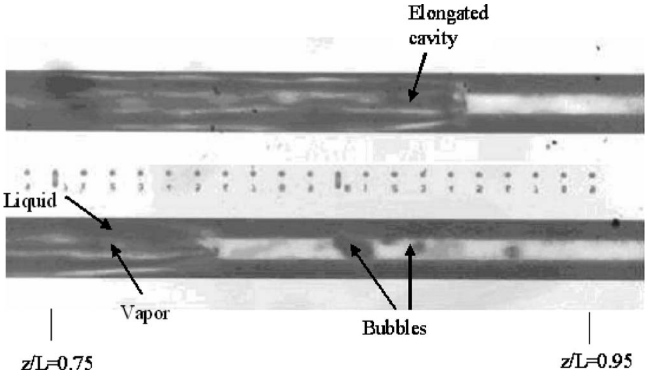

Fig. 9 Elongated bubbles near the exit region at adiabatic condition (σ=**0.0282**)

Five principal flow patterns prevailed in the microdevice during testing: liquid single-phase, liquid jet, transition region (rapid mixing), annular (wavy annular), and bubbly (Fig. 6). Flow patterns observed in the present multichannel device agreed well with previously documented flow patterns in a single micro-orifice device [3], and generally depended on the cavitation number and the downstream location from the constriction element.

At very high cavitation numbers (i.e., low velocities and dynamic heads), the minimum static pressure in the channel is insufficient to trigger cavitation and liquid single-phase flow prevails in the channel. When the minimum pressure in the system reaches a critical value, it promotes cavitation (cavitation inception), where the cavitation intensity and extent are limited. A further reduction in the cavitation number succeeds in lowering the minimum static pressure to the vapor pressure of the liquid and forms a vapor cavity. After reaching this physical limit for flow through orifices, any further attempt to increase the flow rate by reducing the exit pressure is ineffective [1,2,14,15]. However,

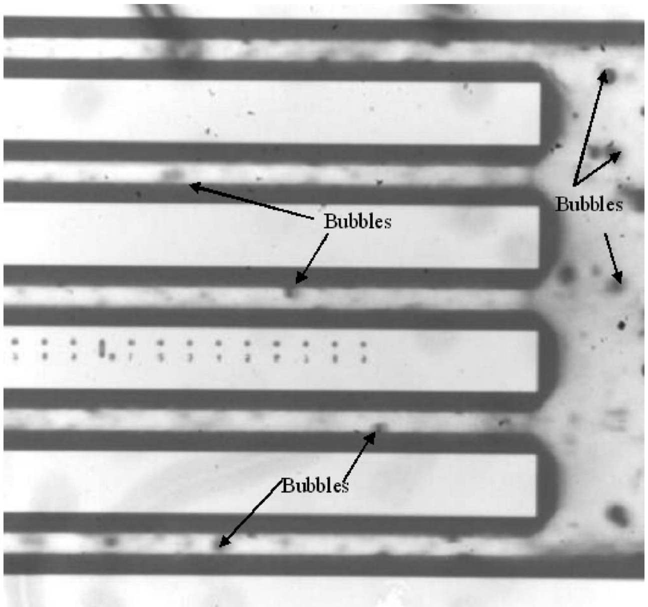

Fig. 10 Bubbly flow at the exit region for short cavities at adiabatic condition (σ=**0.223**)

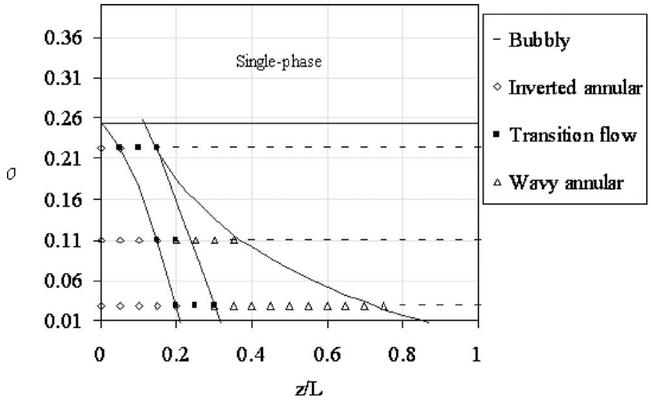

Fig. 11 Flow map under adiabatic conditions

various hydrodynamic cavitating flow patterns are detected depending on the cavitation number. In the present study, tests were conducted either during single-phase flow or under cavitating conditions sufficient to sustain two-phase flows that extended throughout the microchannel.

For a given cavitation number, several flow patterns can coexist depending on the longitudinal location downstream from the micro-orifice. Also, variations between channels were occasionally observed. A stable liquid jet emanated from the orifice exit and stretched several hydraulic diameters (depending on the cavitation number) downstream of the orifice, as shown in Figs. 7 and 8. Alongside the main jet, a thin liquid layer around the twin cavities was formed on the channel sidewalls. Further downstream, the flow became unstable, rapid shedding of vapor slugs were detected, and the void fraction was strongly time dependent, resulting in extensive flow agitation and mixing, which is termed the “transition flow pattern.” The rapid mixing stabilized (to an extent) and gave rise to a solitary vapor bubble. Thus, a wavy annular flow pattern was established (Fig. 9). The vapor then broke up into smaller bubbles and exited the channels as a two-phase bubbly flow pattern for all cavitating conditions examined in the current study (Fig. 10). Figure 11 depicts a flow pattern map as a function of the cavitation number and the longitudinal location.

The Euler number, Eu, as a function of the cavitation index is shown in Fig. 12. As discussed by Mishra and Peles [1,2], to promote the formation of supercavitating flow in micro-orifices, a relatively minor decrease in the cavitation index beyond cavitation inception conditions is required. Furthermore, the additional increase in the pressure drop required to reduce the cavitation number corresponding to supercavitation is comparatively minor. Thus, it can be concluded that the promotion and growth of supercavitating flow patterns come with a miniscule pressure drop penalty.

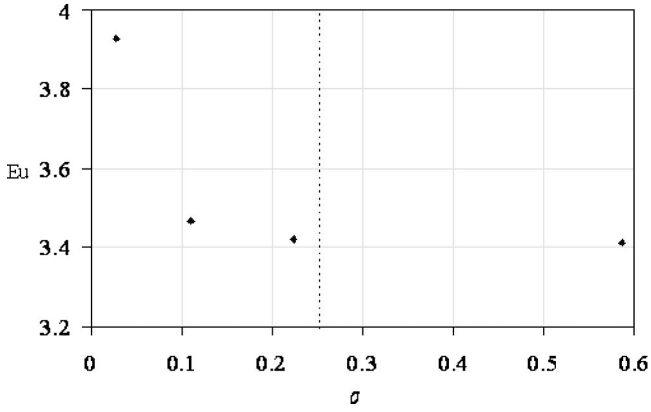

Fig. 12 Dimensionless pressure drop as a function of cavitation index

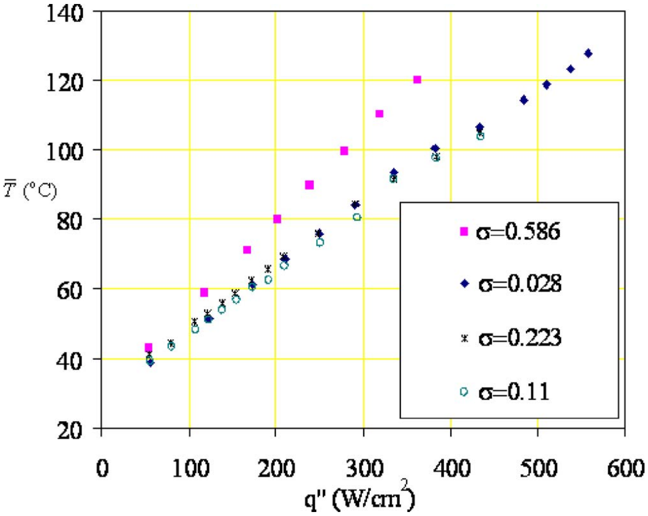

Fig. 13 Average surface temperature as a function of effective heat flux (σ=0.586 for noncavitating conditions, σ=0.028, 0.11, 0.223 for cavitating conditions)

5.2 Diabatic Flow. Figure 13 depicts the average surface temperature as a function of heat flux for noncavitating and cavitating flow patterns at mass velocities of 1814 kg/m^2 s. As can be seen, a significant reduction in the surface temperature was obtained by promoting cavitating flows. In addition, comparable surface temperature was notable for all cavitating conditions. While the linear temperature increase of the noncavitating flow can be fully predicted by assuming constant heat flux conditions [17], the temperature-heat flux characteristics of the cavitating flows require further clarifications, which can be obtained by evaluating the heat transfer coefficient trends and visualization of the flow patterns. As shown in Fig. 14, the average heat transfer coefficient for both the cavitating and noncavitating flows was fairly constant up to ~400 W/cm^2. From 383 to 558 W/cm^2, the heat transfer coefficient gradually increased for cavitating conditions, and then

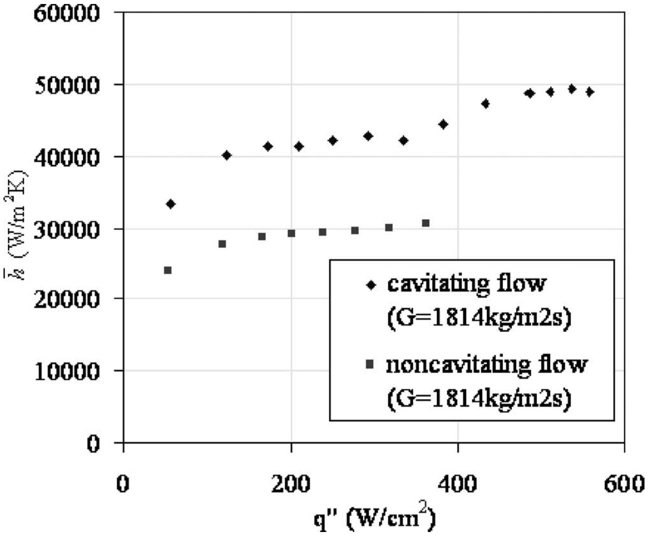

Fig. 14 Heat transfer coefficients at cavitating (σ=0.0282) and noncavitating conditions (σ=0.586)

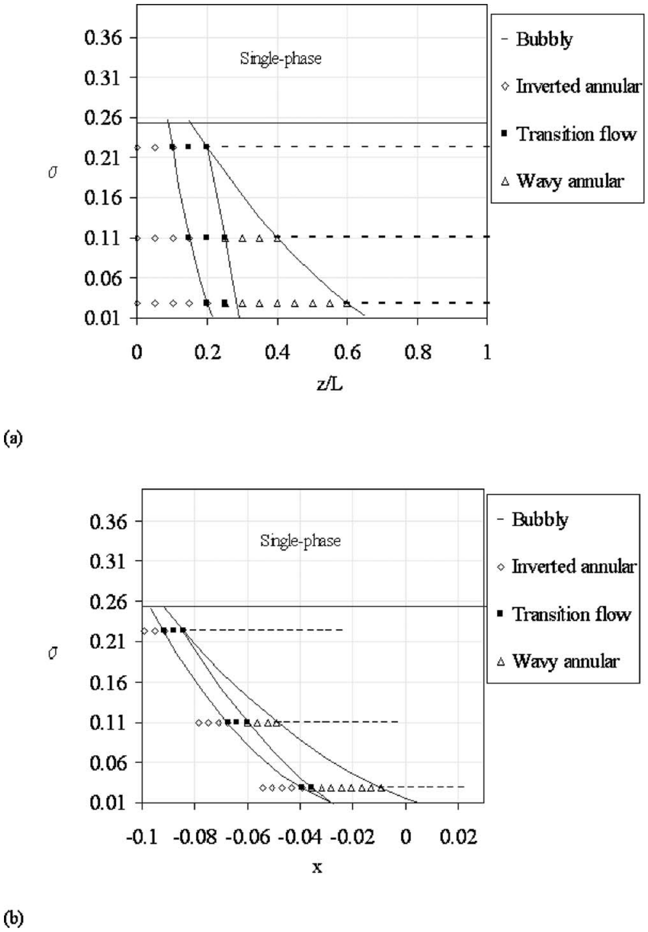

Fig. 15 Flow maps under diabatic conditions ($q''=383\ \mathrm{W/cm^2}$): (*a*) based on the distance from the inlet, (*b*) based on local mass quality

reached a plateau.

It is well documented and correlated that with an increase in heat flux on a heated tube, flow pattern transitions occur and the void fraction significantly increases. As a result, a significant increase in the pressure drop is required to propel the flow with increasing heat flux. However, in the present study, the pressure drop varied little with heat flux. Furthermore, while the flow patterns were strongly affected by the cavitation number, flow visualization studies revealed no significant transition in the flow morphology (for a fixed cavitation number) as the heat flux was varied. This is evident when comparing the flow pattern map for adiabatic conditions (Fig. 11) and for $q''=383\ \mathrm{W/cm^2}$ (Fig. 15). The main difference is that the bubbly flow pattern moderately extended and occupied a larger portion of the channel compared to adiabatic conditions. Nevertheless, at high heat fluxes, bubble nucleation was observed in the channel at the exit region (Fig. 16), and to some extent the void fraction seemed to increase (at the exit).

It is worth noting that with an increase in the heat flux the liquid temperature rose, which effectively reduced the cavitation number. However, since the established cavitating flow patterns are less dependent on the cavitation index than the longitudinal location downstream of the orifice, the increased flow temperature is expected to be less significant in dictating cavitation flow patterns, as long as the cavitation number is below a critical value. It can be concluded that the flow patterns and for the most part the void fraction were less affected by boiling phase change, and cavitation events (not boiling) dominated the hydrodynamic flow field. Attributing the morphological flow field solely to cavitation implicitly implies that the heat transfer mechanism was controlled by cavitation events and was independent of the thermal conditions.

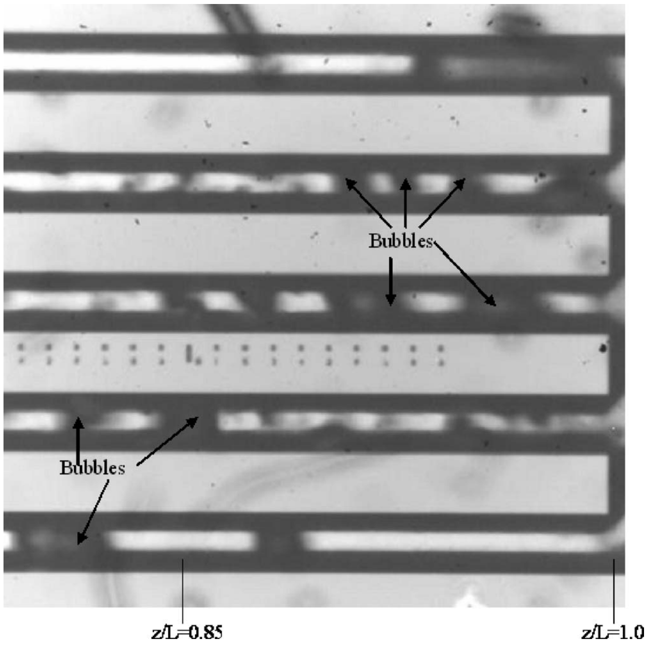

Fig. 16 Nucleation at the exit region for short cavities ($\sigma=0.223$, $q''=383\ \mathrm{W/cm^2}$)

Flow patterns are commonly linked to the mechanisms dominating heat transfer under various thermal-hydraulic conditions. The cavitating flow map (Fig. 15) provides a useful means to determine the heat transfer mechanisms pertaining to various conditions, and several fundamental mechanisms can be hypothesized to predominate depending on the cavitation number, longitudinal location downstream of the orifice, and to a very limited extent the heat flux. These mechanisms are as follows:

- Single-phase convection
- Two-phase convective evaporation
- Nucleate boiling

From flow visualization studies and the independence of the average heat transfer coefficient on the heat flux at low and moderate heat fluxes, it can be concluded that convective heat transfer predominates the thermal mechanism for $q''<400\ \mathrm{W/cm^2}$. However, the prime convective mode (i.e., convective evaporation or liquid single-phase convection) responsible for the heat transfer enhancement, as evident from Fig. 15, was not identified. The heat transfer rate directly consumed by phase change at the thin liquid film/vapor interface was not determined.

Even if the liquid single phase can be related to the thermal augmentation, the hydrodynamic field assumes several forms, which can affect the heat transfer rate. The heat transfer coefficient could vary depending on the location in the channel. However, the average heat transfer coefficient seemed to be independent of the flow pattern (as long as two-phase flow was present throughout the channel) established under different cavitation numbers. This might suggest that the heat transfer coefficient of the various flow morphologies is comparable (relative to single-phase channel flow), at least under the conditions investigated in the present study.

All three liquid convective heat transfer modes (liquid jet, annular, and transition flow patterns) are hypothesized to contribute to the heat transfer enhancement relative to noncavitating flow conditions. The annular and liquid jet flow patterns are analogous to annulus flow inside a concentric tube. As discussed by Kays

Table 2 Heat transfer modes in the current study

Cavitating conditions	Heat transfer mechanism	Comments
Noncavitating	Single-phase convection	
Cavitating	Single-phase convection	Liquid jet at the inlet, wavy annular flow, and mixing in the flow transition region are responsible for this mode of heat transfer
Cavitating	Convective evaporation	This mode of heat transfer exists at the boiling portion of microchannels (near the exit) and accounts for the convective part of boiling heat transfer
Cavitating	Nucleate boiling	Bubble nucleation from channel walls constitutes this mode of heat transfer and becomes significant near the exit region at large heat fluxes

and Parkins [18], the concentric arrangement has a minor to moderate effect on the Nusselt number of the outer tube. However, because the hydraulic diameter for concentric annulus is directly proportional to the gap size, the heat transfer coefficient significantly increases with the reduction of the liquid layer thickness, and therefore heat transfer is augmented. Collier and Thome [19] used the above argument to explain the increased heat transfer coefficient during annular two-phase flow in comparison to single-phase liquid flowing alone in the channel. The transition flow pattern promotes intense liquid mixing and consequently enhances advection, which results in higher heat transfer coefficients. Additionally, the intense mixing, together with the acceleration of the liquid (due to a reduction in the liquid cross-sectional area), might promote early transition to turbulent flow (the noncavitating Reynolds number is 580 at 35°C), and therefore enhances heat transfer.

Although nucleate boiling is included in the above categorization, its dominance was expected to be very limited and restricted to the exit region at high heat fluxes. The average heat transfer characteristics certainly do not lend support for the dominance of nucleate boiling at least at low to moderate heat fluxes (up to $\sim 400\ \mathrm{W/cm^2}$). However, the moderate increase in the heat transfer coefficient at heat fluxes above $\sim 400\ \mathrm{W/cm^2}$ (Fig. 14) might be indicative of significant bubble nucleation due to boiling (and subsequent heat transfer enhancement) at the exit region (Fig. 16). Nonetheless, before any conclusion can be drawn, local temperature measurements are required to fully validate/invalidate the importance of nucleate boiling in controlling heat transfer at the exit region. Table 2 provides a summary of the heat transfer modes dominating at various geometrical and cavitating conditions.

6 Conclusions

Hydrodynamic cavitation in microchannels under various adiabatic and diabatic conditions were studied and its effect on heat transfer was evaluated. The main conclusions drawn from this study are as follows.

1. Significant heat transfer enhancement, an increase of approximately 67%, was obtained under supercavitating flow conditions in comparison to noncavitating flow conditions for the same mass velocity. Once supercavitating flow conditions were instigated, no further heat transfer enhancement was obtained with the reduction of the cavitation index.
2. Minor deviation (1%–1.5%) in the pressure drop between single-phase flow and supercavitating flow conditions were registered. These results compared favorably with previous studies on cavitation in microsystems.
3. Flow patterns in the multipassage microchannel device used in this study showed a similarity to previously reported patterns in a single micropassage device [3] under adiabatic conditions, and were dependent on the cavitation number and the longitudinal location in the channel.
4. Flow patterns under diabatic and adiabatic flow conditions were similar.
5. Nucleate boiling heat transfer mechanism appeared to be less dominant than convective boiling at low and moderate heat fluxes ($q'' < 400\ \mathrm{W/cm^2}$). However, at high heat fluxes, nucleate boiling dominated at the exit region.
6. Although the pressure drop required to instigate cavitation was relatively large (200–600 KPa), in the current configuration (inlet orifices), other methods to promote cavitation while maintaining a low pressure drop can be considered and should be sought to exploit the advantages of this enhanced heat transfer method.

Acknowledgment

This work was partly supported by the National Science Foundation under CTS 0520604. Graduate student support from Rensselaer Polytechnic Institute is gratefully appreciated. The microfabrication was performed in part at the Cornell NanoScale Facility (a member of the National Nanotechnology Infrastructure Network), which is supported by the National Science Foundation under Grant No. ECS-0335765, its users, Cornell University, and industrial affiliates.

Nomenclature

A_f = Total fin surface area, m^2
A_p = Planform area (surface area of silicon block), m^2
A_t = Total heat transfer area $(A_b + \eta_f A_f)$, m^2
Eu = Euler number $[\Delta p/(1/2\rho u^2)]$
G = Mass velocity, kg m^{-2} s^{-1}
$\bar{h}$ = Average heat transfer coefficient, W m^{-2} °C^{-1}
H = Channel height, fin height, m
I = Electrical current, Amps
k_s = Thermal conductivity of the silicon block, W m^{-1} °C^{-1}
L = Channel length, m
m = Fin parameter in Eq. (8)
N = Number of microchannels
P = Electrical power, W
p_e = Exit pressure, kPa
p_i = Inlet pressure, kPa
p_v = Vapor pressure, kPa
Pr = Prandtl number
q'' = Heat flux, W cm^{-2}
$\dot{Q}_{\text{loss}}$ = Heat loss, W
R = Electrical resistance, Ω
t = Thickness of the silicon block, m
T = Temperature, °C
$\bar{T}$ = Average surface temperature, °C
T_e = Exit temperature, °C
$\bar{T}_F$ = Average fluid temperature, °C

$\overline{T}_{\text{heater}}$ = Average heater surface temperature, °C
T_i = Inlet temperature, °C
u = Liquid velocity at the inlet restrictor, m/s
V = Electrical voltage, V
W = Channel width, m
x = Local mass quality
z = Axial distance from the inlet, m

Greek

Δp = Pressure drop, kPa
η_f = Fin efficiency
η_0 = Overall surface efficiency
ρ = Density kg m^{-3}
σ = Cavitation number

Subscript

amb = Ambient
e = Exit
F = Fluid
f = Fin
i = Inception, inlet
s = Surface

References

[1] Mishra, C., and Peles, Y., 2005, "Cavitation in Flow Through a Micro-Orifice Inside a Silicon Microchannel," Phys. Fluids, **17**(1), pp. 013601-01–013601-15.
[2] Mishra, C., and Peles, Y., 2005, "Size Scale Effects on Cavitating Flows Through Micro-Orifices Entrenched in Rectangular Microchannels," J. Microelectromech. Syst., **14**, pp. 987–999.
[3] Mishra, C., and Peles, Y., 2005, "Flow Visualization of Cavitating Flows Through a Rectangular Slot Micro-Orifice Ingrained in a Microchannel," Phys. Fluids, **17**, pp. 113602–113602-14.
[4] Mishra, C., and Peles, Y., "Development of Cavitation in Refrigerant (R-123) Flow Inside Rudimentary Microfluidic Systems," accepted in J. Microelectromech. Syst..
[5] Mishra, C., and Peles, Y., "An Experimental Investigation of Hydrodynamic Cavitation in Micro-Venturis," submitted to Phys. Fluids.
[6] Kim, H.-Y., Kim, Y. G., and Kang, B. H., 2004, "Enhancement of Natural Convection and Pool Boiling Heat Transfer via Ultrasonic Vibration," Int. J. Heat Mass Transfer, **47**, pp. 2831–2840.
[7] Fand, R. M., 1965, "The Influence of Acoustic Vibrations on Heat Transfer by Natural Convection From a Horizontal Cylinder to Water," J. Heat Transfer, **87**, pp. 309–310.
[8] Li, K. W., and Parker, J. D., 1967, "Acoustical Effects on Free Convective Heat Transfer From a Horizontal Wire," J. Heat Transfer, **89**, pp. 277–278.
[9] Wong, S. W., and Chon, W. Y., 1969, "Effects of Ultrasonic Vibration on Heat Transfer to Liquids by Natural Convection and Boiling," AIChE J., **15**, pp. 281–288.
[10] Iida, Y., and Tsutsui, K., 1992, "Effects of Ultrasonic Waves on Natural Convection, Nucleate Boiling and Film Boiling Heat Transfer From a Wire to a Saturated Liquid," Exp. Therm. Fluid Sci., **5**, pp. 108–115.
[11] Zhou, D. W., Liu, D. Y., Hu, X. G., and Ma, C. F., 2002, "Effect of Acoustic Cavitation on Boiling Heat Transfer," Exp. Therm. Fluid Sci., **26**, pp. 931–938.
[12] Bergles, A. E., and Newell, P. H., Jr., 1965, "The Influence of Ultrasonic Vibrations on Heat Transfer to Water Flowing in Annuli," Int. J. Heat Mass Transfer, **8**, pp. 1273–1280.
[13] Bergles, A. E., 1964, "The Influence of Flow Vibrations on Forced-Convection Heat Transfer," J. Heat Transfer, **86**, pp. 559–560.
[14] Tullis, J. P., 1989, *Hydraulics of Pipelines*, Wiley, New York.
[15] Tullis, J. P., 1971, "Choking and Supercavitating Valves," J. Hydraul. Res., **97**, pp. 1931–1945.
[16] Kline, S., and McClintock, F. A., 1953, "Describing Uncertainties in Single-Sample Experiments," Mech. Eng. (Am. Soc. Mech. Eng.), **75**, pp. 3–8.
[17] Incropera, F. P., and DeWitt, D. P., 2002, *Introduction to Heat Transfer*, 4th ed., Wiley, New York, pp. 393–396.
[18] Kays, W. M., and Perkins, H. C., 1972, in *Handbook of Heat Transfer*, edited by W. M. Rohsenow and J. P. Hartnett, McGraw-Hill, New York, Chap. 7.
[19] Collier, J. G., and Thome, J. R., 1994, *Convective Boiling and Condensation*, 3rd ed., Oxford Science Publications, Oxford, pp. 255–259.

Pool Boiling Using Thin Enhanced Structures Under Top-Confined Conditions

Camil-Daniel Ghiu

Yogendra K. Joshi
e-mail: yogendra.joshi@me.gatech.edu

G.W. Woodruff School of Mechanical Engineering,
Georgia Institute of Technology,
Atlanta, GA 30332

An experimental study of pool boiling using enhanced structures under top-confined conditions was conducted with a dielectric fluorocarbon liquid (PF 5060). The single layer enhanced structures studied were fabricated in copper and quartz, had an overall size of 10×10 mm^2, *and were* 1 mm *thick. The parameters investigated in this study were the heat flux* (0.8–34 W/cm^2) *and the top space* S (0–13 mm). *High-speed visualizations were performed to elucidate the liquid/vapor flow in the space above the structure. The enhancement observed for plain surfaces in the low heat fluxes regime is not present for the present enhanced structure. On the other hand, the maximum heat flux for a prescribed* 85°C *surface temperature limit increased with the increase of the top spacing, similar to the plain surfaces case. Two characteristic regimes of pool boiling have been identified and described: isolated flattened bubbles regime and coalesced bubbles regime.* [DOI: 10.1115/1.2349503]

1 Introduction

Nucleate pool boiling, a very efficient way of transferring heat from a surface to a stationary bulk liquid, can be further intensified using enhanced structures [1–3]. Most of the published studies on this topic have treated only the unconfined case, that is, the movement of vapor/liquid was unrestricted around the structure. Pool boiling in confined spaces has applications in electronics cooling, where the available space is at a premium. Thus the assessment of boiling heat transfer under tight spatial constraint conditions, and its comparison with the open top case, is of significant importance.

Nucleate pool boiling from plain surfaces in narrow spaces constituted the subject of several experimental investigations, starting with the pioneering work of Katto and Yokoya [4] and Katto et al. [5]. They investigated the pool boiling of water in the narrow space created between two parallel, horizontal discs of 10 mm diameter brought in close proximity. For low to intermediate heat fluxes, the top confinement has a surprisingly beneficial effect, enhancing the heat transfer. The reason for the enhancement is believed to be the formation and subsequent evaporation of a thin liquid film beneath the squeezed bubbles. On the other hand, the performance decreases in the high heat flux regime. The magnitude of the critical heat flux is also diminished with increased confinement. Ishibashi and Nishikawa [6] studied the boiling in an annular vertical narrow space between two concentric cylinders, one heated and one not. Two flow regimes (isolated bubbles and coalesced bubbles) were identified. A correlating expression was also proposed. Yao and Chang [7] developed a boiling map having the Bond number and a specially defined boiling number as coordinates. Several boiling regimes (termed isolated deformed bubbles, slightly deformed bubbles and coalesced deformed bubbles) were identified based on visual observations. Fujita et al. [8] performed systematic experiments on heat transfer characteristics of pool boiling in a confined space formed between a rectangular heating surface and an opposed unheated plate. The heat transfer coefficients were found to increase with decrease of gap size at moderate heat fluxes. Bonjour and Lallemand [9] identified three regimes (nucleate boiling with isolated deformed bubbles, nucleate boiling with coalesced bubbles, and partial dryout) for boiling in a narrow rectangular vertical space. A new flow pattern map for confined boiling was proposed to determine the regimes.

The vast majority of studies dealing with boiling from enhanced surfaces were performed in an unconfined space. Very few authors investigated boiling from enhanced surfaces under spatial constraints. Nowell et al. [10] studied the influence of a confining plate on boiling FC-72 from a microconfigured heat sink. The heat sink was manufactured by etching discrete reentrant cavities in a silicon wafer. Five different gap sizes were tested (unconfined, $S=1$ mm, $S=2$ mm, $S=4$ mm, $S=6$ mm). The thermal performance decreased significantly for $S=1$ mm, whereas all the other gap sizes tested yielded approximately the same results as the unconfined case, within experimental uncertainty. Ramaswamy et al. [11] found that the top and side spacings have only a marginal effect on the boiling performance of a stack of six layers of structures of the present form (Fig. 1). A possible explanation for no marked difference between the various gap sizes is the three-dimensional morphology of the structure under consideration. Each layer contributes to the total heat flux so that constricting the top alone does not affect the thermal performance in a significant way. Chien and Chen [12] were apparently the only authors to study the effect of confinement from a single-layered enhanced structure. They tested a structure having cross-grooves in a special dielectric liquid (HFC 4310) at 75.5°C. The effective surface opening diameter and the total opening area were the most influential parameters for the boiling performance. A slight enhancement of heat transfer for confined case versus the unconfined case was noticed at low heat fluxes. In summary, no significant heat transfer enhancement resulting from top confinement could be recorded, for the range of heat fluxes tested.

The previously mentioned studies employing enhanced structures under constraint did not include visualizations of the boiling phenomena. Therefore, the specific heat transfer mechanisms were hypothesized based on the limited information offered by the boiling curves. The present study aims at a deeper understanding of the physics underlying the boiling under top confinement using enhanced structures. The gap between the enhanced structure and the confinement plate constitutes the main geometrical parameter varied in several steps. Boiling curves and high-speed visualizations of the boiling at a maximum frame rate of 2100 frames/s were obtained to elucidate the complicated boiling phenomena. The objectives of this study are therefore to

---

Contributed by the Heat Transfer Division of ASME for publication in the Journal of Heat Transfer. Manuscript received October 14, 2005; final manuscript received June 16, 2006. Review conducted by Raj M. Manglik.

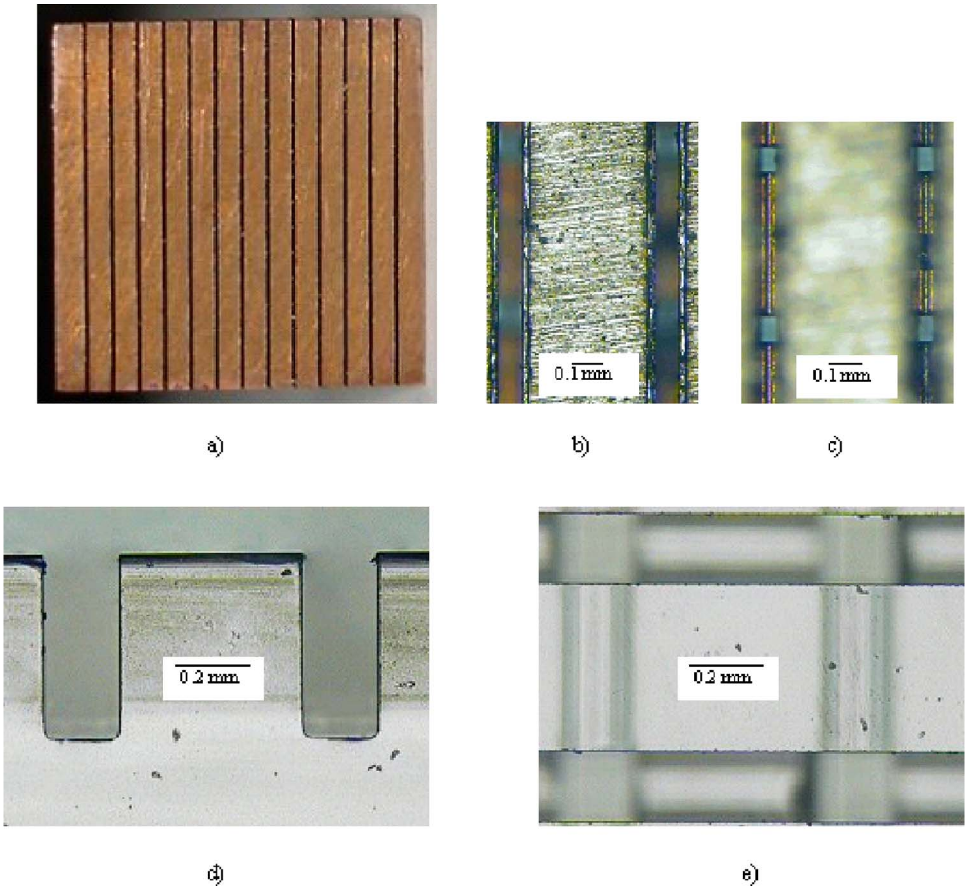

Fig. 1 Enhanced structures used in this study. (*a*) Frontal view of structure C-0.105-0.7. (*b*) Magnified micrographs of two top channels of the structure C-0.105-0.7. (*c*) Pore formation at the intersection of microchannels. (*d*) Magnified lateral view of the quartz structure Q-0.200-0.7. (*e*) Magnified top view of the quartz structure Q-0.200-0.7.

a. clarify the influence of top confinement on boiling heat transfer from enhanced structures,
b. elucidate the heat transfer mechanisms through high-speed visualizations, and
c. characterize the boiling phenomena by identifying the regimes (modes) established for different top gaps and heat flux levels.

2 Experimental Setup and Procedure

A schematic diagram and optical micrographs of the enhanced structures utilized in this study are presented in Fig. 1. The structures were single layered and fabricated in copper and quartz with the overall dimensions $10 \times 10 \times 1$ mm^3. Detailed geometrical parameters are presented in Table 1. The single-layered structures were placed in a horizontal position inside a thermosyphon loop consisting of an evaporator chamber, connecting tubes, and a condenser. Figure 2(*a*) shows the cartridge heater assembly attachment to the structure, which was utilized for heating and surface temperature measurement. Four copper-constantan sheathed thermocouples (0.127 mm wire diameter) were embedded in the copper rod housing the cartridge heater, starting 4 mm below the enhanced structure. The thermocouples were used to calculate the temperature at the base of the enhanced structure (by extrapolation) as well as the heat flux at the base of the enhanced structure, assuming one-dimensional heat conduction. In calculating the heat flux, a value of $k=388$ W/m·k was used for the thermal conductivity of copper, as indicated by the material vendor. For quartz, the value employed was $k=1.2$ W/m·K. A more detailed discussion on structure fabrication and experimental setup can be found in a previous paper published by the authors [3]. A quartz tube having a square cross section was mounted vertically above the enhanced structure. This device permitted the variation of the top spacing S (Fig. 2(*b*)). A square quartz plate with the same dimensions as the enhanced structure ($10 \times 10 \times 1$ mm^3) was attached at one end of the tube and served as the confining surface/visualization port.

Prior to each experimental run, the setup components were cleaned with ethanol. After the cleaning, the thermosyphon loop was filled with a fresh quantity of PF 5060. A note should be made about the wettability of the working fluid. The dielectric fluoro-

Table 1 Geometric characteristics of the structures employed in the present study

Structure identification	Channel width W_t (mm)	Channel pitch P_t (mm)	Channel depth H_t (mm)	Top spacing S (mm)
C-0.105-0.7	0.105	0.70	0.6	0, 0.15, 0.35, 0.6, 0.7, 1, 1.75, 13
Q-0.105-0.7	0.105	0.70	0.6	0.5
Q-0.200-0.7	0.200	0.70	0.6	0.5

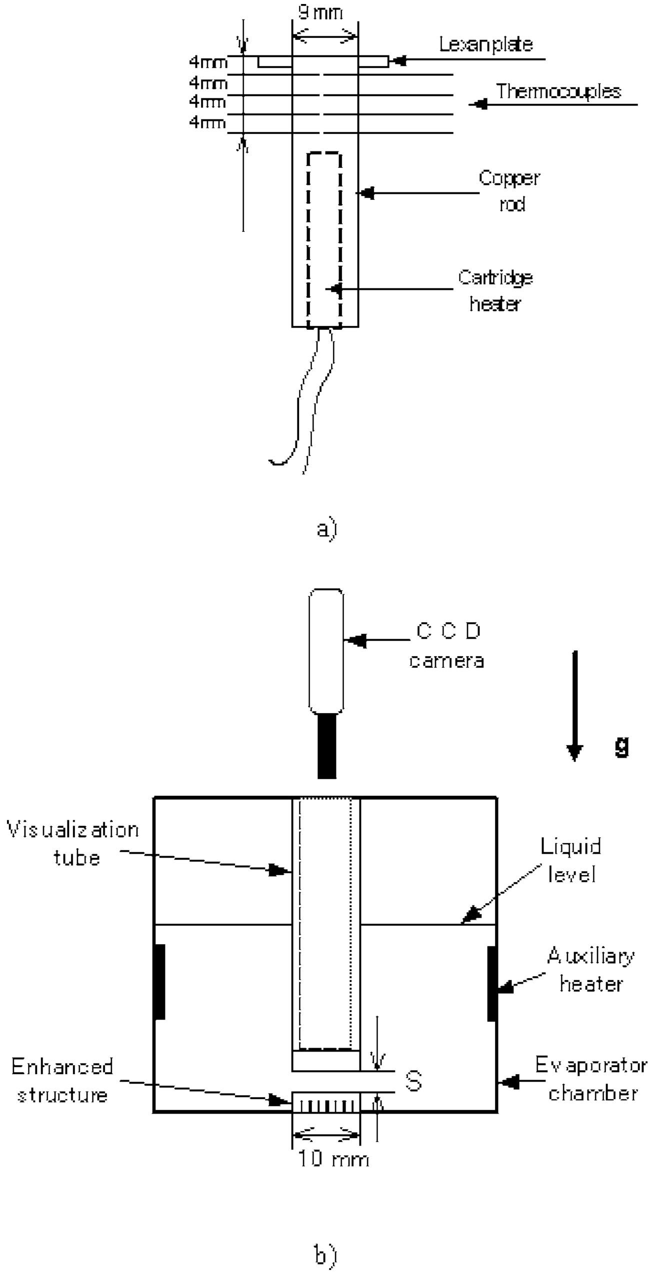

Fig. 2 Schematic of the setup: (*a*) heater assembly and (*b*) boiling chamber with the visualization tube

carbons have an extremely low contact angle with most surface materials. For PF 5060 with copper, the value cited in literature is less than one degree [13]. The pool of liquid was kept at saturation (~56°C at 1 atm) during the experiments. For heat inputs $q > 5$ W (heat flux 4.8 W/cm^2) through the copper rod, saturated boiling conditions existed. For lower heat inputs four auxiliary heaters (shown in Fig. 2(*b*)) were employed in the boiling chamber, in addition to the main heater, to maintain saturation conditions throughout the run. A degassing operation preceded every. During degassing the system pressure was always the atmospheric pressure, while an electrical power input of ~10 W was applied via the cartridge heater. The liquid was boiled vigorously for about one hour, and then allowed to cool down until it reached room temperature. During the cooling period, the thermosyphon loop was isolated from the atmosphere. This procedure prevented some of the desorbed gases to get absorbed again in the liquid. It also ensured that the dissolved gas concentration was the same at the beginning of every run (see Ref. [3]).

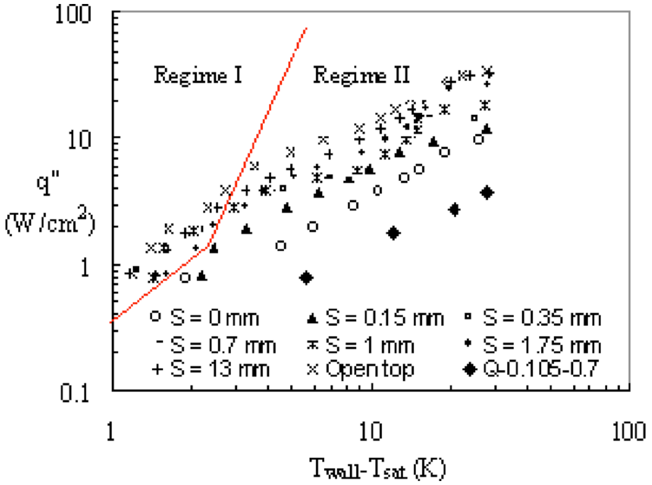

Fig. 3 Boiling curves for various top gaps. The lines delineate the observed flow regimes.

The electrical power to the cartridge heater was provided in decrementing steps to avoid possible hysteresis effects. The temperatures at various locations on the cartridge and the fluid bulk were monitored continuously. After reaching steady state, defined as the temperature at all locations remaining within a band of 2°C, temperatures were recorded for 35 min and mean values were subsequently used to determine the surface temperature and the heat input. The electrical power input was calculated by multiplying the voltage drop across the heater with the line current. The heat loss (defined as the difference between the electrical power input and the heat input) was always within 10%. The heat flux was calculated based on the area of the structure footprint (10×10 mm^2). The experiments were performed for power inputs resulting in a maximum temperature at the base of the enhanced structure of 85°C. This simulates conditions of interest in cooling of silicon-based electronic devices.

A Phantom high-speed CCD camera was used for visualization purposes. For stability and alignment purposes, a tripod equipped with a multi-axis bubble level supported the camera. The camera can capture a maximum of 1000 frames per second at full resolution (512×512 pixels). With a reduction in the field of view,

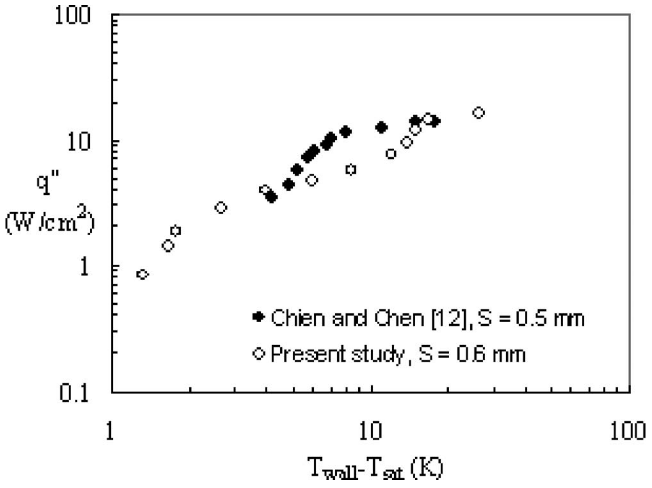

Fig. 4 Comparison between present data and Chien and Chen [12] data.

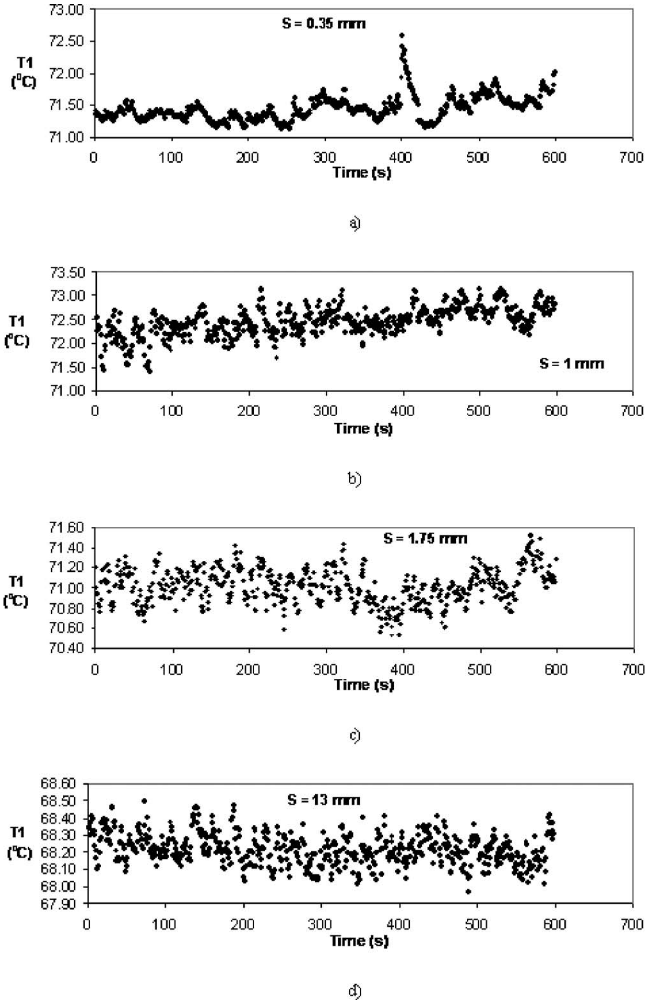

Fig. 5 Temperature traces at steady state (structure C-0.105-0.7, $q''=12\ \mathrm{W/cm^2}$). (*a*) $S=0.35$ mm. (*b*) $S=1$ mm. (*c*) $S=1.75$ mm. (*d*) $S=13$ mm.

higher frame rates can be achieved. A range of frame rates (minimum 100 fr/s, maximum 2100 fr/s) was employed. A zoom lens (Navitar 12×Zoom) attached to the camera through an adapter (Navitar 0.67×) was used to magnify the area of interest and work at close distances to the enhanced structure. The lens is capable of a variable magnification of 1–12 times the original size of the object. A 150 W Moritex fiber optic light source was used for providing light to the structure. Movies and still pictures were taken from the top and sides of the structures. After capture, the movies were played back at slower speed. From the movies selected frames (single pictures) were extracted.

3 Measurements and Uncertainty Analysis

The thermocouples and the data acquisition system were calibrated against a precision mercury thermometer at ice point to an uncertainty of 0.1 K. The precision resistor employed for current measurement was accurate to 1%. The uncertainty in the channel width (5 μm) was due to the uneven width with the depth. The uncertainty in the top spacing S was estimated at 25 μm. The resulting maximum uncertainty in the heat flux was ±15% at low heat fluxes (with over 85% of the data within ±10%). The uncertainty in the wall superheat values was ±0.2 K.

4 Results

4.1 Boiling Curves. The boiling curves obtained for various top gaps for the copper structure C-0.105-0.7 are presented in Fig. 3. The presence of a confining plate at a certain distance above the top surface of the enhanced structures changes the shape of the boiling curve relative to the open top case. The plate restricts the vapor/liquid movement above the structure; it is therefore expected that the boiling phenomena will differ from the open top case. For an open case configuration, the vapor rises unrestricted towards the free surface of the liquid pool. With a confining plate, the vapor accumulates at the top quartz surface prior to leaving laterally.

The shift to the left of the boiling curves with increasing S indicates improvement in heat transfer performance, nearly approaching the unconfined pool boiling performance for $S=13$ mm. Two features are particularly remarkable from the examination of the boiling curves. First, the enhancement of heat transfer over the open case at low heat fluxes is no longer present. This result is in contrast with the data reported for plain surfaces [3–5], but similar to the findings of previous investigations involving enhanced structures [10,12]. The particularity of boiling from enhanced structures is the generation of vapor primarily inside the structure, followed by its ejection into the surrounding pool. The nucleation is therefore replaced by expulsion from specific locations. A possible explanation for the lack of enhancement is based on the fact that enhanced evaporation is already taking place inside the structure. The nature of the working fluids employed also plays a significant role. For PF 5060, the latent heat of vaporization is very low ($h_{fg}=88$ kJ/kg at atmospheric pressure) compared to coolants such as water.

The second characteristic feature in Fig. 3 is the decrease in performance with decreasing S at high heat fluxes. The largest heat flux attainable (with the wall temperature maintained below 85°C) increased with the increase of the top spacing. This value was not known a priori; therefore a trial and error method was applied to arrive at the highest value of q'' with the maximum surface temperature of 85°C. For $S=0.15$ mm, the highest heat flux is $q''=12.2\ \mathrm{W/cm^2}$. This value increases to $q''=26.6\ \mathrm{W/cm^2}$ for $S=1.75$ mm. A top space of 13 mm ensures a similar performance at high heat fluxes as for open top.

The shapes of the boiling curves plotted in Fig. 3 reflect the effect of confinement on the boiling from enhanced structures. For $S=0$ mm (completely closed top) the curve is almost linear (in log-log coordinates). As the top gap increases, the corresponding boiling curves deviate from the linearity. A common characteristic of curves for $S=0.35-1.75$ mm is their S shape. At low heat fluxes the curves are almost linear with a steep slope yielding a high heat transfer coefficient. For the intermediate range of heat fluxes the curves become concave. The slope of the curve decreases corresponding to a decrease in performance. This decrease in performance can be attributed to a change in the liquid/vapor conditions in the space above the enhanced structure. The increase in vapor production is not doubled by a corresponding increase in the vapor release capability. This creates an almost stationary vapor blanket on top of the enhanced structure, as seen in the visualizations later. An almost vertical region follows the concave portion of the boiling curve. It is believed that a very efficient (high heat transfer coefficient) mode of boiling, valid for a narrow range of heat fluxes and top gaps, is established. Finally, the curves take a convex, descendent form.

Figure 3 also includes a boiling curve for structure Q-0.105-0.7. The results correspond to a top gap $S=0.5$ mm. The curve displays the expected decrease in thermal performance due to the additional thermal resistance of the transparent enhanced structure.

A comparison of the present boiling data and the results of Chien and Chen [12] is presented in Fig. 4. A set of data from the current investigation (for $S=0.6$ mm) is plotted along with a boil-

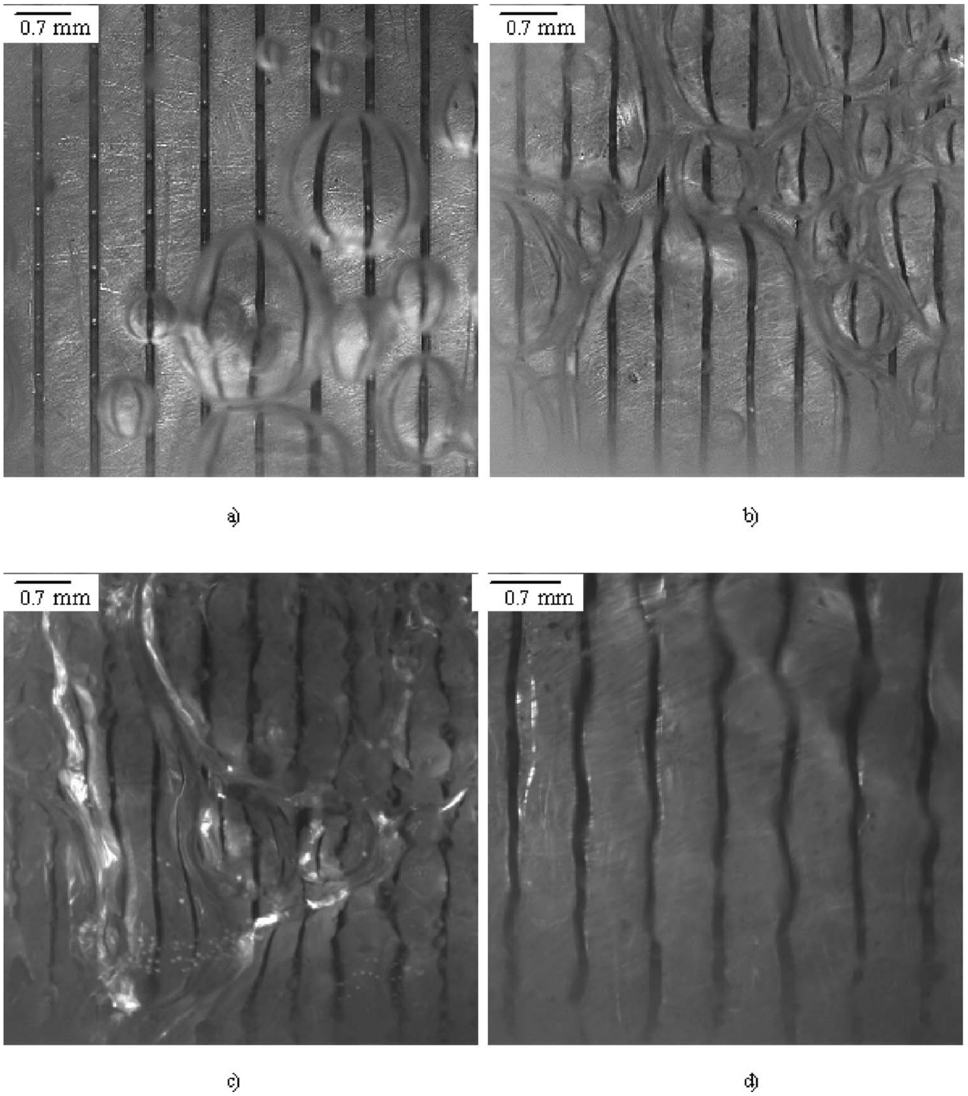

Fig. 6 Visualization of boiling for top gap $S=1.75$ mm. (*a*) Individual bubbles are present, $q''=0.8\ \mathrm{W/cm^2}$. (*b*) Coalescence occurs producing bubble clusters, $q''=5.7\ \mathrm{W/cm^2}$. (*c*) Almost entire space is filled with vapor, $q''=14.5\ \mathrm{W/cm^2}$. (*d*) Vapor filled space with a wavy interface, $q''=24.4\ \mathrm{W/cm^2}$.

ing curve from their study (for $S=0.5$ mm). The authors did not report data for heat fluxes $q''\leqslant 3\ \mathrm{W/cm^2}$. For intermediate heat fluxes ($4\ \mathrm{W/cm^2}\leqslant q''\leqslant 14\ \mathrm{W/cm^2}$) their enhanced structures exhibited a much better heat transfer performance. The two curves intersect at higher heat fluxes ($14\ \mathrm{W/cm^2}\leqslant q''$). Several differences in the experimental conditions should be mentioned: the Chien and Chen data are obtained with cross-grooved enhanced structures placed vertically in a pool of HFC4310 at saturation ($T_{\mathrm{sat}}=75.5\,^\circ\mathrm{C}$ at atmospheric pressure). The vertical configuration may have a beneficial effect on the heat transfer performance, due to buoyancy induced circulation. The data from Chien and Chen [12] were used for comparison in the present study as the closest match in experimental conditions that could be found in the literature.

The steady-state temperature measurements show interesting characteristics. A sufficiently long time (1 hour nominally) was allowed to pass between the application of power level and the start of data collection. Figure 5 presents several temperature records for $q''=12\ \mathrm{W/cm^2}$, each corresponding to a different top gap S. The temperature T_1 was measured at a location situated 4 mm below the top surface of the copper rod. Figure 5(*a*) ($S=0.35$ mm) shows a fairly smooth temperature profile, with one spike of $\sim 1\,^\circ\mathrm{C}$. The dominant frequency obtained using a fast Fourier transform is 0.01 Hz. A considerable difference between the maximum and minimum recorded temperatures ($\sim 1.5\,^\circ\mathrm{C}$) characterize the temperature recording for $S=1$ mm (Fig. 5(*b*)). As the top gap increases, the temperature trace presents oscillations of lesser amplitude ($1.2\,^\circ\mathrm{C}$) (Fig. 5(*c*), $S=1.75$ mm). This is probably the effect of the decreasing influence of the confining plate on the boiling phenomena with increasing top gap S. Figure 5(*d*) (recorded for a maximum top gap $S=13$ mm) displays a temperature profile with minimum/maximum values within $0.5\,^\circ\mathrm{C}$. For this last case, the dominant frequency is higher (0.04 Hz). It can be inferred that as the top gap increases, the vapor formations depart move easily from the space above the structure. This fact is reflected in the dominant frequency captured in the FFT.

4.2 Visualizations. High-speed visualizations were performed from the top and sides of enhanced structures made of both copper and quartz. The quartz plate placed parallel to the top surface of the structure (Fig. 2(*b*)) permitted visualization of

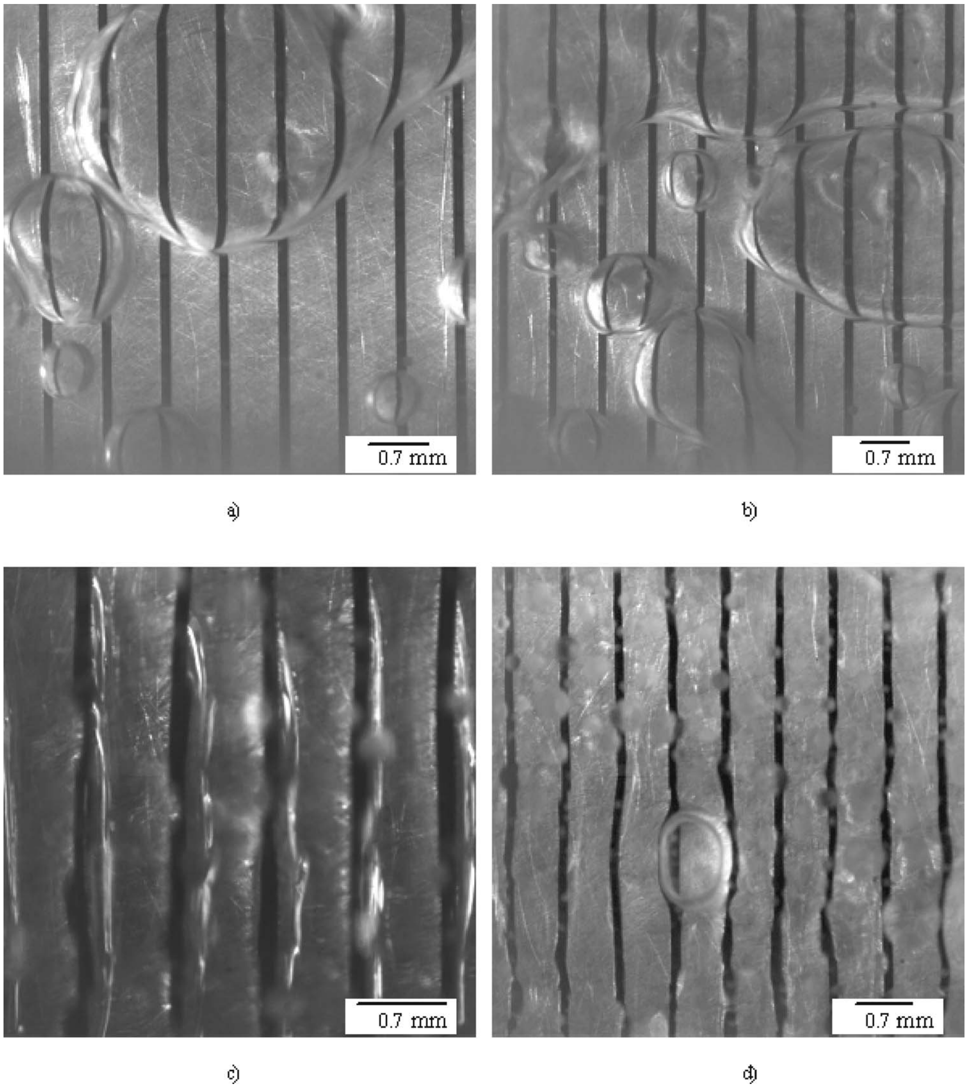

Fig. 7 Visualization of boiling for top gap $S=1$ mm. (*a*) Vapor covers portions of the top surface, $q''=0.9\ \mathrm{W/cm^2}$. (*b*) Individual bubbles are feeding the vapor formations from below, $q''=5.6\ \mathrm{W/cm^2}$. (*c*) Higher magnification view of the top channels, $q''=14.5\ \mathrm{W/cm^2}$. (*d*) Boiling phenomena at the highest tested heat flux, $q''=18.3\ \mathrm{W/cm^2}$.

liquid-vapor conditions above the enhanced structure. The acquired data consisted of movies and still pictures. The photographic observations are described in the following sections.

4.2.1 Copper Structure. The enhanced structure C-0.105-0.7 was employed for both heat transfer measurements and flow visualizations. A frontal top view of the structure is presented in Fig. 1(*a*). Figures 6–9 present the boiling phenomena for selected top gaps. The top channels are seen as dark vertical lines in these figures.

a. $S=1.75$ mm. Figure 6 captures representative instances of boiling for top gap $S=1.75$ mm. The influence of the confining plate is weakly felt for the low heat fluxes. Since the distance between the confining plate and the structure is quite large, the bubbles could be observed forming and emerging from the structure at low heat fluxes. Figure 6(*a*) presents the boiling phenomena at the lowest heat flux tested ($q''=0.8\ \mathrm{W/cm^2}$). Bubbles can be seen emerging from the subsurface pores and feeding larger vapor formations at the top surface. The inactive pores (the shining spots on the left side of the structure) can also be noticed. No bubble nucleation from the top surface of the structure was observed. With the increase in heat flux, the vapor fills almost entirely the space above the structure (Fig. 6(*b*), $q''=5.7\ \mathrm{W/cm^2}$). However, the vapor formations maintain their individuality. An even higher level of heat flux brings about more dynamic vapor behavior: the vapor masses coalesced almost entirely, and the upper vapor/liquid interface becomes wavy. As a result, the top surface of the enhanced structure cannot be seen clearly anymore (Fig. 6(*c*), $q''=14.5\ \mathrm{W/cm^2}$). The last picture of this set shows a single vapor cluster above the structure, with a wavy interface (Fig. 6(*d*), $q''=24.4\ \mathrm{W/cm^2}$).

b. $S=1$ mm. Starting at the lowest tested heat flux ($q''=0.9\ \mathrm{W/cm^2}$) vapor formations could be seen accumulating at the top of the structure. These vapor masses are the result of the coalescence of small bubbles emerging from the pores (Fig. 7(*a*)). With the increase in heat flux, the fraction of the top surface filled with vapor formations increases. In Fig. 7(*b*) ($q''=5.6\ \mathrm{W/cm^2}$) several individual bubbles feeding the coalesced vapor regions from underneath (top right corner) are noticeable. A higher

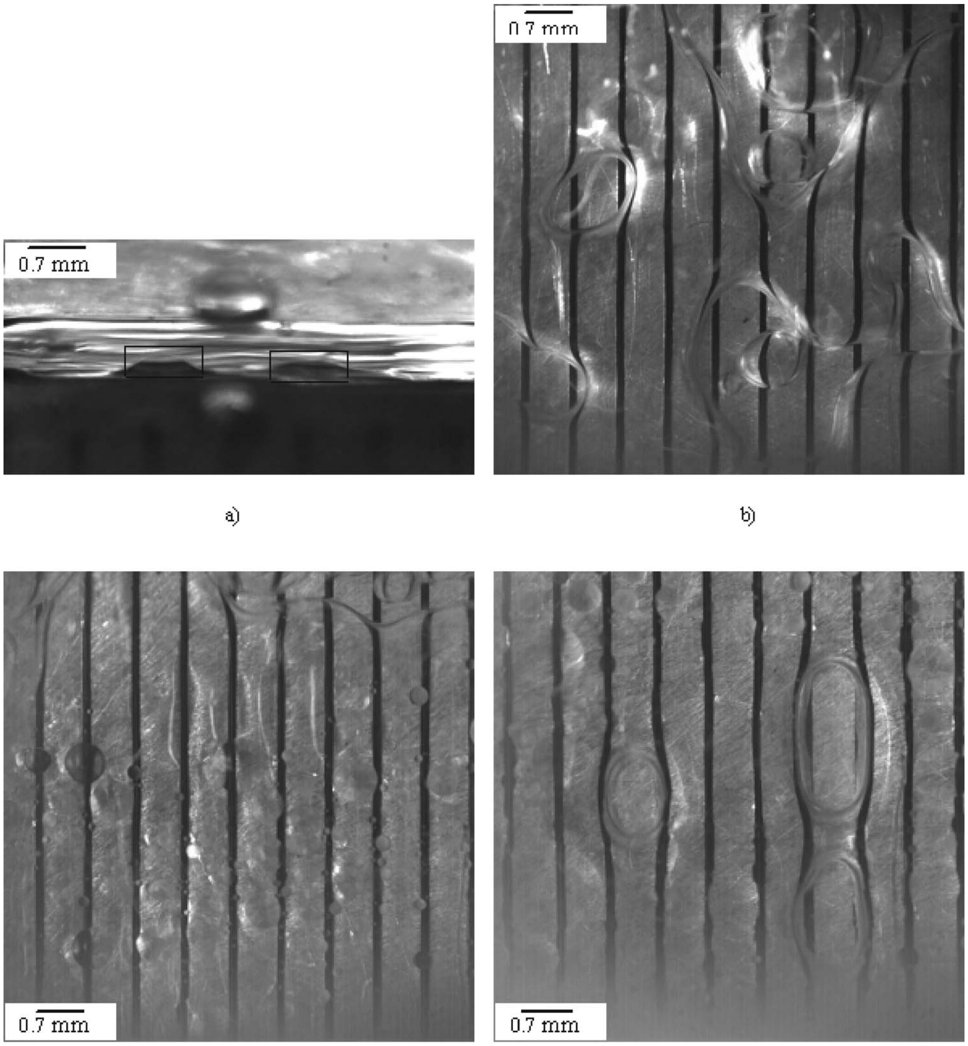

a)

b)

c)

d)

Fig. 8 Visualization of boiling for top gap $S=0.7$ mm. (*a*) Lateral view of two bubbles entering the vapor mass, $q''=0.8\ \mathrm{W/cm^2}$. (*b*) Coalesced vapor formations occupy much of the top space, $q''=3.8\ \mathrm{W/cm^2}$. (*c*) Wavy interface, droplets on top surface, $q''=7.6\ \mathrm{W/cm^2}$. (*d*) Liquid plugs entrapped in the vapor mass, $q''=16.5\ \mathrm{W/cm^2}$.

magnification is used to illustrate specific vapor formations occurring at a higher heat flux (Fig. 7(*c*), $q''=14.5\ \mathrm{W/cm^2}$). Liquid droplets start to adhere to the lower surface of the confining quartz plate. Some of the events occurring at the highest heat flux tested are shown in Fig. 7(*d*). Remarkable are the wavy interface and the liquid encapsulated in elongated slugs. Due to the wavy liquid/vapor interface, the individual bubble feeding could not be observed for this level of heat flux.

c. $S=0.7$ mm. Further decreasing the top gap makes the confinement influence more pronounced. Figure 8(*a*) presents a side view of phenomena occurring at $q''=0.8\ \mathrm{W/cm^2}$. This lateral view shows two bubbles emerging from the structure and feeding the vapor space above. The bubbles are bell-shaped. For better visibility, these are marked with black lines. At a higher heat flux ($q''=3.8\ \mathrm{W/cm^2}$) vapor formations occupy the majority of the top space, with some individual bubbles still visible (Fig. 8(*b*)). At higher heat flux the upper liquid/vapor interface becomes wavy, with some liquid droplets residing on the surface of quartz plate facing the enhanced structure ($q''=7.6\ \mathrm{W/cm^2}$). At a much higher heat flux, liquid portions taking the shape of slugs entrapped in the vapor mass are noticed (Fig. 8(*d*)). ($q''=16.5\ \mathrm{W/cm^2}$).

d. $S=0.35$ mm. A sequence of 8 frames captured at a rate of 500 frames/s is presented in Fig. 9(*a*). It shows the growth and coalescence of two individual flattened bubbles for $q''=0.9\ \mathrm{W/cm^2}$. The frames presented are 4 ms apart, except the last two, which are 2 ms apart. The limited space available above the structure forces the bubbles to grow laterally. At some point, coalescence occurs and larger vapor clusters form. Another feature revealed by the visualizations was the existence of thin liquid films between the top surface of the structure and the vapor mass (Fig. 9(*b*), $q''=5.8\ \mathrm{W/cm^2}$). The edges of the films are more clearly seen in Fig. 9(*c*) ($q''=14.3\ \mathrm{W/cm^2}$). Liquid entrapment in the form of slugs takes place; such a formation is visible at the bottom of the image.

4.2.2 Quartz Structures. Intrinsic limitations restrict the amount of information offered by visualizations from the copper enhanced structure. The accessible regions are the envelope surfaces of the structure and partially the top channels. The use of a

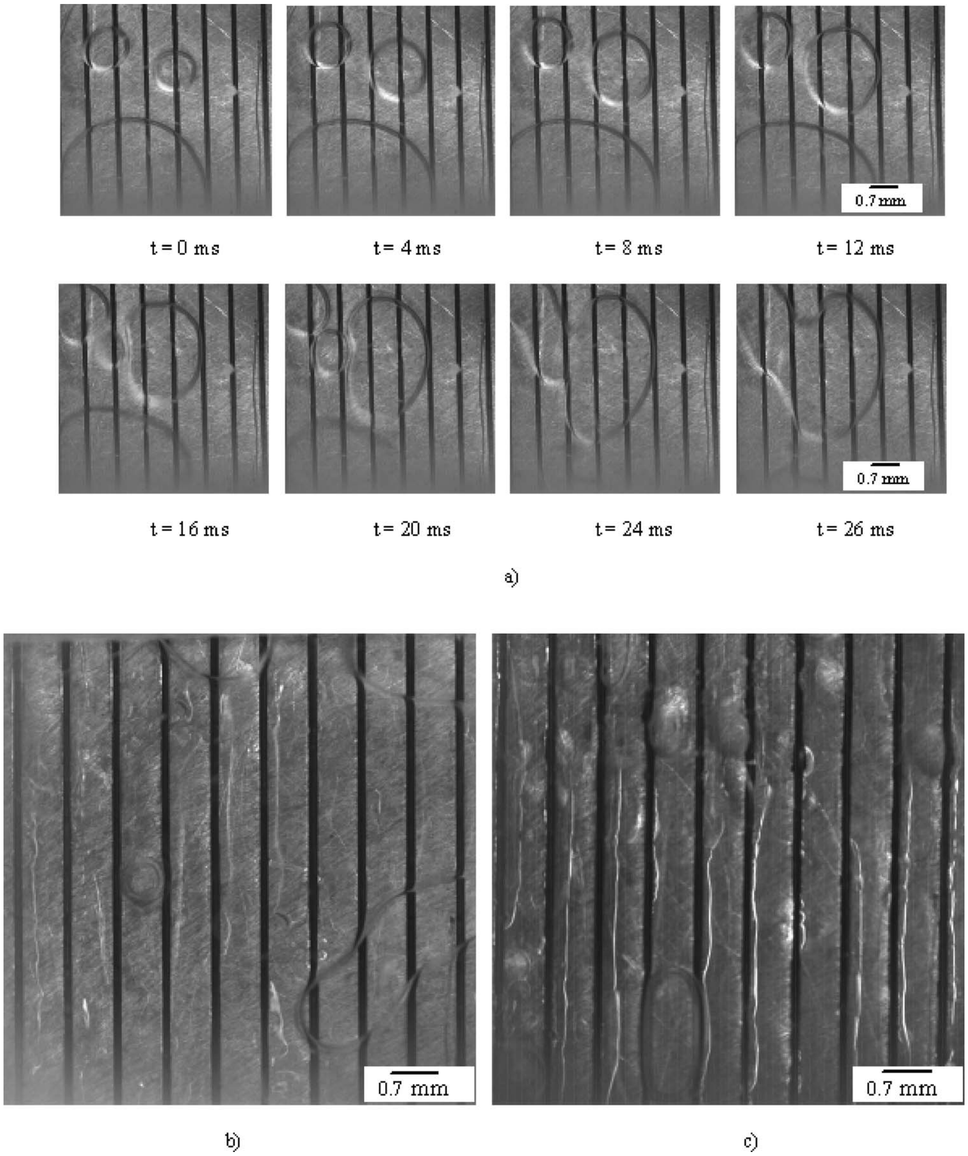

Fig. 9 Visualization of boiling for top gap $S=0.35$ mm. (*a*) Growth and coalescence of two individual bubbles, $q''=0.9$ W/cm^2. (*b*) Thin liquid films forming on the top surface, $q''=5.8$ W/cm^2. (*c*) Thin liquid film edges and liquid plugs, $q''=14.3$ *W*/cm^2.

transparent material for the enhanced structures can extend the field of view and lead to a qualitative understanding of the two-phase phenomena occurring in the interior of the structure. Quartz was chosen for the current investigation due to its easy manufacturability. The detailed geometrical dimensions for the quartz structures employed in the current study are included in Table 1. Figures 1(*d*) and 1(*e*) illustrate magnified lateral and frontal views of two top channels of the quartz structure Q-0.200-0.7.

The visualizations, performed from above the structure, provide useful insights. Due to the transparent nature of quartz, the bottom channels are available for optical investigation. In Fig. 10, $S=0.5$ mm, the top channels are oriented vertically and the bottom channels horizontally. Boiling started at discrete sites located on the heated surface of the bottom channels. Once a nucleation site becomes active, the vapor bubble, bounded by the channels walls, expands laterally and towards the top channels through the pores. The vapor takes the shape of an elongated slug, which advances and retreats periodically. The region above the structure is only partially occupied by flattened vapor bubbles (Fig. 10(*a*), $q''=1.8$ W/cm^2). No vapor formation can be seen in most of the channels. Maintaining the same heat flux, a higher magnification view (Fig. 10(*b*)) allows the observation of liquid films formed between the advancing vapor slug and solid walls. The slug forms below a vapor formation situated in the top gap formed between the enhanced structure and the confining quartz plate. The increase in heat flux increases the quantity of vapor produced in the bottom channels and released towards the top of the structure. Figure 10(*c*) ($q''=3.8$ W/cm^2) presents a few top channels being supplied with vapor from the bottom channels. This vapor advection takes place through the pores. The vapor takes an elongated form, expanding laterally prior to joining the vapor mass residing above the structure. For the highest heat flux tested with the quartz structure (Fig. 10(*d*), $q''=4.8$ W/cm^2), vapor fills the entire top gap, with a few liquid portions towards the edges of the structure. Vapor slugs of various lengths, emerging from the pores, can be seen in the top channels.

The advancing/receding vapor slugs constitute the main feature of boiling from enhanced structures. With the increase in the heat

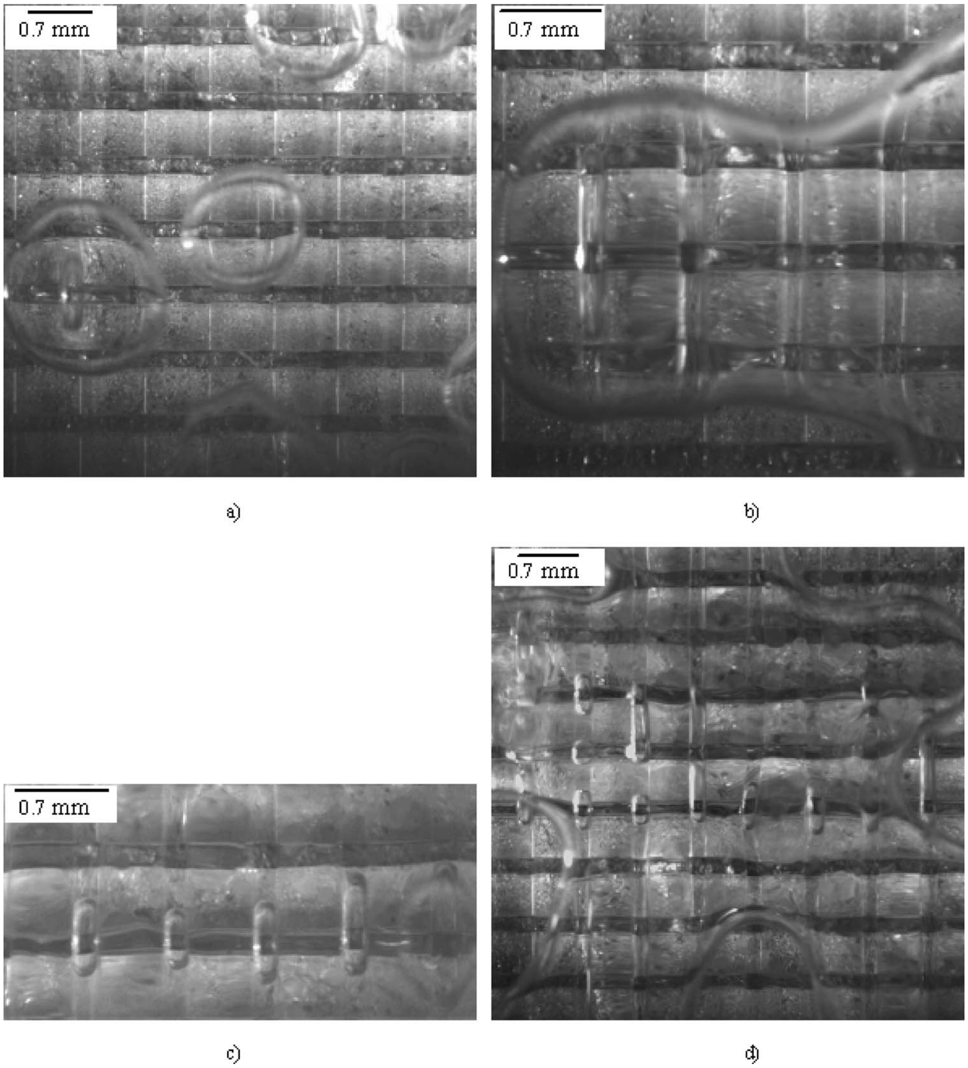

Fig. 10 Visualization of boiling for structure Q-0.200-0.7. (*a*) A few flattened vapor bubbles rise above the structure, $q''=1.8$ W/cm^2. (*b*) Vapor slug forming inside a bottom channel, $q''=1.8$ W/cm^2. (*c*) Deformed vapor bubbles reside in the top channels, $q''=3.8$ W/cm^2. (*d*) Vapor fills the entire gap space, $q''=4.8$ W/cm^2.

input, more vapor slugs are forming. They are moving faster along the channels; their lifetime decreases considerably. Coalescence/breakage occurs at a higher rate.

4.2.3 Discussion. Despite the fact that two orders of magnitude separate the values of copper and quartz thermal conductivity, the visualizations performed with transparent structures provide useful information about the specifics of boiling from enhanced structures in general. These observations can be extrapolated to the phenomena occurring with copper structures. It is assumed that the mechanism of vapor formation and coalescence in the bottom channels, followed by migration to the top channels through the pores, is similar. This conjecture is supported by several boiling events observed for structure C-0.105-0.7. At low heat fluxes, the vapor is formed in the bottom channels and ejected through the pores into the liquid pool. Another remarkable phenomenon is the lack of nucleation sites on top channels.

The data collected for different top gap spaces S and over a large range of heat fluxes allow a division of the nucleate boiling curve into subregimes. This division is marked with solid line segments in Fig. 3. The regimes are the *isolated flattened bubbles* regime (regime I in Fig. 3) occurring at low heat fluxes and large top gaps and the *coalesced bubbles* regime (regime II in Fig. 3) for high heat fluxes or low heat fluxes and small top gaps. Characteristics of the *isolated flattened bubbles* regime are individual bubbles are ejected from the top channels and feed the vapor clusters from below. The heat transfer coefficient is the highest for this regime. The *coalesced bubbles* regime implies the existence of a hovering vapor mass covering almost entirely and permanently the top surface of the structure. This vapor cluster entraps liquid drops inside; it presents a wavy upper liquid/vapor interface.

The proposed division of the boiling curve into two subregimes is applicable for boiling from structures made of high thermal conductivity materials. However, its validity may be extended to enhanced structures made of low thermal conductivity materials, but for a different range of heat fluxes.

5 Conclusions

1. The heat transfer performance of the enhanced structures in nucleate pool boiling under top-confined conditions depends significantly on the top gap parameter S. The enhancement observed for plain surfaces in the low heat flux regime is not present for the present enhanced structure. The maximum

heat flux dissipated increased with the increase of the top spacing, similar to the plain surface case.

2. The vapor is generated primarily inside the bottom channels. It is ejected through the pores as bubbles toward the top channels. Here the vapor deforms, taking the shape of elongated slugs extending laterally prior to detachment and accumulation into a vapor mass at the bottom surface of the confining plate.
3. The nucleate boiling region of the boiling curve can be broadly divided into the regimes of *isolated flattened bubbles and coalesced bubbles*.

Acknowledgment

This work was supported by Semiconductor Research Corporation Contract No. 649.001 and Defense Advanced Research Projects Agency HERETIC Program under Contract No. N00164-99-C-0039.

Nomenclature

A = area of the structure (projected) (m^2)
h_{fg} = latent heat of vaporization (kJ/kg)
H_t = channel depth (m)
k = thermal conductivity (W/m·K)
P_t = channel pitch (m)
q'' = heat flux based on projected surface area (W/m^2)
q = heat rate (W)
S = top gap distance (m)
T_{sat} = saturation temperature of liquid, PF 5060 (K)
T_{wall} = temperature at base of enhanced structure (K)
W_t = channel width (m)
ΔT_w = wall superheat (K)

References

[1] Nakayama, W., Nakajima, T, and Hirasawa, S., 1984, “Heat Sink Studs Having Enhanced Boiling Surfaces for Cooling of Microelectronic Components,” ASME Paper No. 84-WA/HT-89.

[2] Ramaswamy, C., Joshi, Y., Nakayama, W., and Johnson, W. B.,2003, “Effects of Varying Geometrical Parameters on Boiling From Microfabricated Enhanced Structures,” ASME J. Heat Transfer, **125**, pp. 103–109.

[3] Ghiu, C.-D., and Joshi, Y., 2005, “Boiling Performance of Single-Layered Enhanced Structures,” ASME J. Heat Transfer, **127**, pp. 675–683.

[4] Katto, Y., and Yokoya, S., 1966, “Experimental Study of Nucleate Pool Boiling in Case of Making Interference-Plate Approach to the Heating Surface,” Proc. Third International Heat Transfer Conf., Chicago, IL, Vol. 3, pp. 219–227.

[5] Katto, Y., Yokoya, S., and Teraoka, K., 1977, “Nucleate and Transition Boiling in a Narrow Space between two Horizontal, Parallel Disk Surfaces,” Bull. JSME, **20**, pp. 638–643.

[6] Ishibashi, E., and Nishikawa, K., 1969, “Saturated Boiling Heat Transfer in Narrow Spaces,” Int. J. Heat Mass Transfer, **12**, pp. 863–894.

[7] Yao, S.-C., and Chang, Y., 1983, “Pool Boiling Heat Transfer in a Confined Space,” Int. J. Heat Mass Transfer, **26**, pp. 841–848.

[8] Fujita, Y., Ohta, H., Uchida, S., and Nishikawa, K., 1988, “Nucleate Boiling Heat Transfer and Critical Heat Flux in Narrow Space between Rectangular Surfaces,” Int. J. Heat Mass Transfer, **31**, pp. 229–239.

[9] Bonjour, J., and Lallemand, M., 1998, “Flow Patterns During Boiling in a Narrow Space Between Two Vertical Surfaces,” Int. J. Multiphase Flow, **24**, pp. 947–960.

[10] Nowell, R. M., Bhavnani, S. H., and Jaeger, R. C., 1995, “Effect of Channel Width on Pool Boiling From a Microconfigured Heat Sink,” IEEE Trans. Compon., Packag. Manuf. Technol., Part A, **18**, pp. 534–539.

[11] Ramaswamy, C., Joshi, Y., Nakayama, W., and Johnson, W. B., 1999, “Thermal Performance of a Compact Two-Phase Thermosyphon: Response to Evaporator Confinement and Transient Loads,” J. Enhanced Heat Transfer, **6**, pp. 279–288.

[12] Chien, L.-H., and Chen, C.-L., 2001, “Experiments of Boiling on Cross-Grooved Surfaces in a Confined Space,” Proc. National Heat Transfer Conf., Anaheim, CA, pp. 1–8.

[13] Danielson, R. D., Tousignant, L., Bar-Cohen, A., 1987, “Saturated Pool Boiling Characteristics of Commercially Available Perfluorinated Inert Liquids,” Proceedigs of 1987 ASME-JSME Thermal Engineering Joint Conference, Honolulu, HI, P. J. Marto and I. Tanasawa (eds.), Vol. 3, pp. 419–430.

Evaporation/Boiling in Thin Capillary Wicks (I)—Wick Thickness Effects

Chen Li
Graduate Research Assistant
Student member of ASME
Rensselaer Polytechnic Institute,
Department of Mechanical, Aerospace and
Nuclear Engineering,
Troy, NY 12180
e-mail: lic4@rpi.edu

G. P. Peterson
Professor and Chancellor
University of Colorado,
Boulder, CO 80309
e-mail: Bud.Peterson@colorado.edu

Yaxiong Wang
Principal Engineer
Foxconn Thermal Technology Inc.,
Austin, TX 78758
e-mail: yaxiongwang@foxconn.com

Presented here is the first of a two-part investigation designed to systematically identify and investigate the parameters affecting the evaporation/boiling and critical heat flux (CHF) from thin capillary wicking structures. The evaporation/boiling heat transfer coefficient, characteristics, and CHF were investigated under steady-state conditions for a variety of capillary structures with a range of wick thicknesses, volumetric porosities, and mesh sizes. In Part I of the investigation we describe the wicking fabrication process and experimental test facility and focus on the effects of the capillary wick thickness. In Part II we examine the effects of variations in the volumetric porosity and the mesh size as well as presenting detailed discussions of the evaporation/boiling phenomena from thin capillary wicking structures. An optimal sintering process was developed and employed to fabricate the test articles, which were fabricated using multiple, uniform layers of sintered isotropic copper mesh. This process minimized the interface thermal contact resistance between the heated wall and the capillary wick, as well as enhancing the contact conditions between the layers of copper mesh. Due to the effective reduction in the thermal contact resistance between the wall and capillary wick, both the evaporation/boiling heat transfer coefficient and the critical heat flux (CHF) demonstrated dramatic improvements, with heat transfer coefficients up to $245.5\ \mathrm{kW/m^2K}$ *and CHF values in excess of* $367.9\ \mathrm{W/cm^2}$*, observed. The experimental results indicate that while the evaporation/boiling heat transfer coefficient, which increases with increasing heat flux, is only related to the exposed surface area and is not affected by the capillary wick thickness, the CHF for steady-state operation is strongly dependent on the capillary wick thickness and increases proportionally with increase in the wick thickness. In addition to these observations, the experimental tests and subsequent analysis have resulted in the development of a new evaporation/boiling curve for capillary wicking structures, which provides new physical insights into the unique nature of the evaporation/boiling process in these capillary wicking structures. Sample structures and fabrication processes, as well as the test procedures are described in detail and the experimental results and observations are systematically presented and analyzed.* [DOI: 10.1115/1.2349507]

Keywords: experimental study, evaporation, boiling, heat transfer, CHF, thin capillary wick, thickness effects

1 Introduction

Previous investigations of evaporation/boiling from capillary wicking structures [1–10] have demonstrated that capillary pumping can be an effective way to passively enhance both the heat transfer coefficient and the critical heat flux (CHF) in evaporation/boiling heat transfer. In these structures, the enhanced distribution of the liquid on the surface, the increase in the effective surface area, the enhancement of the supply of fluid to the heated area through capillary pumping, and the change in the nucleation site size distribution, all result in significant improvements in both heat transfer performance and the critical heat flux [1]. The ability to predict the critical heat flux and the evaporation/boiling heat transfer coefficient of capillary wicking structures is of critical importance to the application of these structures to two-phase heat transfer devices, such as heat pipes, loop heat pipes (LHP), and capillary pumped loops (CPL), etc. However, the effective utilization of this capability is strongly dependent on a complete understanding of the functional relationship between the various parameters. The recent research on capillary wick performance and modeling is summarized in Table 1. As shown, Liter and Kaviany [1] focused on modulated, capillary wick structure development and successfully improved the CHF by a factor of 3 when compared to the CHF on plane surfaces for pool boiling heat transfer. The theoretical models developed were also capable of accurately predicting the CHF. Williams and Harris [3] developed a step-graded capillary wick structure using stainless steel felt to enhance the capillary limit. Hanlon and Ma [8] investigated the liquid film evaporation and capillary wick thickness effects for sintered copper particle beds, and found that thin film evaporation on the top surface of the wick is the key factor in the improvement of the heat transfer efficiency of the capillary wick and that an optimum thickness exists for a given particle size. Mughal and Plumb [9] improved the capillary wick performance by machining channels on a planar porous media surface. Lao and Zhao [10] studied the evaporation from a channeled, heated wall under antigravity conditions, with glass particle beds of varying sizes, and observed that nucleate boiling did not stop or retard the capillary driven flow through the capillary wick structure as previously hypothesized.

In reviewing the recent investigations of evaporation/boiling or pool boiling from the porous media coated surfaces listed in Table 1, it is apparent that the geometric properties of the structure, such as the wick thickness, volumetric porosity, and particle size, should always be carefully considered. However, of equal importance and not so obvious is the importance of the contact condi-

---

Contributed by the Heat Transfer Division of ASME for publication in the JOURNAL OF HEAT TRANSFER. Manuscript received August 28, 2005; final manuscript received January 11, 2006. Review conducted by Raj M. Manglik.

Table 1 Summary of previous investigations on evaporation/boiling on porous media coated surface

Author(s) [reference] (year)	Porous media [sintered temperature, time] (specific size, coating thickness, porosity)	Working fluid	Heater size	Dominant heat transfer mechanism	Contact between capillary wick and heated wall	Heat transfer coefficient range	CHF	Remarks
Liter and Kaviany [1] (2001)	Modulated sintered spherical copper particles [1016°C, 4 h] ($d_p = 200\ \mu\text{m}$, $6d-9d$, 0.4)	Saturated pentane	$d_{\text{heater}} =$ 5.08 cm	Nucleate boiling	Sintered	10–24 $\text{kW/m}^2\,\text{K}$ (estimated from the paper)	48 W/cm^2	Separate liquid and vapor flow during boiling process; CHF nearly three times over that of a plain surface
Williams and Harris [3] (2003)	Graded planar 316 stainless steel felt ($r_{\text{cross-plane}} = 35-500\ \mu\text{m}$ and $r_{\text{in-plane}} = 170-859\ \mu\text{m}$, 0.43 mm–0.71 mm,0.79–0.85)	Water and methanol	Not specified	Evaporation and boiling	Bonded by 4 mesh stainless steel screen	2.7–4.6 W/°C [water]; 0.9–2.1 W/°C [methanol]	N/A	Step-graded metal felt capillary wicks improve the capillary limit generally; nucleate boiling and vapor formation was determined to be the cause of the failure
Hanlon and Ma [8](2003)	Planar Sintered spherical copper particles bed [900°C, 12–45 mins] ($d_p = 635\ \mu\text{m}$, 2–6 mm, 0.43)	Water	$1 \times 2\ \text{cm}^2$	Film evaporation	Not specified	5–9 $\text{KW/m}^2\,\text{K}$	N/A	Evaporation heat transfer in the sintered capillary wick structure depends on the thin film evaporation; optimum characteristic thickness for maximum heat removal exists
Mughal and Plumb [9] (1996)	Planar and channeled porous metal foam ($r_c = 230\ \mu\text{m}$, 3.175–4.762 mm,0.94–0.95)	R11	$6.35 \times 7.6\ \text{cm}^2$	Evaporation	Not specified	0.25–2.5 $\text{kW/m}^2\,\text{K}$ (estimated from the paper)	N/A	Interrupted capillary wick structure enhances heat transfer capacity
Lao and Zhao [10](1999)	Spherical glass beads (rc=275–1280 μm, 80 mm, not specified)	Water	$2.8 \times 9.9\ \text{cm}^2$ with four channels	Evaporation	Not specified	2–7.5 $\text{kW/m}^2\,\text{K}$	12–26.89 W/cm^2	Heat flux applied from top of porous media (anti gravity flow); subcooling 20°C–50°C; nucleate boiling does not stop capillary force that is from the capillary wick

tions between the heated wall and the capillary wick. Further study indicates that this condition is actually the dominant factor in the determination of the overall thermal resistance between the heated wall and the capillary wick, and as a result, to a large extent, governs the overall behavior of evaporative/boiling heat transfer and CHF. As indicated in Table 1, Liter and Kaviany [1] used a sintering process to enhance the contact conditions and as a result, obtained very high heat transfer coefficients, even for pentane in pool boiling. Williams and Harris [3] bonded the capillary wicking material, in this case a coarse stainless steel mesh, onto the heating surface. In the other investigations reviewed and summarized in Table 1, the techniques employed to control or augment the contact conditions between the capillary wick and the heated wall were not specified.

The principal enhancements of the capillary wick structure can be divided into four categories, those resulting from (1) the reduction in the heat flux density on the heated wall, due to the fin effect; (2) the presence of contact points connecting the capillary wick and the wall, which effectively interrupts the formation of the vapor film and thereby reduces the critical hydrodynamic wavelength; (3) the increased nucleation site density and evaporation area; and (4) the improved liquid supply resulting from the capillary induced flow. In the current investigation, an optimum sintering process was developed and employed to minimize the contact thermal resistance between the individual layers of copper mesh, as well as between the copper mesh and the heated wall. All of the experimental results presented herein utilized an identical, optimized sintering process.

Although capillary wicks have been studied extensively, the effect of thickness has not been adequately addressed. Classical nucleate boiling theory indicates that the bubble departure diameter for a heated wall is on the order of 1 mm [12], and hence, in the current investigation, the range of thickness investigated is limited to 0.21 to 0.82 mm, which is much smaller than the bubble departure diameter, D_d. Given these conditions, it is reasonable to assume that no bubbles will depart from the heated surface and that there will be no bubble flow inside the capillary wicking structure.

The elimination of bubble departure results in two principal advantages: first, the bubble generation frequency $f=1/(t_w+t_d)$ is significantly increased without increasing the time required for the bubbles to depart, t_d; and second, there is no reduction in the liquid supply, due to the presence of bubbles trapped within the porous media. Based upon this analysis, it was hypothesized that the heat transfer from capillary wicking structures, with thicknesses less than the bubble departure diameter, D_d, could lead to significant overall enhancements.

Our objectives in the current investigation are to experimentally verify this hypothesis and determine how the thickness of the capillary wick affects the evaporation/boiling heat transfer characteristics, performance, and CHF for these structures. In the current investigation, thin capillary wicking structures, fabricated from sintered isotropic copper mesh, are utilized. As illustrated in Fig. 1(*a*) and 1(*b*), respectively, two kinds of stacking structures typically occur in multilayer, sintered copper mesh: staggered and inline. These stacking structures can also impact the evaporation/boiling heat transport and CHF from these capillary wicking structures. The staggered structure is more common, easier to produce, and results in greater performance, due to the increase in the exposed surface area and the smaller effective pore size.

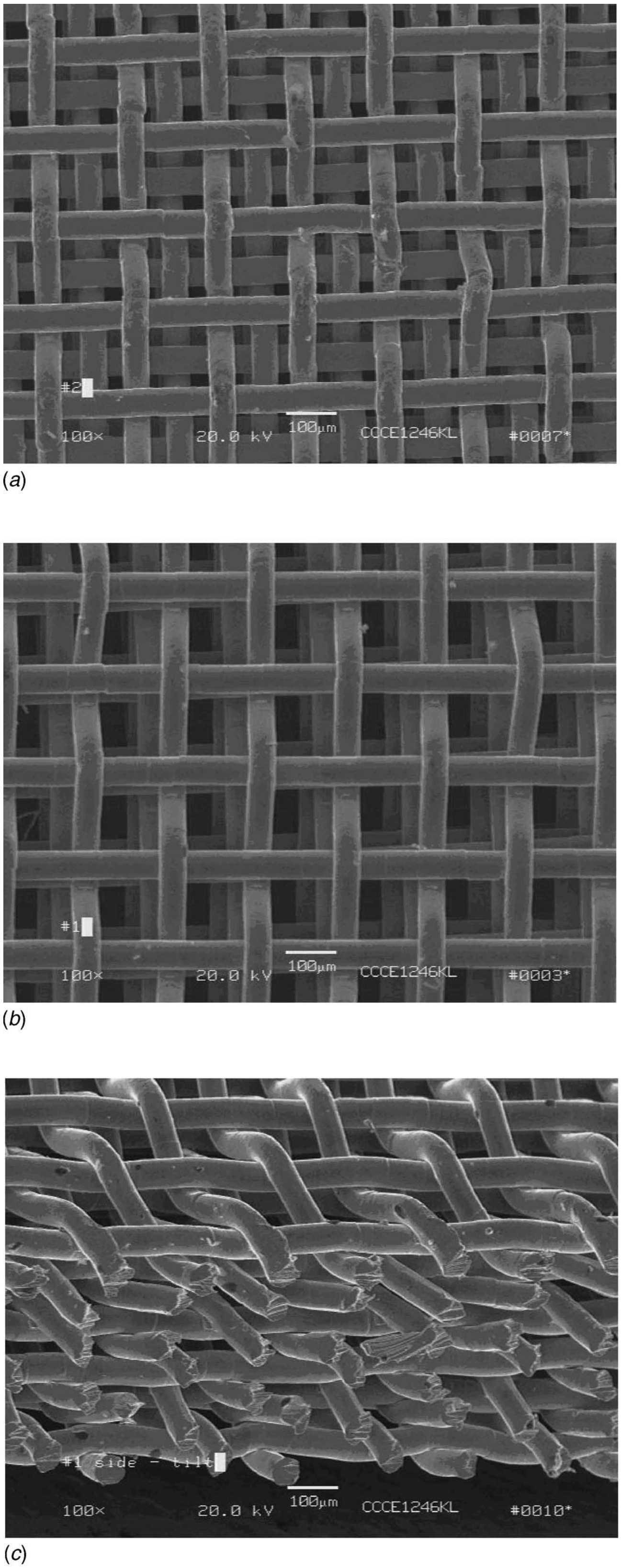

Fig. 1 (a) Top view of staggered sintered isotropic copper mesh; (b) top view of inline stacked sintered isotropic copper mesh; (c) side view of sintered isotropic copper mesh. SEM image of sintered isotropic copper mesh with 1509 m^{-1} (145 $in.^{-1}$), 56 μm (0.0022 in.) wire diameter, and fabricated at a sintering temperature of 1030°C with gas mixture protection (75% N_2 and 25% H_2) for two hours.

2 Description of the Test Articles

The structure of the test sample is illustrated in Fig. 2 and consists of four parts: a single layer of sintered isotropic copper mesh 8 mm wide and 152.4 mm long; an 8 mm × 8 mm square, multilayered sintered isotropic copper mesh section; a 0.03 mm thick copper foil; and an 8 mm × 8 mm square copper heating block with a 7.8 mm threaded cylindrical portion. Three holes, each 4 mm deep and 1 mm in diameter, were drilled into the

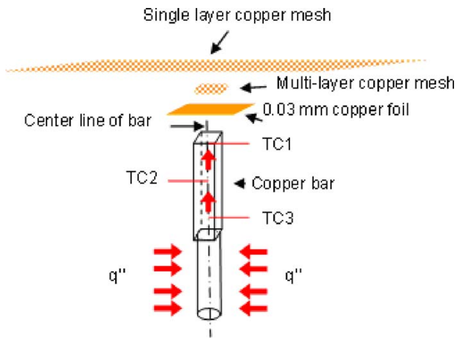

Fig. 2 Schematic of the test sample and thermocouple locations

center of the copper bar at 10 mm intervals. The Special Limit of Error (SLE) K-type thermocouples were soldered into each hole. Using the temperature difference between thermocouples TC1 and 2, and TC2 and 3, and the thermal conductivity of the pure copper heating section, the steady-state 1-D axial heat flux could be calculated and, hence, the steady-state heat dissipation resulting from the evaporation/boiling from the sintered copper mesh surface could be determined with a high degree of accuracy. The thermocouple closest to the top surface, TC1, was located at a distance of 0.5 mm from the surface and when coupled with the axial heat flux, was used to estimate the surface temperature of the copper heating block.

Fabrication of the test article was accomplished in three steps: first, the required number of layers of isotropic copper mesh were sintered together to obtain the desired volumetric porosity and thickness; second, the sintered capillary wick structure was carefully cut into an 8 mm by 8 mm square and covered by a single layer, 8 mm wide and 152.4 mm long; and third, the sintered copper mesh pieces were sintered together and directly onto the copper heating block. In the third step, a stainless steel fixture was used to accurately position each part during the final sintering process. The layer of 0.03 mm thick copper foil was used to protect the porous surface from filling with sealant during assembly and insertion into the test facility. The finished test article is shown in Fig. 3.

The sintering process employed to fabricate the test articles was designed to reduce the effects of the thermal contact resistance between the capillary wick material and the top surface of the heating block. To determine the effectiveness of this process, the temperature drop for a number of combinations of sintering temperatures, time durations, and shielding gas mixtures were evaluated. A sintering temperature of 1030°C in a gas mixture consisting of 75% argon and 25% hydrogen for a time of two hours, was found to provide the optimal conditions for reducing the contact resistance between the sintered mesh and the top surface of the solid copper heating bar. To demonstrate the efficiency of this process, the temperature distribution and resulting thermal conductance of a single, solid copper test article and one that had two separate copper pieces sintered together were evaluated and compared. The results of this comparison are illustrated in Fig. 4. As shown, the measured thermal contact conductance and thermal conductivities for these two configurations are nearly identical.

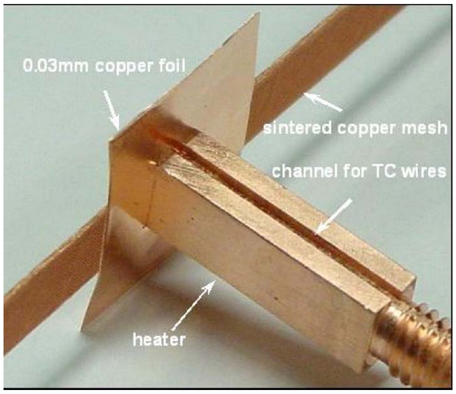

Fig. 3 Illustration of a typical test article

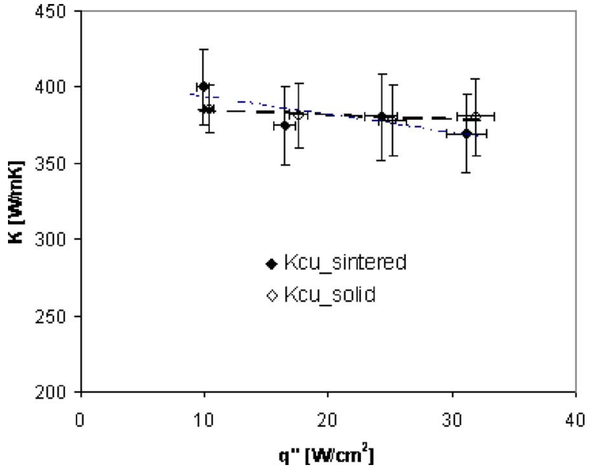

Fig. 4 A comparison of the thermal conductivities of two solid copper bars that were sintered together and a single solid copper bar

Five different test articles were evaluated to determine how the capillary wick thickness affects the evaporation/boiling heat transfer coefficient and the CHF for thin capillary wicking structures. Specifications of the test articles are listed in Table 2, where the test article designation describes the specific characteristics for each. For example, E145-2 denotes a test sample for evaporation, fabricated from 2 layers of 5709 m^{-1} (145 $in.^{-1}$) copper mesh.

3 Experimental Test Facility and Procedure

The experimental test facility is shown in Fig. 5 and consists of a heated aluminum chamber, a reservoir for the distilled water supply, a heating system, and a data acquisition system. Three thermocouples (TC4, 5, and 6) were used to monitor the water temperature in the aluminum chamber throughout the test procedure. A 300 W electrical resistance heater was used to provide power to the heated surface. In addition, two electric heaters were used to maintain the saturation conditions in the test chamber. A Pyrex glass cover on top of the chamber enabled the heated surface to be observed. This glass cover was heated to prevent condensation and the possibility of drops of condensate falling onto the evaporation/boiling surface during the test procedure.

During the test procedure, distilled water, which had been processed to eliminate dissolved gases, flowed from the reservoir into the test chamber and maintained the water at a predetermined level using an overflow system. Care was taken to ensure that the heat transfer occurred only via evaporation/boiling or pool boiling, depending upon the specific test. During the tests, all sur-

Table 2 Specification of the test samples

Sample #	Thickness (mm)	Porosity	Wirediameter(μm)
E145-2	0.21	0.737	56
E145-4	0.37	0.693	56
E145-6	0.57	0.701	56
E145-8	0.74	0.698	56
E145-9	0.82	0.696	56

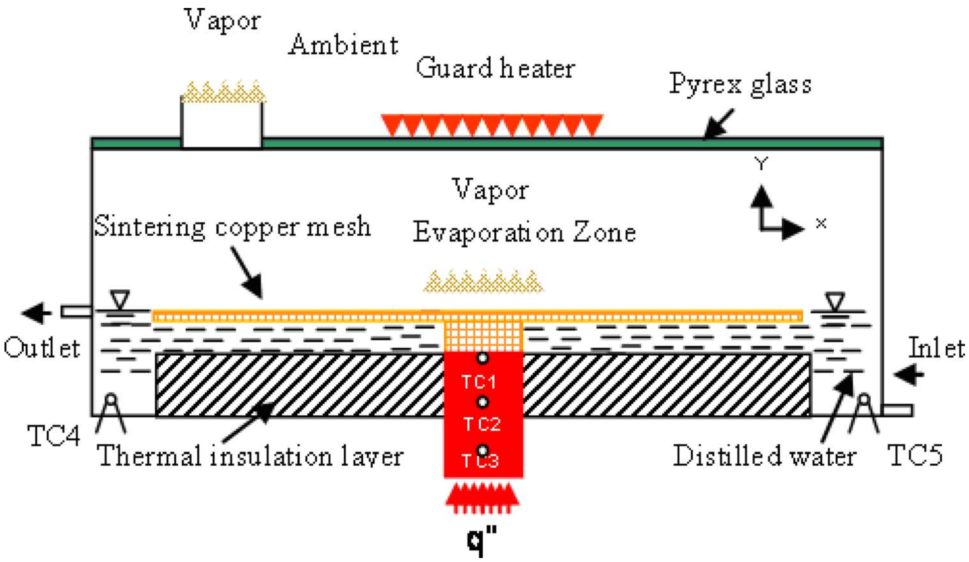

Fig. 5 Schematic of the test facility

faces, with the exception of the evaporation/boiling surface of the test articles, were well insulated using a combination of ceramic and glass fiber insulation materials.

Prior to the recording of any test data, all dissolved gases were removed from the distilled water and the test facility was allowed to reach the steady state, defined as the point at which the temperature reading for any thermocouple varied by less than 0.1°C over a period of ten minutes. The steady-state experimental data were averaged over a period of five minutes and recorded for each power level and then the power was incremented and the process repeated until the capillary structure had reached complete dry-out.

4 System Calibration

The experimental test facility was calibrated prior to the initiation of the test program by measuring the pool boiling characteristics of a smooth flat surface. The experimental results were compared with both the experimental and analytical data available in the literature. Figure 6 and Table 3 present a comparison of the data obtained using the current facility and that obtained by Auracher et al. [11] for pool boiling from a copper surface, 35 mm in diameter. In addition, results from several other investigations on CHF and pool boiling from flat, smooth surfaces are presented and compared [12]. As illustrated, the data obtained in the current investigation are slightly higher than the experimental data and the analytical predictions of several of the other investigators, but correlate quite well overall. The variation between the current data and that reported previously is all within ±10%. The observed variations may be caused by the relative roughness and surface finish conditions, coupled with the small size of the heater (8 mm × 8 mm), which is larger than the capillary length of 2.504, but much smaller than the Taylor wavelength of 15.7 mm for water at 100°C. The results, however, confirm that the current facility can be used to provide highly repeatable data, which is demonstrated in Fig. 6 by two sets of pool boiling curves, and in Figs. 1(*a*) and 1(*b*) in Ref. [14] by several sets of test data from one sample, and accurate estimations of the CHF and evaporation/boiling heat transfer coefficient.

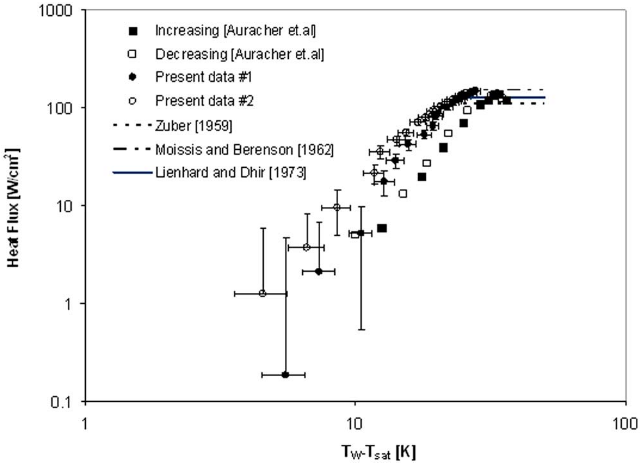

Fig. 6 A comparison of pool boiling data obtained in the current test facility from smooth flat copper surfaces with those obtained by Auracher et al. (2003), and predictions from models of Zuber (1959), Moissis and Berenson (1962), and Lienhard and Dhir (1973)

5 Data Reduction

All the test data were categorized using three key parameters calculated from Eqs. (1)–(3), respectively: the super heat, T_W -T_{sat}; the heat flux, q'' (including the CHF); and the evaporation/boiling heat transfer coefficient, h_{eff}.

$$T_W - T_{\mathrm{sat}} = T_{\mathrm{TC1}} - (T_{\mathrm{TC4}} + T_{\mathrm{TC5}} + T_{\mathrm{TC6}})/3 - q'' t_{\mathrm{STC1}}/K_{cu}, \tag{1}$$

$$q'' = K_{cu}(T_{\mathrm{TC2}} - T_{\mathrm{TC1}})/t_{\mathrm{hole}}, \tag{2}$$

$$h_{\mathrm{eff}} = q''/(T_W - T_{\mathrm{sat}}). \tag{3}$$

In Eq. (1), $T_{\mathrm{sat}} = (T_{\mathrm{TC4}} + T_{\mathrm{TC5}} + T_{\mathrm{TC6}})/3$ and $T_W = T_{\mathrm{TC1}} - q'' t_{\mathrm{STC1}}/K_{cu}$. Here the terms T_{TC1}, T_{TC2}, and T_{TC3} represent the temperature for the three K-type thermocouples used to monitor the temperature in the copper heater, at 10 mm intervals. Data from T_{TC4}, T_{TC5}, and T_{TC6} represent the water temperature in the

Table 3 A comparison of CHF

Auracher et al. [11] (Test data)	139 W/cm^2
Zuber [12] (model)	110.8 W/cm^2
Moissis and Berenson [12] (model)	152.4 W/cm^2
Lienhard and Dhir [12] (model)	126.9 W/cm^2
Present data (test data)	149.7 W/cm^2

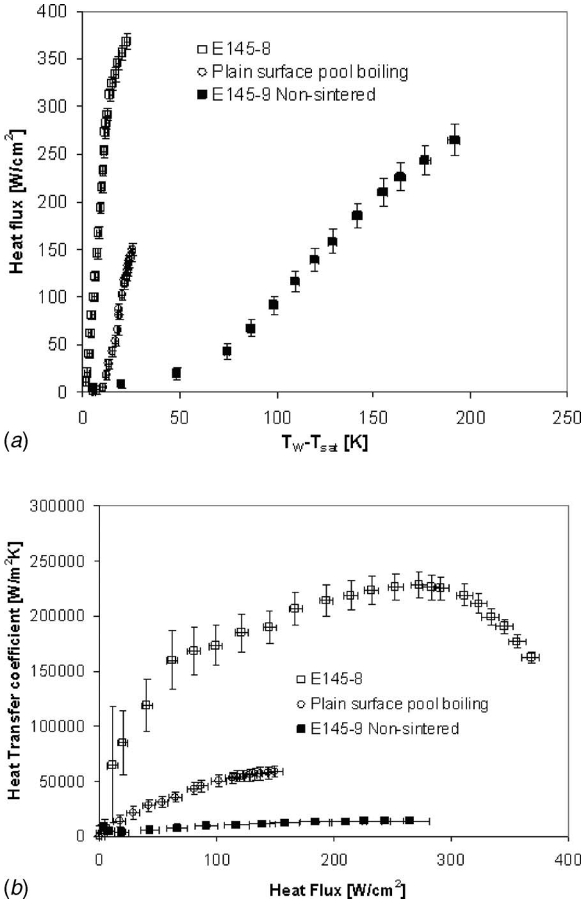

Fig. 7 (a) Heat flux as a function of super heat [T_W-T_{sat}]; (b) Heat transfer coefficient as a function of heat flux

test chamber. Using the measured temperature, T_{TC1}, and the known thermal conductivity, K_{cu}, the temperature at the bottom of the capillary wick structure, T_W, can be derived; and using T_{TC1} and T_{TC2}, the heat flux, q'', dissipated through evaporation/boiling under steady-state conditions can be determined. With these two values, the effective heat transfer coefficient can be estimated by Eq. (3).

The uncertainties of the temperature measurements, the length (or width) and the mass are ±0.5°C, 0.01 mm, and 0.1 mg, respectively. A Monte Carlo error of propagation simulation indicated the following 95% confidence level for the computed results: the heat flux was less than $\pm 5.5\ \mathrm{W/cm^2}$; the heat transfer coefficient was less than ±20%; the superheat (T_{wall}-T_{sat}) was less than ±1.3°C, and the porosity, ε, was less than ±1.5%.

6 Results and Discussion

The experiments were conducted at atmospheric pressure with degassed, distilled water. All surfaces were carefully cleaned using Duraclean™ 1075 prior to each test sequence to assure the identical surface wetting characteristics. Typical test results are summarized in Figs. 7–9 and the results are presented in terms of the heat flux, superheat, CHF, and heat transfer coefficient. In this investigation, the volumetric porosities and pore sizes of all the samples were held constant throughout all of the tests and all data were obtained under steady-state conditions.

6.1 Contact Conditions between Heater and Capillary Wick Structure. From the literature review, it is apparent that the contact conditions at the heated wall-capillary wick interface have been neglected in most of the previous investigations. This is important to note since the contact conditions are a critical factor and

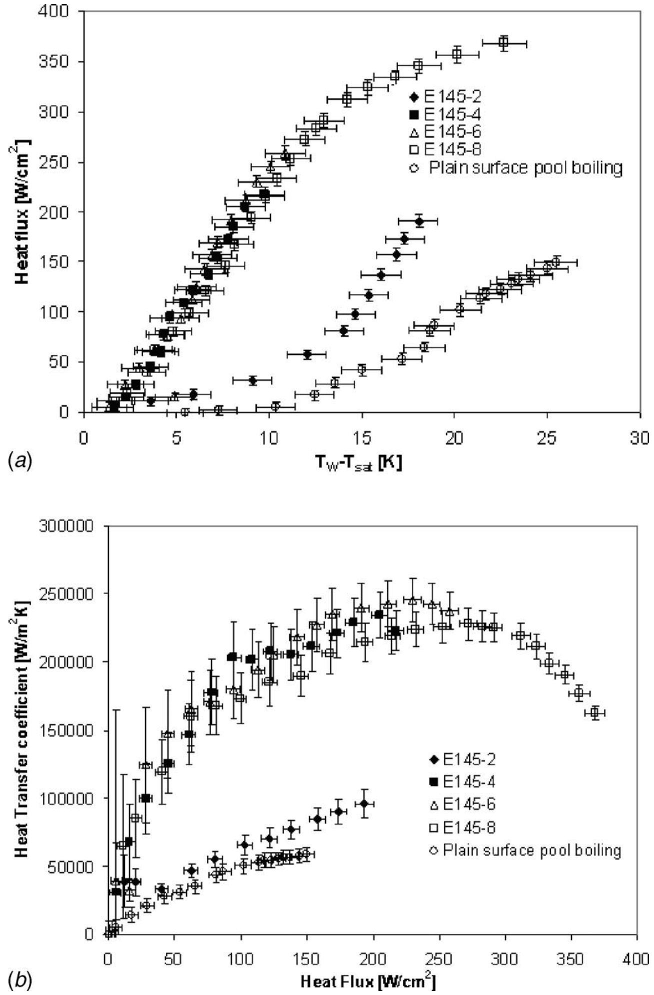

Fig. 8 (a) Heat flux as a function of superheat [T_W-T_{sat}]; (b) heat transfer coefficient as a function of heat flux

can significantly improve the evaporation/boiling heat transport in the capillary wick and, in turn, significantly enhance the CHF. As mentioned previously, the principal functions of the capillary wick structure can be divided into four categories: those resulting from (1) the reduction in the heat flux density on the heated wall due to the fin effect; (2) the presence of the contact points connecting the

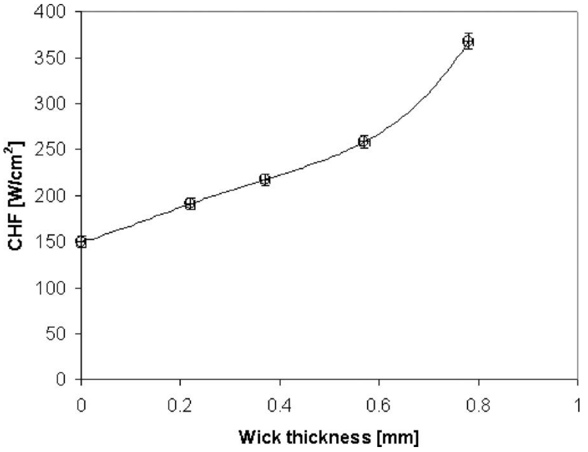

Fig. 9 CHF as function of thickness of sintered isotropic copper mesh

capillary wick and wall, which interrupts the formation of the vapor film or reduces the critical hydrodynamic wavelength; (3) the increased nucleation site density and evaporation area; and (4) the improved liquid supply resulting from the capillary induced flow.

In the evaporation/boiling from capillary wicking structures, a majority of the heat is conducted from the solid wall to the capillary wick, where it is then dissipated via evaporation/boiling from the exposed hot surfaces. If the capillary wicking structure is not sintered or not attached directly to the solid surface, a thin liquid film may exist. This film will significantly increase the thermal resistance between the layers of the wick or between the solid heated wall and the capillary wick. As a result, thermal energy will be accumulated at the heated wall and cause relatively higher wall temperatures. This will, in turn, result in a significant reduction in both the heat transfer performance and the CHF.

In order to maximize and properly evaluate the evaporation/boiling heat transfer performance from the capillary wicks, and, moreover, to maintain evaporation/boiling instead of thin film boiling on the heated wall, it is essential to ensure good contact conditions between the heater and the capillary wicking structure. Figures 7(*a*) and 7(*b*) present three sets of data and illustrate how important this contact is, and how significant the differences resulting from variations in the contact conditions can be. The first set of data was obtained in the current investigation using test article E145-8, which was sintered directly onto the top surface of the heated wall using the sintering procedure described previously. These data are compared with data obtained for a sample in which the sintered capillary structure was bonded to the heating surface by a thermal epoxy (ATI Electro-Grease 8501) and with pool boiling data obtained from a plain flat surface. As illustrated in Figs. 7(*a*) and 7(*b*), the dissipated heat flux and the resulting heat transfer coefficient from E145-9 are both significantly lower than those obtained from E145-8 at the same superheat and heat flux, respectively. In addition and worthy of special note is the fact that the heat transfer performance of E145-9 is also significantly less than that obtained from pool boiling of a plain surface. This dramatic reduction is due to the increase in the contact thermal resistance, which dominates the temperature difference or the superheat as defined in this paper (also employed in most other investigations), between the sintered capillary wick and the heated surface in sample E145-9.

6.2 Effects of Capillary Wick Thickness on Evaporation/Boiling Heat Transfer Performance. Figure 8(*a*) presents the heat flux as a function of the superheat, while Fig. 8(*b*) illustrates the effective heat transfer coefficient as a function of the heat flux. As indicated, the increased nucleation site density and the enhanced evaporation/boiling surface area, result in a substantially better performance than pool boiling from a flat surface. Visual observation indicated that the evaporation and boiling heat transfer occurred simultaneously when the heat flux reached a certain value, which was observed to vary with the capillary wick thickness. During the tests, small bubbles were observed at low heat fluxes, and although the two phases coexist in the porous media, the bubbles or vapor could easily escape from the liquid to the vapor space immediately adjacent to the capillary wick surface. For a given volumetric porosity and pore size, the evaporation/boiling heat transfer coefficient from the sintered copper mesh clearly indicates a very weak dependence on the capillary wick thickness. When the mesh number and wire diameter are held constant, the surface area of the mesh within the test articles will increase proportionally with respect to the thickness, while the exposed surface area remains constant. As illustrated in Fig. 8(*b*), prior to reaching CHF the heat transfer coefficients for the various thicknesses are nearly identical, except for sample E145-2. This implies that it is the exposed surface, rather than the total surface area of the mesh within the test articles that dominates the heat transfer performance in the evaporation/boiling on the capillary wick. One possible explanation for the lower performance of E145-2 is that the surface is actually flooded, due to the difficulties associated with accurately controlling the water level in very thin layers of these capillary structures. This flooding could result in a different heat transfer mechanism than that which occurs in thicker capillary wicking structures. With this exception, however, the test results clearly indicated that the heat transfer performance on thin capillary wicks is not directly related to the capillary wick thickness. These results also imply that care should be taken to control the liquid level for very thin materials in order to develop accurate evaporation/boiling heat transfer models.

The highest performance was obtained for the 0.21 mm thick capillary wick at the CHF, however, when the capillary wick is thicker than 0.37 mm, the maximum heat transfer coefficient is achieved before the CHF has been reached. This implies that the capillary pumping is still effective, even when local dry out occurs. The data obtained for the 0.21 mm thick capillary wick are somewhat different from the other samples tested. The experimental results also suggest that the capillary wick thickness range for optimal evaporation/boiling heat transfer performance is from 0.37 mm to the bubble departure diameter, to D, for sintered copper mesh.

6.3 Effects of Capillary Wick Structure Thickness on the Evaporation/Boiling Characteristics. Figure 8(*a*) indicates that the evaporation/boiling inception superheats are significantly reduced through capillary wicking, compared with that obtained for pool boiling on a plain surface. The value of inception wall superheat varies for samples E145-4 $\sim$ 8 [14], which indicates that this parameter is dependent on wick thickness. Generally the wall superheat at CHF is less than that of pool boiling on a plain surface and increases as a function of the thickness of the capillary wick. In addition, when the heat flux is from 0 $\sim 250\ \mathrm{W/cm^2}$, the variation of the wall temperature superheat with the heat flux input is approximately $0.04\,^\circ\mathrm{C}/(\mathrm{W/cm^2})$, which would be very important and attractive to applications related to temperature control systems, where the temperature stability of a system with relatively large power density changes is important.

For a given surface, the magnitude of the contact angle is expected to strongly affect the temperature overshoot [13]. And in the current investigation, hysteresis and wall temperature overshoot, were both observed at the beginning of the boiling process for several tests. These may be due to the flooding of the capillary wick by the working fluid so that only a relatively small number of sites are available for nucleation [13]. Bergles and Chyu [13] indicated that the simplest way of avoiding these problems is to apply a high heat flux or large temperature difference to initiate boiling.

6.4 Effects of Capillary Wick Structure Thickness on the CHF. The CHF for any evaporation/boiling system is determined by the mechanisms of liquid supply to, and vapor escape from, the phase change interface. For evaporation/boiling from thin capillary wick surfaces, where the liquid is only supplied by capillary pressure, the bubbles break up or collapse at the free liquid-vapor interface, due to local condensation and exposure to a low pressure vapor space and hence, the liquid-vapor counter flow resistance is reduced without bubble flow through the capillary wick. In addition, the contact points connecting the capillary wick and wall, interrupt the formation of the vapor film and/or reduce the critical hydrodynamic wavelength. Thus the CHF for evaporation/boiling from these porous surfaces is greatly enhanced.

Figure 9 demonstrates the dependence of the CHF on capillary wick thickness and indicates that increase in the thickness, results in an increase in the CHF for the range of thickness in this investigation. For a given heat flux, increase in the thickness results in an increase in the cross-sectional area available for fluid flow and a concomitant decrease in the pressure drop of the liquid flowing through the capillary wick. This explains the CHF increase with increasing thickness in certain wick thickness ranges. At the limit, the data for each thickness indicates that the capillary limit has been reached, resulting in localized dry out.

7 Conclusions

An experimental study was successfully conducted to evaluate evaporation/boiling heat transport phenomena and CHF in thin capillary wicking structures. As expected, the evaporation/boiling heat transfer coefficient increases with incremental increases in the power input until a maximum value has been reached. At this point the evaporation/boiling heat transfer coefficient begins to decrease, due to partial dry out of the thin capillary wicking structure, which results in a reduction in the effective area of the heated surface. These results demonstrate that the capillary induced pumping, functions effectively, even during partial dry out and that the capillary limit is one of the mechanisms that governs the CHF.

The experimental results presented here indicate that the interface thermal contact resistance between the heated wall and the porous surface plays a critical role in the determination of the evaporation/boiling heat transfer coefficient and the CHF. For evaporation/boiling from a thin capillary wick with a thickness ranging from 0.37 mm to the bubble departure diameter, D_b, significant enhancement in the heat transfer performance can be achieved and the CHF dramatically improved. The maximum heat transfer coefficients and CHF for the sintered multiple layers of copper mesh evaluated herein, were shown to be as high as 245.5 $\mathrm{kW/m^2\,K}$ and 367.9 $\mathrm{W/cm^2}$, respectively. These values are more than three times those normally obtained for pool boiling from a smooth, flat surface. In addition, the results of this experimental investigation clearly indicated that evaporation/boiling heat transfer performance of capillary wicking structures is independent of wick thickness, which indicates that only the exposed surface area contributes to the heat transfer performance, due to the gravitational effect. The CHF, however, increases with increases in the wick thickness when it is thinner than 1 mm.

Evaporation/boiling inception superheat is found to be greatly reduced and dependent on wick thickness. Wall superheat is generally lower than for pool boiling on a plain surface. Hysteresis, wall temperature overshoot, is also observed at the beginning of boiling for each test. Power inputs greater than the power required to initiate boiling, could avoid this problem.

While the data presented here is informative and in many ways quite conclusive, additional visual observations of the liquid and vapor phases inside of the capillary wick are necessary in order to better understand the fundamental physics occurring in the evaporation/boiling in capillary wicking structures.

Acknowledgment

The authors would like to acknowledge the support of the National Science Foundation under award CTS-0312848. Fruitful discussions offered by Dr. Ji Li and Mr. Hong Li are greatly appreciated.

Nomenclature

D_d = Bubble departure diameter (mm)
h = Heat transfer coefficient ($\mathrm{W/m^2\,K}$)
h_{fg} = Latent heat (kJ/kg)
K = Thermal conductivity (W/mK)
q'' = Heat flux ($\mathrm{W/cm^2}$)
t = Distance or thickness (mm)
t_{w} = Time required for bubble growth (s)
t_d = Time required for bubble departure (s)
T = Temperature (K)
$TC\#$ = Thermocouple number

Greek symbols

ε = Volumetric porosity
σ = Surface tension (N/m)

Subscripts

d = Bubble departure condition
l = Liquid phase
v = Vapor phase
w = Wall
sat = Saturation condition
eff = Effective parameter
Cu = Copper
hole = Holes on heater to hold thermocouple
STC1 = Top surface of copper block to TC1

References

[1] Liter, S. G., and Kaviany, M., 2001, "Pool-Boiling CHF Enhancement by Modulated Porous-Layer Coating: Theory and Experiment," Int. J. Heat Mass Transfer, **44**, pp. 4287–4311.
[2] Udell, K. S., 1985, "Heat Transfer in Capillary Wick Considering Phase Change and Capillarity—The Heat Pipe Effect," Int. J. Heat Mass Transfer, **28**, pp. 77–82.
[3] Williams, R. R., and Harris, D. K., 2005, "The Heat Transfer Limit of Step-Graded Metal Felt Heat Pipe Wicks," Int. J. Heat Mass Transfer, **48**, pp. 293–305.
[4] Tolubinsky, V. I., 1981, "Some Peculiarities of Vaporization Process in a Single Cell of the Heat Pipe Wick," *Proceedings of the 4th International Heat Pipe Conference*, London, England, September 7–10, pp. 375–388.
[5] Smirnov, G. F., and Afanasiev, A., 1981, "Investigation of Vaporization in Screen Wick-capillary Structures," *Proceedings of the 4th International Heat Pipe Conference*, London, England, September 7–10, pp. 405–413.
[6] Abhat, A., and Seban, R. A., 1974, "Boiling and Evaporation from Heat Pipe Wicks with Water and Acetone," ASME J. Heat Transfer, **90**, pp. 405–413.
[7] Styrikovich, M. A., Malyshenko, S. P., Andianov, A. B., and Talaev, I. V., 1987, "Investigation of Boiling on Porous Surface," Heat Transfer-Sov. Res., **19**, pp. 23–29.
[8] Hanlon, M. A., and Ma, H. B., 2003, "Evaporation Heat Transfer in Sintered Porous Media," ASME J. Heat Transfer, **125**, pp. 644–652.
[9] Mughal, M. P., and Plumb, O. A., 1996, "An Experimental Study of Boiling on a Wicked Surface," Int. J. Heat Mass Transfer, **39**(4), pp. 771–777.
[10] Lao, Q., and Zhao, T. S., 1999, "Evaporation Heat Transfer in a Capillary Structure Heated by a Grooved Block," J. Thermophys. Heat Transfer, **13**, pp. 126–133.
[11] Auracher, H., Marquardt, W., Buchholz, M., Hohl, R., Luttich, T., and Blum, J., 2001, "New Experimental Results on Steady-State and Transient Pool Boiling Heat Transfer," Therm. Sci. Eng., **9**, pp. 29–39.
[12] Tong, L. S., and Taung, Y. S., 1997, *Boiling Heat Transfer and Two Phase Flow*, 2nd ed., Taylor & Francis, London, England.
[13] Bergles, A. E., and Chyu, M. C., 1982, "Characteristics of Nucleate Pool Boiling From Porous Metallic Coatings," ASME J. Heat Transfer, **104**, pp. 279–285.
[14] Li, C., and Peterson, G. P., "Evaporation/boiling on Thin Capillary Wick (II) – Effects of Volumetric Porosity and Mesh Size," ASME J. Heat Transfer, **128**, pp. 1320–1328.

Evaporation/Boiling in Thin Capillary Wicks (II)—Effects of Volumetric Porosity and Mesh Size

Chen Li
Graduate Research Assistant
Rensselaer Polytechnic Institute,
Department of Mechanical, Aerospace and
Nuclear Engineering
Troy, NY 12180
e-mail: lic4@rpi.edu

G. P. Peterson
Professor and Chancellor
University of Colorado,
Boulder, CO 80309
e-mail: Bud.Peterson@colorado.edu

*Presented here is the second of a two-part investigation, designed to systematically identify and investigate the parameters affecting the evaporation from and boiling within, thin capillary wicking structures with a range of volumetric porosities and mesh sizes. The experimental studies were investigated under steady-state conditions at atmospheric pressure. Part I of the investigation described the wicking fabrication process and experimental test facility, and focused on the effects of the capillary wick thickness (ASME J. Heat Transfer., **128**, pp. 1312–1319). In Part II, we examine the effects of variations in the volumetric porosity and the mesh size. The experimental results presented here indicate that the critical heat flux (CHF) was strongly dependent on both the mesh size and the volumetric porosity; while the evaporation/boiling heat transfer coefficient was significantly affected by mesh size, but not strongly dependent on the volumetric porosity. The experimental results further illustrate that the menisci at the CHF are located in the corners, formed by the wire and the heated wall and between the wires in both the vertical and horizontal directions. The minimum value of these three menisci determined the maximum capillary pressure generated through the capillary wick. The experimental results and observations are systematically presented and analyzed, and the local bubble and liquid vapor interface dynamics are examined theoretically. Based on the relative relationship between the heat flux and superheat, classic nucleate boiling theory, and the visual observations of the phase-change phenomena, as well as by combining the results obtained here with those obtained in Part I of the investigation, the evaporation/boiling heat transfer regimes in these capillary wicking structures are identified and discussed.*
[DOI: 10.1115/1.2349508]

1 Introduction

Evaporation/boiling in capillary wicking structures has been shown to be an effective heat transfer mechanism in a wide variety of applications, such as heat pipes, loop heat pipes (LHP), capillary pumped loops (CPL), etc. As a result, the parameters that govern these phenomena are of considerable interest. A summary of the recent investigation has been presented in Part I of this two-part investigation [1]. In that review, the range of capillary wick structures previously investigated was summarized, along with the fabrication procedures used, the size of the heat source employed, and the contact condition between the heated wall and the capillary wick [2–12]. The resulting conclusions were that of all the various parameters investigated to date, one of the most critical parameters, the contact condition, was also the one most often neglected. In Part I, the contact condition between the capillary wicking structure and the heated surface was found to be a key factor that affects both the heat transfer efficiency and the CHF. In addition, the effects of capillary wick thickness on the evaporation/boiling in capillary wicking structures made from uniform layers of sintered isotropic copper mesh were also presented. The experimental results indicated that the sintering process developed in Part I could achieve nearly perfect contact at the heated surface/capillary wick interface. It was also demonstrated that the evaporation/boiling heat transfer is nearly independent of the capillary thickness, while the CHF increases with increasing thickness, if all other geometric properties, i.e. volumetric porosity and mesh size, were held constant. In Part I, extremely high heat transfer performance and CHF values were successfully achieved from thin capillary wicks fabricated from sintered isotropic copper mesh. These structures achieved some of the highest heat transfer enhancement and CHF values reported in the literature. In addition, this structure was easy to fabricate and allowed precise control of both the thickness and volumetric porosity.

In addition to the effects of the capillary wick thickness, two fundamental questions must be addressed before the evaporation/boiling mechanism from these structures is fully understood. These are: First, what is and where does the critical meniscus radius, which is controlled by the wire diameter and the mesh number, occur in these types of structures? And second, how does the volumetric porosity affect the evaporation/boiling performance, characteristics and CHF? For thin capillary wicking structures fabricated from sintered isotropic copper mesh, the critical meniscus radius and the effective pore size in the liquid flow direction are controlled by the mesh size (including wire diameter and mesh number) and the compression factor. In [14] the value of $(W+d)/2$ was recommended as the effective pore radius to estimate the capillary pressure for multiple wire-mesh screens, for both sintered and simple contact situations. Because the evaporation/boiling phenomenon is a complicated and dynamic process, the determination of the critical meniscus radius is quite challenging. In the evaporation/boiling process from a capillary wicking structure, the menisci are initially formed at the horizontal mesh openings. As the heat flux increases, the evaporation at the liquid-vapor interface is intensified. In these situations, the liquid meniscus recedes into the wick, reducing the meniscus radius, which results in an increase in the capillary pressure. However, in some cases, the capillary pressure generated through the

---

Contributed by the Heat Transfer Division of ASME for publication in the JOURNAL OF HEAT TRANSFER. Manuscript received August 28, 2005; final manuscript received January 11, 2006. Review conducted by Raj M. Manglik.

Table 1 Specification of the test samples

Sample #	Wire diameter (μm)	Porosity	Pore size (μm)
E145-4	56	0.692	119.3
E145-6c	56	0.56	119.3
E145-7c	56	0.409	119.3
E100-2	114	0.632	139.7
E60-1	191	0.67	232.8
E145-8[a]	56	0.698	119.3

[a] This sample is 0.74 mm thick

meniscus curvature may not be sufficient to drive or pump the required amount of working fluid to the heating area. Visual observations indicate that these menisci are not only formed at the horizontal mesh openings, but may also be formed at other locations in the capillary wick structure, i.e., the vertical mesh openings or the corners formed at the junction of the wire and the heating wall.

In the current investigation, the effects of the critical meniscus radius/the effective pore size and volumetric porosity are investigated systematically by varying the mesh size including the wire diameter and mesh number, and the distance between wire layers, respectively. This approach provides new physical insights into the evaporation/boiling phenomena from the capillary wicking structures. To accomplish this, the optimum sintering process developed in Part I [1] was employed to minimize the contact thermal resistances between the individual layers of copper mesh, as well as between the copper mesh and the heated wall. All of the experimental results presented herein utilized an identical sintering process.

The literature review indicates that heat transport models and regimes for evaporation/boiling from capillary wicking structures have been studied by a number of investigators. Hanlon and Ma [9] studied evaporation on sintered copper particle beds, both analytically and experimentally. This study indicated that there exist two heat transfer models: one for thin liquid film evaporation and one for nucleate boiling; that the thin film evaporation heat transfer on the top surface of the wick is the dominant factor in the enhancement of the evaporating heat transfer, and that nucleate boiling causes a decrease in heat transfer performance. The heat transfer models for heat pipes shown later as Fig. 11 were presented and discussed by Faghri [14]. Four models were presented and discussed: conduction-convection, receding liquid, nucleate boiling, and film boiling. In addition, the dynamics of the liquid-vapor interface and its effects on the evaporation/boiling in capillary wicks were mentioned indirectly. In the following, visual observations and analytical analyses, along with the heat transfer regimes, local bubble dynamics, and liquid vapor interface dynamics are all systematically presented and discussed.

2 Results and Discussion

All of the experiments were conducted using the experimental test facility and test procedures described in Part I [1]. Specifications of the test samples used in the current investigation are listed in Table 1. Typical test results are summarized in this section and are presented in terms of the heat flux including the CHF, wall superheat, and heat transfer coefficient.

2.1 Effects of Mesh Size. To investigate the effects of variations in the mesh size on the evaporation/boiling heat transfer performance and CHF at steady-state condition, three test articles, E145-4, E100-2 and E60-1, with approximately identical thicknesses and volumetric porosities, were evaluated in an atmospheric environment. For comparisons, the pool boiling curve on a plain surface is added in Figs. 1(*a*) and 1(*b*).

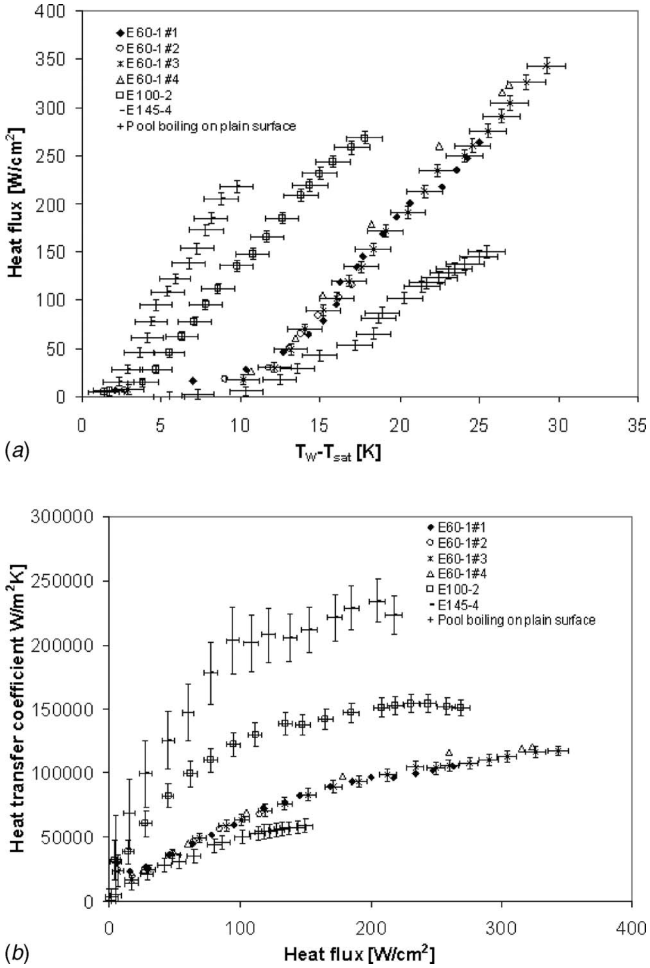

Fig. 1 (a) Heat flux as a function of superheat [$T_{\mathrm{wall}}-T_{\mathrm{sat}}$] as a function of mesh size; (b) heat transfer coefficient as a function of heat flux as a function of mesh size

2.1.1 Effects of Mesh Size on Evaporation/Boiling Heat Transfer Performance. Figure 1(*a*) presents the heat flux as a function of the superheat, while Fig. 1(*b*) illustrates the effective heat transfer coefficient. As shown, the evaporation/boiling heat transfer coefficient increases with incremental increases in the input power until a maximum value has been reached. At this point the evaporation/boiling heat transfer coefficient begins to decrease, due to partial dry out of the wick structure and the heated surface. This implies that the capillary force is still effective in helping to provide fluid to the heated area even at partial wick dry out, which is consistent with the findings of the experimental investigation in Part I [1]. Furthermore, the heat transfer performance on the 2362 m^{-1} copper mesh (60 $\mathrm{in.}^{-1}$), a relatively coarse mesh, reached values as high as 117.3 $\mathrm{kW/m^2\,K}$, which is still superior to pool boiling on a plain surface.

With the exception of the initial region and the region following partial dry out, the input heat flux, q'', and the wall super heat, T_W-T_{sat}, exhibit a strong linear relationship. Figure 1(*a*) also indicates that the evaporation/boiling heat transfer performance of the capillary wick increases with increasing mesh number or decreases in the mean pore size. While it is clear that both the total surface area and the exposed surface area would increase proportionally with an increase in the mesh number, an increase in the total surface area or an increase in the exposed surface could account for the increase in the heat transfer coefficient with wire diameter. However, in Part I [1] it was illustrated that only the

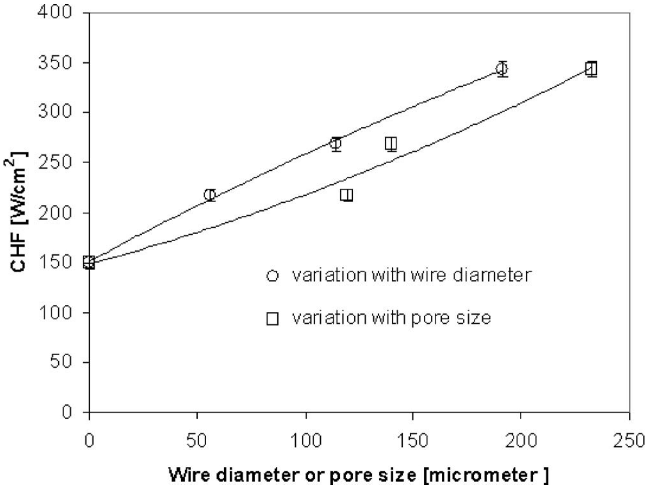

Fig. 2 CHF as a function of wire diameter or pore size of sintered isotropic copper mesh

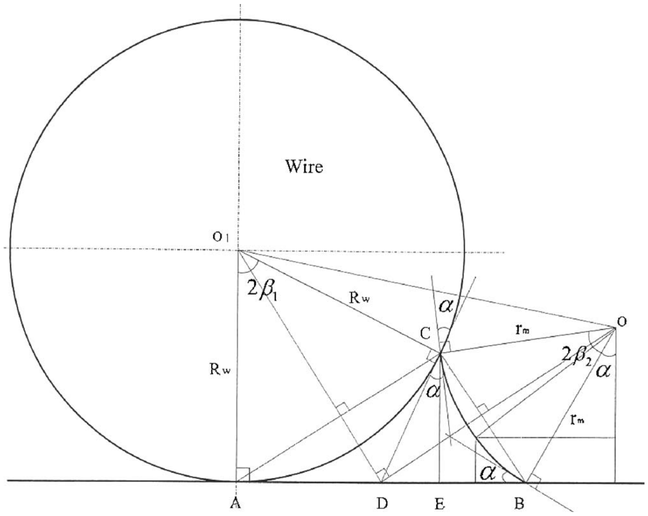

Fig. 3 Schematic of the meniscus between the wire and the wall [17]

exposed surface area plays a role in the evaporation/boiling process in these types of capillary wick structures in gravitational fields. When the volumetric porosity and thickness are held constant, increases in the mesh number may result in an enhanced exposed surface area which, in turn, would result in substantially improved performance.

2.1.2 Effects of Mesh Size on Evaporation/Boiling Characteristics. Figure 1(*a*) indicates that the evaporation/boiling inception superheat is generally dependent on the mesh size and can be reduced through the use of capillary wicking structures when compared with pool boiling on a plain surface. For a given wick thickness and volumetric porosity, the evaporation/boiling inception superheat increases with mesh size increases. One possible reason is due to the pore size reduction. For example, sample E60-1 is made from relatively coarse copper mesh and has evaporation/boiling inception point close to that of pool boiling on a plain surface, i.e., when pore size is big enough, the effect of capillary wicking is deteriorated and the reduction of boiling inception superheat would diminish. The superheat at CHF also demonstrates an increasing relationship with increasing mesh size.

2.1.3 Effects of Mesh Size on the CHF. As discussed in Part I [1], the CHF for any evaporation/boiling system, is determined by the mechanism of liquid supply to, and vapor escape from, the phase change interface. For the evaporation/boiling from thin sintered isotropic mesh surfaces, the bubbles break up or collapse at the free liquid-vapor interface and the liquid-vapor counterflow resistance is reduced without bubble flow through the capillary wick. In addition, the contact points connecting the wick and wall, serve to interrupt the formation of the vapor film and/or reduce the critical hydrodynamic wavelength. Thus the CHF for evaporation/boiling from these porous surfaces is greatly enhanced.

Figure 2 demonstrates the dependence of the CHF on the wire diameter and indicates that increases in the wire diameter would result in an increase in the CHF. This demonstrates that besides the menisci formed between the wires in the horizontal direction [14], menisci are also formed between the wire and the wall, as shown in Fig. 3 [17]. These factors also play a role in the resupply of the liquid. In the evaporation/boiling process in these capillary wicking structures, the capillary pressure is the only pressure source available to pump water to the heated area and the contact angles are assumed to be constant, since identical materials, sintering and cleaning processes (Duraclean™ 1075) were employed to assure identical wetting characteristics. In Fig. 3, α, r_m, and R_w denote the contact angle between the liquid and solid surface, the meniscus radius formed between the wire and heating wall, and the wire diameter, respectively. From Fig. 3, it is clear that wires with smaller diameters also can have a small meniscus radius when the interface is close to the bottom of the wire, but from a fluid mechanics perspective, when a meniscus with a small radius is formed between wires with smaller diameters and the heating wall, the cross-sectional flow area of the liquid is much smaller than that formed between wires with larger diameters. Thus, the flow resistance for smaller wires is much higher than that for larger wires when the meniscus radius is the same, i.e. the capillary pressure generated is the same, but the flow resistance is greater. Generally larger wires can generate higher capillary pressures with a relatively lower flow resistance; therefore the CHF would be higher for wires with larger diameters when the thickness and volumetric porosity of the capillary wicking structures are held constant.

2.2 Effects of Wick Volumetric Porosity. In order to determine how the volumetric porosity of a thin capillary wick structure affects the evaporation/boiling heat transfer performance and the CHF on thin capillary wicking structures, three samples, E145-4, E145-6c, and E145-7c, which, as shown in Table 1, are approximately the same thickness, were fabricated using an identical copper mesh. The required variations were achieved by compressing the layers, thereby changing the distance between layers. From Figs. 4(*a*) and 4(*b*), the thickness of the six-layer test article is reduced significantly when compared with the regular six-layer test article. This compression process does not change the horizontal pore size, but does impact the vertical pore size, which is greatly reduced. Results from these three samples are plotted and compared in Figs. 5(*a*) and 5(*b*). For comparison, the pool boiling curve on a plain surface has also been added to Figs. 5(*a*) and 5(*b*).

2.2.1 Effects of Volumetric Porosity on Evaporation/Boiling Heat Transfer Performance. Figure 5(*a*) presents the heat flux as a function of the superheat, while Fig. 5(*b*) illustrates the effective heat transfer coefficient as a function of the heat flux. These two figures present some of the same characteristics as previous cases studied and the resulting curves are consistent with results previously reported by Li et al. [1]. In addition, the lower the volumetric porosity of the wick, the higher the heat transfer performance, even though the improvement is relatively small. The reason for this is thought to be due to the increase in the effective thermal conductivity with decreases in the volumetric porosity, i.e., for a given heat flux, the capillary wick could be utilized efficiently and hence, more cavities could be activated in wicks with higher ef-

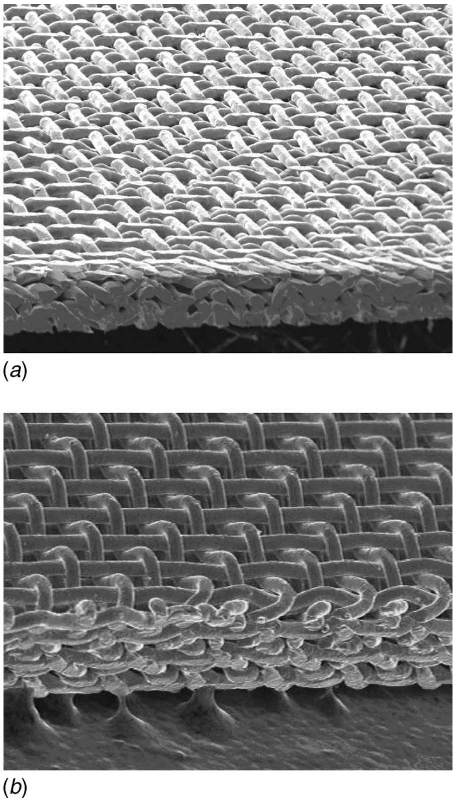

Fig. 4 (a) SEM image of the compact six layer sample; SEM images of sintered isotropic copper mesh with 1509 m^{-1} (145 in.$^{-1}$), 56 μm (0.0022 in.) wire diameter, and fabricated at sintering temperature of 1030 °C with gas mixture protection (75% N_2 and 25% H_2) for two hours

fective thermal conductivities. Generally, for porous media with the same structure, the effective thermal conductivity increases with decreases in the volumetric porosity.

It is also apparent that wicks with a lower volumetric porosity would result in higher heat flux values after partial dry out. This is because the pore size in the vertical direction becomes smaller after compression, resulting in a smaller capillary radius and hence, a higher capillary pressure. This explains the existence of an optimum porosity when the wick thickness and mesh size are both held constant.

Figure 5(*a*) clearly indicates that the evaporation/boiling inception point is greatly reduced when compared with pool boiling on a plain surface and can be shown to be independent of the volumetric porosity for a given mesh size and capillary wick thickness.

2.2.2 Effects of Volumetric Porosity on the CHF. Mathematically there exist three distinct cases for volumetric porosity: a regular capillary wick covered surface, a solid coated surface, and an empty coated surface, each distinguished by the relative porosity of the coating material or wick. This experimental study investigated the effects of porosity, which varied from 0.409 to 0.692 by changing the distance between the wires in the vertical direction. For $\varepsilon=0$, the heating area is filled with solid metal and thus no phase change can occur on top of the heated wall without the liquid supply. For this case, the CHF is assumed to be 0 W/cm^2. However, when the heating area becomes empty and a pool of liquid is formed above the top of the heater, the CHF is similar to the value obtained for pool boiling in [1]. This experimentally measured value in Part I is presented here in Fig. 6.

Figure 6 illustrates that for a given thickness and mesh size, there exists an optimum volumetric porosity that governs the CHF and evaporation/boiling from thin capillary wicks made of sintered isotropic copper mesh. From a fluid mechanics perspective, increases in the volumetric porosity results in a decrease in the flow head loss. If the maximum capillary pressure generated in the wick is dependent only on the wire diameter and horizontal pore size [14], the CHF would increase with increases in the wick volumetric porosity, because of a decrease in the flow resistance.

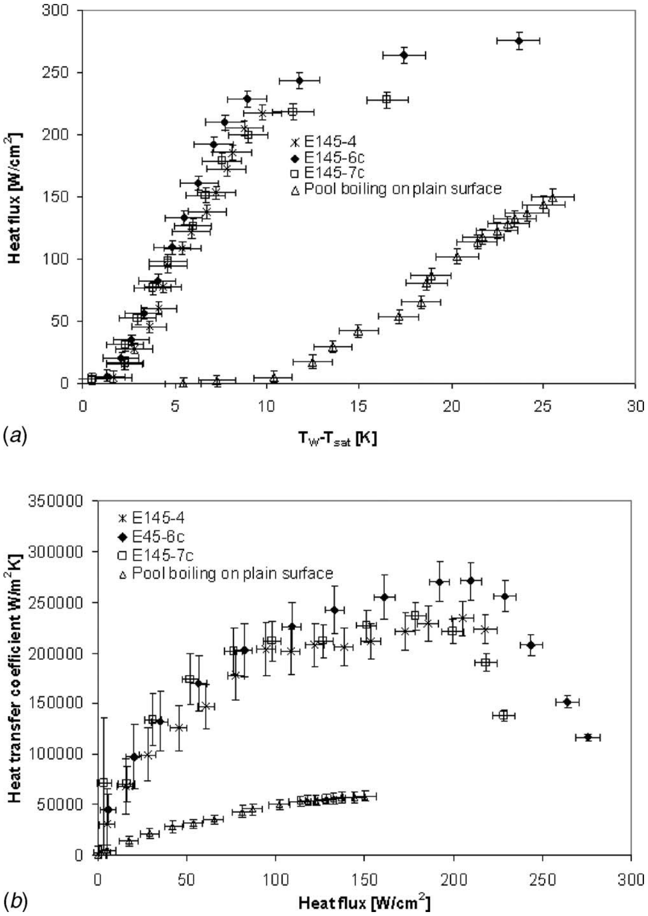

Fig. 5 (a) Heat flux as a function of superheat [$T_{\text{wall}}-T_{\text{sat}}$] as a function of volumetric porosity; (b) heat transfer coefficient as a function of heat flux as a function of volumetric porosity

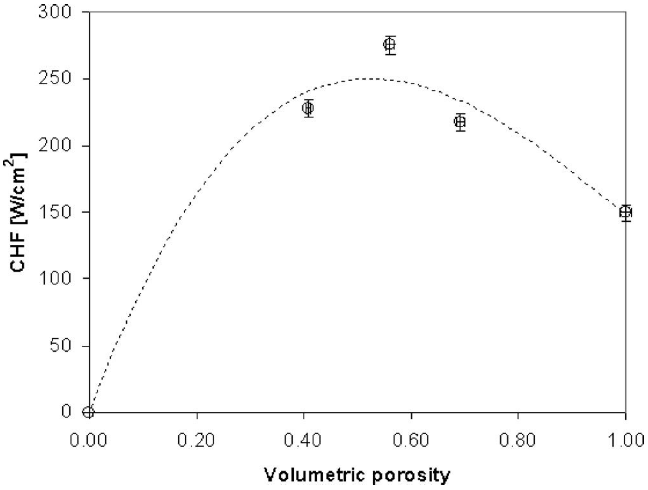

Fig. 6 Test data of CHF as a function of volumetric porosity of the sintered isotropic copper mesh

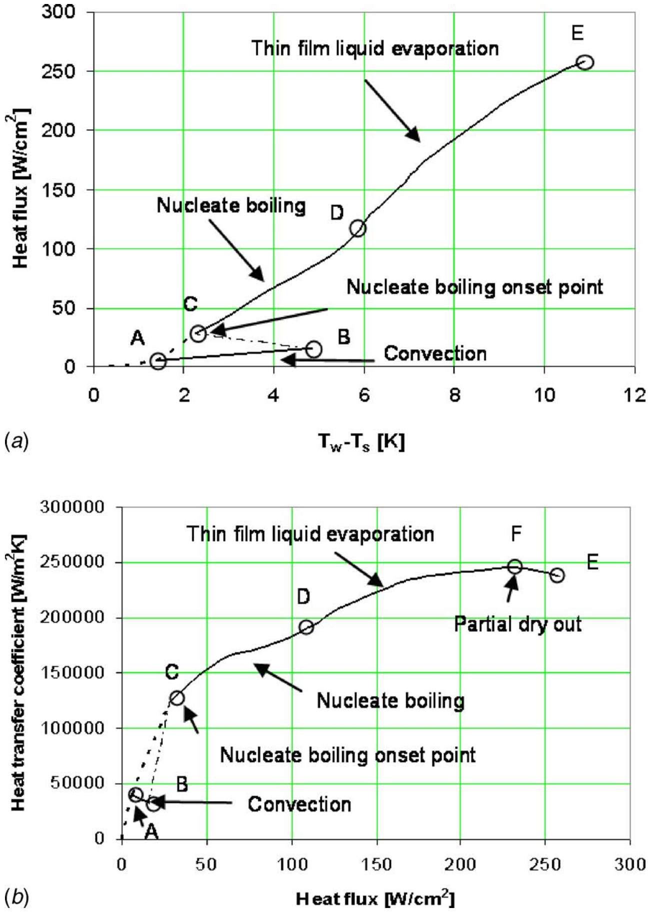

Fig. 7 (**a**) Typical q''-T_{super} curve for evaporation/boiling processes from uniformly sintered copper mesh surfaces (**b**) Typical h_{eff}-q'' curve for evaporation/boiling process from uniformly sintered copper mesh surfaces

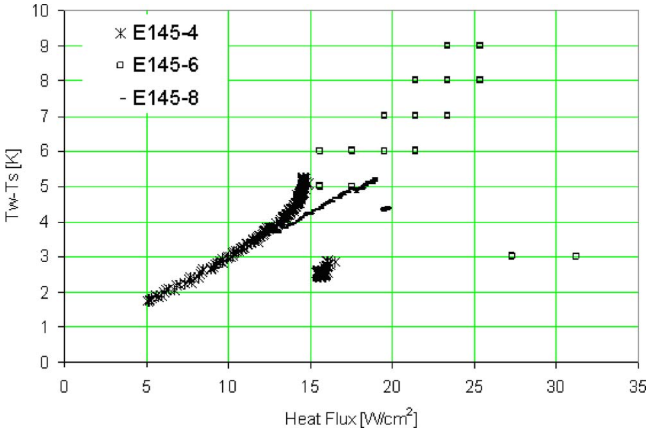

Fig. 8 Onset point of nucleate boiling for evaporation/boiling processes from uniformly sintered copper mesh surfaces

However, as shown in Fig. 6, the CHF decreases after a volumetric porosity of approximately 0.50, which implies an optimum volumetric porosity in the present capillary wick structure. Furthermore, the existence of an optimum volumetric porosity implies that the menisci formed between the wires in the vertical direction also play an important role in the capillary pressure generation. From this analysis and the discussion in Sec. 2.2.3, it is apparent that the minimum meniscus radius, which can occur at the pores between the wires in the horizontal direction or the vertical direction, as well as between the wire and the wall, determines the capillary limit in evaporation/boiling from capillary wick surfaces.

3 Evaporation/Boiling on Thin Capillary Wicks

3.1 Heat Transfer Regime on Thin Capillary Wicks. The results presented in Part I, coupled with the previous discussions, illustrate the characteristics of evaporation/boiling from uniformly sintered copper mesh coated surfaces. It is important to understand what happens in this complex process, in order to optimize the use of these structures in actual applications. Evaporation/boiling phenomenon on uniformly sintered copper mesh surfaces is complicated by the existence of several different regimes and irregular geometric characteristics of the liquid-vapor interface. Based on visual observations of the phase change phenomenon and comparisons of the experimental test data, characteristic q''-T_{super} and h-q'' curves have been proposed, as shown in Figs. 7(*a*) and 7(*b*), respectively. These two curves clearly demonstrate the three regimes that exist: convection, nucleate boiling and thin film evaporation. The transition from one regime to another is accompanied by marked changes in the hydrodynamic and thermal states of the system. When the temperature or heat flux is below a certain value (i.e., the onset of strong nucleate boiling), heat is transferred by convection (AB), which is driven by the temperature difference or a small number of relatively large bubbles. This, then transitions to a region where the nucleate boiling (CD) is the dominant heat transfer mechanism when the temperature or heat flux exceeds the saturation temperature by a value that varies with the capillary wick thickness, pore size and surface characteristics. In Figs. 7(*a*) and 7(*b*), the transition region, BC, does not actually exist. The wall temperature effectively jumps from B to C when it exceeds the evaporation/boiling inception point. In the nucleate boiling regime, numerous bubbles are generated and grow from the nucleation sites on the heated surfaces, i.e. heater wall and wire surfaces, and finally break up or collapse at the free liquid-vapor interface. Increases in the wall temperature or heat flux are accompanied by large increases in the bubble population. These processes, as well as the mutual interaction among bubbles and nucleation sites, result in significant enhancement in the heat transfer performance. It is worth noting that the capillary evaporation also plays an important role in the improvement of performance in the nucleate boiling regime. If the temperature or heat flux is further increased, the meniscus recedes further into the porous material and thin liquid film evaporation (DE) begins. In this region, the liquid film thickness becomes very thin due to a combination of the surface tension and disjoining pressure, making it very hard for bubbles to form and grow from the heated surfaces, and hence, the liquid just evaporates directly from the heated surfaces until they dry out completely, which results in the best performance among these three regimes.

3.2 Onset Point of Nucleate Boiling From a Horizontal Heated Wall. As was the case for pool boiling, in order to reach nucleate boiling, the surface temperature must exceed the saturation temperature by several degrees. Based on the previous discussions, this onset of nucleate boiling from sintered copper mesh surfaces varies with the thickness and mesh size, and is nearly independent of the volumetric porosity. Figure 8 presents the superheat of the heated wall as a function of the heat flux applied, as in the cases of E145-4, 6, and 8. When the wall temperature is lower than the onset of nucleate boiling, it increases with heat flux; however, once it exceeds that critical value, nucleate boiling begins and the wall temperature drops sharply due to the high heat transfer capability of nucleate boiling. Figure 8 demonstrates the transition from convection heat transfer to nucleate boiling heat transfer that occurs on sintered copper mesh surfaces, which can be easily identified on either a typical q''-T_{super} or h_{eff}-q'' curve, i.e., point B to C. This figure also illustrates that nucleate boiling occurs in the capillary wicks and significantly improves the heat transfer performance, which is different from the findings of Hanlon and Ma [9].

For some surfaces, section AB can be easily overlooked because the value of the onset of nucleate boiling is small and is not easily predicted. In addition, in some cases the step increase of the heat flux used may be larger than the value at which the onset of nucleate boiling occurs, making it impossible to distinguish one region from another.

The reason that the superheat necessary to activate nucleate boiling varies with the capillary wick thickness and mesh size, remains somewhat unclear. The current experimental investigation only illustrates that these phenomena do, in fact, occur for evaporation/boiling on the capillary wick. The available data indicate that the onset point of nucleate boiling increases with decreases in the mesh size and thickness, but this appears to have no direct relationship with the capillary wick volumetric porosity.

3.3 Local Bubble Generation from a Horizontal Heated Wall. From classical nucleate boiling theory, it is clear that the characteristics of the actual surface are very complicated and that the many nucleation cavities with various shapes and sizes all affect the boiling characteristics. Bubbles are typically generated from the largest cavities first, since this process requires less energy, with the smaller cavities subsequently activated as the heat flux increases. Although the mechanisms of bubble generation from sintered copper mesh surfaces agree with the classical theory, there appears to be some subtle influences due to the presence of the capillary wicking structure that should be noted.

Inside the sintered copper mesh, there are a variety of different two-dimensional menisci formed at the various corners, due to the surface tension. The liquid-phase pressure that exists prior to thin liquid film evaporation in this kind of porous media is determined by the capillary forces generated at the different menisci, and the thin liquid film thickness is determined by the disjoining pressure. Since copper, when treated as described herein, wets well with water, the pressure in the cavity is given by Eqs. (1) and (2):

$$P_v = P_l + 2\sigma/r \tag{1}$$

$$P_l = P_{\text{atm}} - 2\sigma/r_m \tag{2}$$

where r and r_m are the radius of the curvature of the bubble interface and meniscus, respectively.

Equations (1) and (2) indicate that both the liquid pressure and the liquid thickness would decrease as the size of the meniscus radius decreases. The local evaporation/boiling process on the uniformly sintered copper mesh coated surface has five typical configurations, as illustrated in Fig. 9: the initial state (*a*), convection (*b*), nucleate boiling (*c*), thin liquid film evaporation (*d*), and dry out (*e*). In this process, water is supplied only via the capillary forces, which can be deduced from the surface tension and the geometric parameters of the meniscus. At a lower heat flux, smaller amounts of larger bubbles are generated and grow within the heated liquid. In addition, a thin liquid film is formed on the upper wire surfaces. In most cases, boiling and evaporation occur simultaneously and the bubble movement causes liquid convection. If the heat flux increases, the meniscus radius must decrease in order to provide the capillary force needed to pump water into the heated area. Thus, the bubble population and bubble generation frequency, as well as the thin liquid film area all increase. As the heat flux continues to increase, the meniscus radius recedes towards the corner along the solid heated surfaces, forming a thin liquid film, which, due to the disjoining pressure makes it difficult for a bubble to form and grow. At this point, liquid film evaporation becomes the dominant mode. If the heat flux continues to increase, the central portion of the mesh will dry out, due to a loss of liquid supply.

3.4 Local Bubble Dynamics From the Heated Surface. The most noticeable difference between classical nucleate boiling in pool boiling and the evaporation/boiling processes from a thin, i.e., less than 1 mm, sintered copper mesh, is that in the latter, the bubbles never grow large enough to release, hence, there is no bubble departure from the horizontal heated wall. Generally, the bubble departure diameter is estimated by

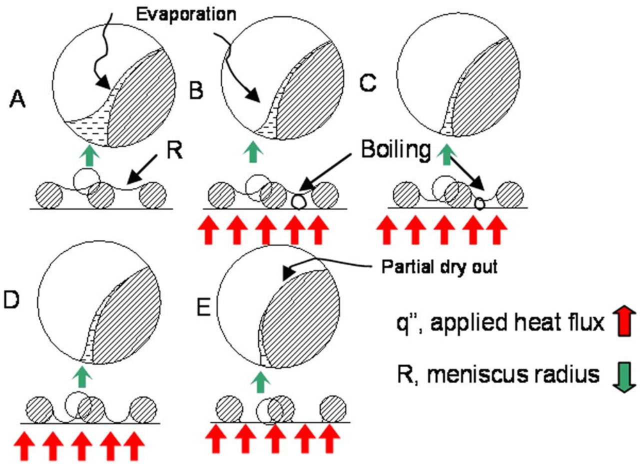

Fig. 9 Local evaporation/boiling processes from wire surfaces and the corners between the wire and the heated surface

$$D_d = \text{Bo}^{1/2}\left(\frac{2\sigma}{g(\rho_l - \rho_v)}\right)^{1/2} \tag{3}$$

The Bond number depends on the bubble contact angle and stochastic processes; i.e., in actuality the observed bubble departure diameter has a statistical distribution around some mean. Numerous investigations over the past 70 years have been carried out to estimate the Bond number. This departure diameter model was first proposed by Fritz [13] and is shown below as Eq. (4),

$$D_d = C_d\alpha\left(\frac{2\sigma}{g(\rho_l - \rho_v)}\right)^{1/2}. \tag{4}$$

Two more models are selected to compare with the model of Fritz. One model was developed by Cole and Rohsensow [13] and is shown as Eq. (5) below

$$\left(\frac{g(\rho_l - \rho_v)D_d^2}{\sigma}\right)^{1/2} = C'_d\left(\frac{\rho_l C_{pl} T_{\text{sat}}}{\rho_v h_{\text{fg}}}\right)^{5/4} \tag{5}$$

where $C_d = 0.0148$ for hydrogen bubbles and water vapor, in water, and the contact angle, ϕ, is in degrees. Here, $C'_d = 1.5 \times 10^{-4}$ for water. The second model presented here was proposed by Jensen and Memmel [15].

$$\text{Bo}^{1/2} = 0.19(1.8 + 10^5 K_1)^{1/2} \tag{6}$$

where, in Eq. (6) $K_1 = (\text{Ja}/\text{Pr}_l)\{[g\rho_l(\rho_l - \rho_v)/\mu_l^2][\sigma/g(\rho_l - \rho_v)]^{3/2}\}^{-1}$ and the Jacob number, Ja, is defined by $(T_W - T_{\text{sat}})C_{pl}\rho_l/(\rho_v h_{\text{fg}})$. For copper-water combinations, the contact angle α is 55°, which was experimentally determined by Wu and Peterson [16]. The departure diameters estimated using Eqs. (4)–(6), for this situation are all greater than 1 mm. These estimations are listed in Table 2, where the minimum value given is even greater than the thickest capillary wick presented herein, 0.82 mm.

The typical localized bubble generation and growth from the heated surfaces, i.e., the top wall of the heater and wire surfaces, are illustrated in Fig. 10. When a relatively low heat flux is applied, only large cavities are activated, so large bubbles are generated and grow from the heated surface. These large bubbles grow, but never depart from the heated wall. Instead, they collapse at the free liquid-vapor interface, due to local condensation and pressure differences before they can grow large enough to gain

Table 2 A comparison of the bubble departure diameter

			D_d(mm)
Fritz's model [13]			2.884
Cole and Rohsensow's model [13]			2.426
Jensen and Memmel [15]	T_w-T_{sat}	1 K	1.032
		5 K	1.169
		15 K	1.482
		30 K	1.897

sufficient buoyancy energy to detach from the wall surface. A higher heat flux activates smaller cavities, and causes an increase in the number of bubbles and a decrease in the average bubble size. The mutual interaction among bubbles results in higher heat transfer performance. With a further increase in the heat flux, the mean bubble size continues to decrease and the bubble generation frequency increases dramatically. In addition, for thin liquid films with high pressures (induced by the disjoining forces), it is hard for the bubbles to grow, and as a result, the liquid evaporates directly from the thin liquid surface. In other words, when bubbles cannot depart from the heated wall, there is a lower flow resistance between the bubble and the liquid, as well as a higher bubble generation frequency and the resulting heat transfer performance will be significantly enhanced.

3.5 Liquid Vapor Interface Dynamic and Drying-out Process on Thin Capillary Wicks. The behavior of the liquid-vapor interface is one of the key characteristics that govern the evaporation/boiling on capillary wicking structures. In [14], the heat transfer from capillary wicking structure surfaces was discussed and four models were presented as shown in Fig. 11. In addition, the dynamics of the liquid-vapor interface and its effects on the evaporation/boiling in capillary wicks were discussed indirectly. The principal points in [14] can be summarized as follows: At low heat fluxes, combined conduction and convection is the main heat transfer mode and, if the wick is horizontal, the liquid-vapor interface is parallel to the heating surface. As the heat flux increases, the evaporation at the liquid surface is intensified, and the liquid-vapor interface recedes uniformly, generating a greater capillary force. In the receding liquid model, there is no boiling and conduction still governs the heat transfer across the liquid surface. The capillary limitation may be encountered in this phase. When the heat flux is further increased, nucleate boiling may take place within the wick. Bubbles grow at the heated wall and escape to the liquid surface, where they burst rapidly. Nucleate boiling may represent a heat transfer limit in the nucleate boiling model, since, as the heat flux increases to a specific value, large quantities of bubbles are generated at the heated wall. These bubbles coalesce and form a vapor layer adjacent to the heated wall. This vapor layer is the principal cause of the heat transfer limit often encountered. In [14], the heat transfer limit for evaporation in capillary wicks was described as being similar to that occurring in pool boiling heat transfer. The thickness factor was not considered in [14] when evaporation/boiling behavior was discussed.

In the present work, however, the wick thickness is confined to thicknesses of less than 1 mm, which is smaller than the bubble departure diameter, D_b. As discussed previously, at this thickness, a much higher heat transfer performance and higher CHF were achieved. The control volume shown in Fig. 12 is utilized to analyze the liquid vapor interface behavior in evaporation/boiling in capillary wicks. At saturation conditions, the mass and energy conservation equations can be defined as:

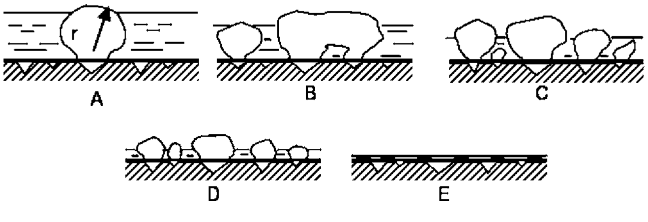

Fig. 10 Local bubble dynamics and evaporation in evaporation/boiling processes on the surface

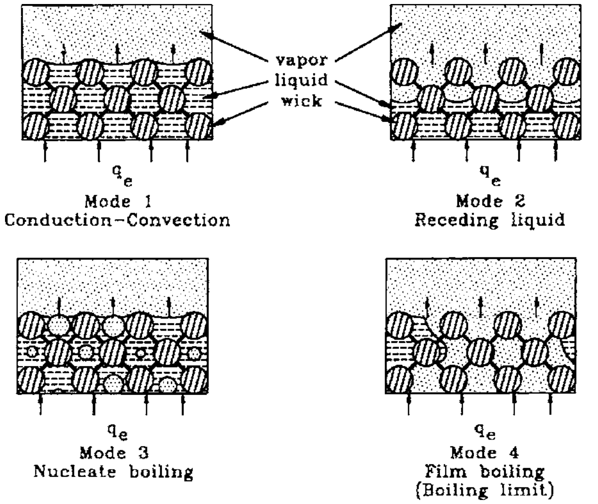

Fig. 11 Models of heat transfer and vapor formation in wicks [14]

$$\dot{m}_{l,in} = \dot{m}_{l,\text{out}} + \dot{m}_v \tag{7}$$

$$h_{\text{fg}}\, d\dot{m}_v = q''\, dx \tag{8}$$

Solving Eqs. (7) and (8), the liquid-vapor interface configuration at steady state can be determined by

$$y = y_0 - \frac{q''x}{G_l h_{\text{fg}}} \tag{9}$$

Here, G_l is the liquid flow rate and y_0 is the initial position of the liquid, i.e., the wick thickness. If the heat flux, q'', is ideally uniform, the liquid-vapor interface would be a straight line with a slope of $-q''/G_l h_{\text{fg}}$. However, because the thermal insulation is not perfect, the actual heat flux profile along the heated wall is parabolic, as shown in Fig. 13. The interface would be irregular due to the meniscus, but the overall shape would be curved, thinner in the center, and thicker at the edges. The overall liquid-vapor interface dynamics has four typical modes, which are presented in Fig. 14. Mode A is the initial state, in which the liquid-vapor interface is parallel to the heated wall. As the heat flux is increased, vaporization begins and the meniscus begins receding, which generates a greater capillary force, increasing the amount of liquid supplied to the heated area. The receding of the menisci is

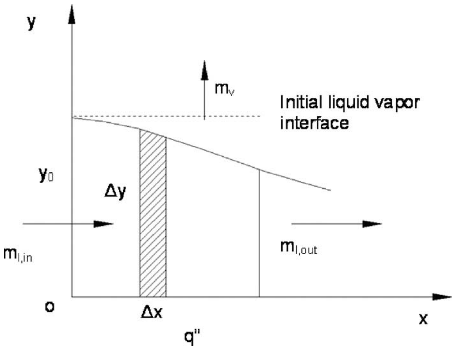

Fig. 12 Control volume of the liquid-vapor interface

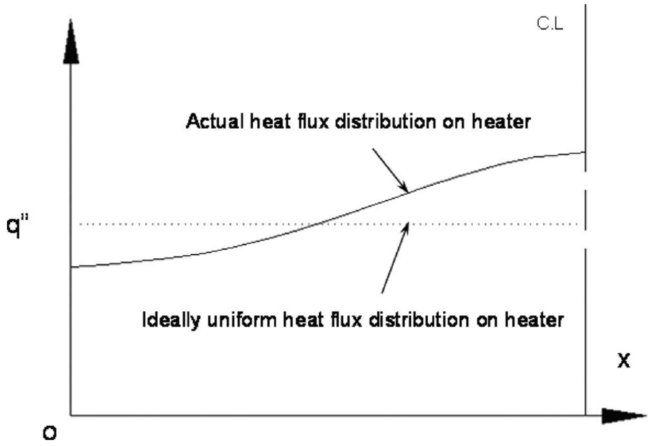

Fig. 13 Heat flux distribution along the flow direction of the heater

not uniform because of the constant and continuous liquid mass reduction along the heated wall, which results from more vaporization of the liquid as the center of the heated area is approached. During this process, menisci are formed between the wires in the horizontal and vertical directions, and even between the wire and the heated wall after the initial dry out occurs.

This analysis is consistent with the experimental results presented in Sec. 2.2.2. As the heat flux is further increased, the curvature of the liquid-vapor interface becomes smaller and the initial dry out point first appears at the center of the heated section of the wall. For evaporation/boiling on a capillary wick structure, the appearance of this initial dry out does not represent the CHF. The capillary wick will still function under higher heat fluxes until sufficient liquid can no longer be provided. As shown in Fig. 15, the dry out regions are clearly evident for each of the different heat flux levels tested. Here, the white rings represent the dry out region for each heat flux level tested. At each heat flux, steady-state operation is achieved and a specified region of the wick remains dry. These rings represent the capillary limit for the evaporation/boiling in the capillary wick for a specified heat flux.

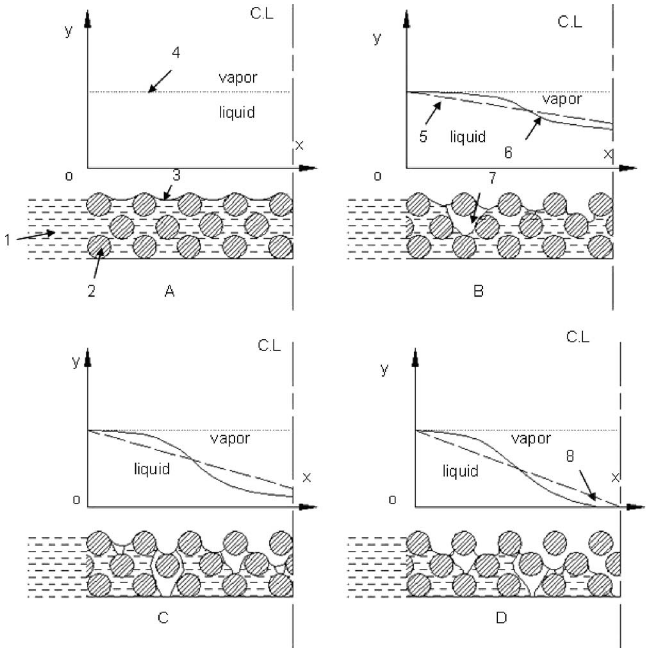

Fig. 14 Liquid-vapor interface and heat transfer model in the capillary wick structure 1. distilled water; 2. copper wire; 3. liquid-vapor interface; 4. initial liquid-vapor interface position; 5. interface position curve at uniform heat flux; 6. interface position at actual heat flux; 7. vapor bubble; 8. first dry out point

4 Conclusions

The minimum meniscus radius is ultimately the determining factor in CHF for the evaporation/boiling from capillary wicking structures, and the results presented here illustrate that the menisci are formed not just between the wires in the horizontal direction, but also between the wires in the vertical direction, and between the wire and the wall. An optimal volumetric porosity has been shown to exist for CHF in the capillary wicks, depending upon the thickness and mesh size. When the wire diameter and wick thickness are held constant, the experimental data shows that the heat transfer performance increases with decreases in the volumetric porosity of the wick, but the improvement is not significant. The reason for this small improvement is thought to be due to the increase in the effective thermal conductivity with decreases in the porosity, i.e., for a given heat flux, more cavities are activated in wicks with higher effective thermal conductivities.

Some key characteristics of the evaporation/boiling from capillary wicks are detailed in the discussion. When the capillary wick thickness is less than 1 mm, the bubbles break up or collapse at

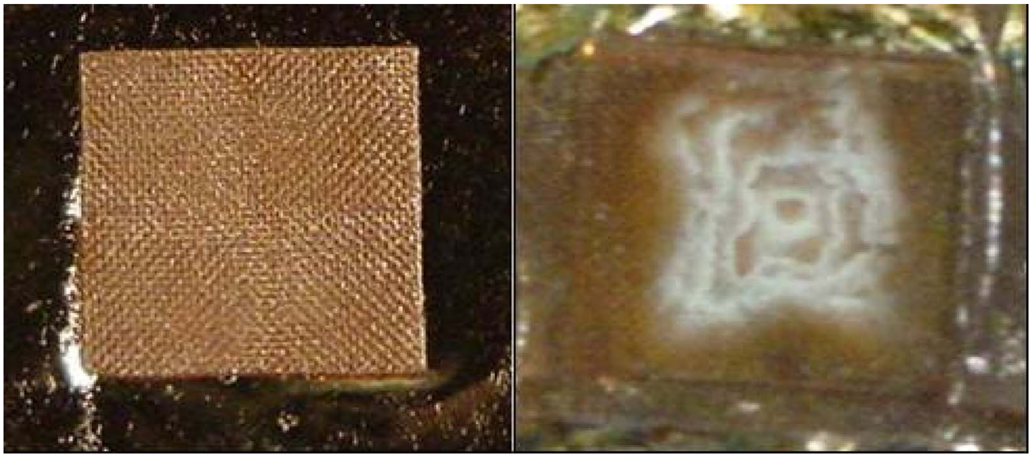
(*a*) (*b*)

Fig. 15 (*a*) Capillary wick surface before applied heat flux; (*b*) capillary wick after dry out. Progressive dry out processes in a capillary wick during evaporation/boiling

the free liquid-vapor interface, due to local condensation and the pressure difference, instead of departing from the heated wall. This feature could enhance the heat transfer capability and CHF dramatically, due to reductions in the counterflow liquid and vapor resistance and the enhancement in the bubble generation frequency. Analysis of the liquid-vapor interface dynamics shows that the liquid thickness in the wick, decreases nonlinearly along the heated wall, and the first dry out point occurs in the center of the heated area. This analysis also demonstrates that menisci are formed not just between wires in the horizontal direction, but also between wires in the vertical direction and between wires and the heated wall. These new theoretical findings are consistent with both the current and previously presented experimental results.

Both the experimental test data and the visual observations support the concept that the heat transfer limit for evaporation/boiling in capillary wicks is the result of a capillary limit, and that the characteristic receding of the meniscus into the wick structure is not uniform, but rather decreases as the center of the heated area is approached. The different heat transfer regimes for evaporation/boiling in these different capillary wick structures have been proposed and discussed based on the current and previous experimental investigations as well as the visual observations of the phase change phenomena and the heat flux—superheat relationship.

The test data obtained herein, illustrate that the evaporation/boiling inception is strongly dependent on the pore size in the horizontal direction and the wick thickness, however, it is weakly dependent on volumetric porosity. Hysteresis was also observed from evaporation/boiling on the capillary wick in this experimental investigation.

Acknowledgment

The authors would like to acknowledge the support of the National Science Foundation under award CTS-0312848. Fruitful discussions offered by Dr. Ji Li and Mr. Hong Li are greatly appreciated.

Nomenclature

A–E = points number in Fig. 3
Bo = Bond number
C_d = Constant in Eq. (3)
C'_d = Constant in Eq. (4)
C_p = Specific heat at constant pressure [J/kg.K]
D_d = Bubble departure diameter (mm)
G = Flow rate $(\mathrm{kg/m^2s})$
g = Gravitational acceleration $(\mathrm{m/s^2})$
h_{fg} = Latent heat (KJ/kg)
Ja = Jacob number
K = Thermal conductivity (W/Mk)
K_1 = Parameter in Eq. (6)
$\dot{m}$ = Mass flow rate (kg/s)
M = Mesh number $(\mathrm{m^{-1}})$
O = Center of circle
P = Pressure (Pa)
$\mathrm{P}r$ = Prandtl number
q'' = Heat flux $(\mathrm{W/cm^2})$
R = Bubble radius (mm)
r_m = Meniscus radius (mm)
R = Wire radius (mm)
t = Distance or thickness (mm)
t_w = Time required for bubble growth (s)
t_d = Time required for bubble departure (s)
T = Temperature (K)
W = Width of mesh opening
X = X coordinate
Y = X coordinate

Greek Symbols

α = Contact angle (degree)
β = Angle (degree)
ε = Volumetric porosity
σ = Surface tension (N/m)
ρ = Density $(\mathrm{kg/m^3})$

Subscripts

in = Flow in direction
l = Parameter related to the liquid phase
out = Flow out direction
v = Parameter related to the vapor phase
w = Parameter related with the wall
sat = Parameter related with the saturation condition
eff = Effective parameter

References

[1] Li, C., Peterson, G. P., and Wang, Y., 2006, “Evaporation/Boiling on a Capillary Wick (I)—Wick Thickness Effects,” ASME J. Heat Transfer, **128**, pp. 1312–1319.
[2] Liter, S. G., and Kaviany, M., 2001, “Pool-Boiling CHF Enhancement by Modulated Porous-Layer Coating: Theory and Experiment,” Int. J. Heat Mass Transfer, **44**, pp. 4287–4311.
[3] Udell, K. S., 1985, “Heat Transfer in Capillary Wick Considering Phase Change and Capillarity—The Heat Pipe Effect,” Int. J. Heat Mass Transfer, **28**, pp. 77–82.
[4] Williams, R. R., and Harris, D. K., 2005, “The Heat Transfer Limit of Step-Graded Metal Felt Heat Pipe Wicks,” Int. J. Heat Mass Transfer, **48**, pp. 293–305.
[5] Tolubinsky, V. I., 1981, “Some Peculiarities of Vaporization Process in a Single Cell of the Heat Pipe Wick,” *Proceedings of the 4th International Heat Pipe Conference*, London, England, September 7–10, pp. 375–388.
[6] Smirnov, G. F., and Afanasiev, A., 1981, “Investigation of Vaporization in Screen Wick-Capillary Structures,” *Proceedings of the 4th International Heat Pipe Conference*, London, England, September 7–10, pp. 405–413.
[7] Abhat, A., and Seban, R. A., 1974, “Boiling and Evaporation from Heat Pipe Wicks With Water and Acetone,” ASME J. Heat Transfer, **90**, pp. 405–413.
[8] Styrikovich, M. A., Malyshenko, S. P., Andianov, A. B., and Talaev, I. V., 1987, “Investigation of Boiling on Porous Surface,” Heat Transfer-Sov. Res., **19**, pp. 23–29.
[9] Hanlon, M. A., and Ma, H. B., 2003, “Evaporation Heat Transfer in Sintered Porous Media,” ASME J. Heat Transfer, **125**, pp. 644–652.
[10] Mughal, M. P., and Plumb, O. A., 1996, “An experimental Study of Boiling on a Wicked Surface,” Int. J. Heat Mass Transfer, **39**, pp. 771–777.
[11] Lao, Q., and Zhao, T. S., 1999, “Evaporation Heat Transfer in a Capillary Structure Heated by a Grooved Block,” J. Thermophys. Heat Transfer, **13**, pp. 126–133.
[12] Auracher, H., Marquardt, W., Buchholz, M., Hohl, R., Luttich, T., and Blum, J., 2001, “New Experimental Results on Steady-State and Transient Pool Boiling Heat Transfer,” Therm. Sci. Eng., **9**, pp. 29–39.
[13] Tong, L. S., and Taung, Y. S., 1997, *Boiling Heat Transfer and Two Phase Flow*, 2nd ed., Taylor & Francis, London, England.
[14] Faghri, A., 1995, *Heat Pipe Science and Technology*, Taylor & Francis, London, England.
[15] Jensen, M. K., and Memmel, G. J., 1986, “Evaluation of Bubble Departure Diameter Correlations,” *Proceedings of 8th Int. Heat Transfer Conf.*, Vol. 4, pp. 1907–1912.
[16] Wu, D., and Peterson, G. P. 1991, “Investigation of the Transient Characteristics of a Micro Heat Pipe,” J. Thermophys. Heat Transfer, **5**, pp. 129–134.
[17] Yaxiong, W., 2001, “The Theoretical Analysis and Experimental Investigation of a Flexible, Lightweight Radiator with Micro Heat Pipe,” Ph.D. dissertation, Texas A&M University.

Qingjun Cai
e-mail: qcai@rwsc.com

Chung-lung Chen

Rockwell Scientific Company,
1049 Camino Dos Rios,
Thousand Oaks, CA 91360

Julie F. Asfia
The Boeing Company,
5301 Bolsa Ave, MC H013-B308,
Huntington Beach, CA 92647
e-mail: Julie.asfia@boeing.com

Operating Characteristic Investigations in Pulsating Heat Pipe

Pulsating heat pipe (PHP) is an interesting heat transfer device. In this paper we focus on PHP heat transfer characteristics versus its operating temperature. In experiments of copper and stainless steel PHPs, results indicate that, at a same input power, both the total temperature differences (from the evaporator to condenser) and the evaporator temperature fluctuations are relevant to operating temperature. The minimal total temperature difference and temperature fluctuation appear at an operating temperature ranging from 120°C *to* 160°C. *Experimental analysis of the evaporator temperature fluctuations show that single phase cooling in PHP causes a large total temperature difference and temperature fluctuation. Phase change proportion increases at the optimal operating temperature. Static mechanical balance combining with dynamic elastic oscillation system is used to interpret PHP temperature variations versus the operating temperature.* [DOI: 10.1115/1.2349509]

Introduction

As power consumption on electrical and electronic systems increases, high heat and high-density heat dissipation on their devices increase rapidly as well. Pulsating heat pipe (PHP), a low cost and lightweight, passive device rugged enough for and capable of high heat load cooling, is expected to be an ideal thermal solution in electric/electronic cooling. Pulsating heat pipe, also called oscillation heat pipe (OHP) or meandering capillary-tube heat pipe (MCTHP), was first presented by Akachi in 1990 [1]. According to its operating mechanism, the history of this technology can be traced to Kurzweg and Zhao's "dream pipe" investigation on heat transfer by high frequency oscillation in capillary tubes in 1984 [2].

A typical PHP consists simply of a looped or unlooped capillary tube with multiple turns. The inner diameter of the tube is constrained by a Bond number (Bo) less than 2, which represents the rate of liquid slug gravitational and surface tension forces in a capillary tube, as shown in Eq. (1). For a common liquid, the inner diameter of a PHP should be less than 3 mm to maintain liquid capillary slugs.

$$\mathrm{Bo} = d^2 \cdot g(\rho_l - \rho_v)/\sigma \tag{1}$$

After the PHP tube is vacuumed and filled, a certain percentage operating liquid, alternating liquid and vapor slugs automatically forms, and the atmosphere inside the PHP is in a saturated state. At a steady state of PHP operation, heat transfer is achieved by continuous oscillation movements from its evaporator to its condenser, which is caused by instant pressure imbalance among different turns. Both the phase change and sensible heat exchanges are considered to participate in PHP heat transfer.

Deep studies on PHP operating characteristics and mechanism have been extended since the late 1990's. Experimentally, Akachi et al. [3,23] first explained the principle and features of PHP and gave some examples of applications. In a 30-turn R-142b copper PHP, Miyazaki and Akachi [4,25] investigated oscillation pressure characteristics for various fill ratios and orientations. Maezawa et al. [5,24] studied a PHP consisting of 20-turn copper tube (ID 1.0 mm) with a total length of 24 m. In their experiments, the charge ratio and PHP inclination were investigated, and temperature fluctuations at adiabatic section wall were analyzed. In another experiment, diameter 1.0 and 2.0 mm PHPs with 50% R-142b filling was compared. The performance of PHP at the bottom heat mode was better than horizontal operation mode. Nishino [6] measured the effective thermal conductivity of PHPs at different operating conditions. Gi et al. [7] observed the flow pattern with R142b as the working fluid and concluded that 50% to 60% fill ratios are the best for the Teflon PHP. Based on the Gi et al. PHP fill ratio, Tong et al. [8] conducted similar visualization experiments to observe the flow circulation in a seven-turn looped Pyrex glass PHP. Lin et al. [9,10] investigated the heat transport capacity of a 1.75 mm inner diameter and 40-turn copper-acetone PHP. Their experimental results indicated that PHP does not operate appropriately at a fill ratio of 25%, and the desired fill ratio is 38%. With the same experimental setup, results with FC-72 and FC-75 show that fluorocarbon PHP with 50% fill ratio has a higher heat transport capability than that of 38% fill ratio, and orientation has no significant impact on PHP performance. Cai et al. [11,12] investigated heat transfer characteristics at transparent and copper PHPs, and therefore concluded that thin liquid film evaporation/boiling and interface evaporation of vapor bubbles suspended in liquid slug are two main modes of the phase change. Khandekar et al. [13] conducted detailed reviews on PHP experiments and simulations. Vapor and liquid slug behaviors were observed in a transparent PHP, and the fill ratio effect was evaluated at a 2.0 mm 5-turn vertical copper PHP. In addition, Chandratilleke et al. [14] introduced PHP technology to cryogenic cooling application. Miyasaka tested two turns PHP at micro gravity environment for satellite EFTs cooling. Zuo et al. [15] applied a sintered powder wick in a PHP and demonstrated a cooling capability of 300 W/cm^2 without dryout. Katoh et al. [16] introduced PHP technology in avionics device cooling. Thermal resistance of avionics chassis wall was significantly reduced by an embedded PHP. In theoretical investigations, Miyazaki [17] first presented a wave equation of pressure oscillation based on the analytical model of self-excited oscillation and compared with experimental results. Zuo et al. [15] established a working liquid oscillation correlation with Newton's law. In terms of dumped mechanical vibration theory, Ma et al. [18] simulated PHP oscillation movements and plotted oscillation relations varying with working fluid, operating temperature, dimensions of PHP, and filled liquid ratio. Wong et al. [19] simplified the PHP operating mechanism with a

---

Contributed by the Heat Transfer Division of ASME for publication in the JOURNAL OF HEAT TRANSFER. Manuscript received September 9, 2005; final manuscript received February 6, 2006. Review conducted by Raj M. Manglik. Paper presented at the 2005 ASME International Mechanical Engineering Congress (IMECE2005), November 5-11, 2005, Orlando, Florida, USA.

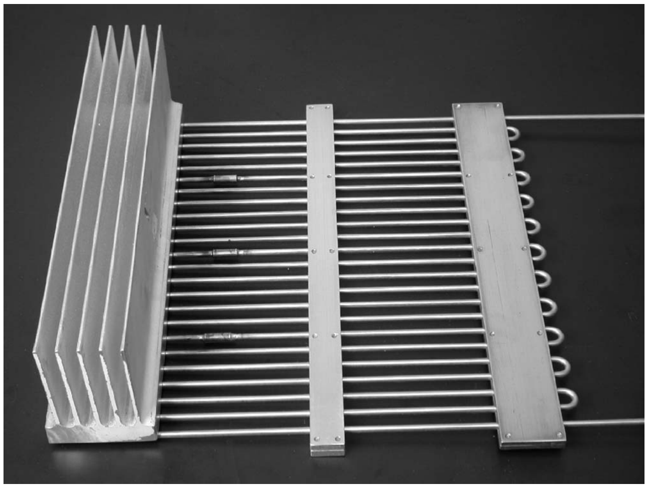

Fig. 1 Testing stainless steel PHP

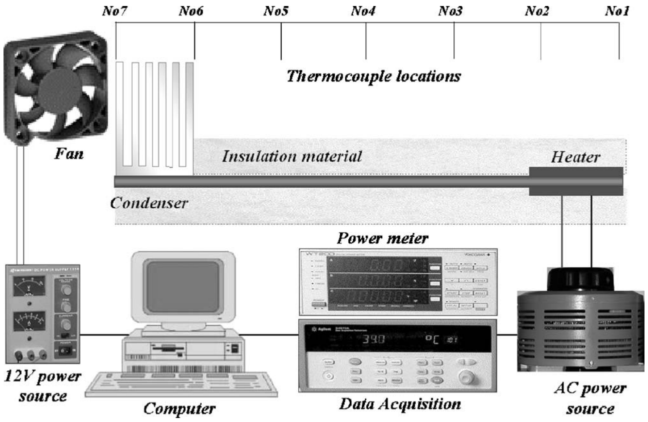

Fig. 2 Schematics of test system

spring and mass system and predicted the kinematics behaviors of liquid slugs and vapor bubbles. Shafil et al. [20] and Zhang et al. [21] developed an analytical model to simulate behaviors of liquid slugs and vapor bubbles in both unlooped and looped PHPs. They concluded that the number of liquid slugs and vapor bubbles reduces to the number of evaporators (turns) regardless of the initial quantity of liquid slugs and vapor bubbles, and that heat transfer in PHPs is due to the exchange of sensible heat.

Heat transfer in PHP is a very complicated procedure. Its operating mechanism is becoming more and more known and detected. However, investigations into this technology are still needed. As for current research, results are inconsistent; and PHP parameter effects, such as material, size, geometer, high-G, noncondensable gas, criterion of turns' number of PHP, still bring some uncertainty for a comprehensive understanding. These inconsistencies and uncertainties eventually limit further extensive applications of PHP technology. As indicated in the PHP application on avionics system, heat transfer capability was strongly relevant to PHP operating temperature. In this paper we explored new avenues of releasing PHP heat transfer characteristics versus PHP operating temperature.

Experimental Setups

Since experiments of PHP operating characteristics versus temperature cover a large range of testing temperature, high internal vapor pressure beyond 210°C brings safety considerations at the tube bended section and end seals. Thus, besides a copper PHP, two high strength stainless steel PHPs are designed. Figure 1 shows a PHP test prototype made of a 3.175 mm (OD) stainless steel tube. In terms of the difference of inner diameters, the stainless steel PHPs with inner diameters 1.568 and 1.397 mm are marked as PHP-A and PHP-B, respectively. The copper PHP has the same dimensions as PHP-A. Both the stainless steel PHPs and copper PHP have 12 turns and 20 cm length (5.0 m in total). Distilled water is selected as an operating liquid for high heat flux heat transfer because of high latent heat. The copper PHP and stainless steel PHPs adopt unlooped structures by which PHP vacuum and liquid inject procedures can be simplified. The liquid charge process is that it first vacuums the PHP, injects the vacuum degassed liquid, seals the injection end, slowly vacuums the other end until first liquid slug appears, and finally pinches and solders the seals. Three typical fill ratios, 40%, 55%, and 70%, are chosen. An aluminum heat sink is mounted on one end of the PHP functioning as the condenser, and copper clampers are designed to increase the thermal contact surface at the PHP evaporator end. Both the evaporator and condenser sections are 2.5 cm in length.

The test system schematic is shown in Fig. 2. The experimental prototype is horizontally set up. Except for the exposed condenser, PHP is thermally insulated by 4.0 cm silica fiber blankets. High temperature heating tapes are pressed on both sides of the copper clamper and heat the PHP evaporator. Two series of thermocouples are mounted along the PHP wall, and each series consists of 7 thermocouples from the evaporator to the condenser. The condenser of test PHP is cooled by air convection driven by a cooling fan. A 12-V power supply is used to rotate the fan. In experiments, lower PHP operating temperatures are obtained by increasing the fan's rotational speed, and higher PHP operating temperatures need lower flow speed to decrease heat exchange between the condenser and ambient. A data collection system including a data-acquisition, a one-channel power meter and a computer is set up to record and process experimental data.

At each input power, temperature effect of PHP is investigated by measuring PHP thermal conduction at different operating temperatures. Unlike the operating temperature in a conventional heat pipe, an operating PHP has a large total temperature difference (ΔT) from the evaporator to condenser, defined in Eq. (2). In this paper, average evaporator temperature (in steady state) is defined as PHP operating temperature, since it is closer to a saturated condition. In addition, to investigate the temperature gradient along a PHP, local temperature differences are defined as:

$$\begin{aligned} \Delta T &= T_{\mathrm{tc}7} - T_{\mathrm{tc}1} \\ \Delta T_e &= T_{\mathrm{tc}1} - T_{\mathrm{tc}3} \\ \Delta T_a &= T_{\mathrm{tc}3} - T_{\mathrm{tc}5} \\ \Delta T_c &= T_{\mathrm{tc}5} - T_{\mathrm{tc}7} \end{aligned} \tag{2}$$

ΔT_e, ΔT_a, and ΔT_c defined above represent temperature differences at the evaporator, adiabatic and condenser sections, respectively.

Experimental Results

In the test system described above, temperature measurements are conducted at steady states for each input power and operating temperature. The temperature spots drawn in the figures are their average values versus time. The temperature measurement bias of thermocouple is within ±0.5°C, and input power varies within ±2.0 W. The maximum heat loss is less than 5% of the total input power while PHP operates at a high temperature and heat load.

Experimental results of the water copper PHP with a 40% fill ratio are plotted in Fig. 3. For each input power level from 100 to 400 W, the total temperature difference (ΔT) shows a "from decreasing to increasing" procedure. At the temperature ranging from 120°C to 150°C, the PHP reaches its maximum

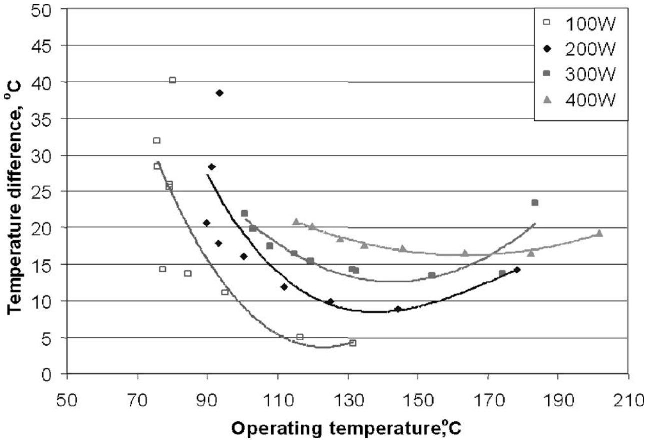

Fig. 3 Test results of the copper PHP, 40%, water

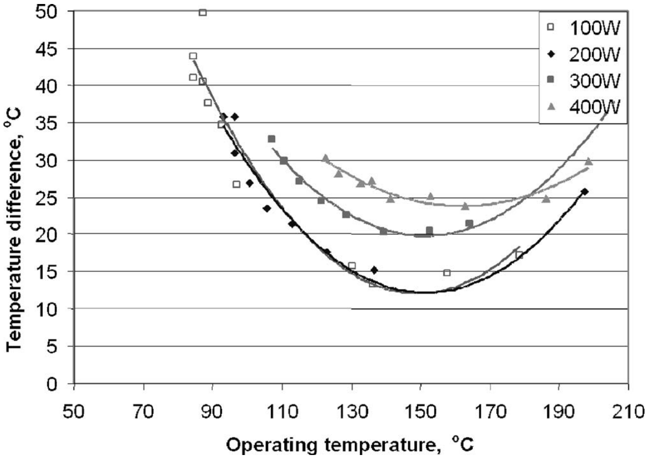

Fig. 5 Test results of the copper PHP, 70%, water

thermal conductivity and minimizes its total temperature difference. For a 100 W test, the minimal total temperature difference is only 3°C–4°C, comparing a 40°C large ΔT at 75°C. With increase of heat loads (from 100 to 400 W), the minimal total temperature difference increases and corresponding operating temperature rises.

Since the heat exchange rate of the PHP condenser is limited by the mode of air-cool, lower operating temperatures at a high heat load are not available. On the other hand, the increasing operating temperature is finally stopped by high internal saturated pressure at 200°C–210°C approximately.

Similar experimental results are shown in Figs. 4 and 5 for the copper PHP tests with 55% and 70% fill ratios. At every heat load level, the total PHP temperature difference exhibits the same trend that first reduces and then increases. Variations of total temperature differences are seriously relevant to the operating temperature. From 40% to 70%, the increases of the fill ratio raise total temperature difference at each corresponding operating temperature and narrow the optimal operating temperature range (Fig. 5).

To further understand PHP characteristics at a higher operating temperature, stainless steel PHP-A and PHP-B are tested, and results are plotted in Figs. 6 and 7. Prior to the 240°C maximum operating temperature reached, similar curves imply that a same physical mechanism governs their operation. By comparing the two figures, PHP-B that has the smaller inner diameter has less sensitivity on heat load changes. PHP-A has larger total temperature difference variation while input powers are changed. For both stainless steel PHP tests, the total temperature differences undergo rapid increase after reaching their minimal values.

By comparing Figs. 5 and 6, it is shown that PHP material properties causes very different operating performance. With the same fill ratio and geometry, the copper PHP shows smaller ΔT at each power level. Moreover, the material effect is also embodied on PHP startup. PHP-A and B with 40% fill ratio does not work at all power levels. When the fill ratio becomes 55%, a preheating

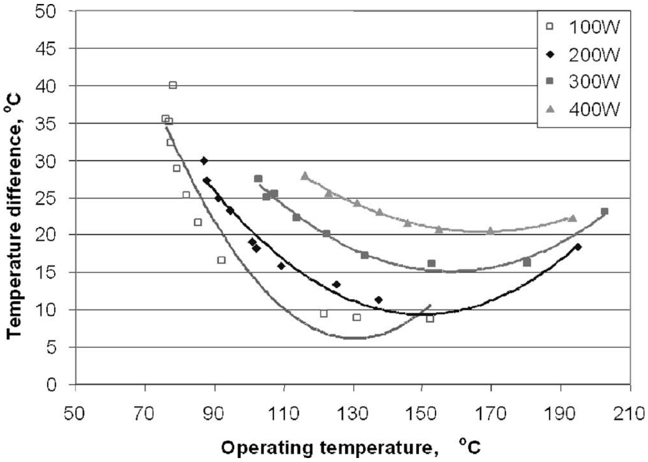

Fig. 4 Test results of the copper PHP, 55%, water

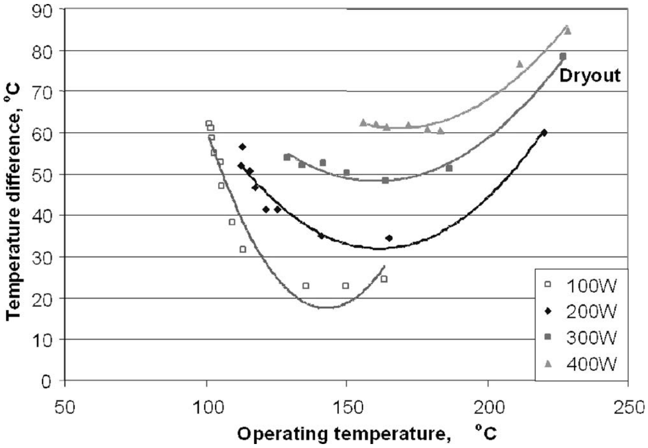

Fig. 6 Test results of stainless steel PHP-A, 70%, water

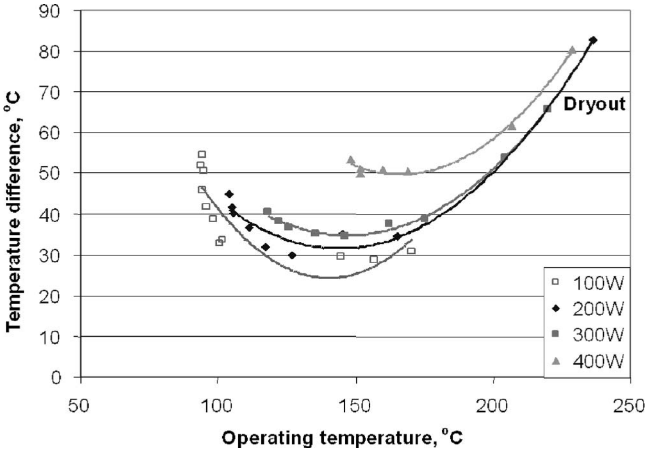

Fig. 7 Test results of stainless steel PHP-B, 70%, water

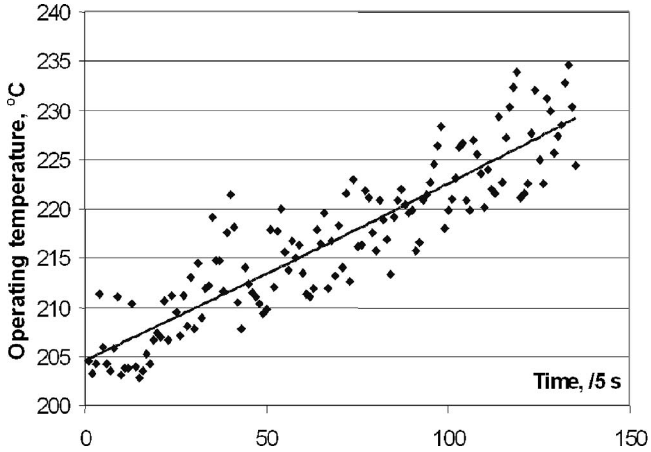

Fig. 8 Dryout phenomenon in PHP-B, 70%, and 300 W

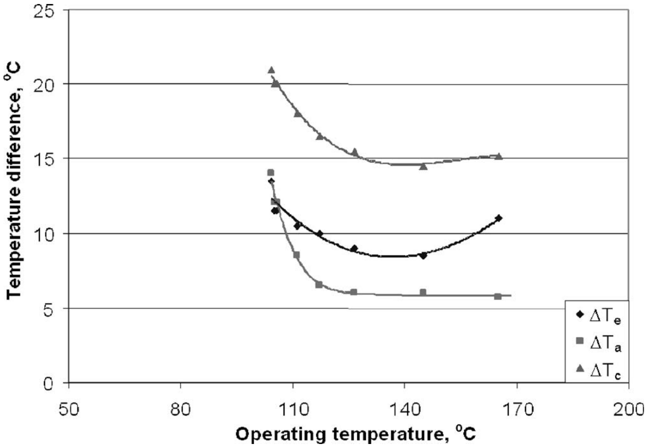

Fig. 10 Temperature difference at different sections, PHP-B, 70%, 200 W

condition is needed to start their operation. Only at 70% fill ratio shown in Figs. 6 and 7, the stainless steel PHPs could normally work. Dryout occurs in both stainless steel PHPs when operating temperatures exceed 220°C and input power is above 200 W. Disparate with a conventional heat pipe, the phenomenon of PHP dryout accompanies continuous oscillation motions and gradually increases the evaporator temperature, as shown in Fig. 8.

In Figs. 9 and 10, local temperature differences at the evaporator, adiabatic and condenser sections, ΔT_e, ΔT_a, and ΔT_c, are plotted to understand heat transfer performance at different PHP sections. For the 40% water copper PHP shown in Fig. 9, all local ΔT tends to rapidly decrease prior to 125°C. After that point, ΔT_a and ΔT_c tend to be constant at the tested operating temperature range, and only ΔT_e starts to increase. After this point, the increase of total PHP ΔT is more related to the variation of ΔT_e. The local ΔT at adiabatic section has only 0.2°C temperature difference when the operating temperature is above 125°C. Similar test results in Fig. 10 are for the PHP-B with 70% water. All local ΔT curves are lifted up because of poor thermal conductivity of stainless steel material.

Temperature fluctuation of the PHP evaporator is a critical characteristic and is caused by operating liquid (from the condenser side) wetting dry evaporator sections. Figures 11 and 12 show the temperature fluctuations of the PHP evaporator via operating temperatures. By comparing test results of the copper PHP shown in Figs. 11(*a*) and 11(*b*), the PHP with 40% water has a greater fluctuation amplitude than the PHP with 70% fill ratio at a lower operating temperature. For test results plotted in Fig. 11(*a*), temperature fluctuation amplitude reduces from 13°C to less than 1°C when the operating temperature increases from 80°C to 135°C. As shown in Fig. 11(*b*), further increasing operating temperature from 160°C to 180°C tends to increase tem-

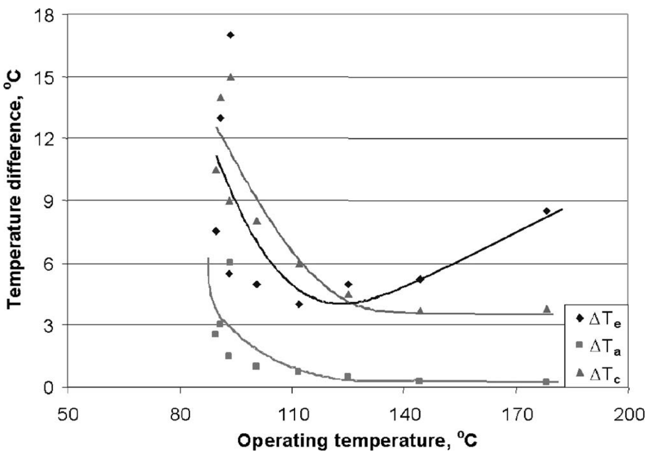

Fig. 9 Temperature difference at different sections, Copper PHP, 40%, 200 W

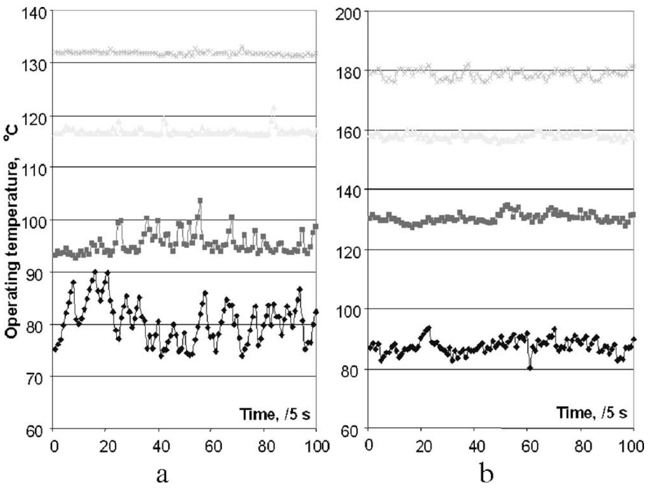

a

b

Fig. 11 Temperature fluctuation, copper PHP, 40 & 70%, 100 W

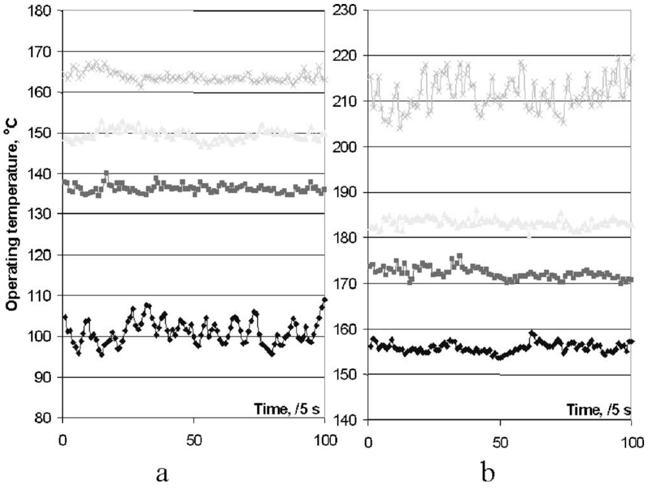

a

b

Fig. 12 Temperature fluctuation, PHP-A, 70%, 100 and 400 W

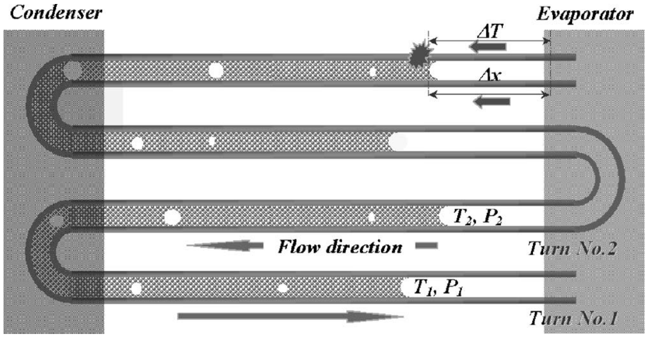

Fig. 13 PHP startup and oscillation mechanisms

perature fluctuation amplitude. The stainless steel PHP-A shows a clearer increase of temperature fluctuation amplitude when operating temperature is above 200°C shown in Fig. 12(*b*). As a summary, oscillation frequency, and temperature fluctuation amplitude validate the relationship: Lower frequency always accompanies larger fluctuation amplitude and high frequency oscillation reduces temperature fluctuation amplitude to the minimal.

Combining Fig. 11 with Figs. 3 and 5; the minimum temperature fluctuation amplitudes also correspond to the minimum total temperature differences; the larger ΔT always accompanies the occurrence of larger temperature fluctuation amplitude. These results could be analyzed qualitatively in the following discussions.

Results Analysis

In all heat pipes including the PHP, the saturated state appears at the vapor/liquid interface, where both liquid and vapor have the same saturated temperature. However, in the PHP, the vapor/liquid interfaces may not be located at the evaporator and condenser when the evaporator and condenser undergo temporary dry and subcooled liquid fill, respectively. The positions of saturated condition dynamically vary with oscillation movements. When the evaporator is dry and overheated, the interface moves to somewhere in the middle of the PHP. When the evaporator is filled by liquid slug or painted with liquid film after liquid slugs pass, the saturated condition shows in the evaporator. As a result, the PHP temperature wall-to-wall measurements do not directly reflect saturated temperature and pressure distributions. Based on this point, PHP tube material effect and ΔT variation versus operating temperature are analyzed as below.

As a critical factor impacting PHP performance, PHP material properties not only affect thermal conduction resistance, but also govern the startup mechanism of oscillation and PHP operation. At the incipience shown in the upper portion of Fig. 13, when heat starts to enter PHP, long liquid slugs and vapor bubble form because of evaporation in the evaporator and condensation in the condenser. Due to heat transfer along the tube wall, oscillation movements are initiated by evaporation, which first occurs at the closest liquid slug/vapor interface to the evaporator. In this procedure, the Δx from the evaporator to the closest liquid slug and tube material conductivity decide the starting ΔT for initiating. If the thermal conductivity of the PHP tube material is low, such as stainless steel, a large ΔT is expected prior to the PHP start. At lower fill ratio (larger Δx), PHP is even failed to start. After PHP starts, lower thermal conductivity of the tube wall weakens heat transfer to interface and increases dryout time in the evaporator, temperature fluctuations, and the total temperature difference.

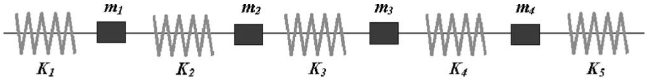

Fig. 14 Model of oscillation movement of PHP

An analysis of ΔT variation versus PHP operating temperature is conducted from two viewpoints. First, from a static mechanical balance viewpoint, the schematic in Fig. 13 (the bottom two tubes) illustrates the interaction between saturated pressure differences and flow resistance. The T_1 and T_2 mean the saturated temperature located at PHP turn No.1 and No.2 (close to the evaporator). The P_1 and P_2 are the corresponding saturated pressures. During PHP operating, each oscillation movement pushes liquid slugs to move to an adjacent turn and condenses vapor. When the liquid slug reaches the hot adjacent turn, intense boiling/evaporation caused by liquid wetting the dry surface induces a new oscillation. Assume the inertia force is negligible, the mechanical balance is statically established between pressure difference between the two vapor/liquid interfaces P_2-P_1 and flow friction. Temperature difference between adjacent turn T_1-T_2 represents the evaporator temperature fluctuation and reflects magnitude of flow resistance. Since vapor flow resistance is negligible compared with liquid, liquid viscosity and velocity are main variants of flow resistance ($\Delta P = 32\ \mu_l LV/d^2$). Liquid (water) viscosity rapidly reduces when operating temperature increases, which lowers flow resistance and increases oscillation frequency.

Verified from experimental results, at lower operating temperature, the higher flow resistance needs a larger saturated pressure/temperature difference (T_2-T_1) for oscillation movements. To prepare this condition, stagnations of liquid slugs in the condenser and the dry evaporator is extended. Therefore, the lower oscillation frequency observed experimentally enforces single phase cooling and increases the PHP total temperature difference and fluctuations. With an increase of operating temperature, the lowered flow resistance and therefore enhanced oscillation frequency (velocity) reduce the liquid subcooling duration in the condenser and send warmer liquid to the evaporator. Consequently, single-phase cooling and temperature fluctuation are lowered. The lowest PHP ΔT and temperature fluctuation amplitude shown in Figs. 3 and 11(*a*), respectively, indicate that both the evaporator and condenser are close to saturated conditions; the evaporator is mostly wetted; and heat transfer of the phase change is enhanced to the maximum.

However, the analysis above cannot effectively explain the rise of ΔT and temperature fluctuation when PHP operating temperature continues increasing after the optimal spot (>120°C–160°C). Understanding the mechanism during that period requires considerations from the viewpoint of the dynamic elastic system.

As shown in Fig. 14, an operating PHP can be simplified as a series spring system with mass blocks. Each PHP turn can be looked at as a spring with a mass block. The mechanical energy balance in this system is between kinetic loss caused by flow resistance and expansion work of saturated vapor. Based on the mathematical model described by Ma, et al. [22], the spring and mass block system can be expressed as:

$$\frac{d^2x}{d\tau^2}+\frac{c}{m}\frac{dx}{d\tau}+\frac{k}{m}x=\frac{B}{m}[1+\cos(\varpi\tau)] \tag{3}$$

Here, k is

$$k=\frac{A\rho_v RT}{L_v} \tag{4}$$

From Eq. (4), the effective spring elasticity k represents the compression capability of vapor slugs, and increases when vapor density (operating temperature) increases. That means, at high operating temperature, the spring system becomes firmer and needs a higher pressure difference to maintain the effective oscillation amplitude supplying liquid from the condenser to the evaporator. As results, an increased pressure difference causes a temperature fluctuation increase, extends the liquid stagnation at the condenser, and increases the total PHP temperature difference. From this point, the occurrence of dryout indicates the effective PHP oscillation mechanism is significantly weakened. However, even in the dryout state, oscillation movements still exist (Fig. 8), which leads to the gradual increase of the evaporator temperature.

Conclusions

Based on the experimental results and analysis discussed above, investigations of PHP operation characteristics lead to the following conclusions:

(1) PHP temperature characteristics indicate that the minimal PHP total temperature difference and fluctuation appear at the optimal operating temperature ranging from 120°C to 160°C.
(2) Single phase cooling in the PHP causes a large total temperature difference (between the evaporator and condenser) and fluctuation. Phase change proportion increases at the optimal operation condition.
(3) Variations of the PHP total temperature difference versus operating temperature can be explained through static mechanical balance combining with dynamic elastic oscillation system. The reduction of flow resistance and the increase of system elasticity are critical factors.

Further investigations will be conducted to mathematically model and simulate the PHP temperature effect and to predict the dryout phenomenon.

Acknowledgment

The authors thank The Boeing Company for sponsorship and Mr. Howard Carter for continuous support in this program.

Nomenclature

B = coefficient defined for Eq. (3)
c = coefficient defined for Eq. (3)
d = diameter, m
k = system effective elasticity, N/m
L = length, m
m = mass, kg
P = pressure, Pa
R = gas constant, J/(mol K)
T = temperature, °C
V = velocity, m/s
x = oscillation amplitude, m

Greek symbols

Δ = difference
ρ = mass density, $\mathrm{kg/m^3}$
μ = liquid viscosity, $\mathrm{N\,s/m^2}$
τ = time, s
ω = oscillation frequency, /s

Subscripts

a = adiabatic section
e = evaporator
c = condenser
l = liquid
v = vapor
tc = thermocouple

References

[1] Akachi, H., 1990, U. S. Patent No. 4921041.
[2] Kurzweg, U. H., and Zhao, L. D., 1984, "Heat Transfer by High-Frequency Oscillations: A New Hydrodynamic Technique for Achieving Large Effective Thermal Conductivities," Phys. Fluids, **27**, pp. 2624–2627.
[3] Akachi, H., 1996, U. S. Patent No. 5490558.
[4] Miyazaki, Y., and Akachi, H., 1996, "Heat Transfer Characteristics of Looped Capillary Heat Pipe," *Proceedings of 5th International Heat Pipe Symposium*, Australia, pp. 378–383.
[5] Maezawa, S., Gi, A., Minamisawa, K., and Akachi, H., 1995, "Thermal Performance of Capillary Tube Thermosyphon," *Proceedings 9th Int. Heat Pipe Conference*, Vol. 2, pp. 791–795.
[6] Nishino, S., 1999, "Oscillatory-Flow Heat-Transport Device (Force Oscillatory Flow Type and Bubble Driven Type), Pipe," *Proceedings of 11th Int. Heat Pipe Conference*, pp. 39–45.
[7] Gi, K., Fumiaki, S., and Maezawa, S., 1999, "Flow Visualization Experiment on Oscillating Heat Pipe," *Proceedings of 11th Int. Heat Pipe Conference*, pp. 166–169.
[8] Tong, B. Y., Wong, T. N., and Ooi, K. T., 2001, "Closed-loop Pulsating Heat Pipe," Appl. Therm. Eng., **21**, pp. 1845–1862.
[9] Lin, L., 2001, "Experimental Investigation of Oscillation Heat Pipes," J. Thermophys. Heat Transfer, **15**, pp. 395–400
[10] Lin, L., 2000, "Heat Transfer Characteristics of an Oscillation Heat Pipe," AIAA-2000–2281.
[11] Cai, Q. J., Chen, R. L., and Chen, C. L., 2002, "An Investigation of Evaporation, Boiling, and Heat Transport Performance in Pulsating Heat Pipe," *Proceedings of HTD in 2002 IMECE*, IMECE2002–33334.
[12] Cai, Q. J., Chen, C. L., and Asfia, J., 2005, "Applications of Heat Pipe Technologies in Avionics System for Aerospace Vehicle," *Thermophysics Conference 43rd AIAA Aerospace Sciences Meeting and Exhibit*, Reno.
[13] Khandekar, S., Dollinger, N., and Groll, M., 2003, "Understanding Operational Regimes of Closed Loop Pulsating Heat Pipes: An Experimental Study," *Applied Thermal Engineering*, Elsevier Science, New York Vol. 23, No. 6, pp. 707–719.
[14] Chandratilleke, R. G., Hatakeyama, H., and Nakgome, H., 1996, "Development of Loop Heat Pipes for Cryogenic Applications," *Proceedings of 5th International Heat Pipe Symposium*, Australia, pp. 397–404.
[15] Zuo, Z. J., North, M. T., and Ray, L., 1999, "Combined Pulsating and Capillary Heat Pipe Mechanism for Cooling of High Heat Flux Electronics," *Proc. of the ASME Heat Transfer Division*.
[16] Katoh, T., Amako, K., and Akachi, H., 2000, "MCHP (Meandering Capillary-Tube Heat Pipe) for Avionics Cooling," *Proceedings of NHTC'00*, NHTC2000–12163.
[17] Miyazaki, A., 1996, "Heat Transfer Characteristics of Visible Looped Pipes," *Proceedings of 5th International Heat Pipe Symposium*, Australia, pp. 384–389.
[18] Ma, H. B., Maschmann, M. R., and Liang, S. B., 2002, "Heat Transport Capability in a Pulsating Heat Pipe," AIAA 2002–2765.
[19] Wong, T. N., Tong, B. Y., Lim, S. M., and Ooi, K. T., 1999, "Theoretical Modeling of Pulsating Heat Pipe," *Proceedings of 11th International Heat Pipe Conference*, Japan, pp. 159–163.
[20] Shafli, M. B., Faghri, A., and Zhang, Y., 2001, "Thermal Modeling of Unlooped and Looped Pulsating Heat Pipes," *Proceedings of 2001ASME Int. Mech. Eng. Congress and Exposition*.
[21] Zhang, Y. W., and Faghri, A., 2002, "Heat Transfer in a Pulsating Heat Pipe with Open End," Int. J. Heat Mass Transfer, **45**, pp. 755–764.
[22] Ma, H. B., Hanlon, M. A., and Chen, C. L., 2001, "An Investigation of Oscillation Motions in a Pulsating Heat Pipe," *Proceedings of NHTC'01*, NHTC2001–20149.
[23] Akachi, H., Polasek, F., and Stulc, P., 1996, "Pulsating Heat Pipes," *Proceedings of 5th International Heat Pipe Symposium*, Australia.
[24] Maezawa, S., Nakajima, R., Gi, K., and Akachi, H., 1996, "Experimental Study on Chaotic Behavior of Thermohydraulic Oscillation in Oscillating Thermosyphon," *Proceedings of 5th International Heat Pipe Symposium*, Australia, pp. 131–137.
[25] Miyazki, Y., Polasek, F., and Akachi, H., 2001, "Oscillating Heat Pipe," *30th Int. Conf. On Environmental Systems*, 2001–01–2375, France.

Journal of Heat Transfer

Technical Brief

Pool Boiling Experiments on Multiwalled Carbon Nanotube (MWCNT) Forests

Hee Seok Ahn

Nipun Sinha

Mechanical Engineering Department,
Texas A&M University,
College Station, TX 77843-3123

Mei Zhang
NanoTech Institute and Department of Chemistry,
University of Texas at Dallas,
Richardson, TX 75083

Debjyoti Banerjee
Mechanical Engineering Department,
Texas A&M University,
College Station, TX 77843-3123

Shaoli Fang

Ray H. Baughman

NanoTech Institute and Department of Chemistry,
University of Texas at Dallas,
Richardson, TX 75083

In this study, two silicon wafer substrates were coated with vertically aligned multiwalled carbon nanotubes (MWCNT) "forests" and were used for pool boiling studies. The MWCNT forests (9 and 25 μm *in height) were synthesized on the silicon wafer substrates using chemical vapor deposition (CVD) process. The substrates were clamped on a cylindrical copper block with embedded cartridge heaters. The heat flux was measured using sheathed K-type thermocouples, which were placed inside the cylindrical copper block. Pool boiling experiments using refrigerant PF-5060 as the working liquid were conducted to obtain the pool "boiling curve." The experiments were conducted in nucleate and film boiling regimes to investigate the effect of MWCNT height on pool boiling performance. Reference (control) experiments were also performed with an atomically smooth bare silicon wafer (without MWCNT coating). The results show that the MWCNT forests enhanced critical heat flux (CHF) by* 25–28 % *compared to control experiments. For the film boiling regime, Type-B MWCNT (*25 μm *in height) yields 57% higher heat flux at Leidenfrost point (film boiling regime) compared to control experiments. However, for the Type-A MWCNT (*9 μm *in height) the film boiling heat flux values are nearly identical to the values obtained for the control experiments performed on bare silicon.*
[DOI: 10.1115/1.2349511]

Keywords: carbon nanotube, CNT, pool boiling, critical heat flux, Leidenfrost boiling, silicon wafer

Introduction

Boiling is the most efficient mode of heat transfer. Hence, it is considered an attractive option for the emerging thermal management schemes. In addition, perturbing various transport mechanisms in boiling is important for energy conversion devices, insulation schemes for cryogenic systems, energy storage, materials processing, and futuristic applications (e.g., ablation cooling for high-speed civil transport). Many researchers reported the enhancement of boiling heat transfer by using novel materials or structures. Ramaswamy et al. [1] conducted experiments by employing enhanced structures consisting of six layers of copper plates with rectangular channels cut on either side of the plates. The combined effect of the system pressure and liquid subcooling on the boiling performance of the enhanced structure was studied in these experiments. The authors reported that boiling heat flux increased on the enhanced structures. The combined effects of subcooling and system pressure were also found to augment the boiling heat flux on the enhanced structures. Mudawar and Anderson [2] performed pool-boiling experiments using multiple levels of enhanced surfaces on a pin fin and obtained critical heat flux (CHF) of 105.4 $\mathrm{W/cm^2}$ and 159.3 $\mathrm{W/cm^2}$ using FC-72 as a working fluid under saturated and subcooled conditions (for 35°C liquid subcooling), respectively. Coursey et al. [3] used graphite foams for pool-boiling experiments. The effects of chamber pressure, liquid level, and working fluid on nucleate boiling were reported in this study. The thermal conductivity of the component graphite ligaments in the foams was reported to be five times higher than for copper. The thermal diffusivity of bulk graphite foam was reported to be four times that of aluminum due to the higher thermal conductivity and lower density. The authors reported that using graphite foams as an evaporator in a thermosiphon enhanced cooling for a fixed wall temperature, especially at lower chamber pressure. The enhanced cooling at lower pressure can be attributed to a decrease in saturation temperature, which corresponds to an increase in wall superheat (for a fixed wall temperature).

After discovery of carbon nanotubes (CNT) in 1991 by Iijama [4], there has been a growing interest for various applications of CNT. CNT have very broad range of thermal, electrical, and struc-

---

Contributed by the Heat Transfer Division of ASME for publication in the JOURNAL OF HEAT TRANSFER. Manuscript received November 8, 2005; final manuscript received May 29, 2006. Review conducted by Ramendra P. Roy.

Table 1 Thermo-physical properties of PF-5060 at atmospheric pressure [6]

Property	Liquid	Vapor
Density, $\mathrm{kg/m^3}$	1610.68	12.52
Kinematic viscosity, $\mathrm{kg/m^3}$	2.78×10^{-7}	1.15×10^{-6}
Prandtl number	9.8	0.81
Specific heat, J/kg-K	1132.62	651
Thermal conductivity, W/m-K	0.0539	0.0124
Surface tension, N/m	8.448×10^{-3}	
Latent heat of vaporization, J/kg	85034.34	

tural properties that can be tailored to various molecular structural types (length, diameter, and orientation). According to Berber et al. [5], the thermal conductivity value of CNT is 6600 W/m K (around 17 times higher than that of copper) at room temperature and drops drastically to 3000 W/m K (around eight times higher than that of copper) at 400 K.

In this study, the effect of nanostructured surfaces on pool boiling was studied for nucleate and film boiling regimes. The aim of this study was to explore the physics of the transport mechanisms during pool boiling on nanostructured surfaces. The ultimate goal is to understand the transport mechanisms on the nanoscale and therefore prepare the foundations for developing new methods for augmenting heat transfer.

The nanostructured surfaces were realized by the synthesis of vertically aligned multiwalled carbon nanotubes (MWCNT) on atomically smooth silicon wafer substrates using chemical vapor deposition (CVD) process. An experimental apparatus was built for pool boiling studies that consisted of a viewing chamber containing a heater unit. The silicon wafer substrate with either the nanostructured surface or the atomically smooth bare surface was clamped on the heater unit and pool boiling experiments were performed on these surfaces. The property values of the working fluid (PF-5060, manufactured by 3M Co.) are listed in Table 1 [6].

Experimental Apparatus

The experimental apparatus used in this study consists of: (i) a viewing chamber, which is used to house; (ii) a heater unit; and (iii) a silicon substrate clamped on top of the heater unit. The voltage signals from the thermocouples embedded in the heater unit were recorded using a computer-controlled high-speed data acquisition system. Figure 1 shows the schematic diagram of the experimental setup.

Heater Unit. A heater unit was mounted inside the viewing chamber. The heater unit was fabricated by enclosing the cylindrical copper block (8.89 cm dia) inside an annular steel jacket. The annular steel jacket was used to prevent any boiling from occurring on the sides of the copper block. A silicon wafer was placed on top of the copper block and clamped with an annular steel disk. A Pyrex® wafer was placed between the silicon wafer and the copper block to minimize the electrical noise from heaters. Five cartridge heaters were placed in the copper block (three of 500 W rating and two of 300 W rating, manufactured by Watlow Inc.). Twelve K-type thermocouples were flush mounted inside holes drilled at different depths and radial locations along the side of the copper block. One thermocouple was placed in the liquid PF-5060 to ensure the bulk liquid was maintained at saturation temperature.

Synthesis and Growth of MWCNT on Silicon. MWCNT forests were grown on the silicon wafer using chemical vapor deposition (CVD) techniques. The MWCNT structures were uniform in height (Fig. 2(*a*)). Two different heights of MWCNT forests were used in the experiments: with heights of 9 and 25 μm, respectively. The heights of MWCNT were selected so that one is smaller and the other is greater than the dynamic value of the minimum vapor film thickness in film boiling. According to numerical and experimental results by Banerjee and Dhir [7,8] and Banerjee et al. [9], the dynamic values of the minimum vapor film thickness in film boiling of PF-5060 is $\sim 15-20\ \mu$m. Figure 2 shows the SEM images of the silicon wafer substrates containing MWCNT forests. Typically, the vertically aligned MWCNT “for-

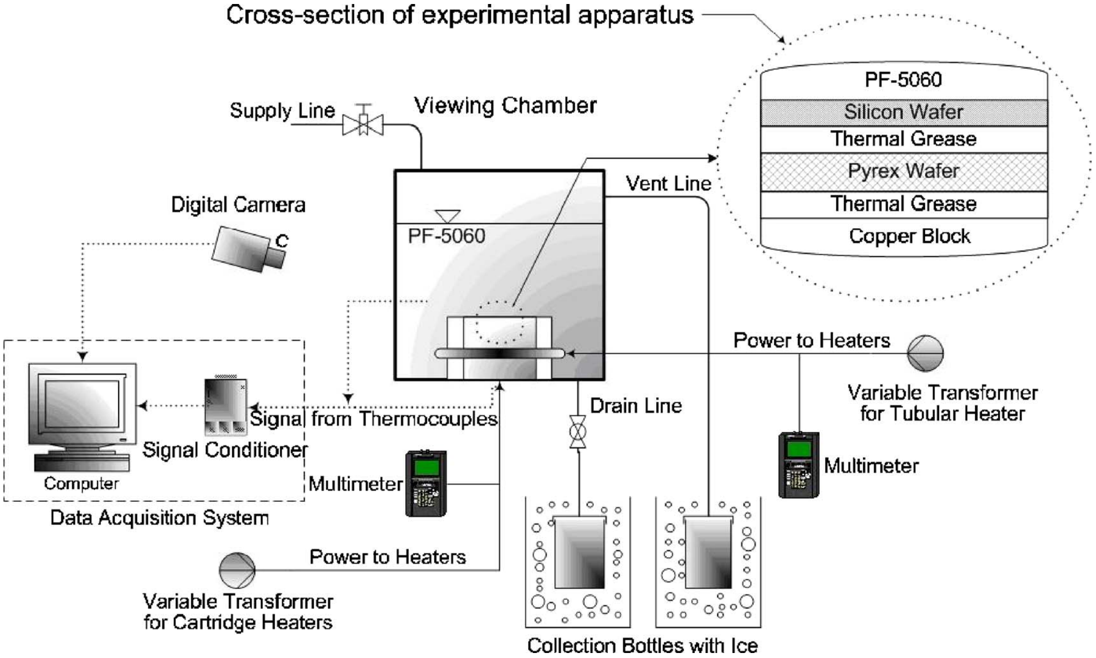

Fig. 1 Schematic diagram of experimental apparatus consisting of: (1) viewing chamber, (2) heater apparatus, and (3) silicon wafer surface with multiwalled carbon nanotube (MWCNT) forests

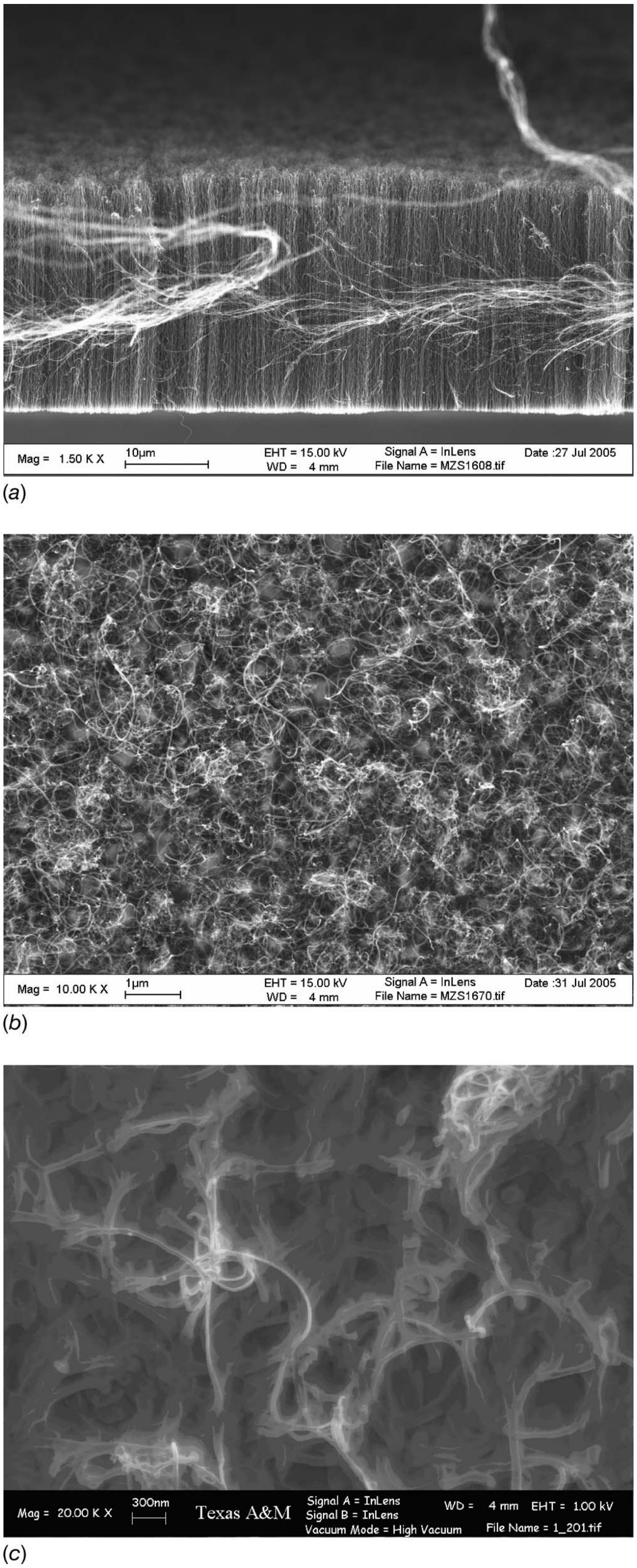

Fig. 2 SEM image of type-B MWCNT (25 μm in height) synthesized on silicon substrate: (*a*) side view before experiment, (*b*) top view before experiment, and (*c*) top view after experiment

ests” are synthesized using the CVD process—by flowing 5 mol.% C_2H_2 at 580 sccm (standard cubic centimeters per minute) in He at atmospheric pressure in a quartz tube maintained at 680°C. To obtain MWCNT of desired height, the synthesis time can range from a few seconds to ~10–20 min since the growth rates of the MWCNT are ~1–2 μm/min. Prior to performing CVD synthesis of MWCNT an iron film of 5 nm thickness was deposited on the silicon wafer by electron beam evaporation to serve as a catalyst. Earlier investigations [10] using SEM and thermal gravimetric measurements indicated that the purity of the synthesis process was very high (~96–98% Carbon in the form of MWCNT) with 2–4% Fe and amorphous carbon. No carbon particles were observed in these tests. The diameter of the vertically aligned MWCNT varied from ~8–16 nm. The CVD process results in nucleation and growth of the MWCNT on a random pitch of ~8–16 nm on the silicon substrate, resulting in a high surface coverage and high surface density of the nanotubes. Therefore, the surface density of the MWCNT was not controlled in this nanosynthesis process. Details about the CVD process for synthesis and growth of MWCNT forests are described in [10].

Experimental Procedure

Pool boiling experiments were conducted under steady-state conditions. The voltage input to the heaters was adjusted by a variac and increased from 13 V to 35 V in increments of 3–5 V for obtaining the nucleate boiling segment of the boiling curve until the maximum heat flux condition (critical heat flux (CHF)) was reached. Incrementing the input voltage by ~0.5 V beyond CHF resulted in transition boiling and rapid increase in temperature of the heater apparatus. The input voltage was then reduced progressively until stable film boiling was obtained. During film boiling, the voltage was reduced in steps of ~0.5–2 V until transition boiling was obtained. This procedure was used to estimate the “hysteresis” in the boiling curve. Typically, each voltage setting required 2–3 h to obtain steady state and required a total time of ~24–36 h to conduct each experiment.

Before starting each experiment, the liquid pool was boiled using a tubular heater that was installed around the steel jacket. This was performed to remove any dissolved gases in PF-5060 and to heat the side-walls of the viewing chamber so that rapid convergence to steady-state conditions could be obtained. During the experiments, especially at lower superheats, the input power to the tubular heater was adjusted by a variac in order to maintain the liquid temperature in the pool at the saturation temperature of PF-5060 (56°C). The working liquid was periodically replenished into the pool to maintain the liquid level within a height of 3.2–4.5 cm above the boiling surface during the experiments. Typically, the liquid level was replenished after recording each steady-state data and required ~2–3 h of waiting time for obtaining steady-state temperature conditions after each replenishment.

After steady-state conditions were reached, the temperatures from the wire-bead K-type thermocouples (embedded in the copper block) were recorded with a computer-controlled high-speed data acquisition system. The data acquisition system consisted of NI SCXI-1102C Analog MUX, and PCI-6251 DAQ board with Pentium-4 3.2 GHz computer, and controlled by a software program coded using LABVIEW 7.1 (Manufactured by National Instruments). To ensure that the working liquid was maintained at saturation temperature, the temperature from a thermocouple submerged in the liquid pool was continuously recorded and monitored.

Data Reduction

The heat flux [in watts per meters squared] was evaluated from the gradient of the temperature profiles in the copper block

$$q'' = -k\frac{\Delta T}{\Delta x} \tag{1}$$

where k is the thermal conductivity of the copper block (watts/meter Kelvin), ΔT is the temperature difference between two thermocouples lying in the same vertical plane [in degrees Celsius], and Δx is the distance (in meters) between the thermocouples.

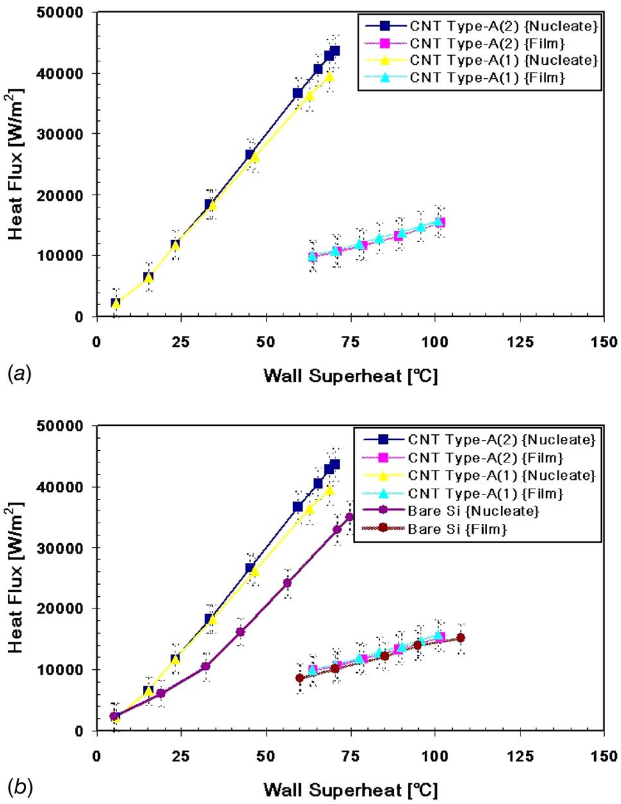

Fig. 3 Saturated pool boiling curve for PF-5060 on type-A MWCNT (9 μm in height) synthesized on silicon wafer. Saturation temperature of PF-5060=56°C. (*a*) Pool boiling curve for PF-5060 on type-A MWCNT. (*b*) Comparison of pool boiling curve of type-A MWCNT with bare silicon. (the numbers in parenthesis denote the experimental run.)

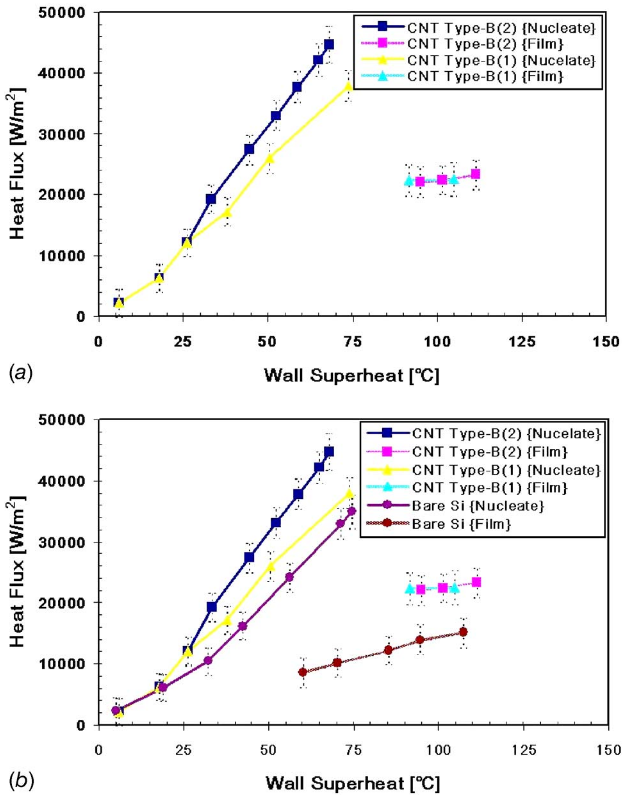

Fig. 4 Saturated pool boiling curve for PF-5060 on type-B MWCNT forests (25 μm in height) synthesized on silicon wafer. The saturation temperature of PF-5060=56°C. (*a*) Pool boiling curve for PF-5060 on type-B MWCNT. (*b*) Comparison of pool boiling curve for type-B MWCNT with bare silicon (the numbers in parenthesis denote the experimental run).

In this experiment, the wall temperatures were calculated by utilizing thermal resistance values obtained from prior temperature measurements using surface micromachined thin film thermocouple (TFT) on the silicon wafer [11]. From these experiments [11], the correlation of the thermal resistance (R_t (watts/degrees Kelvin)) between the silicon wafer surface (at the boiling surface) and top of the copper block in nucleate and film boiling regime was

$$R_t = (-4 \times 10^{-4})T_c + 0.2302 \text{ (nucleate boiling);}$$

$$R_t = 0.1037 \text{ (film boiling)} \tag{2}$$

where T_c is the temperature at top surface of the copper block (degrees Celsius) obtained from the embedded thermocouples.

The wall temperature was calculated using Eq. (3).

$$T_w = T_c - q''A_wR_t \tag{3}$$

where, T_w is the wall temperature (degrees celsius), A_w is the boiling area (meters squared). The experimental uncertainties for q'' (and, therefore, R_t) in these experiments was ±15.5% and ±20.5% in nucleate and film boiling, respectively [11].

The uncertainty of the heat flux and the heat transfer coefficient in boiling were calculated using Kline and McClintock method [12] as follows:

$$\frac{\omega_{q''}}{q''} = \sqrt{\left(\frac{\omega_k}{k}\right)^2 + \left(\frac{\omega_{\Delta T}}{\Delta T}\right)^2 + \left(\frac{\omega_{\Delta x}}{\Delta x}\right)^2} \tag{4}$$

where ω is the statistical uncertainty value for each variable.

The uncertainty in determination of the vertical distance between two thermocouples embedded in the copper block was estimated to be ±3.0%, which was determined by the machining accuracy. The uncertainty of the thermal conductivity of the copper block was assumed to be ±1.0% based on thermophysical property table [13]. The uncertainty in determination of the temperature difference was estimated from a number of sources. Since 16 bit precision was used in the data acquisition hardware the absolute precision was ±0.005°C, based on the temperature range chosen for the experiment. From the room-temperature measurements using thermocouples embedded inside the copper block the deviation was less than ±0.05°C. The total uncertainty of temperature differential was estimated to be ±5.4% at CHF and ±21.7% at minimum heat flux (MHF). Therefore, the total experimental uncertainties for the wall heat flux were estimated to be ±7.9% and ±28.5% at CHF and MHF points, respectively.

Experimental Results

A reference (control) experiment was performed using an atomically smooth bare silicon wafer. The effect of surface imperfections (e.g., cavities, grooves, etc.) on pool boiling was therefore eliminated using the bare silicon wafer. With commercial substrates (e.g., copper) the differences in distribution of the surface cavities on different substrates could make the boiling heat transfer data inconsistent for comparison. The control experiment therefore provides a consistent reference for the heat transfer augmentation due to presence of the different types of MWCNT. Also, by eliminating the effects of surface cavities—the complexities of the thermofluidic transport mechanisms are reduced. This helps to understand the physics of the boiling process on the MWCNT and to estimate the contribution to the total heat flux from the nano-structured surfaces compared to atomically smooth substrates.

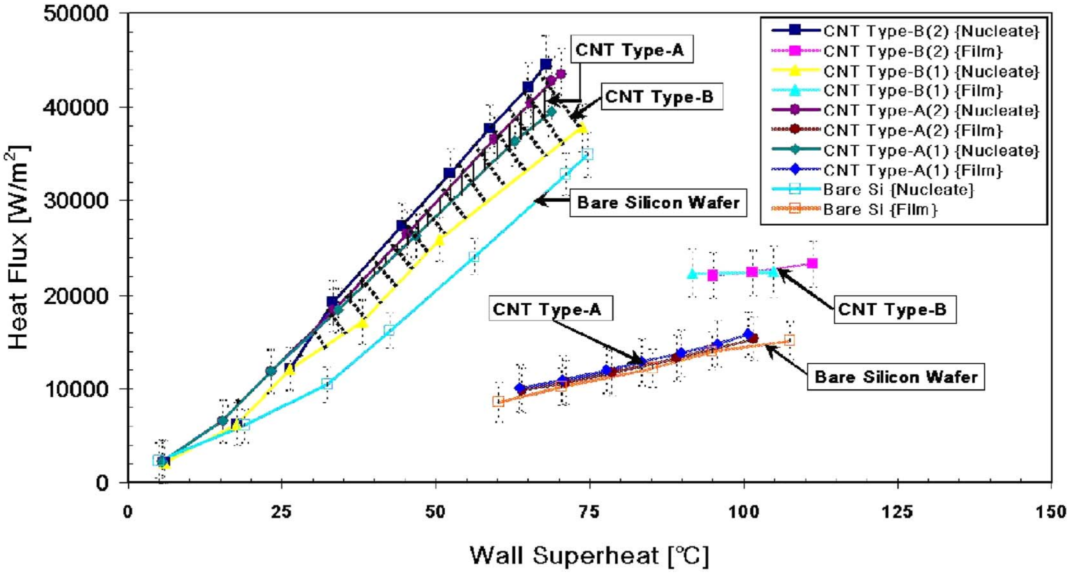

Fig. 5 Comparison of saturated pool boiling curve for PF-5060 on bare silicon and MWCNT synthesized on silicon. The MWCNT are of two different heights: type-A MWCNT (9 μm in height) and type-B MWCNT (25 μm in height). Saturation temperature of PF-5060=56°C (the numbers in parenthesis denote the experimental run).

Type-A MWCNT Forests (9 μm in height). Experiments were conducted for Type-A MWCNT forests deposited on a silicon wafer (height of MWCNT forests was 9 μm). Figure 3(*a*) shows the pool boiling curve obtained from experiments for the type-A MWCNT. No incipience excursion was observed in these experiments. The CHF point was obtained at wall superheat of 69°C, and the associated heat flux was 3.95×10^4 W/m^2. The experiment was repeated, and the CHF was obtained at wall superheat of 70°C with a heat flux value of 4.35×10^4 W/m^2.

On a bare silicon wafer, boiling inception was recorded at 3.2°C wall superheat (Fig. 3(*b*)). No incipience excursion was observed in these experiments. Critical heat flux (CHF) was achieved at 3.5×10^4 W/m^2 for a wall superheat of 75°C. The Leidenfrost point (MHF (minimum heat flux) in film boiling) was obtained at wall superheat of 60°C with an associated heat flux of 0.86×10^4 W/m^2. The difference in the wall superheat between the CHF and Leidenfrost points was ~15°C. The nucleate boiling heat fluxes are 25% lower than for type-A MWCNT.

In the film boiling regime, nearly identical heat flux values were obtained (within the bounds of the experimental uncertainty) for the two experimental runs with type-A MWCNT and bare silicon. The Leidenfrost point was found to occur at wall superheat of 64°C. The wall superheat at Leidenfrost point for type-A MWCNT forests is 4°C higher than that for bare silicon wafer. At the Leidenfrost point, the heat flux was 0.98×10^4 W/m^2, which is 14.4% higher than that for the bare silicon wafer. For type-A MWCNT forests, the difference in wall superheat between the CHF and Leidenfrost points is around 6°C (this is less than half of the corresponding difference for the bare silicon wafer).

Experiments Using Type-B MWCNT Forests (25 μm in height). Figure 4(*a*) shows the experimental results conducted with the type-B MWCNT forests deposited on a silicon wafer (height of MWCNT forests was 25 μm). As shown in Fig. 4, the heat flux values measured in nucleate boiling during the first experiment is smaller than the second experiment. On visual observation the MWCNT forests were found to contain two scratch marks, less than a centimeter long, on the edge of the wafer (possibly from the clamp) at the conclusion of the first experiment. However, on performing visual observation after the second experimental run, the MWCNT forests were found to be unaffected. For both experiments using type-B MWCNT, no incipience excursion was observed.

The heat fluxes in nucleate boiling for type-B MWCNT is less than that obtained for type-A MWCNT. However, the heat fluxes for type-B MWCNT are still higher than that for bare silicon wafer. The type-B MWCNT has lower heat flux at CHF point compared to type-A MWCNT, even though the wall super heat at CHF point is significantly higher than that for type-A MWCNT. The measured heat flux and the wall superheat at CHF point for type-B MWCNT were 3.79×10^4 W/m^2 and 74°C, respectively, for the first experimental run. The heat flux value and the associated wall superheat at CHF point were 4.46×10^4 W/m^2 and 68°C, respectively, for the second experimental run. This value of heat flux for type-B MWCNT is 28% higher than for bare silicon.

For the two trials with type-B MWCNT, CHF was obtained at 74°C and 68°C. On increasing the temperature beyond CHF conditions, a combination of nucleate and film boiling was observed. The film boiling region was localized near outer the edge of the

Table 2 Critical heat flux (CHF) and minimum heat flux (MHF) values for bare silicon, type-A MWCNT (9 μm), and type-B MWCNT (25 μm)

	Critical heat flux (CHF)		Minimum heat flux (MHF)	
	CHF$\times10^{-4}$ (W/m^2)	T_w-T_{sat}(°C)	MHF$\times10^{-4}$ (W/m^2)	T_w-T_{sat}(°C)
Bare Si	3.49	75	0.86	60
Type-A	4.35	70	0.98	64
Type-B	4.46	68	2.21	95

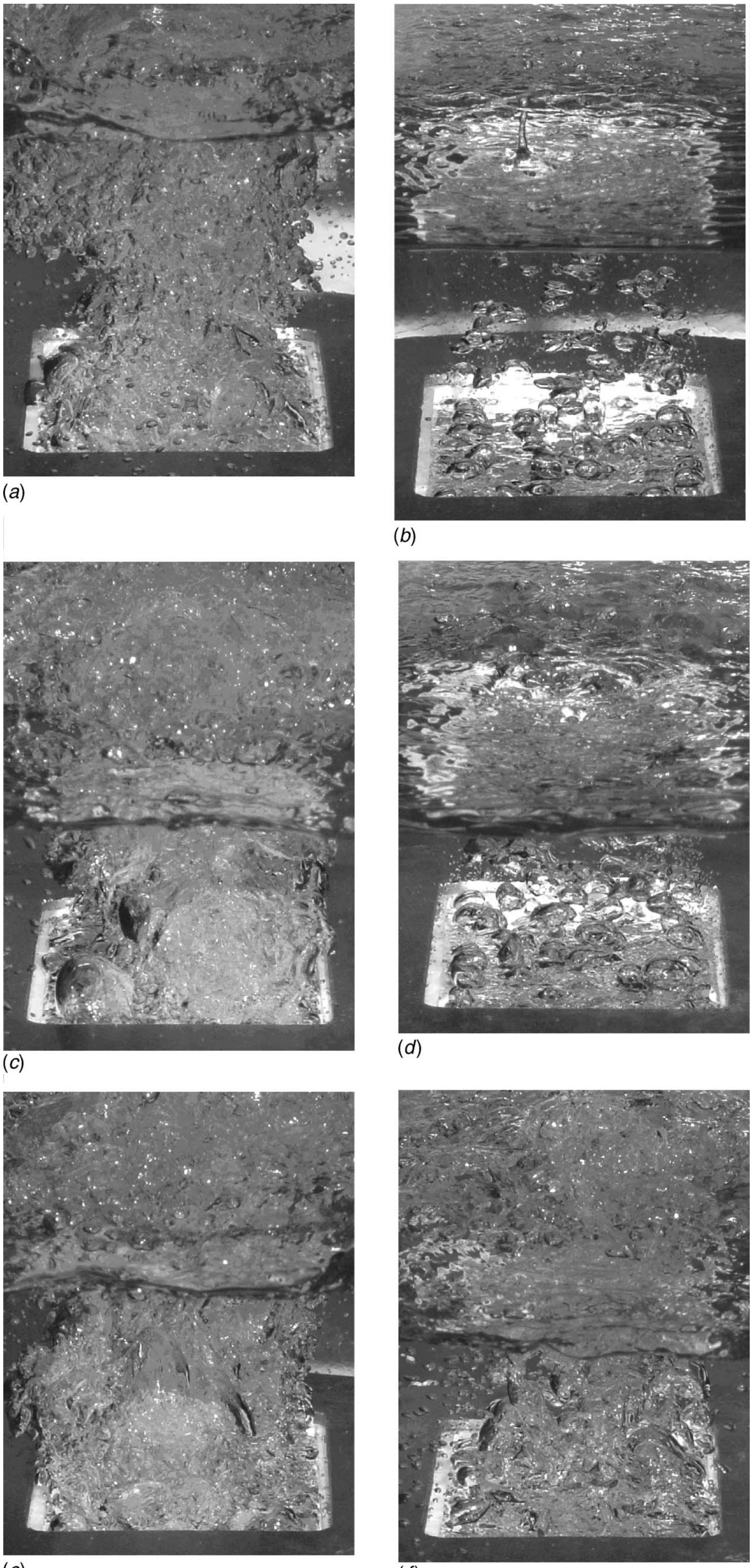

(*a*) (*b*) (*c*) (*d*) (*e*) (*f*)

Fig. 6 Images of boiling obtained during the experiments: (*a*) near CHF point on bare silicon wafer, (*b*) near Leidenfrost point on bare silicon wafer, (*c*) near CHF point on type-A MWCNT, (*d*) near Leidenfrost point on type-A MWCNT, (*e*) near CHF point on type-B MWCNT, and (*f*) near Leidenfrost point on type-B MWCNT

silicon wafer (near the clamps), and the nucleate boiling region was localized in the center of the silicon wafer. This is characteristic of transition boiling regime. For wall superheats exceeding 105°C, a continuous vapor film was observed over the whole area of the exposed wafer.

For film boiling regime, the heat flux for type-B MWCNT is higher than that for bare silicon. The heat flux measured near Leidenfrost point (at wall superheat of 95°C) for type-B MWCNT was 2.21×10^4 W/m^2, which is 57% higher than that for bare silicon at the same wall superheat. Figure 4(*b*) shows a comparison of pool boiling curve for type-B MWCNT with bare silicon.

The effect of MWCNT forests (types A and B) on pool boiling is compared to that of the bare silicon wafer in Fig. 5. For nucleate boiling regime, type-A and type-B MWCNT forests have higher heat flux values than that for bare silicon at each of the data points for different wall superheat. The heat flux at CHF for type-A and type-B MWCNT are higher than for bare silicon. From the results, it can be concluded that the MWCNT enhances nucleate boiling heat flux, but the height of MWCNT is not a sensitive parameter.

For film boiling regime, the heat flux for type-B MWCNT is higher than that for type-A MWCNT and bare silicon. However, within the bounds of the experimental error - the heat flux values are almost identical for type-A MWCNT and the bare silicon wafer in the film boiling regime. The results show that the longer MWCNT enhances the film boiling performance and shifts Leidenfrost point to a higher superheat. The critical heat flux and minimum heat flux values are summarized in Table 2.

Figure 6 shows representative images of the various boiling regimes observed in the experiments. The images were obtained using Sony CyberShot DSC-P10 Digital Camera. As shown in the images obtained at CHF conditions in Fig. 6(*a*), 6(*c*), and 6(*e*), type-A and type-B MWCNT showed more vigorous ebullition of bubbles. For the images of film boiling at Leidenfrost point in Fig. 6(*b*), 6(*d*), and 6(*f*), the vapor film was clearly visible in the form of a shiny "mirror" type surface for bare silicon and type-A MWCNT. However, the area occupied by the shiny "mirror" type surface for type-B MWCNT was reduced in size and a larger proportion of the boiling area was covered with departing vapor bubbles. The images also show that the sizes of the departing bubbles are smaller, and there are larger numbers of bubble departure sites for type-B MWCNT (than type-A MWCNT or bare silicon). The images show that the vapor film was disrupted during film boiling over type-B MWCNT leading to formation of larger number of sites for bubble departure. Such disruptions of the vapor film were not observed for type-A MWCNT or bare silicon wafer, and consequently, the number of bubble departure sites was less compared to type-B MWCNT. Also, the bubble departure sites were observed to be more evenly spaced compared to type-B MWCNT. Figure 2 shows SEM images of the type-B MWCNT forests (using Zeiss 1530 VP FE-SEM at the Microscopy and Imaging Center at Texas A&M University) obtained before and after the boiling experiments were conducted. The SEM image in Fig. 2(*b*) was obtained before performing the boiling experiments and shows a network of threadlike MWCNT structures on the top surface. Figure 2(*c*) was obtained after performing the boiling experiments and at a higher magnification. The images show that the MWCNT are virtually identical before and after the experiments were conducted. This demonstrates that boiling experiments did not affect the inherent morphology of the MWCNT.

Discussion

The experimental results are consistent with numerical models reported in the literature. Earlier studies [7–9] predicted that the dynamic values of the minimum vapor film thickness in film boiling of PF-5060 are ~15–20 μm. The authors had discussed that surface roughness (or surface structures) greater than 10 μm could disrupt the vapor films leading to possible collapse of film boiling. It is observed that for type-B MWCNT (height of 25 μm) the film boiling heat flux is enhanced considerably compared to type-A MWCNT (height of 9 μm). This shows that MWCNT forests with heights greater than 10 μm possibly disrupt the vapor film.

The numerical study by Banerjee et al. [9] also demonstrated the existence of "cold spots" in film boiling. Cold spots are regions of lower surface temperature than the surrounding. The study [9] showed that cold spots serve as focused conduits for heat transfer in film boiling. The size of the cold spots was found to increase with the heater conductivity and resulted in higher average heat flux. Since MWCNT has higher thermal conductivity than the silicon substrate the efficacy of the cold spots in transferring heat is enhanced due to the presence of MWCNT. MWCNT structures that disrupt the vapor film at the minimum vapor film thickness (which is collocated with the cold spots) would further enhance transient heat transfer by inducing liquid-solid contacts. This is also expected to augment heat transfer by transient quenching of the surface. Hence, type-B MWCNT forests augment film boiling heat flux while for type-A MWCNT forests it is almost identical to bare silicon.

In contrast, the nucleate boiling heat flux is less sensitive to the height of MWCNT forests. Since the pitch of the MWCNT fibers are ~8–16 nm, it is expected that the nucleation mechanisms are considerably different compared to a conventional surface (where the size of nucleation cavities are typically ~5–10 μm dia). On nanostructured surfaces, the continuum models are not applicable since slip flow conditions would exist due to noncontinuum effects. The bubble nucleation potentially occurs on the exposed tip of the MWCNT. If the working liquid wets the MWCNT (e.g., PF-5060), it would penetrate the space between the nanotubes. For a poorly wetting liquid (e.g., for water on MWCNT), air or vapor layer can be trapped in the space between the nanotubes [14]. Inception of bubbles within the MWCNT is improbable due to the high superheats that are required for nucleation.

Conclusions

The results obtained from boiling experiments on vertically aligned multiwalled carbon nanotubes (MWCNT) of two different heights (type A: 9 μm and type B: 25 μm) are summarized as follows:

1. MWCNT forests are found to augment critical heat flux by ~25–28% compared to control experiments.
2. Enhancement of nucleate boiling heat flux is not found to be sensitive to the height of the MWCNT forests.
3. In contrast, the film boiling heat flux is strongly sensitive to the height of the MWCNT forests. For type-B MWCNT (25 μm in height) the heat flux is enhanced by 57% compared to control experiments. However, for type-A MWCNT (9 μm in height) the heat flux values are similar to the control experiments. This is consistent with models for film boiling reported in the literature.
4. SEM images for the top view of the MWCNT structures obtained before and after the experiments show that the boiling experiments did not affect the inherent morphology of the MWCNT structures.

The mechanisms causing heat flux augmentation are identified as follows: (i) the high conductivity of MWCNT compared to the silicon substrate resulting in higher sensible heat transfer (conduction and convection); (ii) larger sized cold spots leading to higher average heat flux; (iii) vapor film collapse caused by MWCNT; (iv) enhanced liquid-solid contacts resulting in transient quenching of the surface; and (v) the enhanced surface areas resulting from the presence of MWCNT in the form of "nanofins."

Acknowledgment

The authors gratefully acknowledge support from the Texas Engineering Experimentation Station and the Mechanical Engineering Department. Access to laboratory facilities by Dr. S. Lau at Texas A&M is gratefully acknowledged. FE-SEM acquisition was supported by the National Science Foundation (Grant No. DBI-0116835).

Nomenclature

A_w = wall area on which boiling occurs
R_t = Thermal resistance
T = temperature
k = thermal conductivity
q'' = heat flux
x = distance

Greek symbols

Δ = difference
ω = uncertainty

Subscripts

c = top surface of copper block
sat = saturation
w = wall of a silicon wafer (at boiling side)

References

[1] Ramaswamy, C., Joshi, Y. K., Nakayama, W., and Johnson, W. B., 2000, "Combined Effects of Sub-cooling and Operating Pressure on the Performance of a Two-Chamber Thermo-Siphon," IEEE Trans. Compon. Packag. Technol., **23**(1), pp. 61–69.

[2] Mudawar, I., and Anderson, T. M., 1993, "Optimization of Enhanced Surfaces for High Flux Chip Cooling by Pool Boiling," ASME J. Electron. Packag., **115**, pp. 89–100.

[3] Coursey, J. S., Roh, H., Kim, J., and Boudreaux, P. J., 2002, "Graphite Foam Thermosyphon Evaporator Performance: Parametric Investigation of the Effects of Working Fluid, Liquid Level, and Chamber Pressure," *Proceeding of the ASME IMECE 2002*, New Orleans, LA, Paper No. 2002-33733.

[4] Iijima, S., 1991, "Helical Microtubules of Graphitic Carbon," Nature (London), **354**, pp. 56–58.

[5] Berber, S., Kwon, Y. K., and Tomanek, D., 2000, "Unusually High Thermal Conductivity of Carbon Nanotubes," Phys. Rev. Lett., **84**, pp. 4613–4616.

[6] Banerjee, D., 1999, "Numerical and Experimental Investigation of Subcooled Film Boiling on a Horizontal Plate," Ph.D. thesis, University of California, Los Angeles.

[7] Banerjee, D., and Dhir, V. K., 2001, "Study of Subcooled Film Boiling on a Horizontal Disc, Part 1: Analysis," ASME J. Heat Transfer, **123**, pp. 271–284.

[8] Banerjee, D., and Dhir, V. K., 2001, "Study of Subcooled Film Boiling on a Horizontal Disc, Part 2: Experiments," ASME J. Heat Transfer, **123**, pp. 285–293.

[9] Banerjee, D., Son, G., and Dhir, V. K., 1996, "Conjugate Thermal and Hydrodynamic Analysis of Saturated Film Boiling From a Horizontal Surface," ASME HTD, 334, Part 3, pp. 57–64.

[10] Zhang, M., Fang, S., Zakhidov, A. A., Lee, S. B., Aliev, A. E., Williams, C. D., Atkinson, K. R., and Baughman, R., 2005, "Strong, Transparent, Multifunctional, Carbon Nanotube Sheets," Science, **309**, pp. 1215–1219.

[11] Ahn, H. S., Sinha, N., and Banerjee, D., 2005, "Micromachined Temperature Sensor Arrays for Studying Micro-scale Features in Film Boiling," *Proceedings of the ASME-IMECE 2005*, Orlando, Nov. 5–11, ASME.

[12] Kline, S. J., and McClintock, F. A., 1953, "Describing the Uncertainties in Single Sample Experiments," Mech. Eng. (Am. Soc. Mech. Eng.), **75**, pp. 3–8.

[13] Mills, A. F., 1999, *Heat Transfer*, 2nd ed., Prentice-Hall, Englewood Cliffs, NJ.

[14] Krupenkin, T. N., Taylor, J. A., Schneider, T. M., and Yang, S., 2004, "From Rolling Ball to Complete Wetting: The Dynamic Tuning of Liquids on Nanostructured Surfaces," Langmuir, **20**(10), pp. 3824–3827.

Journal of Heat Transfer

Discussion

Discussion: "Dynamics of Bubble Motion and Bubble Top Jet Flows From Moving Vapor Bubbles on Microwires" (Christopher, D. M., Wang, H., and Peng, X., 2005, Journal of Heat Transfer, 127, pp. 1260–1268)

Irakli G. Shekriladze
Prof.
Head of Laboratory of Hydrodynamics and Heat Transfer,
Georgian Technical University,
77, Kostava Street, GTU,
0175 Tbilisi, Georgia
e-mail: shekri@geo.net.ge

In the paper [1] the results of experimental investigation and numerical modeling are presented of sliding vapor bubble dynamics through subcooled boiling on microwires. A conclusion is made on the nongravity character of the observed phenomena and the primary role of thermocapillary Marangoni flow. In the following discussion, insufficient relevancy of the model [1] is shown in the context of evaluation of the role of thermocapillarity.

In the view of the further development of boiling heat transfer theory, it is an essentially proper interpretation of experimental data on boiling nongravity dynamical effects [1–6]. Comprehensive multifactorous modeling of subcooled flow boiling [7], among other factors, involves also bubble sliding effects. Another, so-called model of "the theatre of director" [8–10] (leading to universal correlation of developed boiling heat transfer data) is built upon the assumption on the triggering of liquid jets by growing bubbles (pumping effect of growing bubble (PEGB) [11,12]). Besides, just this effect claims to play a leading role in the main part of the fixed-in [1–6] phenomena.

PEGB is linked to the sharp variability of evaporative reactive force applied to a bubble interface during the start of its growth in the zone of the highest temperature gradient [11,12]. Generated in such a way, the pressure gradient covers all liquid boundary layer [13] speeding-up liquid jet flow [12] efficiently contributing in integral heat transfer. To the point, an assumption on the decisive role of the same evaporative reactive force [11,12] forms a basis for the advanced new model of a boiling heat transfer crisis [14].

As distinct to PEGB, Marangoni flow is drived by surface force generated by the gradient of surface tension on an interface with a variable temperature, although both flow schemes are roughly similar.

During boiling of saturated liquid, directly measured and indirectly evaluated jet flow velocities vary in the range 1–5 m/s [2–4,15]. According to a review of experimental data [16], steady-state Marangoni flow around a stationary air bubble varies in the range 0.1–5.0 mm/s. Thereby a sensible contribution of this flow in saturated boiling effects is out of the question, moreso as the temperature field on the vapor bubble interface is strongly smoothed by phase conversion.

Subcooled boiling dynamical effects [1,5,6] (bubble slippage 15–40 mm/s, fluid flows 15–100 mm/s) mainly are observed at the stage of decay of PEGB. At such low velocities the contribution of Marangoni flow in general may be much more tangible. However, interpretation by the model [1] of these dynamical effects evidently contrasts the aforementioned typical values.

There are two potential sources of the overestimation of Marangoni flow velocities by the model [1]: the usage of a very small value of accommodation coefficient (0.03) and considering of steady-state flow.

According to [17], the accommodation coefficient is near unity at the vapor-liquid interface. However, as it is indicated in [1], phase conversion may be affected by noncondensable airs. Nevertheless, the absence of the concrete substantiation of accepted value makes its accuracy questionable. Besides, no consideration is made of the concentration of noncondensables on the condensation side of the bubble interface.

As regards the steady-state approach, it fully excludes the possibility of analysis of the main ("explosive") stage of PEGB. Slippage of a bubble is much calmer but the unsteady-state by its nature phenomenon resulted by a fluid asymmetric unsteady-state temperature field.

The sliding bubble permanently enters new zones and redevelops a fluid velocity field. Besides, parallel to the microwire, the component of fluid flow even changes sign through bubble passage. A corresponding correction may significantly reduce the velocities evaluated by the model [1].

Problems with the adaptation of the Marangoni effect to studied phenomena manifest itself also through an analysis of double-jet flow observed during the same process of subcooled boiling [6].

As thermocapillary Marangoni flow may generate liquid outflow only from the zone of minimum surface temperature, fixed in [6], liquid jets (outgoing from the zone of maximum temperature between a bubble and microwire) may not be linked to thermocapillarity. These jets evidently are speeded-up by volume forces generated under the bottom part of the bubble (as regards division of the jet flow, it may be linked to specific geometry of the system bubble microwire). Accordingly, double-jet flow [6] turns out to be another proof of the basic role of PEGB in nongravity boiling dynamics.

As regards the problem of the full-scale theoretical and experimental investigation of PEGB in general, it still remains pressing with respect to further research of the wide diversity of boiling heat transfer processes.

References

[1] Christopher, D. M., Wang, H., and Peng, X., 2005, "Dynamics of Bubble Motion and Bubble Top Jet Flows From Moving Vapor Bubbles on Microwires," ASME J. Heat Transfer, **127**, pp. 1260–1268.
[2] Subbotin, V. I., Kaznovski, S. P., and Korotaev, S. K., 1970, "Investigation of

Vapor Bubble Dynamics in Boiling of Water on Thin Wires under Natural Convection," At. Energ., **28**, pp. 9–13.

[3] Van Stralen, S. J., Zijl, W., and De Vries, D. A., 1977, "The Behaviour of Vapour Bubbles During Growth at Subatmospheric Pressures," Chem. Eng. Sci., **32**, pp. 1189–1196.

[4] Wang, H., Peng, Christopher, D. M., X. F., Wang, B. X., and Lee, D. J., 2002, "Jet Flow Phenomena during Nucleate Boiling," Int. J. Heat Mass Transfer, **45**, pp. 1359–1363.

[5] Wang, H., Peng, X., Christopher, D. M., W. K. Lin, and Pan, C. 2005, "Investigation of Bubble-Jet Flow During Subcooled Boiling on Wires," Int. J. Heat Fluid Flow, **26**, pp. 485–494.

[6] Wang, H., Peng, X., Christopher, D. M., and Garimella, S. V., 2005, "Jet Flows Around Microbubbles in Subcooled Boiling," ASME J. Heat Transfer, **127**, pp. 802.

[7] Basu, N., Warrier, G. R., and Dhir, V. K., 2005, "Wall Heat Flux Partitioning During Subcooled Flow Boiling: Part 1—Model Development," ASME J. Heat Transfer, **127**, pp. 131–140.

[8] Shekriladze, I. G., and Ratiani, G. V., 1966, "On the Basic Regularities of Developed Nucleate Boiling Heat Transfer," Bull. Georgian Acad. Sci., **42**, pp. 145–150.

[9] Shekriladze, I. G., 1981, "Developed Boiling Heat Transfer," Int. J. Heat Mass Transfer, **24**, pp. 795–801.

[10] Shekriladze, I. G., 1998, "Frozen Pathways to Breakthrough in Boiling Heat Transfer Theory," *Proc. 11th Int. Heat Transfer Conference*, Kyongju, Korea, 2, pp. 474–478.

[11] Shekriladze, I. G., 1966, "On the Mechanism of Nucleate Boiling," Bull. Georgian Acad. Sci., **41**, pp. 392–396 (English version: NASA TM X-59398, 1967, pp. 1–10).

[12] Shekriladze, I. G., Mestvirishvili, Sh. A., Rusishvili, J. G., Zhorzholiani, G. I., Ratiani, V. G., 1980, "Studies in the Mechanism of Boiling and Enhancement of Evaporative Cooling Coefficients," Heat Transfer-Sov. Res., **12**, pp. 91–95.

[13] Schlichting, H., 1979, *Boundary-Layer Theory*, McGraw-Hill, New York.

[14] Kandlikar, S. G., 2001, "A Theoretical Model to Predict Pool Boiling CHF Incorporating Effects of Contact Angle and Orientation," ASME J. Heat Transfer, **123**, pp. 1071–1079.

[15] Afgan, O. N., 1976, *Boiling Liquids Superheat*, Pergamon, Oxford.

[16] Betz, J., and Straub, J., 2001, "Numerical and Experimental Study of the Heat Transfer and Fluid Flow by Thermocapillary Convection Around Gas Bubble," Heat Mass Transfer, **37**, pp. 215–227.

[17] Rose, J. W., 1998, "Interphase Matter Transfer, the Condensation Coefficient and Dropwise Condensation," *Proc. 11th Int. Heat Transfer Conference*, Kyongju, Korea, Vol. 1, pp. 89–104.

Closure to "Discussion: "Dynamics of Bubble Motion and Bubble Top Jet Flows from Moving Vapor Bubbles on Microwires" (Christopher, D. M., Wang, H., and Peng, X., 2005, Journal of Heat Transfer, 127, pp. 1260–1268)"

D. M. Christopher
Thermal Engineering Department,
Tsinghua University,
Beijing, China 100084

H. Wang
School of Mechanical Engineering,
Purdue University,
W. Lafayette, IN 47907

X. Peng
Thermal Engineering Department,
Tsinghua University,
Beijing, China 100084

S. V. Garimella
School of Mechanical Engineering,
Purdue University,
W. Lafayette, IN 47907

Shekriladze points out that the pumping effect of the growing bubble (PEGB) model can also predict jet flows similar to those described in our results [1,2], which we have attributed to Marangoni flow. PEGB is caused by the evaporative reactive force due to vapor recoil, which is most significant along the bottom part of the bubble interface closest to the heated surface during the initial growth period. Shekriladze [3] points out that the PEGB is most significant during saturated boiling and is less important for subcooled boiling. He also expresses concerns about our assumptions for the accommodation coefficient and the steady-state analysis.

Vapor recoil, which is the physical mechanism for the PEGB model, will certainly affect the bubble shape and flow near the bubble base during the initial vapor bubble growth phase during nucleate boiling. This is because the very large temperature differences initially present near the bubble base result in very high initial rates of evaporation. However, our results pertained to relatively stable bubbles, long after they have reached an essentially stable size for relatively long periods of time (several seconds). By this time, the initially high temperature gradients are already drastically reduced by the large initial evaporation rates near the contact line. The vapor recoil is expected to push some flow out from underneath the bubble as the meniscus is pushed out by the vapor recoil pressure, but this effect would be small and limited to very early times. Anderson and Davis [4] noted that this effect is only significant very near the contact line in an evaporating droplet. Nikolayev and Beysens [5] made a similar observation for a growing vapor bubble. They showed that the vapor recoil pushes the receding contact line, thus modifying the interfacial curvature. These curvature changes would then most likely balance much of the vapor recoil pressure, in preference to the pressure in the liquid region being significantly increased. In addition, a gradient in the vapor recoil force along the interface would not create a similar gradient in the liquid region but would also likely change the interface curvature that would create a force to balance much of the vapor recoil force.

Shekriladze [3] also notes that the effect of vapor recoil is much lower in a highly subcooled environment. Since our experiments were conducted at typical subcoolings of approximately 40°C [2] or 60°C [1] in water and 30°C in ethanol [1], the vapor recoil effect would be expected to be insignificant for our conditions.

Shekriladze also questions the use of a steady-state analysis in our models. In numerous cases during the experiments done for this work, the initiation process for the bubble top jet flows was observed visually as shown by Wang et al. [2]. This initiation of the jet flows occurred after the bubble size had remained essentially constant; moreover, the bubble size continued to remain constant during and after the growth of the jet flows. These steady-state jet flows occurred long after the initial temperature gradient had been reduced so that they cannot be attributed to the vapor recoil effect. The jets continue to emanate from the moving bubbles for a relatively long time relative to the bubble growth time; thus, this phenomenon could be construed to be at steady state in the bubble's frame of reference. We believe, therefore, that the steady-state assumption was justified based on our experimental observations.

Shekriladze also questions whether the locations from which the jets leave the bubble are realistic. Very distinct pairs of jets were observed experimentally to develop around stationary, steady-state bubbles [2] and sometimes around moving bubbles [1]. As shown previously [6], the multiple jets were predicted by the Marangoni flow analysis and were found to emanate from more than one cold spot on the bubble interface in some cases. The jets form due to the complex flow of subcooled liquid up around the wire and the bubble. The main reason for this jet formation is that, for bubbles with diameters larger than or similar to the wire diameter, the upward flow of subcooled liquid from below the wire impinges on the bubble interface which is about even with or extends out beyond the wire, as shown in Fig. 1, causing relatively cold spots on either side of the lower half of the bubble (the exact location depending on the bubble size and the subcooling). These cold spots do not form on the top half of the bubble due to the lack of cooling flow impinging on the top surface. The cold spots on the lower parts of the bubble interface on the larger bubbles, therefore, serve as the sources for the multiple experimentally observed Marangoni jets.

Shekriladze's reference to the experiments of Betz and Straub [7] further corroborate the present results. In Ref. [7], the liquid velocities were measured near gas bubbles in various liquids with the liquid being driven against gravity by Marangoni flow. Betz and Straub characterized their results in terms of $\mathrm{Pe}=wB/\alpha$, where w is the tangential velocity, B is the bubble height that is essentially equal to the diameter for small bubbles, and α is the thermal diffusivity. Values of Pe in their work ranged from 150 to 200. For water, the bubble diameters were on the order of 0.1 mm [2], and for ethanol the diameters were approximately 0.2 mm [1]. A value of $\mathrm{Pe}=200$ would then give liquid velocities of 340 mm/s in water and 81 mm/s in ethanol, which agrees with the order of magnitude of the measured and calculated velocities based on Marangoni flow as the driving force [1,2]. Betz and Straub [7] as well as numerous other published studies by Straub and his colleagues concluded that the experimentally observed jet flows around gas or vapor bubbles [8], which were similar to the current observations for vapor bubbles, are due to Marangoni flow in the same manner as described in [1,2,6].

Shekriladze correctly states that the value of the accommodation coefficient continues to be a significant source of uncertainty that requires further investigation. As noted by Marek and Straub [9], the "evaporation and condensation coefficients of water obtained theoretically or experimentally scatter over a rather large range of more than two decades…". The small value of 0.03 for the accommodation coefficient used in the present work con-

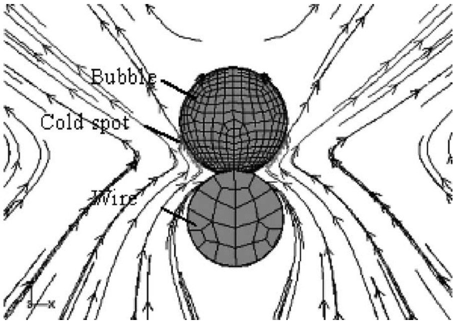

Fig. 1 Predicted pathlines for multijet flow

ducted in glass vessels is consistent with Marek and Straub's [9] additional comment that "even small contaminations of the surface significantly reduce the interfacial mass transfer…. Evaporation and condensation in glass vessels can be strongly hindered by the accumulation of dissolved glass components on the interface." Marek and Straub [9] referred to several studies that all confirm this strong reduction in the accommodation coefficient. The lowest value of the accommodation coefficient given in their review [9] was 0.002 for water in a glass vessel. Hickman [10] noted that the throttling due to evaporation into a saturated vapor rather than into a vacuum would significantly reduce the evaporation coefficient. Hickman also found that very high evaporation coefficients close to unity could only be obtained with moving liquid water in a vacuum where the surface is continually refreshed by the moving stream and the evaporating molecules are immediately removed by the vacuum. In our work, where the surface is not being refreshed as in a moving stream and was almost stationary for the stationary bubbles (except for the Marangoni flow along the interface), a value of 0.03 was adopted based on the comprehensive review of Paul [11] and Hickman's [10] statement (for nonflowing and nonvacuum conditions) that "the consensus, backed by different experiments, has been that not more than one molecule of water in 25, approaching the surface from either side, actually merges with the interfacial layer."

In summary, we contend that these additional results confirm our previous conclusions [1,2] that the experimentally observed jet flows around relatively long-lived, steady-state moving or stationary vapor bubbles in highly subcooled nucleate boiling result from Marangoni flow induced by the temperature gradients along the bubble interface. During the initial bubble growth transient, when the temperature gradients and evaporation rates are very high, the vapor recoil effect would influence the bubble shape, especially the microlayer shape near the contact line, and the liquid flow very near the base. At later times, when the vapor recoil effect is insignificant; the vapor recoil effect is not expected to produce the essentially steady-state jets observed in the experiments.

Acknowledgment

This project was supported by the National Natural Science Foundation of China (Contract No. 50476014).

References

[1] Christopher, D. M., Wang, H., and Peng, X., 2005, "Dynamics of Bubble Motion and Bubble Top Jet Flows From Moving Vapor Bubbles on Microwires," ASME J. Heat Transfer, **127**, pp. 1260–1268.
[2] Wang, H., Peng, X., Christopher, D. M., and Garimella, S. V., 2005, "Jet Flows Around Microbubbles in Subcooled Boiling," ASME J. Heat Transfer, **127**, p. 802.
[3] Shekriladze, I. G., 1998, "Frozen Pathways to Breakthrough in Boiling Heat Transfer Theory," *Proc. Eleventh Int. Heat Transfer Conference*, Kyongju, Korea, 2, pp. 474–478.
[4] Anderson, D. M., and Davis, S. H., 1995, "The Spreading of Volatile Liquid Droplets on Heated Surfaces," Phys. Fluids, **7**, pp. 248–265.
[5] Nikolayev, V. S., and Beysens, D. A., 1999, "Boiling Crisis and Non-Equilibrium Drying Transition," Europhys. Lett., **47**, pp. 345–351.
[6] Wang, H., Christopher, D. M., Peng, X. F., and Wang, B. X., 2005, "Jet Flows From a Bubble During Subcooled Pool Boiling on Micro Wires," Sci. China, Ser. E: Technol. Sci., **48**, pp. 385–402.
[7] Betz, J., and Straub, J., 2001, "Numerical and Experimental Study of the Heat Transfer and Fluid Flow by Thermocapillary Convection Around Gas Bubble," Heat Mass Transfer, **37**, pp. 215–227.
[8] Straub, J., 2000, "Microscale Boiling Heat Transfer Under 0 g and 1 g Conditions," Transp. Res. D, **39**, pp. 490–497.
[9] Marek, R., and Straub, J., 2001, "Analysis of the Evaporation Coefficient and the Condensation Coefficient of Water," Int. J. Heat Mass Transfer, **44**, pp. 39–53.
[10] Hickman, K. C. D., 1954, "Maximum Evaporation Coefficient of Water," Ind. Eng. Chem., **46**, pp. 1442–1446.
[11] Paul, B., 1962, "Complication of Evaporation Coefficients," J. Am. Rocket Soc., **32**, pp. 1321–1328.